Phase Behaviour of Supercooled Liquid Silicon

A Thesis

Submitted For the Degree of

DOCTOR OF PHILOSOPHY

in the Faculty of Science

by

Vishwas V Vasisht

THEORETICAL SCIENCES UNIT
JAWAHARLAL NEHRU CENTRE FOR ADVANCED SCIENTIFIC RESEARCH
Bangalore – 560 064

MARCH 2013

I dedicate this thesis to my parents and my brother

DECLARATION

I hereby declare that the matter embodied in the thesis entitled "**Phase Behaviour of Supercooled Liquid Silicon**" is the result of investigations carried out by me at the Theoretical Sciences Unit, Jawaharlal Nehru Centre for Advanced Scientific Research, Bangalore, India under the supervision of Prof. Srikanth Sastry and that it has not been submitted elsewhere for the award of any degree or diploma.

In keeping with the general practice in reporting scientific observations, due acknowledgement has been made whenever the work described is based on the findings of other investigators.

Vishwas V Vasisht

CERTIFICATE

I hereby certify that the matter embodied in this thesis entitled "**Phase Behaviour of Supercooled Liquid Silicon**" has been carried out by Mr. Vishwas V Vasisht at the Theoretical Sciences Unit, Jawaharlal Nehru Centre for Advanced Scientific Research, Bangalore, India under my supervision and that it has not been submitted elsewhere for the award of any degree or diploma.

Prof. Srikanth Sastry
(Research Supervisor)

Synopsis

This is a synopsis of the thesis entitled **"Phase Behaviour of Supercooled Liquid Silicon"**, delivered by Vishwas V Vasisht of the Theoretical Sciences Unit, Jawaharlal Nehru Centre for Advanced Scientific Research, Bengaluru, India.

In this thesis an exhaustive simulation study of supercooled silicon (modeled by Stillinger-Weber potential for silicon) is presented. The study can be segregated into three main topics, namely (1) liquid-liquid transition, critical point and phase behaviour, (2) structural and dynamic properties of liquid phase and (3) crystal nucleation. These three topics are organized into six chapters. The introductory chapter covers the investigations of liquid silicon pursued over three decades, where salient experimental, theoretical and simulation results are elaborated. In the chapter 2, a brief discussion of computational methods used in this thesis is given. The chapter 3 is devoted to the work on phase behaviour of supercooled silicon, in which an evidence for the existence of a liquid-liquid critical point associated with the liquid-liquid phase transition is presented. The phase diagram of supercooled silicon which includes the liquid-liquid coexistence line, the liquid-liquid critical point, the loci density extrema, compressibility extrema and spinodal is also presented in this chapter. The chapter 4 pertains to the study of structural and dynamic properties of supercooled silicon. As the system transform from a high density liquid to low density liquid, the network of atoms having local tetrahedral arrangement grows and in the low density phase, the network spans the whole system. A strong relationship between local structural arrangement and diffusivity over a wide range of temperature and pressure is

found. A hierarchy of anomalies related to thermodynamics, dynamics and structural order (as first discussed is the case of water) is also found in liquid silicon. The last section of this chapter pertains to the breakdown of Stokes-Einstein (SE) relationship. The locus of SE breakdown temperature at different pressure values is found along with the loci of onset temperature, dynamic heterogeneity and compressibility maxima. The breakdown of SE relation is found to happen in the vicinity of onset temperature. In the chapter 5 the crystal nucleation aspect of supercooled silicon is presented. The crystal nucleation barrier as a function an order parameter which is related to the crystalline nucleus size is calculated along different isobars varying from positive to negative pressure values and for various under-cooling temperatures (18% to 35%). The nucleation barrier and critical nucleus size is found to decrease by an order of magnitude, approaching the low density liquid phase. The role of low density liquid atoms in the mechanism of crystal nucleation in silicon is analysed. A wetting layer of low density atoms is found around the crystalline nucleus. In the concluding chapter the important question about the reliability of Stillinger-Weber potential in describing the behaviour of real silicon is discussed. Structural, dynamical and thermodynamic quantities obtained from the SW potential is compared with available *ab initio* simulations data and experimental data, to provide a critical assessment of the applicability of classical simulation results to real silicon. This chapter ends with a summary of results discussed in this thesis.

Contents

List of Figures

Chapter 1

Introduction

Silicon, the second most abundant element in the earth's crust, is ubiquitous in the form of silica and silicates in the natural world. In the elemental form, it is an essential component of the semiconductor technology. It was first prepared in its amorphous form by J.J. Berzelius and later the crystalline form by H.E. Sainte-Claire Deville [185] in the 1800's. The crystalline and amorphous solid are the two most familiar forms of silicon, which have been studied extensively. The crystalline form of silicon is a tetravalent semiconductor (as is the amorphous solid) and upon melting at $1687K$ at ambient pressure, transforms to a metallic liquid with higher coordination number, around 6. Liquid silicon is relatively less studied, given the elevated temperatures at which it exists. Nevertheless, it has been a subject of substantial experimental, theoretical and computational investigation, both at temperatures above the melting temperature, and in the supercooled and stretched (negative pressure) states. The investigations of the metastable liquid (*see* FIG. 1.1) have been motivated, as this thesis seeks to demonstrate, by fundamental questions regarding (i) the eventual fate of metastable liquids upon deep undercooling and stretching, (ii) the interest in the possibility of a novel transition between two distinct liquid forms in a class of "tetrahedral" liquids to which silicon belongs, and (iii) the role of the thermodynamics of metastable liquid states on the kinetics of phase transformations, particularly to the crystalline state.

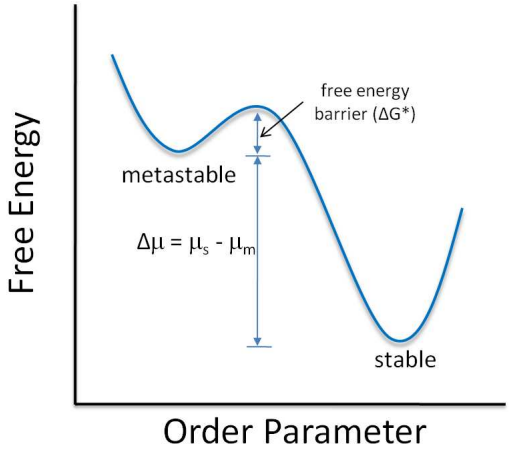

Figure 1.1: The schematic representation of Landau free energy as a function of order parameter. A metastable phase corresponds to a local minimum in free energy in comparison with the global minimum associated with the stable phase. The metastable phase has to cross the *free energy barrier* ΔG^* to transform into a stable phase. Here $\Delta\mu$ is the chemical potential difference between stable phase (μ_s) and metastable phase (μ_m).

Based on the extrapolated Gibbs free energies of amorphous solid and liquid phases for germanium, and a scaling of temperatures for the case of silicon, Bagley and Chen [14] and independently Spaepen and Turnbull [154] suggested a first order phase change from the amorphous solid to the liquid near $T = 1349K$ for silicon, below the freezing point of liquid $T_m = 1687K$. Subsequent experimental as well as simulations studies [24, 30, 45, 99, 116, 131, 132, 167, 174, 183] of non-crystalline silicon supported this notion though the precise nature of the transition was unclear owing to the limited availability of information. Using a two-state model, Aptekar [10, 48] in 1979 proposed a phase diagram that described the liquid and amorphous states as *two states of one noncrystalline (liquid) phase*, and further predicted a negative pressure critical point. The perspective that the transition from amorphous silicon to the liquid should be viewed as a liquid-liquid, rather than an (amorphous)solid-liquid transition, attracted renewed interest in light of an independent proposal of a liquid-liquid transition in

the case of water [125], and the growing appreciation that such a possibility was in principle also applicable to other substances such as, *e. g.* silica [135], which exhibited thermodynamic and structural features similar to water.

The analogy was pursued by Angell *et al.* [5] who proposed a first order liquid-liquid transition line as a feature in the pressure-temperature phase diagram of silicon, based on simulation evidence using the Stillinger-Weber (SW) potential of silicon [159]. The experimental work of Deb *et al.* [39] observed a pressure induced amorphous-amorphous transition and speculated a possibility of an underlying liquid-liquid transition (LLT), to be found at ambient pressure at around ($1400K$). From extensive simulations of silicon using the SW model potential Sastry and Angell [142] found evidence of a liquid-liquid transition at zero pressure at around $1060K$, which was also subsequently supported by *ab initio* simulations [59, 77]. Considerable recent simulation and experimental evidence lends support to the idea of a liquid-liquid transition at ambient pressures in silicon [11, 20, 39, 59–61, 68, 76,77,106–108,120,141,142,148,176]. Computational studies [11,59,76] have also demonstrated the liquid-liquid transition to be from a metallic high temperature liquid to a low temperature liquid with substantially reduced conductivity, which have been recently verified in an experiment [20]. However, such a transition is also consistent with a "critical point free" scenario, proposed recently by Angell [4], and hence, the existence of a critical point needs independent verification.

The supercooled liquid phase being a metastable phase eventual transform in to a stable crystalline phase through an activated process. According to the classical nucleation theory (CNT), a small nucleus of the stable phase can form within the bulk of the metastable phase, due to the thermal fluctuations. The nucleus of the new phase will dissolve and re-form till it reaches a *critical* size upon which the nucleus of stable phase continues to grow till the metastable phase is completely transformed into the stable phase. Formation of the critical nucleus is associated with a free energy barrier (*see* FIG. 1.1) which has to be overcome and this process is called nucleation.

Liquid silicon transform into a stable cubic diamond crystal silicon, a

technologically important material. Recent simulation studies of crystal nucleation mechanism [18,44] have speculated that the low-density liquid phase influence the formation of the crystalline nucleus. Hence there is a need for an extensive study to understand the influence of liquid-liquid transition [142] in supercooled liquid silicon on the crystal nucleation process. A better understanding of the underlying microscopic mechanism of the crystallisation process may help in better crystal processing abilities. Therefore the interest in the study of nucleation of supercooled liquid silicon stems from both fundamental understanding as well as application point of view.

In this thesis we present an exhaustive simulation study of supercooled liquid silicon modeled by the Stillinger-Weber empirical potential [159]. Our study can be segregated into three main topics, namely (1.) liquid-liquid transition, critical point and phase behaviour, (2.) structural and dynamic properties of liquid phase and (3.) crystal nucleation. We organise these studies into seven chapters. The introductory chapter covers the investigations on the liquid and metastable liquid phases of silicon pursued over three decades, where we elaborate on salient experimental, theoretical and simulation results. We broadly divide the investigations into those that address an "amorphous solid to liquid" transition, and those that address a "liquid-liquid" transition in supercooled liquid silicon. The parallel developments in the case of water (and later by extension, other tetrahedral liquids) were aimed at developing an explanatory framework for its anomalous properties. Therefore in this chapter, we describe the various scenarios put forward for fluids exhibiting density and related anomalies. The liquid-liquid transition has been investigated in various materials, including water, silica, carbon and hydrogen, which form a very significant component of our natural world. We mention some of these works at the end of this chapter. In chapter 2, we discuss computational methods and protocols, used in our study of supercooled liquid silicon. Chapter 3 is devoted to the work on phase behaviour of supercooled liquid silicon, in which we provide an evidence for existence of a liquid-liquid critical point associated with the liquid-liquid transition. The phase diagram of supercooled liquid silicon which includes the liquid-liquid coexistence line, the liquid-liquid critical point, the loci of density extrema,

compressibility extrema and the spinodal is also presented in this chapter. In Chapter 4 we describe structural and dynamic properties of supercooled liquid silicon. As the system transforms from a high density liquid to a low density liquid, the network of atoms having local tetrahedral arrangement grows and in the low density phase, this tetrahedral network spans the whole system. A strong relationship between local structural arrangement and diffusivity over a wide range of temperature and pressure is found. A hierarchy of anomalies, as first discussed is the case of water [52], is also found in liquid silicon. The last section of this chapter pertains to the breakdown of the Stokes-Einstein (SE) relationship. The locus of the SE breakdown temperature at different pressure values is found along with the loci of the onset temperature, dynamic heterogeneity and compressibility maxima. The breakdown of the SE relation is found to occur in the vicinity of the onset temperature. In chapter 5 we present an analysis of crystal nucleation in supercooled liquid silicon. The crystal nucleation barrier as a function an order parameter which is related to the size of the crystalline nucleus is calculated along different isobars varying from positive to negative pressure values and for various under-cooling temperatures (18% to 35%). The nucleation barrier and critical nucleus size is found to decrease by an order of magnitude, as the low density liquid phase is approached. The role of low density liquid-like regions in the mechanism of crystal nucleation in high density liquid silicon is analysed. A wetting layer of low density atoms is found around the crystalline nucleus. In chapter 6 the important question about the reliability of the Stillinger-Weber potential in describing the behaviour of real silicon is discussed. We compare structural, dynamical and thermodynamic quantities obtained from the SW potential with available *ab initio* simulations data and experimental data, to provide a critical assessment of the applicability of classical simulation results to real silicon. The concluding chapter contains a summary of results discussed in this thesis.

1.1 Early Work on Metastable Silicon

The earliest experimental work on metastable silicon includes studies carried out by Bagley and Chen [14], Spaepan and Turbull [154], Donovan *et al.* [45] and Thompson *et al.* [167]. Bagley and Chen [14], and independently Spaepen and Turnbull [154], used the available thermodynamic data for germanium (such as the heat capacities measured by Chen and Turnbull [28]), and the kinetics of crystal growth, to estimate the temperature dependence of the excess Gibbs free energy of amorphous and liquid silicon. The significantly different entropies of the two limiting states leads to the prediction (by extrapolation) of a slope discontinuity in the Gibbs free energy, or a first order phase transition from a four coordinated amorphous to a metallic liquid state. The estimated transition temperature was T_{al} at $1349K$ for silicon (by scaling the melting points of germanium and silicon). Later Donovan *et al.* [45,46] performed differential scanning calorimeter (DSC) measurements on amorphous silicon, produced by ion implantation and based on Gibbs free energies deduced, estimated T_{al} to be $1420K$. We show in FIG. 1.2 the Gibbs free energies estimated by Donovan *et al.* [46]. This transition was also confirmed by experiments (using a pulsed-laser melting technique) carried out by Thompson *et al.* [167].

The theoretical analysis of the thermodynamics of supercooled liquid silicon, presented by Aptekar [10] treats the liquid as a two component solution (along lines explored in related contexts by Rappaport [128], Ponyatovsky *et al.* [48, 123]). The two components are characterised by different local bonding environments (covalent or metallic). Correspondingly, the Gibbs free energy of the liquid is written as

$$G_l = G_1(1-\omega) + G_2\omega + W(1-\omega)\omega + RT[\omega\log\omega + (1-\omega)\log(1-\omega)] \quad (1.1)$$

The parameter ω describes the *degree of metallisation* and is determined by the equilibrium condition of the liquid. Writing the free energy difference between the two pure liquids G_1 and G_2 phenomenologically, and using values for the various parameters involved from available experimental data,

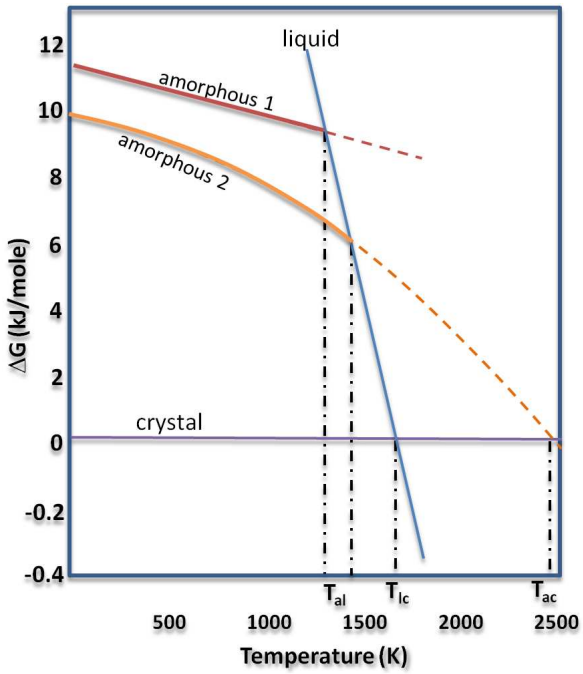

Figure 1.2: An estimate of excess Gibbs free energy (ΔG) against temperature suggesting a first order transition. The brown and orange solids lines represent two extreme estimates of ΔG for the amorphous phase and the dashed lines are extrapolation of these ΔG into the liquid phase. The blue line shows ΔG for the liquid phase and the purple line is the reference crystal phase value. T_{al}, T_{lc} and T_{ac} represent liquid-amorphous, crystal-liquid and crystal-amorphous phase transition temperatures respectively. [Adapted from Donovan *et al.* [46] with permission.]

Aptekar estimated phase diagrams for germanium and silicon, showing in each case that the liquids exhibit metastable, negative pressure, liquid-liquid critical points. Although this analysis is motivated by high pressure transformation of semiconductors to metallic states, this analysis also offers a rationalisation of results concerning the transformation of amorphous silicon to liquid upon heating.

Given the difficulties in experimental studies of extreme states of matter (high undercooling, high temperatures, pressures *etc*), computer simulations have, over the last few decades, helped gain insights into states that are hard

to probe experimentally. Unlike in experiments, it is a relatively simpler task to explore a wide range of temperatures and pressures in simulations and thus bracket the region of interest for further experimental verification. For more than three decades computer simulation studies of silicon have been carried out using various empirical interaction potentials (a comparative study of six different empirical potential is given in the reference [15]) and also using first principle simulations [59, 76, 117, 173]. One of most widely used potential [5, 11, 24, 99, 142] for studying silicon in computer simulations is the Stillinger-Weber (SW) potential [159]. Using the SW potential in molecular dynamics (MD) simulations, Broughton and Li [24] performed one of the earliest studies of the liquid, crystal and amorphous phase diagram of silicon. In this work Broughton and Li found that the crystal and liquid phases are well represented by the SW potential, but the thermodynamics of the amorphous phase is poorly described and that the supercooled liquid phase does do not undergo a first order transition to an amorphous state upon cooling. Luedtke and Landman [99] showed that this failure to obtain amorphous silicon *via* direct cooling of the melt in simulations is related to the quench rates employed. These authors [99] noted that upon cooling, a sharp change in the energy and density of the system occurred at $T \sim 1060K$ followed by a slow variation in these properties as cooling continues to $T = 300K$. These authors compared their system obtained from quenching with the amorphous phase obtained from an alternate method (involving tuning of coefficient of three body part of the SW potential) and found that both the systems have comparable structural composition. Angell *et al.* [5] using the SW potential explored a relatively wide range of temperature and pressure to chart out the phase diagram of metastable silicon. These authors also suggested a well defined transition, at $T \sim 1060K$, from a highly diffusive liquid states to a non-diffusive "amorphous phase", with a coordination number of 4.1. The phase diagram as suggested by Angell *et al.* is shown in FIG. 1.3 (note that at higher pressures, the transition occurs at lower temperatures, leading to a negatively sloped transition line).

As noted earlier, the work of Angell *et al.* [5] made contact with the possibility of a liquid-liquid transition in the case of water, which had been

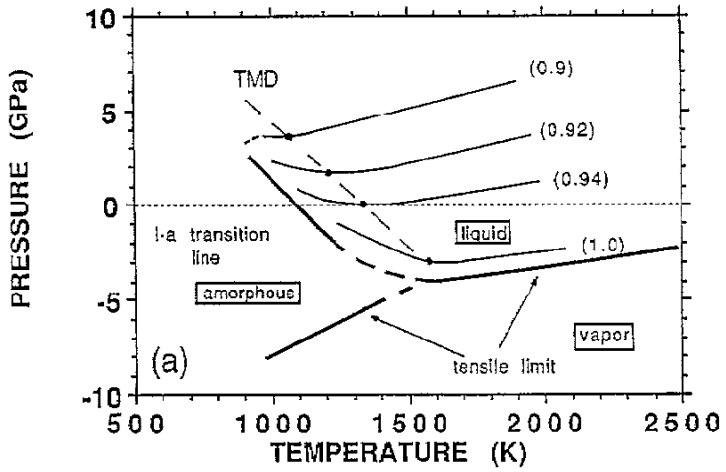

Figure 1.3: Phase diagram proposed by Angell *et al.* [5] based on simulations of the SW potential, with a liquid-amorphous transition line that is negatively sloped. Also shown are the locus of density maxima and the tensile limit line. [From Angell *et al.* [5] with permission.]

proposed as one of the possible scenarios within which to understand the anomalous properties of water. Since these scenarios are relevant for further discussion we present in the chapter on *Phase behaviour of supercooled liquid silicon*, we review them briefly in the next section.

1.2 Scenarios for Liquids Displaying Thermodynamic Anomalies

It is well known that ice floats on water, owing to the solid form having a lower density than the liquid. It is also well known that liquid water has the maximum density at ambient pressure at $4°C$, below which the density *decreases* as temperature decreases, contrary to the normal behaviour wherein liquids become denser as the temperature decreases. Hence, the decrease in density of water with temperature is described as *anomalous*. The temperature at which the density is maximum depends on pressure, and the

locus of these maxima is termed as the temperatures of maximum density (TMD). In water the TMD line is negatively sloped at the positive pressures in the (P, T) plane. Liquid water also shows anomalous behaviour in thermodynamic quantities like compressibility (K_T) and heat capacity (C_P). The compressibility of water, at ambient pressure, decreases with a decrease in temperature like any other liquid, but reaches a minimum at $46°C$. Below this temperature the compressibility increases with a decrease in temperature and shows an apparent divergence at $-45°C$ [156] when only the anomalous component of the compressibility is considered. The specific heat capacity of liquid water also shows a similar behaviour, reaching a minimum at $36°C$ and diverging at around $-47°C$ [8]. Water also shows anomalous behaviour in its dynamical properties. The diffusivity of liquid water increases with increase in pressure which is abnormal for liquids. The work of Errington and Debenedetti [52] identifies a region in the phase diagram where the structure of the liquid behaves anomalously. This work also found that the anomalies in density and diffusivity occur within the structurally anomalous region (in (ρ, T) as well as in (P, T) plane). In the case of silicon, even though simulations have predicted anomalies similar to that of water (discussed in chapter 3 and 4), experimentally none of the anomalies have been verified yet since these anomalies are found at deeply undercooled state points and hence avoiding nucleation poses a technological challenge.

Various models and scenarios (based on thermodynamic constraints) have been developed to explain the thermodynamic anomalies of water [25,40,110], (and by extension, other liquids with water-like anomalous behaviour, including silicon) which are briefly discussed in this section. The observation of negative melting curves in various systems including water and silicon, means (from the Clausius-Clapeyron relation $dP/dT = \Delta S_m/\Delta V_m$, and assuming that the entropy of the crystal is lower than that of the liquid) that the liquid density will be greater than that of the solid phase. This is a feature that is typical of the substances to which the considerations in this section apply.

Below, we describe some of the scenarios that have been explored as a way of rationalising the thermodynamics of liquids displaying anomalies,

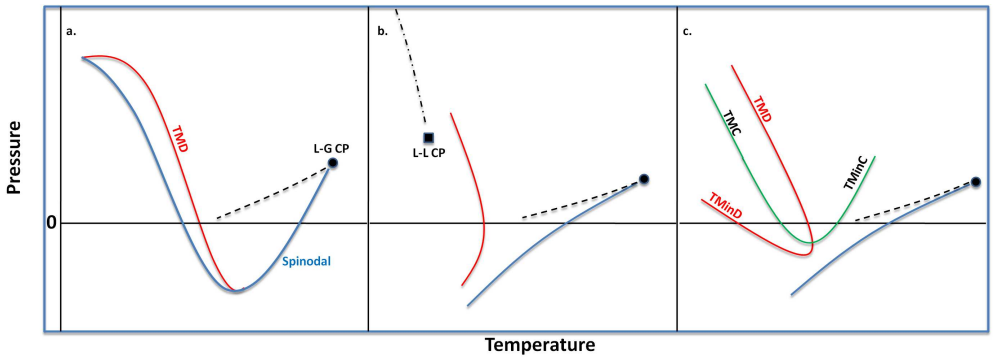

Figure 1.4: The schematic phase diagrams in the pressure-temperature (P, T) plane illustrating three scenarios for liquids displaying anomalous thermodynamic behavior. (a.) The spinodal retracing scenario. (b.) The liquid-liquid critical point scenario. (c.) The singularity free scenario. The green lines represent the locus of compressibility extrema, and the red lines the locus of density extrema. The dashed and dot-dashed lines represent liquid-gas and liquid-liquid transition lines, and the blue lines represent the liquid-gas spinodal.

such as water. These are: (1.) the stability limit conjecture [40, 43, 155, 156], (2.) the liquid-liquid critical point scenario [125], (3.) the singularity free scenario [143] and (4.) the critical point free scenario [4].

The stability limit conjecture: The anomalous increase in water's heat capacity and compressibility with decrease in temperature, with apparent power law divergences at $T_s = 228K$ [156] was conjectured by Speedy [155] to be due to the approach to a spinodal line originating from the liquid-gas critical point (a spinodal line is defined by the condition $(\partial P/\partial V)_T = 0$). This spinodal has a positive slope in the (P, T) plane near the critical point, but upon intersection with the negatively sloped TMD line, goes through a zero slope according to the thermodynamic condition $(dP/dT)_{spinodal} = (\partial P/\partial T)_{isochore}$ and retraces to higher pressures with a negative slope. Hence in this scenario the spinodal constitutes both the superheating and supercooling limit of the liquid. Debenedetti and D'Antonio [36, 43] further proposed that thermodynamic consistency also requires that the TMD line must necessarily have an end point. The TMD

line should either intersect a density minima locus (locus of temperature of minimum density - $TMinD$) and hence the liquid shows a normal behaviour in its density or terminate by intersecting at a spinodal curve (FIG. 1.4 (a)). Although some theoretical works have shown that [23, 138, 144] a re-entrant spinodal is present in models with water like properties, no compelling experimental experimental verification exists of this scenario [42].

The liquid-liquid critical point scenario: Poole *et al.* [125] investigated the retracing spinodal scenario using molecular dynamics simulations of the ST2 model of water. In their simulation study, the spinodal was found to be a monotonic function of T. The TMD line, although having a negative slope at high pressures, changes to positive slope at low pressures (FIG. 1.4 (b)). Hence no intersection between the spinodal and the TMD line occurs. Instead the authors found evidence for a second critical point, between two forms of the liquid. Considerable simulation and theoretical investigations since the original work of Poole *et al.* support the possibility of a second critical point [2,67,109,124,126,137,190]. Indeed earlier theoretical analyses using a two state description [10, 128] also generically lead to this possibility [33]. There has been a substantial amount of experimental work to verify the possibility of a liquid-liquid transition in water that has lead to much evidence in support of this possibility, including recent work on confined water as a way of circumventing crystallisation in bulk water experiments [97, 102, 109, 191]. Such evidence has been critically reviewed in [42, 54, 71].

The singularity free hypothesis: Sastry *et al.* [143] proposed that a minimal scenario that was consistent with the salient anomalies did not require recourse to any thermodynamic singularities, such as a critical point or a retracing spinodal. They analysed the interrelationship between the locus of density and compressibility extrema, and showed that the change of slope of the locus of density maxima (TMD) was associated with an intersection with the locus of compressibility extrema (TEC) (FIG. 1.4 (c)). The relation between the temperature dependence of isothermal compressibility at

the TMD and the slope of the TMD is given by

$$\left(\frac{\partial K_T}{\partial T}\right)_{P,TMD} = \frac{1}{v}\frac{\partial^2 v/\partial T^2}{(\partial P/\partial T)_{TMD}} \tag{1.2}$$

where K_T is the isothermal compressibility. The subscript P and TMD represents the slope at constant pressure and at the TMD at a given pressure. Since $\partial^2 v/\partial T^2 > 0$ at the TMD, the above relation shows that for an anomalous liquid exhibiting a negatively sloped TMD, the isothermal compressibility at constant pressure increases upon decreasing temperature and hence such increases in compressibility are not *a priori* an indication of singular behaviour. Calculations with a lattice model displaying the singularity free scenario [90, 129, 143] reveal a line of compressibility maxima at low temperatures. The metastable critical point scenario may be considered to be a special case where the compressibility along the line of compressibility maxima diverges (at the critical point). Alternatively, the singularity free scenario can be described as a limiting case where the critical point moves to zero T [55].

Critical point free scenario: Recently Angell [4] has discussed a possibility, related to some of the early observation of Speedy and Angell [156], in which the high temperature liquid encounters a spinodal at positive pressure, but this is a spinodal associated with a first order transition between two liquid states. Such a first order transition however does not terminate in a critical point, but may terminate at the liquid-gas spinodal. A weaker version of this picture is that no critical point may exist at positive pressures. Analysis of a model calculation by Stokely *et al.* [160] indicates that such a scenario may indeed arise in the limit of extreme co-operativity of hydrogen bond formation.

1.3 Recent Studies of Metastable Silicon

As described before, the early studies of metastable silicon [5, 14, 24, 45, 99, 154, 167] probed the possibility of a liquid-amorphous transition. More recent work has attempted to find evidence that the transition is one between two

liquid phases. In this section we present a brief discussion of these works.

1.3.1 Experimental Studies

Experimental studies of supercooled liquid silicon are very challenging because of high crystallisation rates. To explore supercooled states by cooling from the high temperature liquid, one would need to quench the liquid at rates exceeding $10^9 K s^{-1}$ [68] to avoid crystallisation and hence using simple quenching techniques to study the deeply undercooled metastable liquid silicon is not possible. Alternate methods like chemical vapour deposition and pressure induced techniques [68] have been employed to study the amorphous phase. Studies have been also performed using methods like aerodynamic levitation [9, 75, 86] or electromagnetic levitation [50, 69, 73, 84, 85, 182] to avoid crystallisation induced by the containers during the experiments.

In silicon, the phase change from a low density liquid (LDL) to a high density liquid (HDL) involves a change in electrical conductivity (from a low temperature semiconducting to a high temperature metallic state), which in turn presents a number of measurable properties that can be used to detect the phase transition. Optical micrograph methods have been used to measure the change in optical reflectivity upon a change in phase [107], and the luminescence of the material is also used to detect the phase transition [39]. X-ray diffraction spectra and Raman spectra have also been used to observe the phase transition [39,107]. Experimental measurement of densities is quite difficult but *in-situ* measurement of structural quantities and electronic properties have been reported by various groups [20,50,69,70,73,91,130,145,182].

Evidence for a pressure induced amorphous-amorphous transition in silicon was first shown by Deb *et al.* [39]. These authors studied porous silicon - π-Si (silicon having nano-porous holes in its microstructure and a large surface to volume ratio) because of its luminescence property. At ambient pressure π-Si exhibits red luminescence upon irradiating with an argon laser. With the application of pressure (using a diamond anvil cell) the luminescence shifted to longer wavelengths and became opaque at around $P = 10GPa$. X-ray diffraction measurements showed that at around $P = 7$

to $8GPa$ the crystal diffraction pattern disappears and a broad diffraction pattern, characteristic of an amorphous material, is observed. At around $P = 10$ to $12GPa$, the crystalline peak disappears entirely. The authors performed Raman scattering measurements both during compression and decompression and found that upon compression to $P = 13GPa$, the sharp crystalline feature at around wave number $520cm^{-1}$ disappears, and a broad peak appears between 200 to $400cm^{-1}$, distinct from the Raman signature of a tetrahedral low density amorphous (LDA) silicon (a broad peak around 400 to $500cm^{-1}$). This feature is interpreted as due to transformation to a high density amorphous (HDA) phase. Upon decompression, this feature disappears giving way to a broad peak around 400 to $500cm^{-1}$, which corresponding to the LDA at low pressure. These observation led to the conclusion that π-Si undergoes a pressure induced amorphous-amorphous phase transition. In turn, this amorphous-amorphous transition was suggested to be related to a liquid-liquid transition, employing a theoretical model [118]. The schematic phase diagram of metastable silicon is shown in FIG. 1.5.

Direct optical observation and electrical resistance measurements carried out on amorphous silicon by McMillan *et al.* [107] showed that the HDA is highly reflective and the LDA phase is non-reflective (*see* FIG. 1.6). From the electrical resistance measurements the authors found that there is an abrupt decrease in resistivity across the LDA-HDA transition around $P = 11GPa$, indicating a transformation to metallic HDA. The sample was verified to be in its amorphous state (using Raman spectroscopy), since pressure induced crystallisation to β-Sn phase could also lead to a drop in resistivity.

The above experiments suggest the possibility of a liquid-liquid transition but are performed under conditions at which the amorphous forms of silicon are solid. In an attempt obtain a more direct evidence that the transition is between two liquids, Hedler *et al.* [68] performed ion bombardment experiments on amorphous silicon. The plastic deformations they observe of the samples are similar to the deformation seen in conventional glasses undergoing the glass transition, and the authors deduce a glass transition of around $1000K$.

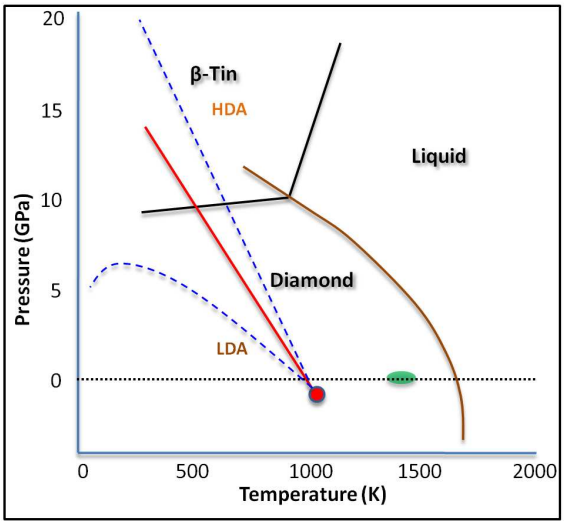

Figure 1.5: The schematic phase diagram of metastable silicon in the pressure-temperature (P, T) plane discussed in [35,39]. The brown line represents the liquid-crystal (cubic diamond) transition line, extended into the β-tin phase. The black lines represent the liquid-β-tin and the cubic diamond-β-tin transition lines. The red line is the liquid-liquid transition line ending at a critical point represented by a red circle. The blue dotted lines represent spinodals associated with the liquid-liquid transition. The green oval represents the amorphous-liquid transition as predicted by some of the earlier experiments [14, 45, 154]. [Adapted from McMillan [35, 39] with permission.]

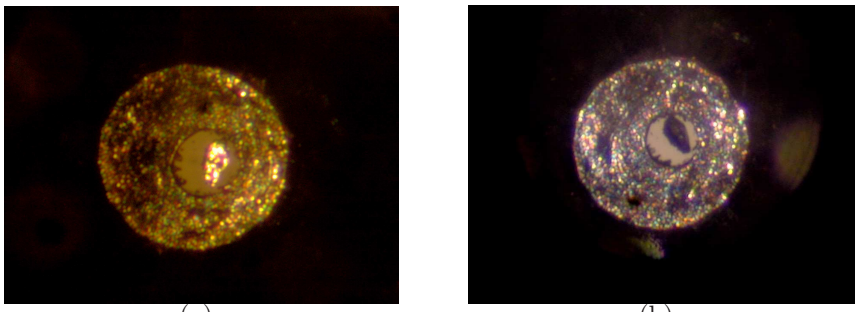

(a) (b)

Figure 1.6: Optical micrographs of an amorphous silicon sample show that HDA at $P = 16.6GPa$ (left) is highly reflective and LDA at $P = 13.5GPa$ (right) is non-reflective (compared to the surrounding metal gasket). [With permission from McMillan and Daisenberger [34, 107].]

Simulations using classical interaction potential as well as in *ab initio* simulations predict the liquid-liquid transition in supercooled liquid silicon [11, 59, 61, 75, 108, 142, 176] and this transition has been characterised in different ways including a change in coordination number as well as the electronic properties. The LDL phase has coordination number ~ 4 and is less metallic than the 5 coordinated HDL phase. Different Experimental groups have tried to measure the coordination number seeking evidence for liquid-liquid transition. To circumvent the container induced crystallisation these experiments are carried out by levitating the sample. The coordination number obtained from different experimental reports are put together in FIG. 1.7. With the state of the art in experimental techniques, the lowest temperature achievable, keeping the sample in liquid state, is around $T = 1380K$ [84]. As it can be seen from FIG. 1.7, there is quite a large spread in the coordination numbers as calculated from different experimental groups. Secondly in the measured range of temperatures the coordination number remains greater than 5. These results do not agree with the predicted liquid-liquid phase transition temperature at ambient pressure from earlier experimental works, and this issue needs to be understood properly. A possible explanation is that the coordination number is quite sensitive to the density of the liquid (a quantity which is difficult to measure in experiments). Another possibility is that indeed the previous estimates of the transition temperature are high.

Recently, Beye *et al.* [20] used femto-second pump-probe spectroscopy, examining the expected changes in the electronic structure of silicon and hence attempting a direct verification of the liquid-liquid transition, by monitoring the evolution of electronic density of state (DOS). After exciting a sample of the crystal with a pump X-ray pulse, they monitored the evolution of the electronic DOS, and found it to evolve in a two step process, with the intermediate step showing clear resemblance to the DOS of LDL, and the DOS at later times resembling that of the HDL phase. Although the process during which these measurements are made are highly non-equilibrium in nature and there are gaps in our understanding, these results point the way to how direct evidence for the liquid-liquid transition under extreme metastable conditions may be obtained experimentally.

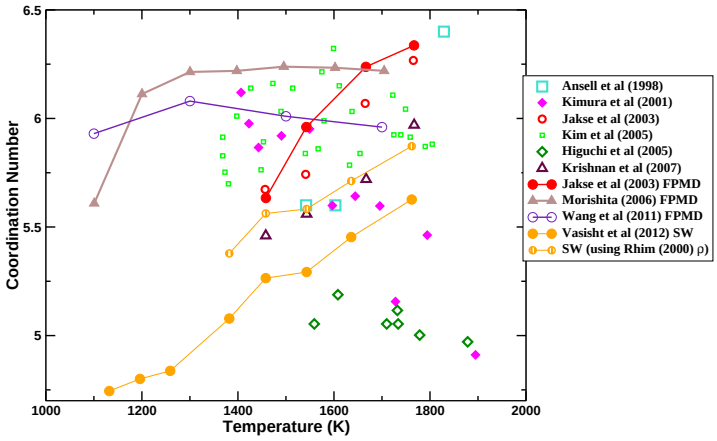

Figure 1.7: Compilation of coordination number measurements plotted against temperature (at $P = 0GPa$) as reported by different experimental reports, first principle MD (FPMD) simulations as well as classical simulations results. [From Ansell *et al.* [9], Kimura *et al.* [85], Jakse *et al.* [75], Kim *et al.* [84], Higuchi *et al.* [69], Krishnan *et al.* [86], Morishita [117], Wang *et al.* [180] with permission.]

1.3.2 Simulation Studies: Liquid-Liquid Transition at Zero Pressure

Previous simulation studies, although support a first order transition to a low density liquid upon cooling below $T = 1060K$, are subject to uncertainties of interpretation owing to the low mobility of the low temperature states which did not permit an unambiguous demonstration of a first order *liquid-liquid* transition. The simulation study of Sastry and Angell [142] addressed these uncertainties, by seeking evidence of (a) phase co-existence, and (b) finite mobility in the low temperature phase. To probe whether a first-order transition exists, the authors carried out constant enthalpy (NPH) simulations. A non-monotonic dependence of the enthalpy on temperature was found (FIG. 1.8), which is an indication of a first order phase transition. The transition temperature was found to be around $T = 1060K$ at zero pressure. Similar behaviour is also observed in first principles simulations by Jakse and Pasturel [76] and independently by Ganesh and Widom [59].

Further, Sastry and Angell studied the nature of the two phases, by looking at their structural and dynamic properties. The mean square displacement (MSD) obtained from constant pressure simulations on either side of the phase transition showed a linear behaviour with time, indicating that the phases are in the liquid state with finite diffusivity. The diffusivity values calculated from MSD at various temperatures showed roughly a two orders of magnitude drop as the high temperature liquid transforms into the low temperature liquid (FIG. 1.9). The equilibration times in the low temperature liquid phase (see below) range from tens to hundreds of nanoseconds. The T-dependence of the diffusivity in the high temperature liquid phase (till $T = 1070K$) was found to be highly non-Arrhenius, characteristic of a *fragile liquid* [140].

It has been argued [6] that silicon, along with other tetrahedral liquids

such as water and silica, should undergo a transition from fragile liquid behaviour (non-Arrhenius temperature dependence of viscosity and other transport coefficients) to strong liquid behaviour (Arrhenius temperature dependence) as the liquid makes a transition from the HDL to the LDL (either discontinuously or continuously at pressures below the critical pressure). Since data over a sufficient range of temperatures in the low temperature phase was not available to judge this matter directly for silicon, Sastry and Angell [142] took recourse to an empirical observation that the intermediate scattering function (F(q,t)) shows oscillatory behaviour in strong liquids that becomes more pronounced in small systems. In the HDL phase ($T = 1055K$) no oscillations were observed in the F(q,t) (*see* FIG. 1.10) and upon transition to the LDL phase ($T = 1070K$) oscillatory behaviour appears and it becomes more significant at lower system sizes (*inset* of FIG. 1.10). Independent evidence for such a transition also is obtained by the fact that the heat capacity C_P drops to a value of $3.6Nk_B$ in the low temperature phase [78].

The pair correlation function $g(r)$, fifth neighbour distribution $g_5(r)$, bond angle correlation function (G_3) and local bond orientation order (Q_3) were calculated to study the structural properties of the two liquids. Coordination numbers calculated by integrating the $g(r)$ till its first minimum. The average coordination number was found to change from 5.12 to 4.61 in the high-temperature liquid and around 4.2 in the low-temperature liquid. The fraction of four coordinated atoms increased from about 50% (at high T) to 80% in the low T phase, indicating a greater degree of local tetrahedral order. This change is also reflected in the local bond orientation order Q_3(*see* FIG. 1.11 (a)). The Q_3 values for the low temperature liquid peaked at the crystal's Q_3 value, suggesting a tetrahedral local ordering whereas the high temperature liquid showed a broader peak in Q_3. The fifth neighbour distribution (which is distribution of distances of the 5^{th} nearest neighbour to a given atom) for the high temperature liquid was found to be unimodal indicating that the fifth neighbour resides inside the first coordination shell, whereas the low temperature liquid showed a bimodal $g_5(r)$ distribution (*see* FIG. 1.11 (b)), with the larger amplitude peak shifting to the second neighbour shell in the low temperature phase.

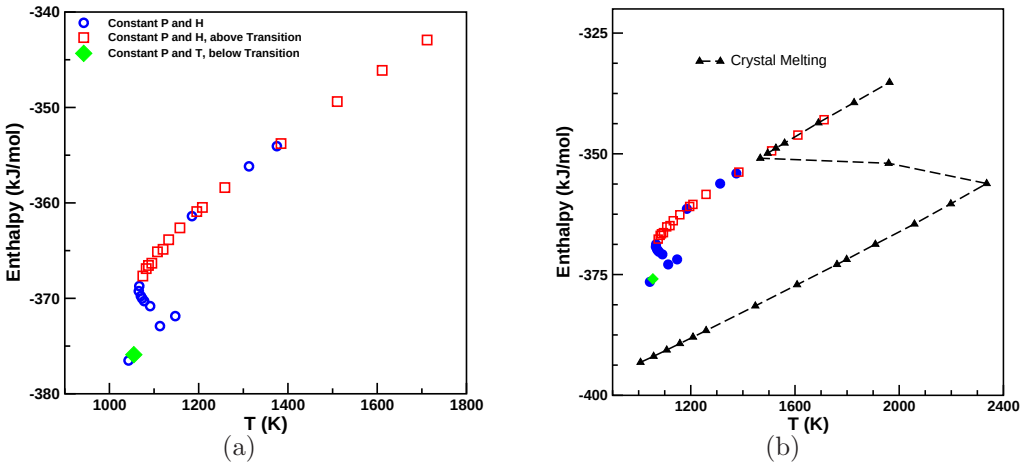

Figure 1.8: (a) The enthalpy against temperature from NPH MD simulations and NPT MD simulations using the SW potential for the supercooled liquid above and below the liquid-liquid transition. (b) The crystal-liquid transition is shown for comparison with the liquid-liquid transition data. [From Sastry *et al.* [142] with permission.]

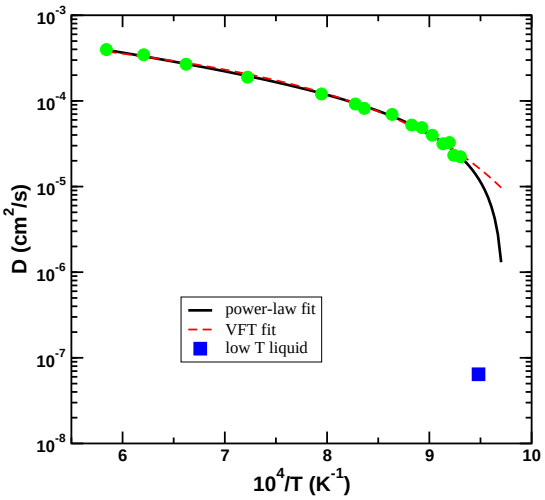

Figure 1.9: The diffusion coefficient D against the inverse temperature, above and below the liquid-liquid transition from MD simulations using the SW potential. In the high temperature liquid phase, the diffusivity show a strongly non-Arrhenius temperature dependence. [From Sastry *et al.* [142] with permission.]

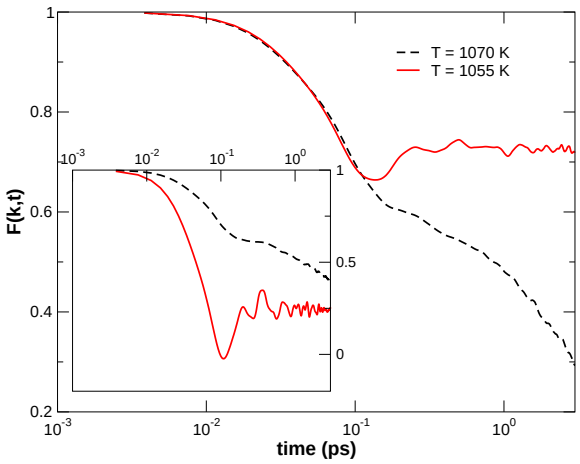

Figure 1.10: (*main panel*) The intermediate scattering function F(q,t) from MD simulations using the SW potential for a system size of 512 atoms, above and below the liquid-liquid transition point at zero pressure. The low temperature liquid displays damped oscillatory behaviour, characteristic of strong liquids. The high temperature liquid shows a monotonic decrease, characteristic of fragile liquids. (*inset*) The intermediate scattering function for a smaller system size (108 atoms). [From Sastry *et al.* [142] with permission.]

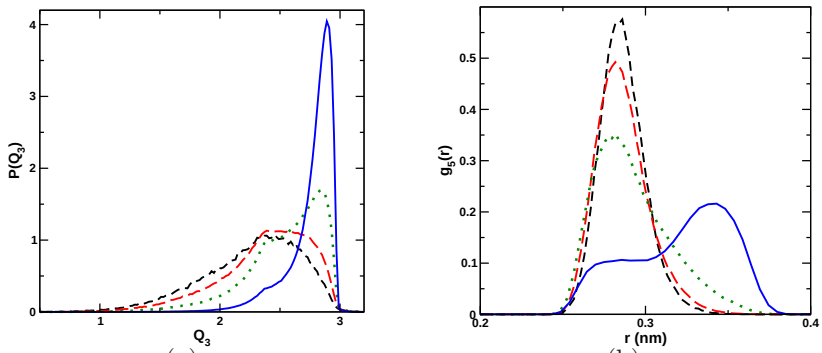

(a) (b)

Figure 1.11: (a) The distribution of local bond orientation order (Q_3) from MD simulations using the SW potential. The continuous blue line is for the low temperature liquid (at $T = 1055K$), which indicates local tetrahedral ordering. (b) The fifth neighbour distance distribution $g_5(r)$. For the high temperature liquid at $T = 1070$ (dotted line), $T = 1259K$ (short dashed line) and $T = 1711$ (long dashed line) $g_5(r)$ show a unimodal peak indicating that the fifth neighbour is within the first coordination shell. For the low temperature liquid (continuous blue line), a bimodal distribution emerges indicating the expulsion of of the fifth neighbour in a majority of cases to distances outside the first coordination shell. [From Sastry *et al.* [142] with permission.]

1.3.3 Electronic Structure

Among liquids that may exhibit a liquid-liquid transition, a feature that is special to silicon (though not uniquely so; see earlier discussions) is the change in electronic properties that accompany the liquid-liquid transition. Indeed, this is a feature that has been exploited in studies from early on in experimental probing of the transition. The amorphous-amorphous transition in silicon has been also found to be a transition from a semiconducting low density state to a metallic high density state. The liquid form of these phases have shown similar change in the conductivity. Given that the change in electronic properties has a strong influence on the effective interatomic interactions, a question has been raised about the extent to which a classical empirical potential can capture the behaviour seen in silicon. To address a part of this question, Ashwin *et al.* [11], performed electronic structure calculations, using an empirical pseudo-potential, for atomic configurations obtained from classical MD simulations using the SW potential. The electronic density of states ($DOS(E)$), obtained from these calculations is shown in FIG. 1.12 and FIG. 1.13. Ashwin *et al.* found that the DOS remains relatively unchanged at high temperatures till $T = 1258K$. A small dip in the DOS(E) at Fermi energy (E_f) was found at $T = 1082K$, near the estimated liquid-liquid transition temperature ($T = 1060K$). In the LDL phase, ($T = 1055K$), even though the DOS(E) remain finite, the authors found a dramatic lowering of DOS(E) at the Fermi level E_f, indicating a change in the conductivity. Further, the states near the Fermi level become localised in the LDL, as shown in FIG. 1.13 (b), and the conductivity drops by roughly an order of magnitude in going from the HDL to the LDL phase. Similar features in the DOS(E) have also been found from first principles calculations [59, 77] as shown in FIG. 1.14 and 1.15, indicating that the results are unlikely to be artifacts arising from the classical nature of the simulations. As described earlier, Beye *et al.* [20, 141], have utilised these changes in the electronic DOS to provide experimental evidence for a liquid-liquid transition. The estimated DOS in their pump-probe measurements are shown in FIG. 1.16.

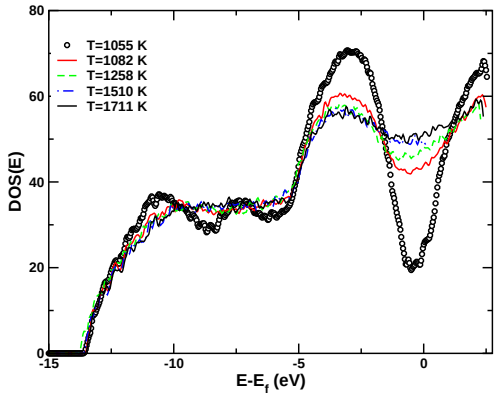

Figure 1.12: Electronic DOS of the low density liquid (LDL) at $1055K$, the high density liquid (HDL) at $1082K$ and the high T liquid phases from DFT calculations on the MD trajectory obtained using the SW potential. [From Ashwin *et al.* [11] with permission]

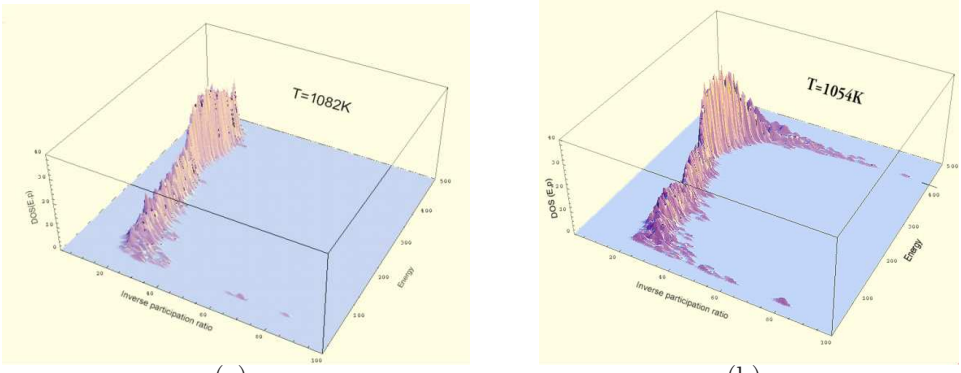

(a) (b)

Figure 1.13: Electronic density of states (DOS) as a function of energy and inverse participation ration for (a) $T = 1082K$, high density liquid, and (b) $T = 1054K$, low density liquid, from density functional theory (DFT) calculations on the MD trajectory obtained using the SW potential. The states near the Fermi energy at $T = 1054K$ are localised. [From Ashwin *et al.* [11] and SS Ashwin *PhD* thesis, JNCASR (2005) with permission.]

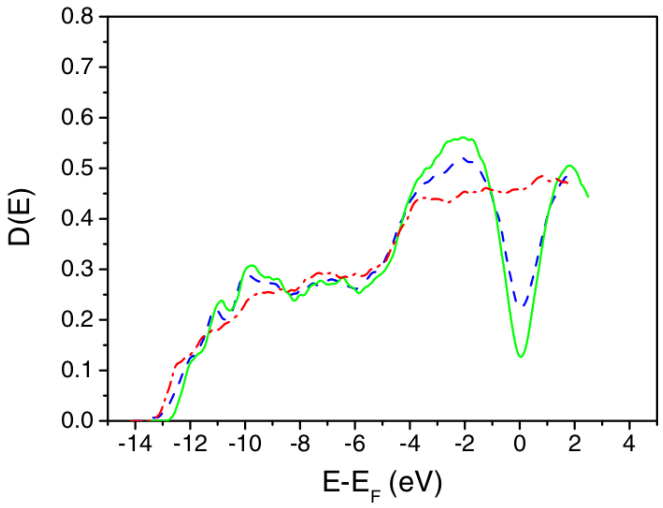

Figure 1.14: Electronic density of states (DOS) of the low density liquid (LDL) at $1050K$(green), the high density liquid (HDL) at $1070K$(blue) and the high T liquid at T_m (red) phases from first principles MD (FPMD) simulations. [From Jakse *et al.* [77] with permission.]

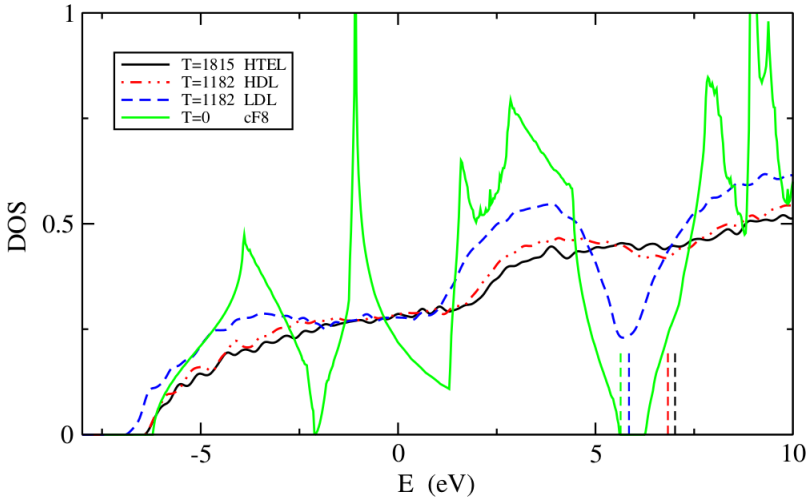

Figure 1.15: The plot of electronic density of states (DOS) of the crystal (green), the low density liquid (LDL) (blue), the high density liquid (HDL) (red) and the high T liquid (black) phases from first principles MD (FPMD) simulations. Fermi energy E_F for each of the phases is represented by vertical dashed lines. [From Ganesh *et al.* [59] with permission.]

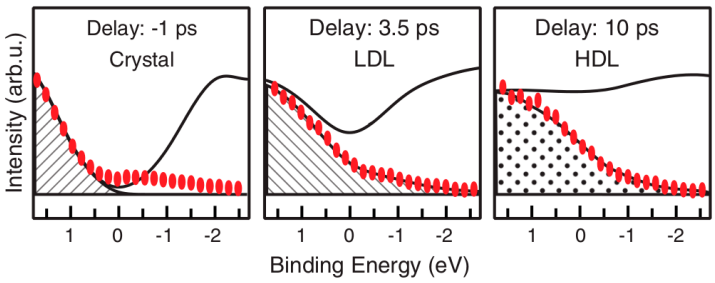

Figure 1.16: Electronic density of states (DOS) of the crystal, low density liquid (LDL), and high density liquid (HDL) phases. Measured data points for the occupied electronic states are represented by red ovals and black lines are from calculations. [From Beye *et al.* [20] with permission.]

For more than three decades, study of liquid-liquid transition has been carried out in various materials which form an important part of our natural world and other substances. We briefly mention next some of these works. We have discussed the liquid-liquid transition studies in water, silica, carbon (which are network forming liquids), phosphorus, alumina-yttrium and triphenylphosphite (which are material in which liquid-liquid transition has been experimentally verified).

1.4 Liquid-Liquid Transition and Critical Point in Various Materials

1.4.1 Water

A liquid-liquid transition and a corresponding liquid-liquid critical point has been proposed to occur in supercooled water as a possible explanation of anomalies observed in the liquid phase of water. Poole and *et al.* [125, 126] performed MD simulations using the ST2 model of water to verify the stability-limit conjecture [155, 156] (the re-entrant liquid spinodal scenario - FIG. 1.17 (a)). Analysis of the spinodal and the TMD line suggested that there is no intersection of a positively sloped liquid-gas spinodal with a negatively sloped TMD line and hence one does not observe the re-entrant liquid spinodal scenario proposed by the stability limit conjecture. The TMD line was found to change its slope from negative (at high pressures) to positive (at low pressures). Further investigation suggested a novel critical point, which was not related to the liquid-gas critical point (FIG. 1.17 (b)). The proposed second critical point scenario was based on the observations of an inflection in the low temperature isotherms, suggesting an approach to a critical point. Further analysis of pair-correlation function $g(r)$, below the hypothesised critical point, suggested the onset of two phase coexistence. The $g(r)$ was compared with the experimental $g(r)$ for the HDA and the LDA phases. In a later study of the ST2 water Poole *et al.* [124], motivated by singularity free thermodynamic analysis, charted out the complete phase diagram which showed the interconnection between the density anomalies, compressibility, heat capacity and liquid spinodal (*see* FIG. 1.18).

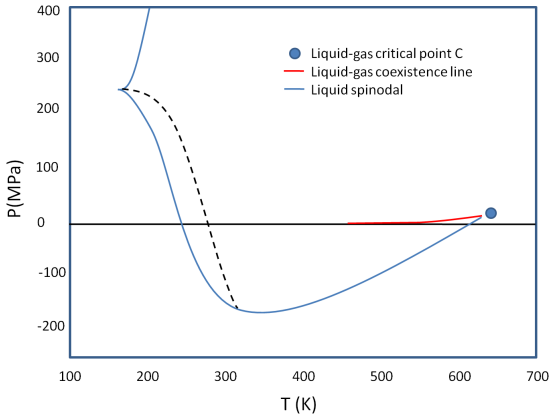

(a)

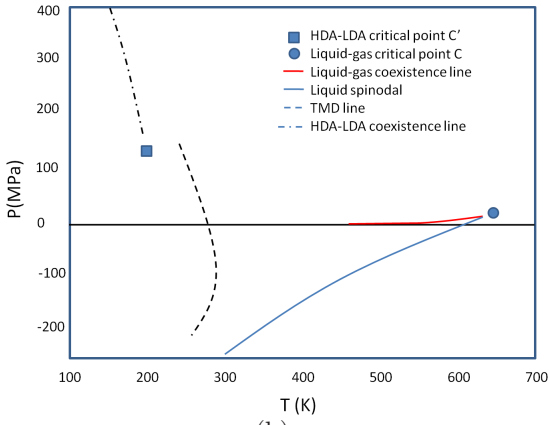

(b)

Figure 1.17: (a) The schematic phase diagram in (P, T) plane showing the liquid-gas(L-G) coexistence line, the L-G critical point, the temperature of maximum density (TMD) line and the spinodal. According to stability-limit conjecture, the spinodal intersects the TMD line and the point of intersection spinodal goes through a minima. (b) Schematic of P-T plot showing the L-G coexistence line, the L-G critical point, the TMD line, the spinodal and HDA-LDA coexistence and critical point. (Adapted from Poole *et. al.* [125, 126] with permission.)

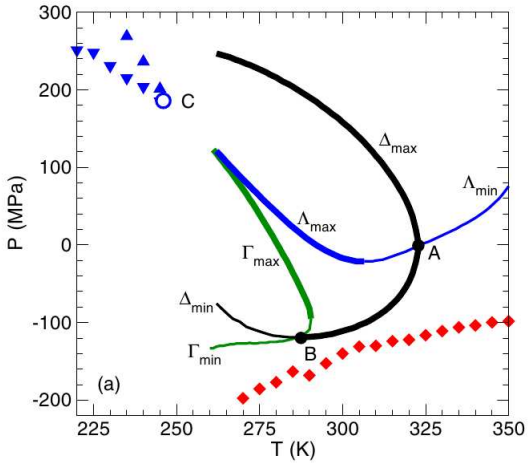

Figure 1.18: The phase diagram of liquid water in (P, T) plane obtained from simulations using the ST2 model potential. C is the location of the liquid-liquid critical point, the diamonds and the triangles represent the spinodals related to liquid-gas critical point and and liquid-liquid critical point respectively, the black line corresponds to density extrema, the blue line corresponds to the compressibility extrema and the green line corresponds to the heat capacity extrema. [From Poole *et al.* [124] with permission].

Computer simulations using various different models of water [2, 67, 124–126, 137, 190] have provided evidence for the liquid-liquid transition. Experimental verification of the simulation results are still inconclusive. Owing to the issues related to crystallisation various indirect paths have been taken to verify the liquid-liquid transition in water [109]. Experimental evidence for liquid-liquid transition have been obtained for confined water [97, 102, 191]. Even though the confinement avoids crystallisation, the relation between the behaviour of confined water and the bulk water is yet be clarified [54,103,189].

Recent studies of Limmer and Chandler [95] and Moore and Molinero [113] have sparked debate about the existence of the liquid-liquid transition. Limmer and Chandler have computed the free energy surface as a function of density and global orientational order Q_6 at various state points and find no free energy basin corresponding to the low density liquid. Moore and

Molinero in their work interpret the low density liquid to be an intermediate-ice phase and the nucleation barrier in the state points near to the low density liquid phase is of the order of T. The work Limmer and Chandler and Moore and Molinero claim that the liquid-liquid phase transition is a transition from the liquid to a solid phase. But these interpretations have been unchallenged [83, 151].

1.4.2 Silica

Using computer simulations, a liquid-liquid transition was predicted by Saika-Voivod *et al.* [135] for silica. In this work, the authors found (for two different model interaction potentials namely BKS and WAC) that in silica for wide range of densities, the potential energy U is a linear function of $T^{3/5}$ (as predicted by Rosenfeld and Tarazona [163] for a simple dense liquid at low temperature). The authors utilize this behaviour and fit the available thermodynamic data from simulations to an equation of state. Extrapolation of this equation of state to low T predicted an existence of a liquid-liquid transition for both models. Further simulations at these low temperatures were carried out to confirm the existence of liquid-liquid transition in silica by examining the local structural changes.

Rosenfeld and Tarazona [163] predicted that there exist an isochoric T dependence of the potential energy U of a simple, dense, cold liquid, which is given by $U = a + bT^{3/5}$. In this work on silica, to begin with, the authors identify the region (in T and V) where the above dependence of potential energy U is obeyed and found that the relation is valid over a wide range of T and V and the coefficients $a(V)$ and $b(V)$ vary smoothly with V. A functional representation of U(V,T) given by $U(V,T) = a(V) + b(V)\,T^{3/5}$ was obtained. Since the internal energy is E = U + U_k, where the kinetic energy $U_k = \frac{9}{2}RT$, R being the gas constant, one can write

$$E(V,T) = a(V) + b(V)T^{3/5} + \frac{9}{2}RT$$

A functional representation of the entropy S(V,T) and hence Helmholtz

free energy A(V,T) ($= E(V,T) - T\ S(V,T)$) was obtained to calculate the equation of state $P(V,T) = \frac{\partial A}{\partial V}|_T$. The entropy S at arbitrary V and T, relative to the entropy of a reference state ($S(V_o, T_o)$) was evaluated by thermodynamic integration which was carried out in two steps, first along an isotherm and then along an isochore. The equation of entropy so obtained is given by

$$S(V,T) = S(V_0, T_0) + \Delta S_T + \Delta S_V$$

where ΔS_T was computed along an isotherm and ΔS_V was computed along an isochore. Using the above equation of entropy, polynomial fits of the V dependence of a and b and one reference isotherm of P a model equation of state was constructed. The authors found that the isochores evaluated directly from simulation and as calculated from the model equation of state matches well and for both WAC and BKS silica there is a range of V in which the curvature of a verses V is negative. The value of a, at $T \to 0$ limit, gives an estimate of U. The Helmholtz free energy in the same limit of $T \to 0$ is U (since $A = U - TS$) and hence the a gives an estimate of A. The negative curvature in a verses V is a precursor to mechanical instability, which the authors suggest as the indication of liquid-liquid phase separation at low T.

Using the model equation of state, authors evaluate locus of three different thermodynamic constraints, which were (1.) the line of temperature of maximum density (TMD), (2.) the spinodal line and (3.) the line of compressibility maxima. The locations of these lines are shown in FIG. 1.19 projected onto the (P,T) plane. The pattern of behaviour in BKS silica is similar to that of water (in which one observes a negatively sloped TMD, no intersection of liquid spinodal and TMD, change of slope of TMD upon intersecting the locus of compressibility maxima), but in WAC silica the TMD line seems to come very close to the spinodal but may not be intersecting, since the spinodal doesn't show any re-entrant behaviour (which is a thermodynamic necessity in case of intersection with TMD). At the low temperature regime, in both the model potentials, a spinodal line which is distinct from the liquid-gas spinodal boundary was found. This spinodal is predicted to be

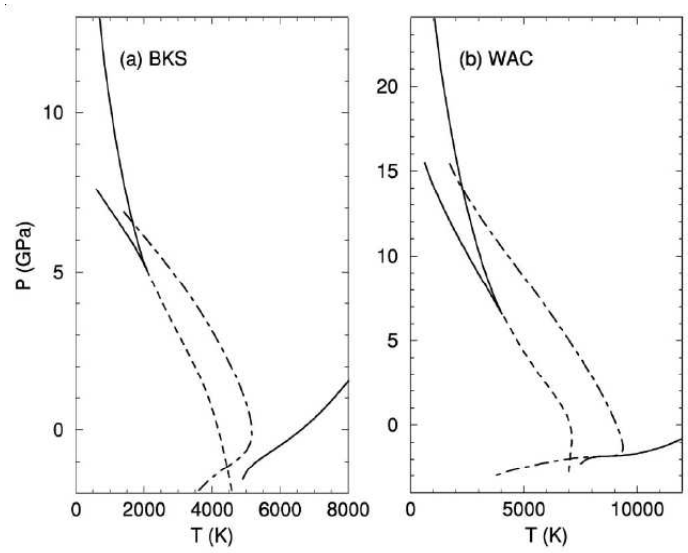

Figure 1.19: Plot of pressure against temperature for BKS (left panel) and WAC (right panel) silica. Plot shows the estimates of the spinodals (solid lines), TMD line (dotted-dashed) and K_T^{max} line (dashed), evaluated from model equation of state [135]. (From Saika-Voivod *et. al* [135] with permission.

the metastability boundary associated with a liquid-liquid phase transition.

To verify if the liquid-liquid spinodal curves predicted by the equations of state are correct, the authors performed equilibrium simulations in these regions to seeking characteristic signs of phase separation. The local coordination environment of silicon atoms were examined to test the occurrences of such a phase separation. The fifth neighbour distribution was calculated at different temperatures along the isochores and they observe that for T above certain critical temperature T_C, $g_5(r)$ distribution was a unimodal function of r and as T decreases the width of the distribution increases. For temperatures near T_C, the distribution becomes bimodal, which indicates the emergence of two distinct 5^{th} nearest neighbour coordination environments. From this observation and the analysis of spatial correlations in Si atoms with similar coordination environment in a bigger system simulation (6000 atoms), the emergence of two distinct phases was predicted. In an indirect

way, the authors estimate the liquid-liquid critical point in real silica to be around $T_C = 730K$, which is well below the glass transition temperature ($T_g = 1450K$) and hence can not be directly observed in supercooled liquid silica.

Karki *et al.* [79] have performed FPMD simulation study of liquid silica which is briefly discussed here. In this work, the authors perform FPMD simulation for 24 silica unit (72 atom) system in NVT ensemble at state points varying from $T = 3000K$ to $6000K$ and pressure ranging up to $150GPa$. The protocol followed in the simulation is as follows: The crystalline structure at each volume is melted and equilibrated at $T = 10000K$ for a period of $3ps$ and then quenched to the desired temperature at which the simulation is performed till the MSD shows a linear regime. The maximum simulation time period (at $T = 3000K$) reported to be around $58ps$. The authors find no evidence of TMD which is in contract with the results from semi-empirical potential simulations discussed above. Also over the entire range of density and pressure no spinodal instabilities was found in these simulations.

The discrepancies and disagreement between classical interaction potential simulation and first principles simulation results either calls into question the accuracy of empirical potential or equilibration issues and intricacies related to pseudo potentials in first principles simulations. Even in the case of carbon results from classical simulations and first principles simulations contradict each other. For the case of silicon a detailed comparative study is presented in later chapter of this thesis (*see* Applicability to real silicon).

1.4.3 Carbon

Carbon, in the context of liquid-liquid transition, is the most debated element in the literature. Experimental investigation by Togaya [168] suggested that there exist a maxima or a cusp in the melting line of graphite in the (P, T) plane. This led to the speculation for existence of a liquid-liquid transition, wherein the liquid-liquid transition line intersect the graphite melting line (*see* FIG. 1.20). Using computer simulations further investigation of the proposed liquid-liquid transition was done. Glosli and Ree [65] performed

classical MD simulation using a empirical Brenner potential and predicated a first order phase transition between two different liquid forms of carbon, which terminates at low T at a triple point on the graphite melting line ($T = 5133K$, $P = 1.88GPa$) and at a critical point at high T ($T = 8801K$, $P = 10.56GPa$). The authors measured the local coordination and found that the coordination is highly correlated with the geometry of the local structure. This means that the fourfold coordinated atoms were found to be nearly tetrahedral (sp^3 hybridized), threefold coordinated atoms were centers of planar structure with neighbors at angles close to 120 deg (sp^2 hybridized) and twofold coordinated atoms were linear (sp hybridized). The LDL phase was found to be predominantly having sp structures and very little sp^3 hybridized atoms, where as the HDL phase was found to be containing mostly sp^3 bonded atoms and very little sp hybridized atoms. The authors report that there exists an intimate relation between the relative stability of sp^2 hybridized atoms and the torsional energy about the sp^2 bonds. Since sp^2-bonded sites was found to be inhibited by a large torsional barrier and a low entropy associated with the π bond, the authors suggest that there is an absence of an sp^2 dominated phase. The authors also comment on the empirical potential, which ignores the van der Waals interaction, and note that the inclusion of such an interaction would reduce the density difference between the LDL and HDL phase.

A first principles MD simulation of carbon was carried out by Wu, Glosli, Galli and Ree [187] which suggest that there is continuous evolution from a sp-bonded liquid to an sp^2-like fluid to an sp^3-like fluid as a function of pressure, above the graphite melting line and hence contradicts the classical Brenner potential results. The primary reason for the contradictory results was found to be the inability of the Brenner potential to calculate the correct torsional energy corresponding to a torsional angle. This deficiency of the classical interaction potential introduced an error in describing the entropy of a three-coordinated carbon liquid and hence sp^2-bonded sites were not found in the classical simulations carried out by Glosli and Ree [65].

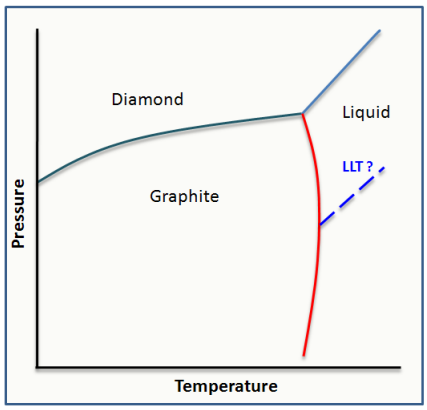

Figure 1.20: Phase diagram of carbon in (P, T) plane showing the three different phases and the respective coexistence lines. The melting line of graphite shows a maxima or cusp. The expected liquid-liquid transition line is shown as dotted line.

1.4.4 Phosphorus

A clear experimental evidence of liquid-liquid transition in black phosphorus was given by Katayama *et al.* [80], who have performed an *in situ* X-ray diffraction measurement on the black phosphorus melt and found that liquid phosphorus (a tetrahedral liquid) undergoes a first order transition from a tetrahedral molecular liquid (below $1GPa$) to a polymeric liquid (above $1GPa$). Black phosphorus is one of the least reactive allotropic forms of phosphorus and has a melting temperature $T_m = 880K$. A schematic phase diagram of black phosphorus is shown in FIG. 1.21. The melting curve of orthorhombic block phosphorus has a maxima at around $1GPa$. In the region of negatively sloped melting curve in the phase diagram, the volume of liquid is less than that of the solid. This feature is associated with the existence of liquid-liquid transition [128]. Katayama *et al.* found in their experiments, at around $T = 1000K$ and $P = 1GPa$, a sharp and rapid change in the structural quantities (structure factor - S(q) and radial distribution function - g(r)) corresponding to a small variation in pressure (around $0.02GPa$). The S(q) of the liquid melt at low pressure was found to resemble that for the

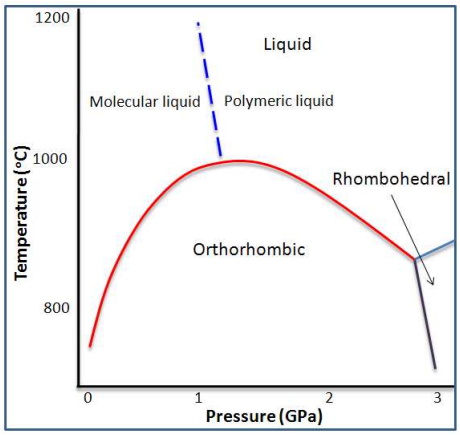

Figure 1.21: Phase diagram of black phosphorus in (P, T) plane showing the three different phases and the respective coexistence lines. The melting line of orthorhombic phase shows a maxima. The liquid-liquid transition line is shown as dotted line (Adapted from Katayama *et. al.* [80] with permission.)

white phosphorus melt (which has a prominent first peak at around 1.5Å^{-1} attribute to correlation between the P_4 molecules) and hence the low pressure phase was determined as a molecular liquid. In the high-pressure form, the analysis of g(r) showed a distinct second peak around 3.5Å was found. Since the strong correlation between the second-nearest neighbours is not consistent with the nature of molecular liquid the authors consider the possibility of a polymeric liquid in which P atoms form network structures. From the comparison of the g(r) of the high pressure form with g(r) of the red amorphous phosphorus(which has a polymeric nature), the authors conclude that it is very likely that the high-pressure liquid is a polymeric liquid.

Monaco *et al.* [112] extended the study of liquid-liquid transition in phosphorus to higher temperatures (up to $2473K$) and lower pressures (up to $0.3GPa$). The slope of the liquid-liquid transition line was found to be negatively sloped in the whole range of examined temperature and pressure. The estimated latent heat was found to be quite large, which seems to be due to the substantial change involved in polymerisation process in fluid. Even though the authors speculate the existence of liquid-liquid critical point no

definite evidence was found in their experiments.

Liquid-liquid transition in phosphorus has been extensively studied using computer simulations. One of the earliest studies using first principles MD was carried out by Morishita [115], in which it was clearly shown that the transition is driven not only by pressure but also by temperature (which was confirmed by experiments from Monaco *et al.* [112]). The author carried out structural analysis by looking at the bond-angle distribution function, which suggested that at low pressure the distribution has a single peak at $\theta) = 60^\circ$ (indicating that the majority of molecules are tetrahedral) and at high pressure the distribution is bimodal (strongly peaked at $\theta) = 90^\circ$ and a weak peak at $\theta) = 90^\circ$), indicative of a polymeric phase. Even though a critical point associated with the liquid-liquid transition was suggested in Car-Parrinello MD simulations [63], further investigation is required to confirm this prediction.

1.4.5 Al_2O_3 Y_2O_3

Phase transitions in liquid mixtures into liquids with different composition is a known phenomena. But the phenomena of the liquid-liquid transition discussed here is different in the sense that the composition remains intact but the phase separated liquids differ in density and other properties. Aasland and McMillan [1] studied the supercooled liquid phase of $Al_2O_3 - Y_2O_3$ (at normal pressure) by hot-state microscopy (a technique which uses a microscope with the ability to control the temperature of the sample). The authors found, during the liquid quenches to obtain glass, spontaneous formation of bubbles of a second liquid phase before the sample glassified. The glass phase of the second liquid form inclusions in the glassy matrix of the first liquid. Using electron probe microanalysis, the composition of the two glassy phases were determined and was found to be identical.

1.4.6 Triphenylphosphite

Cohen *et al.* found that when triphenylphosphite TPP was cooled rapidly enough, it first enters a supercooled liquid state (called liquid I) below the

melting point $T_M = 295K$ as usually liquids do and then into a glassy state (called glass I) at the glass-transition temperature $T_g^I = 205K$. This supercooled liquid was found to behave as a typical fragile glass former. On the other hand, if TPP is quenched to temperatures between $210K$ and $223K$ (above T_g^I) and then annealed at that temperature, a new phase was found to have emerged, which was termed as the glacial phase. Many explanations were given for the nature and origins of this glacial phase, which included the presence of an exotic defect-ordered phase to transformation into a plastic crystal. Tanaka *et al.* [162] provided an experimental evidence which indicated that the TPP undergoes a liquid-liquid transition and that the glacial phase is the glassy state of a second liquid (liquid II). A critical point associated with this liquid-liquid transition has been also reported [89]. Recently an application of liquid-liquid transition in TPP has has also been shown by Kurita *et al.* [88], wherein the authors report that one can control the fluidity and miscibility of its mixture with another molecular liquid (toluene or aniline).

1.5 Crystal Nucleation

In this section we begin with an introduction to the homogeneous nucleation process. Later we briefly discuss the essential ideas behind simulation studies of nucleation.

Nucleation, as mentioned earlier, is the process of transformation of a metastable phase to the stable phase. Nucleation facilitated by surface boundaries, impurities or any other preferential crystallisation sites is termed as the *heterogeneous nucleation*. The *homogeneous nucleation* process involves spontaneous formation of a stable phase nucleus, due to the thermal fluctuations, inside the metastable phase, which is the focus of our study in the system of liquid silicon. Such a formation of nuclei creates an interface with the metastable phase, which is energetically unfavourable and hence these nuclei often melt back in to original phase. On reaching a sufficiently large sizes, the energy penalty due to the surface formation is over come, as the atoms in the metastable phase would find it favorable to be part of the stable nucleus (which is at lower chemical potential). After crossing such a threshold size, the nucleus can only grow and this is termed as the critical nucleus (n^*) and the energy associated with the formation of critical nucleus is called the nucleation barrier (ΔG^* or $W(n^*)$). The critical nucleus size and the nucleation barrier is closely related to the undercooling or supersaturation as we show below.

Let us consider a pure metastable phase at a constant temperature T and applied pressure P_0 (*see* FIG. 1.22). By pure phase, we mean that there is no occurrence of the stable phase in any part of the system. Let N_0 be the number of atoms in the metastable phase and V_0 be the volume. Due to thermal fluctuations, a nucleus of size N_s (with volume V_s) is formed. Let the pressure inside the nucleus be P_s. Since the total number of atoms in the system is conserved, the metastable phase will now have $N_m = N_0 - N_s$ number of atoms with a volume V_m. Let the energy of the system before the formation of nucleus be $U(S_0, V_0, N_0)$ and after the formation be $U(S', V', N')$

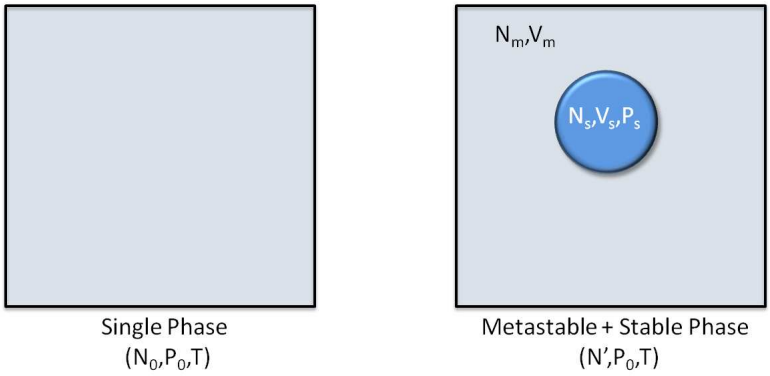

Figure 1.22: A sketch representing system having pure metastable phase (left) and formation of a stable phase with in the metastable phase (right).

which can be written as

$$\begin{aligned} U(S_0, V_0, N_0) &= TS_0 - P_0V_0 + N_0\mu_m(P_0, T) \qquad (1.3) \\ U(S', V', N') &= [TS_m - P_0V_m + N_m\mu_m(P_0, T)] + \\ &\quad [TS_s - P_sV_s + N_s\mu_s(P_s, T)] + \sigma A \qquad (1.4) \end{aligned}$$

Here the subscript m represents the metastable phase and the subscript s represents the stable nucleus. Let the interfacial free energy be σ, the area of the interface be A and the final volume of whole system be $V' = V_m + V_s$. Using the fact that the number of atoms in the system is conserved ($N_0 = N' = N_m + N_s$), we can write the difference in energy as

$$\begin{aligned} \Delta U &= (-P_s + P_0)V_s - P_0(V' - V_0) + T(S_m + S_s - S_0) + \qquad (1.5) \\ &\quad +\sigma A + N_s(\mu_d(P_s, T) - \mu_m(P_0, T)) \\ &= (-P_s + P_0)V_s - P_0\Delta V + T\Delta S + \sigma A + N_s(\mu_d(P_s, T) - \mu_m(P_0, T)) \end{aligned}$$

The change in Gibbs free energy is given by $G = \Delta U + P_0\Delta V - T\Delta S$. By

inserting the above calculated difference in energy we get

$$\Delta G = (-P_s + P_0)V_s + \sigma A + N_s(\mu_s(P_s, T) - \mu_m(P_0, T)) \tag{1.6}$$

Note that the chemical potential is evaluated at the pressure inside the nucleus (P_s). Using the Gibbs-Duhem equation $SdT - VdP + Nd\mu = 0$, we can rewrite the chemical potential in terms of applied pressure (P_0) as

$$N_s\mu_s(P_s, T) = N_s\mu_s(P_0, T) + V_s(P_s - P_0) \tag{1.7}$$

and hence the change in Gibbs free energy ΔG will be

$$\begin{aligned} \Delta G &= N_s(\mu_s(P_0, T) - \mu_m(P_0, T)) + \sigma A \\ &= N_s\Delta\mu + \sigma A \end{aligned} \tag{1.8}$$

where $\Delta\mu$ is the chemical potential associated with moving of a single atom from metastable phase to the stable phase and this quantity is negative. If a nucleus contains n atoms, then the change in Gibbs free energy represent the minimum work $W(n)$ for nucleus formation. The first term is the volume term or the gain term which represent the driving free energy for phase transition and the second term is the surface term or the loss term which represents the energy penalty for the creation of an interface. The volume of the nucleus scales with n and the surface scales with $n^{2/3}$ and hence we can write $W(n) = -bn + an^{2/3}$, where a and b are positive constants. We show the profile of $W(n)$ in FIG. 1.23 (a). The maximum correspond to the size of critical nucleus (n^*) and the free energy barrier ΔG^* and is given by

$$\begin{aligned} n^* &= \left(\frac{2a}{3b}\right)^3 \\ \Delta G^* &= \frac{4a^3}{27b^2} \end{aligned} \tag{1.9}$$

For a spherical nucleus, the surface area $A = 4\pi r^2$ can be expressed in term of volume per unit atom $nv' = (4/3\pi r^3)$, as $A = (36\pi)^{1/3}(nv')^{2/3}$. Hence the

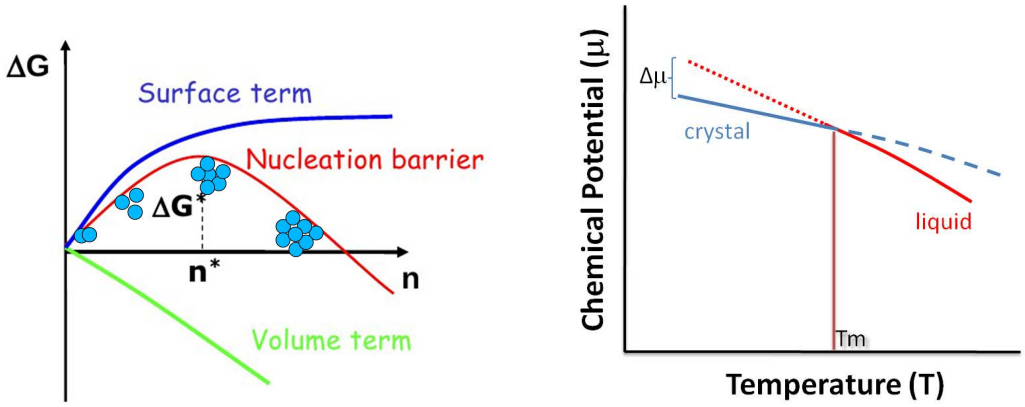

(a) (b)

Figure 1.23: (a) Schematic diagram showing the Gibbs free energy difference (ΔG) as a function of nucleus size (n). (b) Schematic diagram showing the chemical potential as a function of temperature. The dashed line represent the metastable branch and the solid line represent the stable branch of liquid (red) and crystal (blue) phases. The chemical potential difference is zero at the melting temperature (T_m).

maximum corresponds to

$$\begin{aligned} n^* &= \frac{32\pi}{3}\left(\frac{(v')^{2/3}\sigma}{(-\Delta\mu)}\right)^3 \\ \Delta G^* &= \frac{16\pi}{3}\left(\frac{v'\sigma^{3/2}}{(-\Delta\mu)}\right)^2 \\ r^* &= \frac{2\sigma v'}{(-\Delta\mu)} \end{aligned} \tag{1.10}$$

As shown in FIG. 1.23 (b) the chemical potential difference increases with the undercooling. Therefore from Eq. 1.11 we find that the critical nucleus size as well as the free energy barrier should decrease with undercooling. The probability of formation of a critical nucleus depends on the free energy barrier as

$$P(n^*) \propto exp(-\Delta G(n^*)/k_B T) \tag{1.11}$$

The crystal nucleation rate (net number of crystal nucleus passing the critical size per unit time per unit volume) is given by the product of $P(n^*)$ and a

kinetic pre-factor κ

$$\mathrm{I} = \kappa \exp(-\beta \Delta G^*) \tag{1.12}$$

where kinetic pre-factor $\kappa \equiv \rho Z f_+^{n^*}$, where ρ is the number density, Z is the Zeldovich factor and $f_+^{n^*}$ is the attachment rate of atoms to the critical nucleus. The Zeldovich factor $Z = \sqrt{\frac{|\Delta G^{"}(n^*)|}{2\pi k_B T}}$ represents the local curvature of the free energy barrier. The attachment rate $f_+^{n^*} = 24D(n^*)^{2/3}/\lambda^2$ is a function of diffusion coefficient D, mean free path λ and critical nucleus size n^*. Hence the nucleation rates depends both on thermodynamics and dynamics of the system.

Nucleation rates and supercooling limit: From the Eq. 1.12 we know that the nucleation rate depends on two factors namely free energy barrier ΔG^* (a thermodynamic factor) and kinetic pre-factor which basically is a function of diffusivity (D). From the Stokes-Einstein relation ($D/T \propto \tau_\alpha$) we can associate the diffusivity to the relaxation time (τ_α). The free energy barrier diverges at the melting point and decreases exponential as we go lower in temperature. The relaxation time is very small at high temperatures but decreases as one lowers the temperature (following Arrhenius or Vogel-Tammann-Fulcher equation). Hence the nucleation time ($\tau_n \equiv 1/\mathrm{I}$), a product of a decreasing and an increasing function, goes through a minimum (*see* FIG. 1.24). The the nucleation time and the relaxation time together defines a time window within which we can observe a *equilibrated* supercooled liquid phase. If we quench our system faster than the relaxation times, the system will end up in a glassy state and if we quench too slow (slower than the nucleation time) the system will crystallise. Hence the eventual fate of a supercooled liquid depends on the nucleation rates and the relaxation dynamics of the liquid.

Nucleation mechanism and Crystal formation: A better understanding of the nucleation mechanism helps in controlling various properties of crystals, including the size and polymorphism [178]. If process of nucleation is fast (due to small free energy barrier), the crystal forms in many

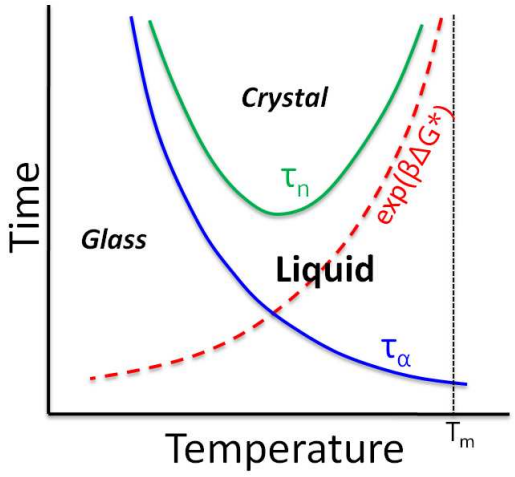

Figure 1.24: Sketch of time against temperature showing the behaviour of relaxation time and nucleation time. Here T_m represents the melting temperature near which the relaxation time of the supercooled liquid is small and the nucleation free barrier diverges.

places in the system and hence depleting the liquid phase, which affects the growth of a single large crystal. With an understanding of the mechanism of nucleation and growth (*e.g.* environment of critical nucleus, preferential arrangement of liquid atoms, favorable local density changes) one grow crystals in a controlled way.

1.5.1 Simulation Studies of Crystal Nucleation

Experimental studies on crystallisation phenomena mainly focus on the nucleation rates [82,177], since direct observation a critical nucleus is a difficult task. In some cases, in which the system has slow timescale and large molecular size, experiments indeed have provided microscopic details (size, shape, configuration of the new phase) [62, 82]. Like in many other cases, where experimental studies are difficult, the computer simulations have provided various insights resulting in the progress of the field and in the following section we discuss essential ideas behind the simulation studies.

Order Parameter

The first and foremost important aspect of simulation/theoretical studies of nucleation is recognising the suitable order parameter to distinguish the phases. We distinguish different phases by choosing an appropriate reaction coordinate or order parameter. In the case of bubble nucleation or liquid drop formation, one can use density as the order parameter. But in the case of crystal nucleation density alone is not a good order parameter, since the difference in density between the crystal and metastable liquid can be very less or even zero. Since the crystal has translational order and orientational order which is distinct from that of a liquid, one can use them as order parameters to distinguish the two phases. Such an order parameter, which depends on the local geometrical arrangement of the atoms, should be a sensitive measure of crystallinity but should not be bound to the symmetry of the crystal, even if one knows a priori the equilibrium crystal phase, since the nucleation pathway can be complex and the liquid phase can nucleate to a phase which is closest in free energy before transforming into a stable crystal phase.

Bond orientational order, introduced by Steinhardt *et al.*, is one such order parameter which meets the above requirement and is discussed in the chapter on *Methods and calculations*.

Nucleation Rate and Free Energy Barrier

Calculation of nucleation rates from an equilibrium simulation (MD or MC) is straight forward task once we have recognised the critical cluster size. We know that up on reaching a critical size (n^*), the cluster should not melt to smaller size. If the time taken reach the critical size is t^*, then we can calculate the nucleation rate as $I \equiv 1/ < t^* > V$, where $< t^* >$ is calculated from averaging t^* from many independent crystallised equilibrium simulation runs. For low super saturations, the critical cluster size will be fairly big and the transformation to crystal phase will be sharp and hence we can obtain a good estimate from t^*. But at high super saturations or deeper undercooling, the critical cluster size will be small (hence difficult to

pinpoint) and the transformation to crystal phase will be slow (owing to the smaller mobility at lower temperatures) and hence obtaining good estimates of t^* will be difficult.

Another quantity of interest is the free energy difference $\Delta G(n)$. According to Eq. 1.11, $\Delta G(n) = -k_B T ln[P(n)]$, where $P(n)$ is the equilibrium distribution of cluster sized n. We can calculate $P(n)$ directly from MD simulations (by recognizing the crystal like particles and cluster of crystalline particles), for clusters small than the critical size only. Since the formation of a critical cluster is a rare event, the probability of formation of a critical cluster will be small. Secondly formation of clusters sized beyond the critical cluster size is a irreversible process. Hence the estimates of $P(n)$ for $n \geq n^*$ we obtained from MD simulations is inaccurate.

To counter the above mentioned issues, various simulation techniques have been developed which basically focus on improving the sampling in the interested region of the phase space - vicinity of the critical cluster. These include umbrella sampling Monte Carlo [170, 171] (which is used in our work for the calculation of free energy barrier - detailed discussion in the chapter on *Methods and calculations*), Transition Path Sampling [22], Forward Flux Sampling [3], Mean First Passage Time ($MFPT$) based method [184] to mention a few methods. A recent article [175] reviews some of these simulation methods.

Chapter 2

Methods and Calculations

In this chapter we discuss silicon model potential, Molecular dynamics and Monte Carlo simulation techniques and other definitions and calculations of various properties (Eg. correlation functions, order parameter *etc.,*) used in this thesis.

2.1 Stillinger-Weber Potential

The Stillinger-Weber (SW) potential [159], by far the most widely used interaction potential for silicon (around 3000 citations), comprises of a two-body and a three-body interaction potential. The crystalline phase of silicon at low pressures has a diamond cubic structure and it melts into a higher density liquid phase. Stillinger and Weber [159], after a search through a class of interaction potentials with two and three body interactions, defined their empirical potential as follows:

$$U_{SW} = \sum_{i<j} v_2(r_{ij}/\sigma) + \sum_{i<j<k} v_3(\mathbf{r}_i/\sigma, \mathbf{r}_j/\sigma, \mathbf{r}_k/\sigma) \tag{2.1}$$

where σ is the diameter of the atom, $\mathbf{r}_i$ is the position of atom i, and r_{ij} is the distance between atoms i and j. The two-body potential is short-ranged and has the form

$$v_2(r) = \begin{cases} A\,\epsilon\,(Br^{-4}-1)\exp\left(\frac{1}{r-a}\right) & r<a \\ 0 & \geq a \end{cases}, \tag{2.2}$$

where $A = 7.049556277$, $B = 0.6022245584$, and $a = 1.8$. The repulsive three-body potential is also short-ranged, and is given by

$$\begin{aligned} v_3(\mathbf{r}_i,\mathbf{r}_j,\mathbf{r}_k) \equiv h(r_{ij},r_{ik},\theta_{jik}) + h(r_{ij},r_{jk},\theta_{ijk}) \\ +h(r_{ik},r_{jk},\theta_{ikj}) \end{aligned} \tag{2.3}$$

where θ_{jik} is the angle formed by the vectors $\mathbf{r}_{ij}$ and $\mathbf{r}_{ik}$ and

$$\begin{aligned} h(r_{ij},r_{ik},\theta_{jik}) &= \epsilon\ \lambda\ \exp[\frac{\gamma}{r_{ij}-a}+\frac{\gamma}{r_{ik}-a}]\,(\cos\theta_{jik}+\alpha)^2 \\ &\quad \times H(a-r_{ij})H(a-r_{ik}), \end{aligned} \tag{2.4}$$

where $\lambda = 21.0, \gamma = 1.20$, and $H(x)$ is the Heaviside step function. The choice $\alpha = 1/3$ in $(\cos\theta_{jik}+\alpha)^2$ favors a tetrahedral arrangement of atoms as found in silicon. The length and energy scales are set by the choice $\sigma = 2.0951$Å, $\epsilon = 209.5kJ/mol$. The choice of parameters were identified by taking into account the stable structural arrangement of the crystal to be cubic diamond, the melting point and the liquid structure. The depth of the potential ϵ and diameter of the atom σ were chosen such that one obtains the correct lattice spacing and atomisation energy of crystalline Si at 0 K. The strength of the three-body potential is determined by the value of λ. Both the two-body and the three-body part of the potential smoothly goes to zero at the cut off a.

2.1.1 Double Sum Implementation

In the Stillinger-Weber potential, calculation of the three-body term obviously involves a triple-loop implementation and hence is computationally

more expensive than the two-body sum. A proposal to reduce the three-body term to a product of two-body terms was put forward by Biswas and Hamann [21] and later by Makhov and Lewis [101] to perform Monte Carlo simulation. Saw *et al.* [146] extended this scheme to calculate the force and hence perform Molecular Dynamics simulations. The expression of the SW potential as suggested by the above mentioned works is given by

$$U_{SW} = \sum_i \sum_{j<i} v_{ij}^{eff} + \sum_i U_i^d \tag{2.5}$$

where v_{ij}^{eff} contains the two-body term of the SW potential (Eq. 2.2) and a correction term (which comes from the double sum implementation of the three-body term). The expression for v_{ij}^{eff} is given by:

$$v_{ij}^{eff} = v_2(r_{ij}) - \lambda[g_{ij}^2(1+\alpha)^2] \tag{2.6}$$

where $g_{ij} = exp\left[\frac{\gamma}{r_{ij}-a}\right]$. The second term in the Eq. 2.5 is the three-body term of SW potential written as double sum and has an expression:

$$U_i^d = \frac{\lambda}{2}\alpha^2 h_i^2 + \lambda\alpha\left|\mathbf{s}_i^2\right| + \frac{\lambda}{2}Tr\left[\mathbf{T}_i^2\right] \tag{2.7}$$

where h_i is a scalar, $\mathbf{s}_i$ is a vector and $\mathbf{T}_i$ is tensor of rank 2, having the following expression:

$$h_i = \sum_{j\neq i} g_{ij} \tag{2.8}$$

$$\mathbf{s}_i = \sum_{j\neq i} g_{ij}\hat{\mathbf{r}}_{ij} \tag{2.9}$$

$$\mathbf{T}_i = \sum_{j\neq i} g_{ij}(\hat{\mathbf{r}}_{ij} \otimes \hat{\mathbf{r}}_{ij}) \tag{2.10}$$

The force expression is as follows:

$$\begin{aligned} -\mathbf{F}_i &= \bigtriangledown U_{SW} \\ &= \sum_{j<i} \frac{1}{r_{ij}} \frac{\partial v_2}{\partial r_{ij}} \mathbf{r}_{ij} - \sum_{j \neq i} 2\lambda(1+\alpha)^2 \frac{g_{ij}}{r_{ij}} \frac{\partial g_{ij}}{\partial r_{ij}} \mathbf{r}_{ij} + \\ &\quad \sum_{j \neq i} (c_{ij} + c_{ji}) \mathbf{r}_{ij} + \sum_{j \neq i} 2\lambda\alpha \frac{g_{ij}}{r_{ij}} (\mathbf{s}_i - \mathbf{s}_j) + \\ &\quad \sum_{j \neq i} 2\lambda g_{ij} \frac{\mathbf{T}_i + \mathbf{T}_j}{r_{ij}^2} \mathbf{r}_{ij} \end{aligned} \tag{2.11}$$

where $(c_{ij} + c_{ji})$ is given by

$$\begin{aligned} c_{ij} + c_{ji} &= \lambda\alpha^2 \frac{\partial g_{ij}}{\partial r_{ij}} \frac{h_i + h_j}{r_{ij}} + \\ &\quad 2\lambda\alpha \left(\frac{\partial g_{ij}}{\partial r_{ij}} - \frac{g_{ij}}{r_{ij}} \right) \frac{\mathbf{r}_{ij}.(\mathbf{s}_i - \mathbf{s}_j)}{r_{ij}^2} + \\ &\quad \lambda \left(\frac{\partial g_{ij}}{\partial r_{ij}} - \frac{2g_{ij}}{r_{ij}} \right) \frac{\mathbf{r}_{ij}.(\mathbf{T}_i - \mathbf{T}_j)}{r_{ij}^3} \mathbf{r}_{ij} \end{aligned} \tag{2.12}$$

We find that this implementation of the SW potential is about six time faster than the conventional implementation of SW potential.

2.1.2 Conversions

In this subsection we provide the reduced to real unit conversion factors for various observable measured using the SW potential. The basic unit of length is σ (the diameter of the atom), energy is ϵ (the depth of the two-body potential) and mass is m (the mass of the atom). Using the basic units we calculate the conversion factors which are shown in the following table. As we discussed in the previous section the Stillinger-Weber potential was parametrised with $\sigma = 2.0951$Å, $\epsilon = 209.5kJ/mol$ and $m = 28.0855gm/mol$. To obtain distance in real units we multiply the reduced distance by a factor 2.0951. Similarly for other variable we show the multiplicative factor in the following table.

Observable	Factor (Unit)
Length	$r^* \times 2.0951$ (Å)
Energy	$E^* \times 209.5$ (kJ/mol)
Mass	$m^* \times 28.0855$ (gm/mol)
Temperature	$T^* \times 25173$ (K)
Pressure	$P^* \times 37.776$ (GPa)
Density	$\rho^* \times 5.0571$ (gm/cm^3)
Time	$t^* \times 76.6$ (fs)
Diffusivity	$D^* \times 0.005730345$ (cm^2/s)
Viscosity	$\eta^* \times 0.029060146$ (poise)

Table 2.1: Conversion factor for various observables calculated from the Stillinger-Weber model potential for silicon.

2.2 Molecular Dynamics Simulation

Molecular Dynamics (MD) simulations have proven to be a powerful simulation tool to study thermodynamic as well as dynamic properties of material (characterised by an interaction potential). Given the information of state point of interest (*e.g.* number of atoms N, applied pressure P or density ρ and applied temperature T) an MD simulation typically involves three main steps which are (1.) Initialisation of the system, (2.) Evolution of system towards equilibrium and (3.) Calculation of equilibrium properties.

Based on the input density and temperature, we do the initialisation of the coordinates and velocities of the atoms. Since the focus of our study is the liquid phase, which is in a disordered state, the atomic coordinates are randomly initialised within the simulation box. We make sure that no two atom's coordinates over lap on each other, since this would lead to unrealistically large energy and force values, which may eventually terminate the simulation. For crystal phase simulations we do a cubic diamond initialisation of atomic coordinates. For a given temperature, the initial velocities of the atoms are drawn from the corresponding Maxwell-Boltzmann distribution.

Evolution of the system involves calculation of forces on the atoms and integration of the equations of motion. If $r(t)$ and $v(t)$ represent the current positions and velocities of the atoms, for the time evolution of the system we need to calculate $r(t + \Delta t)$ and $v(t + \Delta t)$, where Δt is the time step of MD simulation. Various algorithms have been developed for the integration of Newton's equation of motion which include the Verlet algorithm, the Leap-frog algorithm, velocity-Verlet algorithm *etc* [56]. In order to perform MD simulations in a Isochoric-Isothermal (NVT) ensemble or in a Isobaric-Isothermal (NPT) ensemble, we need methods for applying a thermostat and a barostat. This is achieved by methods which use a Lagrangian formulation for obtaining the equations of motion [56]. In our work we have used the LAMMPS MD package [121], which uses the Nose-Hoover thermostat, to perform NVT MD simulations. For NPT MD simulation we use a home grown code which implements the integration algorithm following the work of Brown and Clarke [26]. In all our MD simulations we have used periodic boundary condition and unless otherwise mentioned the system size is 512 atoms and the time step of integration is $\Delta t = 0.005$ in reduced units, which is equivalent to $0.3830 fs$. At each state point we have performed a minimum of 60 million MD steps which corresponds to $22 ns$ and minimum of $3 - 5$ independent samples.

From the equilibrated configurations we have measured the average quantities like pressure, density *etc*, space correlation functions like radial distribution function, structure factor *etc* and time correlation function like intermediate scattering function, van Hove function *etc*. Some of these measurements (*e.g.* static properties like pressure, density *etc*) can be easily calculated while the simulation is in progress ("on the fly"). Even though, on the fly, it is possible to calculate time or space correlation function on the fly [56], it is simpler to output the atomic coordinates and velocities periodically and to calculate after the simulation gets completed. We calculate the temperature of the system from the average kinetic energy using the relation $T = \sum_{i=1}^{N} \frac{m<v_i^2>}{3k_B}$, where m is the mass of the atom, v_i is the velocity of the atom i and k_B is the Boltzmann constant. We can calculate the pressure

from virial equation for the pressure [56] and for pair-wise additive interactions (like the Stillinger-Weber interaction potential), the expression for pressure is given by

$$P = \frac{\rho}{\beta} + \frac{1}{V}\frac{1}{3}\sum_{i}\sum_{j>i}\mathbf{f}(\mathbf{r}_{ij}).\mathbf{r}_{ij} \tag{2.13}$$

where ρ is the number density, $\beta = 1/k_BT$, V is the volume, $f(r_{ij})$ and r_{ij} represent the force and distance between atom i and j respectively. Other quantities which we have computed in this work is discussed in the last section of this chapter. Note that we have outputted the simulation trajectory (containing coordinates and velocities of atoms, simulation box length, instantaneous temperature and pressure) in terms of equally spaced blocks of data. Further in each block the frequency of storing the the data is in log scale. Writing the trajectory in this style, we store the information related to both small time and long time periods, while optimising the demand for data storage.

2.3 Monte Carlo Simulation

Monte Carlo (MC) simulations have been extensively used in the study of equilibrium properties of condensed matter systems. Especially when there are large energy barriers and the system can get trapped at low energy basins, MC is the method of choice since algorithms to overcome such barriers may be defined. MC simulations have been also employed in the study of rare events, like crossing a nucleation barrier. Unlike in an MD simulation, MC simulation method can employ un-physical moves which can overcome the issues related to entrapment in local basins. This advantage comes at a price *i.e.,* we cannot obtain the dynamical properties directly from a conventional MC simulation.

In an MC simulation a series of configurations are generated such that the probability distribution of these configurations will be proportional $\frac{1}{Z}e^{(-\beta E(r^N))}$, where $E(r^N)$ is the Hamiltonian of the system, which depends on coordinates

of the atoms and Z is the partition function. After obtaining such a sequence of configurations which follow the desired equilibrium distribution the average of any thermodynamic property can be calculated as $< A >= \frac{1}{M}\sum_{i=1}^{M} A(r_i^N)$, where M total number of sampled configurations. One of the well known procedures for generating such a sequence of configurations is the Metropolis method. Let o be the current configuration with an equilibrium probability proportional to $N(o)$. The procedure to generate new configuration should be such that an equilibrium distribution of configurations should remain invariant, which is achieved by following the detailed balance condition, according to which, the average number of moves from o to any new state n is equal to the moves from n to o. Hence

$$N(o)\pi(o \to n) = N(n)\pi(n \to o) \tag{2.14}$$

where $\pi(o \to n)$ is the transition probability (from o to n) which can be split into probability associated with the generation of a new state represented by $\alpha(o \to n)$ and an acceptance probability $acc(o \to n)$ which represents the probability with which the new configuration is accepted. In all our simulations we assume α to be symmetric i.e., $\alpha(o \to n) = \alpha(n \to o)$. Hence we get

$$N(o)acc(o \to n) = N(n)acc(n \to o) \tag{2.15}$$

Using the expression for N we can rewrite the above equation as

$$\frac{acc(o \to n)}{acc(n \to o)} = \frac{N(n)}{N(o)} = exp(-\beta[E(n) - E(o)]) \tag{2.16}$$

In the Metropolis algorithm one chooses the following scheme to evolve the system (represented schematically in FIG. 2.1).

$$acc(o \to n) = min(1, \exp(-\beta[E(n) - E(o)])) \tag{2.17}$$

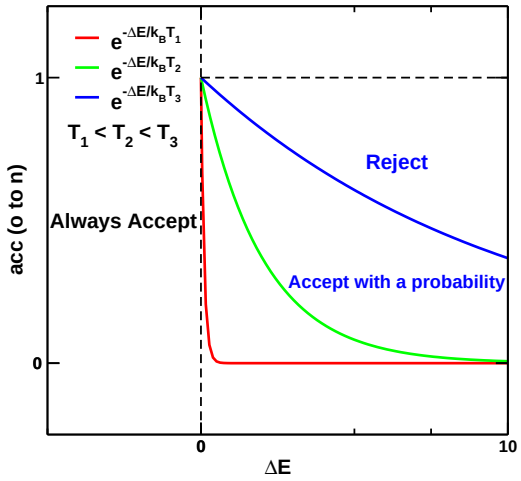

Figure 2.1: A schematic representation of Metropolis algorithm shown for three different temperatures. For $\Delta E < 0$ the trial move is always accepted. At high temperatures acceptance probability is high.

We summarise below the procedure for performing an MC simulation in the NVT ensemble. At a chosen density (ρ) and temperature (T)

1. Randomly select an atom and calculate its energy energy $E(o)$.
2. To generate a trial configuration, a random displacement is given to the atomic coordinate and the new energy $E(n)$ is calculated.
3. The trial move is accepted with a probability $min(1, exp(-\beta[E(n) - E(o)]))$.

In an NPT MC simulation we have to perform a volume change trial move along with the random displacement move. We can perform trial move in the logarithm of the volume and the acceptance criteria for such a trial move is given by

$$acc(o \rightarrow n) = min(1, \exp(-\beta[E(n) - E(o) + P(V_n - V_o) - (N+1)\beta^{-1} ln(V_n/V_o)])) \quad (2.18)$$

where $E(o)$ and $E(n)$ represents the energy of the system before and after

the volume trial move, P is the applied pressure, V_o and V_n is the old and new volume.

As noted in previous work [142] the study of the supercooled phase of silicon faces the challenge of slow equilibration and high crystallisation. To circumvent the issue of slow equilibration we have use the parallel tempering MC technique.

The parallel tempering MC simulation is a method to accelerate the equilibration of a system. The simulation method is based on the replica exchange sampling scheme. At low temperatures the time evolution of atomic coordinates is characterised by long periods of time when the system is stuck in local free energy minima that are separated by large barriers. For proper sampling of the phase space, the system has to make transitions between such minima in an efficient way. In ordinary MC simulations, as it can be seen from FIG. 2.1, the acceptance probability goes down with a lowering of temperature for moves that increase the energy. The solution offered by the parallel tempering MC method is to perform simulations MC simulations at 'M' randomly initialised copies of the system, each copy being at a different temperature. The range of temperatures varies between the temperature of interest and the temperature at which system explores the phase space easily. According to Metropolis criterion we swap copies belonging to different temperatures. If the difference in temperature is very large, according the acceptance criterion, such a swap move will have a very low probability. Hence we use intermediate temperatures, having small differences, to attempt a swap move (which is analogous to using small displacement steps in ordinary MC simulation). In this way, a system would come out of a local free energy minima and hence properly sample the phase space. The acceptance criterion associated with such a swap move is given by

$$acc((1,\beta_1),(2,\beta_2) \rightarrow (2,\beta_1)(1,\beta_2)) = min(1, exp[(\beta_1 - \beta_2)(U(1) - U(2))]) \tag{2.19}$$

where the system 1 and system 2 have energies $U(1)$ and $U(2)$ respectively and β_1 and β_2 represent the inverse temperatures at which simulations are carried out. We decide upon the intermediate temperatures by looking at

the extent of overlap between the distribution of energies of the two system which we attempt to swap. The swap frequency is chosen such that the system spends at least an amount of time corresponding to a mean square displacement of 1σ at the highest T. We note that the above acceptance criterion assumes that all the copies are swapped with their nearest (in T) copies.

We have performed parallel tempering MC in a NPT ensemble, in which we not only swap between temperatures, but also between different pressure values [51]. The acceptance criteria associated with such a swap move is given by

$$\begin{aligned} acc((1,\beta_1,P_1),(2,\beta_2,P_2) \rightarrow (2,\beta_1,P_1),(1,\beta_2,P_2)) \\ = min(1, exp(\Delta(\beta P)\Delta V + \Delta\beta\Delta E)) \end{aligned} \tag{2.20}$$

where

$$\begin{aligned} \Delta(\beta P) &= \beta_2 P_2 - \beta_1 P_1 \\ \Delta V &= V(o)_2 - V(o)_1 \\ \Delta E &= E(o)_2 - E(o)_1 \end{aligned} \tag{2.21}$$

The subscript 1 and 2 represent the systems at different temperature and pressure values. Note that in a NPT MC simulation, for each system, we also have to change the volume of the box and hence involves current volume and its associated energy (represented by $V(o)$ and $E(o)$) and new trial volume and its associated energy ($V(n)$ and $E(n)$). The above acceptance criteria is in terms of current volume and energy.

We have used the *Mersenne Twister* random number generator [105] for all our MC simulations. In each MC cycle the maximum displacement an atom can make is 0.12σ and the maximum change in volume is $0.05\sigma^3$. The parallel tempering MC simulations were performed with a system size of 512 atoms for about 60 million MC cycles. To check the equilibration of the system we verify that each copy of the system gets swapped up and down in temperature T at least 100 times. We also ascertain that every atom in the

system has moved at least $5\sigma^2$.

2.4 Other Calculations and Techniques

2.4.1 Mean Square Displacement

The mean square displacement (MSD) is a measure of average distance an atom travels in a given time interval and is defined as:

$$\left\langle \mathbf{r}^2(t) \right\rangle \equiv \frac{1}{N} \left\langle \sum_{i=1}^{N} \left| \vec{r}_i(t) - \vec{r}_i(0) \right|^2 \right\rangle \tag{2.22}$$

where N is the total number of atoms. The angular bracket represents an average over different time origins. In the FIG. 2.2 we show the MSD profile for a system in the liquid phase, in which we see three distinct regimes of dynamics. At small time interval atoms in the system travels ballistically (with no collisions) and hence we find that the MSD is proportional to t^2. The time interval when the atoms starts to collide with its neighbouring atoms is associated with the caging regime. The MSD shows a plateau like feature, since atoms are less mobile in this time interval. After a certain time interval the atoms come out of the cage and the motion of the atoms can be associated with that of a random walk. In this regime the MSD is proportional to t and motion of the atoms is termed as diffusive (since the evolution of the atoms in this time interval can be approximated by the diffusion equation). The slope of the MSD in the diffusion regime is related to the self-diffusion coefficient through the Einstein-Smoluchowski equation and is given by (for the case of three dimensional system)

$$D = \lim_{t \to \infty} \frac{\langle \mathbf{r}^2(t) \rangle}{6t} \tag{2.23}$$

Since our system of interest is in a metastable phase, the MSD provides a quick way determine whether the system is in a liquid state or it has crystallised, since the diffusion coefficient is quite sensitive to the presence of crystalline clusters in the system.

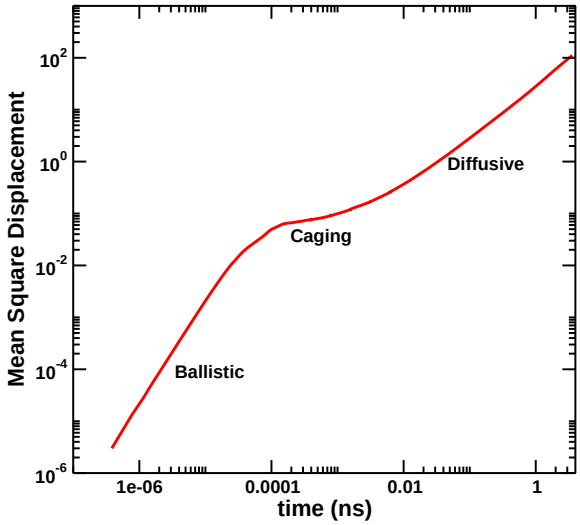

Figure 2.2: Mean square displacement (MSD) of a system in liquid phase showing three regimes of dynamics.

2.4.2 Radial Distribution Function and Fifth Neighbour Distribution

Radial distribution function or pair correlation function ($g(r)$) is a 2-point correlation function which is defined as

$$g(r) = \frac{V}{N^2} \left\langle \sum_i \sum_{j \neq i} \delta(\vec{r} - \vec{r}_{ij}) \right\rangle \tag{2.24}$$

where V is the volume of the system, N is the number of atoms, r_{ij} represents the distance between atoms i and j. Physically, $4\pi r^2 \rho g(r) dr$ gives the number of neighbours a reference atoms has at a distance between r and $r + dr$. Here ρ is the number density of the system. In the FIG. 2.3 we show a typical $g(r)$ profile for a liquid and a crystal system. The minima separate different coordination shells, which are well defined in the case of crystalline system. We can obtain the coordination number (C_{nn}), which is the number of nearest

neighbours to a reference atom, using the relation $C_{nn} = \int_0^{r_c} \rho g(r) 4\pi r^2 dr$, where r_c the distance corresponding to the first minimum of $g(r)$.

The pair correlation function can be decomposed according to the contributions from the successive nearest neighbors of a reference atom to define a sub-RDF $g_i(r)$ [135] such that $g(r) = \sum_{i=1}^{N} g_i(r)$. For $i = 5$ we get the fifth neighbour distribution. Physically, $g_5(r)$ gives the probability of observing a 5^{th} nearest neighbour from a reference atom at a distance between r and $r + dr$. Note that if the 5^{th} is found within the first coordination shell, the $g_5(r)$ has a uni-model peak (*see* FIG. 2.4).

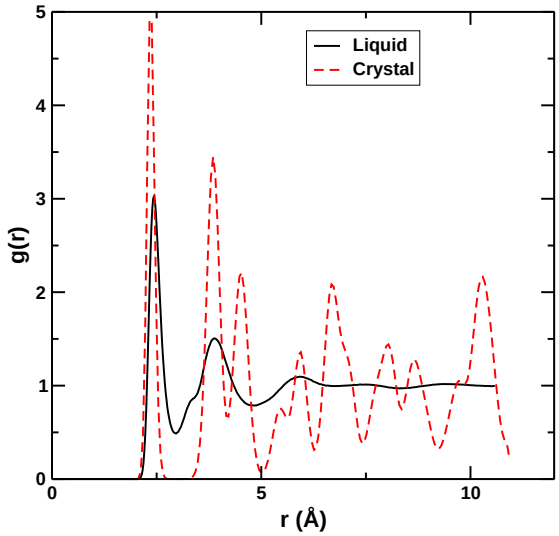

Figure 2.3: Radial distribution function $g(r)$ for a system in liquid and crystal phase.

Static Structure Factor

Structure factor can be obtained from Fourier transform of $g(r)$ as

$$S(\mathbf{q} \neq \mathbf{0}) = 1 + \rho \int e^{i\mathbf{q}.\mathbf{r}} [g(\mathbf{r}) - 1] d\mathbf{r} \tag{2.25}$$

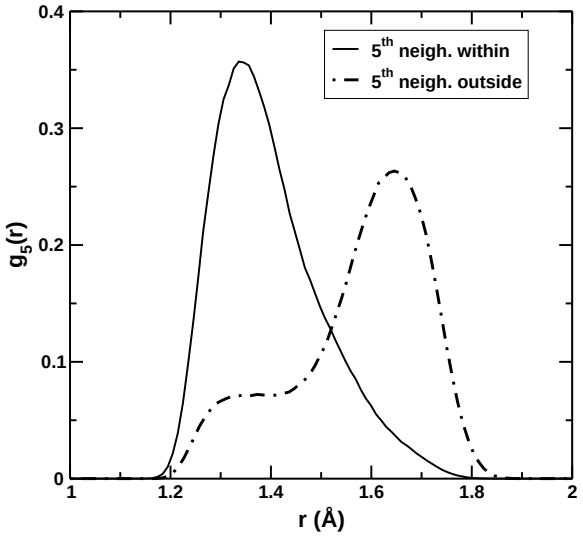

Figure 2.4: Fifth neighbour distribution $g_5(r)$ for a system in liquid phase.

This is an experimentally accessible quantity determined by various scattering techniques. We can also defined $S(q)$ in terms of the density-density correlation function in the Fourier space as

$$S(\mathbf{q}) \;=\; \frac{1}{N} < \delta\rho(\mathbf{q})\delta\rho(-\mathbf{q}) > \tag{2.26}$$

2.4.3 van Hove Function and Intermediate Scattering Function

The van Hove function is a density-density space-time correlation function given by

$$\rho G(\mathbf{r},t) = \left\langle \frac{1}{N}\sum_{i=1}^{N}\sum_{j=1}^{N}\delta(\mathbf{r}+\mathbf{r_j}(0)-\mathbf{r_i}(t)) \right\rangle \tag{2.27}$$

We can separate out the self (same atom at different times) and distinct (different atoms at different times) contributions of the atoms to the $G(\mathbf{r},t)$

and write the above equation as

$$G(\mathbf{r},t) = G_s(\mathbf{r},t) + G_d(\mathbf{r},t)$$

where

$$\begin{aligned} G_s(\mathbf{r},t) &= \left\langle \frac{1}{N}\sum_{i=1}^{N}\delta(\mathbf{r} - |\mathbf{r_i}(t) - \mathbf{r_i}(0)|)\right\rangle \\ G_d(\mathbf{r},t) &= \left\langle \frac{1}{N}\sum_{i=1}^{N}\sum_{j\neq i}^{N}\delta(\mathbf{r} - |\mathbf{r_i}(t) - \mathbf{r_j}(0)|)\right\rangle \end{aligned} \tag{2.28}$$

Physically $G(\mathbf{r},t)d\mathbf{r}$ is the number of atoms j at $\mathbf{r}$ within a region $d\mathbf{r}$ around a point $\mathbf{r}$ at time t given that there was an atom i at the origin at time $t = 0$. For equal time, the distinct part of van Hove function reduces to the pair correlation function *i.e.,* $G_d(\mathbf{r},0) = \rho g(\mathbf{r})$. For $t, r \to \infty$, the self part of van Hove function follows a Gaussian distribution *i.e.,* $G_s(\mathbf{r},t) \to \frac{1}{(4\pi Dt)^{3/2}} exp\left(-\frac{r^2}{4Dt}\right)$, where D is the diffusion constant.

The intermediate scattering function ($F(q,t)$) is the spacial Fourier transform of the van Hove function $G(r,t)$. It can be shown that the intermediate scattering function is the correlation function of the Fourier components of the density, hence we can write

$$F(\mathbf{q},t) = \frac{1}{N}\left\langle \delta\rho(\mathbf{q},t)\delta\rho(-\mathbf{q},0)\right\rangle \tag{2.29}$$

where $\delta\rho(\mathbf{q},t)$ is the local density fluctuation in in Fourier space and is given by

$$\rho(\mathbf{q},t) = \sum_{i=1}^{N}\exp\left(i\ \mathbf{q}\cdot\mathbf{r}_i(t)\right) \tag{2.30}$$

In our work we obtain the alpha relaxation time (τ_α) as the time at which the $F(q,t)$ (at a q value corresponding to the first peak of S(q)) decays by a factor of e.

2.4.4 Structural Order Parameters

In this section we provide the definitions of different measures of structural order which we have used to characterise the local arrangement of silicon atoms.

Translational Order

The translational order t_{trans} [172] is defined as

$$t_{trans} = \frac{\int_0^{\xi_c} |g(\xi) - 1| \, d\xi}{\xi_c} \tag{2.31}$$

where $\xi = r\rho^{(1/3)}$ is the scaled coordinate, r is the distance between the two atoms, ρ is the number density and ξ_c is a cutoff distance, where the system's $g(r)$ goes to 1 to a high degrees of precision. In all our calculations, ξ_c is chosen to be 4.0σ or 8.3Å. Scaled coordinates are used so that the above integral sums over an equivalent number of coordinate shells at each density. For the ideal gas, since $g(r) = 1$, t_{trans} is zero and for a crystal (which has long range crystalline order) t_{trans} has a large but finite value. In the liquid phase the t_{trans} will have a value in between that of the ideal gas and a crystal.

Tetrahedrality Order

The tetrahedrality order (q_{tetra}) [52] is defined as

$$q_{tetra} = 1 - \frac{3}{8} \sum_{j=1}^{3} \sum_{k=j+1}^{4} \left(cos(\psi_{jk}) + \frac{1}{3} \right)^2 \tag{2.32}$$

where ψ_{jk} is the angle formed by the lines joining a reference atom i and its nearest neighbours j and k. The average q_{tetra} varies between 0, for the case of an ideal gas and 1, for the case of a perfect tetrahedral network.

Bond Orientational Order

The bond orientational order [158] is defined using the spherical harmonics evaluated from the knowledge of unit vectors of the neighbouring atoms. Two atoms are considered to be neighbours or bonded if they are within a distance cutoff corresponding to the first minimum of $g(r)$. Let the atom i have j as its neighbour at a distance $|\vec{r}_{ij}|$ and with an orientation $\hat{r}_{ij}$. The bond orientation order around the atom i is given by

$$q_{lm}(i) \equiv \frac{1}{N_n(i)} \sum_{j=1}^{N_n(i)} Y_{lm}(\hat{r}_{ij}) \tag{2.33}$$

where $N_n(i)$ is the number of neighbours of atom i, $Y_{lm}(\hat{r}_{ij}) \equiv Y_{lm}(\theta_{ij}, \phi_{ij})$ are the spherical harmonics calculated along the vector $\hat{r}_{ij}$ between the particles i and j, θ_{ij} and ϕ_{ij} represent the polar and azimuthal angles respectively. By summing $q_{lm}(i)$ over all the ij bonds in the system, instead of only those around an atom i, we can obtain a *global* orientational order Q_{lm}. We can define rotationally invariant global orientational order Q_l as

$$Q_l = \left(\frac{4\pi}{2l+1} \sum_{m=-l}^{l} |Q_{lm}|^2 \right)^{(1/2)} \tag{2.34}$$

In the liquid phase Q_l will have a very small value. As the system size increases, Q_l goes to zero. For the crystal phase Q_l will have a finite value as shown in the the FIG. 2.5 for cubic diamond crystal.

From Eq. 2.33 we can also define a rotationally invariant local orientational order $q_l(i)$ as

$$q_l(i) = \left(\frac{4\pi}{2l+1} \sum_{m=-l}^{l} |q_{lm}(i)|^2 \right)^{(1/2)} \tag{2.35}$$

Note that unlike global orientational order parameter, the $q_l(i)$ will have a finite value for liquid phase also. For the case liquid silicon $q_l(i)$ between 0.2

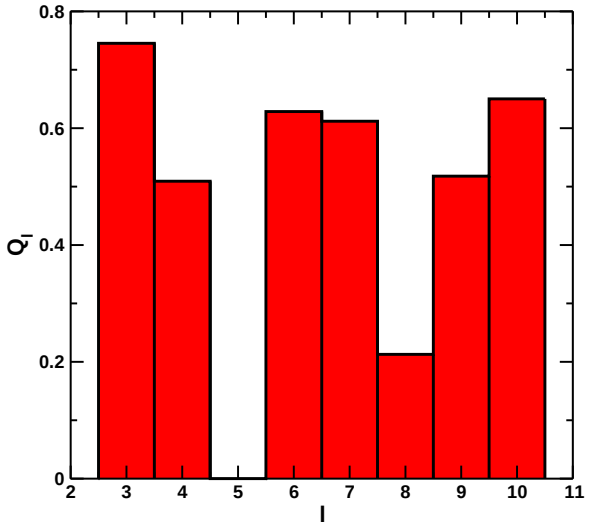

Figure 2.5: The orientational (Q_l) order calculated for cubic diamond crystal unit cell for various l values

and 0.7.

2.4.5 Viscosity (η)

We calculate the shear viscosity η using the Green-Kubo formula [66], wherein we integrate the auto-correlation function (obtained using the LAMMPS MD package [121]) of the stress tensor is given by

$$\eta = \frac{V}{k_B T} \int_0^\infty < P_{\alpha\beta}(t) P_{\alpha\beta}(0) > dt \tag{2.36}$$

where V is the volume of the simulation box, k_B is the Boltzmann's constant and $P_{\alpha\beta}$ is the stress tensor defined as

$$P_{\alpha\beta}(t) = \frac{1}{V} \left(\sum_{i=1}^{N} P_{i\alpha} P_{i\beta}/m + \sum_{i=1}^{N} \sum_{j>i}^{N} r_{ij\alpha} f_{ij\beta} \right) \tag{2.37}$$

$\alpha, \beta \in (x, y, z)$ denotes the component of the vector, r_{ij} is the distance between particle i and j and $f_{ij} = -\partial U^{SW}(r_{ij})/\partial r_{ij}$.

Chapter 3

Phase Behaviour of Supercooled Liquid Silicon

The phenomenon of the liquid-liquid phase transition (LLT) is an unusual phase transformation between two liquids in a single component system. The liquid-liquid transition has been investigated in a wide variety of substances (as we already discussed in the introduction) including water [125], silica [135], germanium [10], carbon [31, 65, 187] and hydrogen [114, 147] - these substances form a very significant component of our natural world.

For the case of silicon, using a two-state model, Aptekar [10, 48] in 1979 proposed a liquid-liquid transition and further predicted a negative pressure critical point. Even though some of the early experimental as well as simulation work proposed a liquid-amorphous transition [14, 24, 30, 45, 99, 116, 131, 132, 154, 167, 174, 183], the precise nature of the transition was unclear owing to the limited availability of information. Based on simulation evidence using the Stillinger-Weber (SW) potential for silicon [159] Angell *et al.* [5] proposed a first order liquid-liquid transition line as a feature in the pressure-temperature phase diagram of silicon. The experimental work of Deb *et al.* [34,39] observed a pressure induced amorphous-amorphous transition and speculated the possibility of an underlying liquid-liquid transition, to be found at ambient pressure at around ($1100K$). From extensive simulations of silicon using the SW model potential Sastry and Angell [142] found

evidence of a liquid-liquid transition at zero pressure at around $1060K$, which was also subsequently supported by *ab initio* simulations [59, 77].

In case of water, computer simulations in various model potentials have shown that the line of liquid-liquid transition ends at a liquid-liquid critical point ($LLCP$) [2,67,124,125,137,190]. But the recent proposal by Angell [4], suggests that a liquid-liquid transition is also consistent with a "critical point free" scenario. Hence the existence of a critical point needs independent verification. In this chapter we discuss such a evidence from computer simulations for critical point with an associated line of first order liquid-liquid transitions in supercooled liquid silicon. We identify the critical temperature and pressure and find that the critical point is indeed at a negative pressure value. Further we construct the whole phase diagram of supercooled liquid silicon and find interconnections between the thermodynamic anomalies and phase behaviour as suggested in previous works [41, 124, 125, 143, 155, 156].

3.1 Liquid-Liquid Critical Point

A liquid-gas critical point marks a second order phase transition which is characterised by the singular behaviour of second derivative of the free energy (*e. g.*, the heat capacity and the isothermal compressibility). The equation of state (pressure *vs.* density) for an isotherm above the critical temperature is continuous, whereas an isotherm below the critical temperature shows a density discontinuity (indication of a first order phase transition). Similar behaviour is expected to be seen in the case of liquid-liquid transition, and hence our approach to find the LLCP is to compute the equation of state (EOS) for a range of temperatures. We have employed Molecular Dynamics (MD) simulations using the SW for silicon for this purpose. Before we go into a detailed discussion of our results we summarise the simulation protocol followed to obtain the equilibrated data.

In order to obtain the equilibrium EOS for the supercooled liquid silicon we have performed constant pressure (NPT) MD simulations (employing an efficient algorithm for energy and force evaluations [146]) with a

time step of $0.383fs$. The system size is 512 atoms for all our MD simulations (unless otherwise mentioned). We have also performed constant volume (NVT) MD simulations with the same system size and time step (using the LAAMPS parallelised MD package [122]). The equilibration of the system was monitored by the observing the mean square displacement (MSD) and from the relaxation of intermediate scattering function and self overlap function $Q(t)$. (Note that the overlap function is defined as $Q(t) = \frac{1}{N}\sum_{i=1}^{N} w\,|\vec{r}_i(t_0) - \vec{r}_i(t+t_0)|$, where $w(r) = 1$, if $r \leq 0.3\sigma$, zero otherwise). At each state point we have simulated a minimum of 3 to 6 independent samples for ~ 100 relaxation times ($\sim 10\ ns$). At low temperatures we find that the crystallisation (monitored by energy jumps and pair correlation function as shown in FIG. 3.1) rates are high. At these state points we have performed around 10 to 50 initial runs, each of 22 ns. Non-crystallising samples (average of 5) were run up to $100ns$ (300 million MD steps) or for a time required for the MSD to reach $1nm^2$ (5 σ^2, where σ is the atomic diameter) or whichever was larger. In order to equilibrate the system at very low temperatures and high negative pressures we have employed parallel tempering Monte Carlo (MC) simulation technique [51, 56] (details related to MD simulations and MC simulations are given in the *Methods and calculations* chapter).

We have performed MD simulations at temperatures ranging from $T = 900K$ to $2500K$ and pressures ranging from $-3.77GPa$ to $+3.77GPa$ to obtain the EOS. From the EOS the upper and lower bound in temperature for the critical point was found. Above the critical temperature the EOS is a continuous and monotonic curve as shown in FIG. 3.2 (a). Below the critical temperature, the system phase separates and hence these isotherms (below $T = 1133K$), in the NPT MD simulations, showed jumps in densities for a small change in pressure (*see* FIG. 3.2 (b)) The NVT MD simulations performed at these temperatures ($T = 1133K$ to $1070K$) (and at densities spanning the range of the density jumps in the NPT MD simulations) showed non-monotonic isotherms (*see* FIG. 3.2 (b)). Such non-monotonicity in simulations arises from metastability on the one hand, and on the other

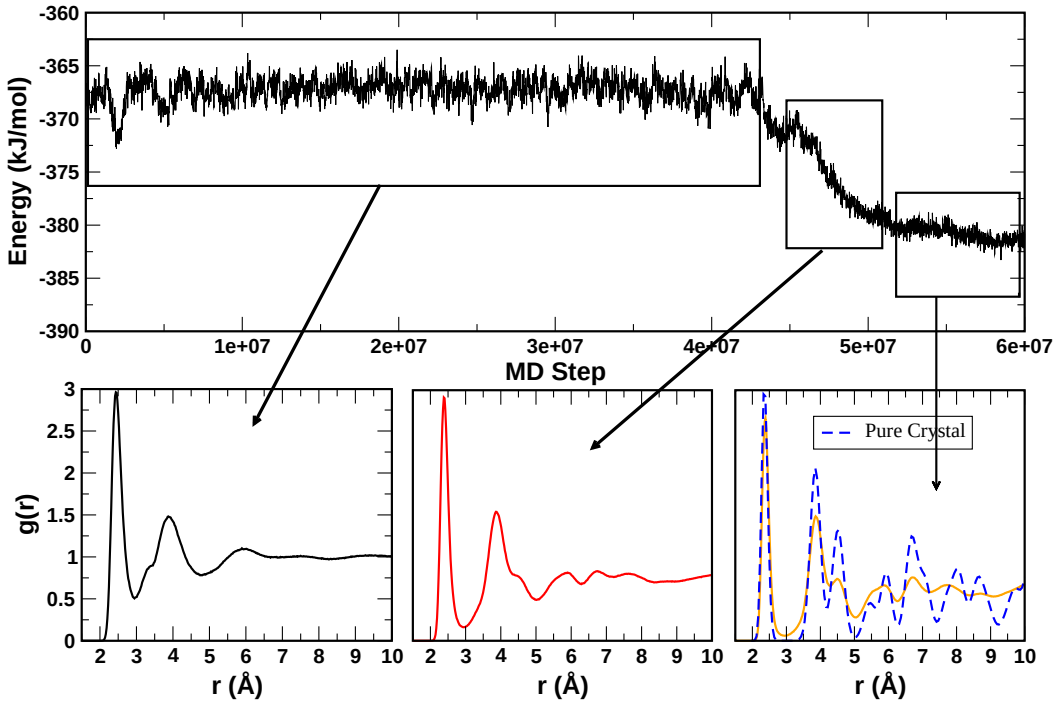

Figure 3.1: Plot of energy (*top panel*) and radial distribution function $g(r)$ (*bottom panel*) for the system that is crystallising ($T = 1075K$ and $P = 0GPa$). As the system crystallises $g(r)$ develops a bump at $4.5\mathring{A}$, which grows into a full peak (for reference the pure crystal g(r) shown - blue dashed-line).

hand, incomplete phase separation owing to finite sample sizes in the unstable region, and constitutes a clear indication of a first order transition. The highest phase-coexisting temperature and lowest continuous isotherm bounds the critical temperature. Similarly, the pressure at which the continuous isotherms are flattest (above the critical temperature) and the pressure at which a density jump is seen (below the critical temperature) determine the bounds for the critical pressure. The estimated critical temperature and pressure are $T_c \sim 1120 \pm 12K$, and $P_c \sim -0.60 \pm 0.15GPa$ respectively.

Approaching the critical point from above leads to increased density fluctuations. We calculated the compressibility (K_T) values from density fluctuations (in the NPT MD simulation), in addition to evaluating the K_T

from the EOS. After doing a polynomial fit to an isotherm obtained from the NPT simulation, we obtain the K_T by taking numerical derivative of the EOS. To calculate K_T from the volume fluctuations we use the relation $K_T = \frac{1}{k_B T} \frac{<V^2> - <V>^2}{<V>}$, where k_B is the Boltzmann constant and V is the volume of the system. In FIG. 3.3, we show the compressibility values calculated from both methods for temperatures above $T = 1133K$. As seen in FIG. 3.3 the EOS estimates agree well with those from density fluctuations in the high pressure side of the compressibility maximum (which corresponds to the high density liquid (HDL) phase), but poorer agreement is obtained for the low pressure side the compressibility maximum (which corresponds to the low density liquid (LDL) phase), because of lack of good sampling.

First principles simulations: In case of carbon and silica, computer simulations using classical empirical potentials have predicted liquid-liquid transition [65, 135] which are contradicted by first principle MD ($FPMD$) simulations [79, 187]. In silicon, Jakse and Pasturel [77] and independently Ganesh and Widom [59] have reported first principle simulation results, both of which support the proposed liquid-liquid transition in silicon. In the work of Ganesh and Widom, the authors report the emergence of a van der Waals-like loop (shown in FIG. 3.4), as a signature of a first order phase transition at temperatures below $1182K$. The maximum time span of these simulations is around $40ps$ [77], which seems to be very small compared to the relaxation times of LDL (tens to hundreds of nanoseconds). But the FPMD calculations are computationally very expensive compared to classical MD simulations. It would be interesting to compare the equilibration times of the system simulated in FPMD and classical MD and do a systematic study of relaxation processes in these two different methods of simulation.

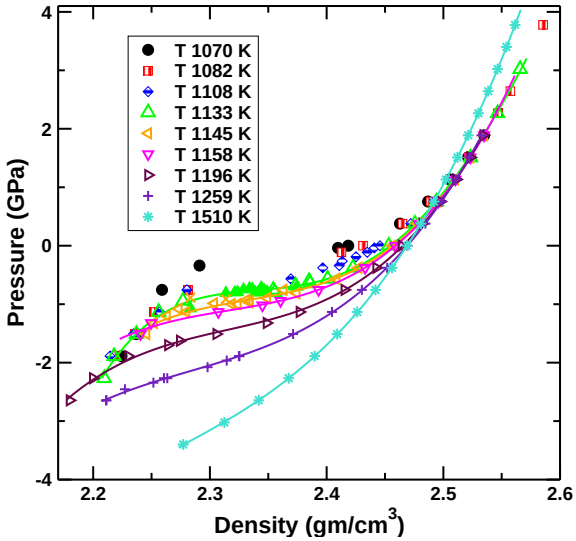

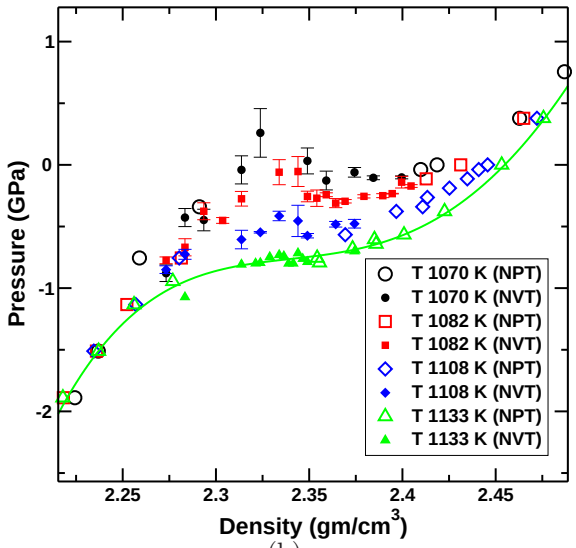

(b)

Figure 3.2: Equation of state from NPT MD and NVT MD simulations. Nine isotherms at temperatures above and below the critical temperature of the liquid-liquid transition are shown. The open symbols represent data from the NPT MD simulations and the opaque symbols represent data from the NVT MD simulation. The solid lines are polynomial fits to the data points. (a) The isotherms above $T = 1133K$ are monotonic and continuous and below $T = 1133K$ show a jump in density for small change in pressure in constant pressure simulations. (b) The NVT MD simulation data for $T < 1133K$ show non-monotonic behaviour indicating a first order phase transition.

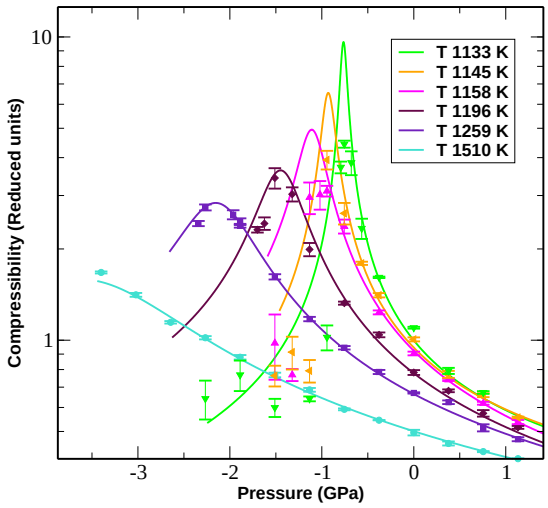

Figure 3.3: Isothermal compressibility against pressure for different temperatures from the NPT MD simulations. All the isotherms shown in the figure are for temperatures above the liquid-liquid critical temperature. With the decrease in temperature the maximum value of the compressibility along an isotherm increases, suggesting an approach to the critical point. The lines represent the compressibility values calculated from the equation of state by numerical differentiation. The symbols represent the compressibility calculated from volume fluctuations.

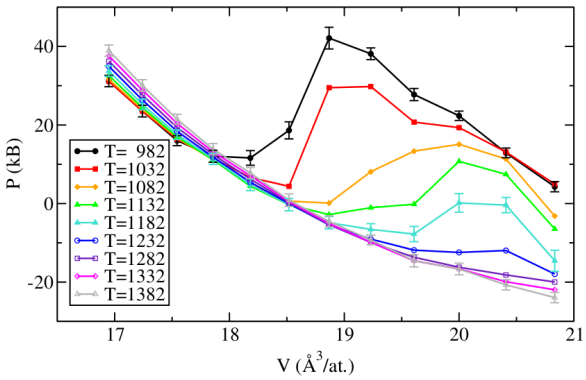

Figure 3.4: Equation of state of supercooled liquid silicon obtained from first principles MD (FPMD) simulations displaying a van der Waals-like loop for $T < 1232K$. [From Ganesh *et al.* [59] with permission.]

3.2 Phase Diagram

In order to obtain the complete phase behaviour of supercooled liquid silicon we have analysed the interplay of various loci of extremal behaviour, namely the spinodal, temperature of density extrema and temperature of compressibility extrema. Loci of temperature of maximum and minimum density, temperature of maximum and minimum compressibility and the spinodal were evaluated by employing, in addition to the MD simulations, parallel tempering MC simulations [51, 56] (at low temperature and pressures) and restricted ensemble MC simulations [32] (for locating the spinodal at low temperatures). Results concerning these features of the phase diagram are described below.

Temperature of maximum density (TMD): The TMD line is defined as the locus of isobaric maxima of density ρ *vs.* T ($(\partial\rho/\partial T)_P = 0$) or the locus of isochoric minima of pressure P *vs.* T ($(\partial P/\partial T)_V = 0$). For pressure values above $P = -3.80GPa$, we have obtained the TMD line from the NPT MD simulations. Below $P = -3.80GPa$, cavitation in the NPT MD simulations was observed and hence the NVT MD simulations were performed to locate isochoric minimum in pressure. In FIG. 3.5 and FIG. 3.6 we show the TMD obtained from density maxima along isobars and pressure minima along isochores respectively.

Temperature of minimum density ($TMinD$): The TMinD line is the locus of density minima points, crossing which, the system returns to the normal behaviour in density (increase in density with the decrease in temperature). Finding the TMinD line in supercooled liquid silicon is quite challenging since we must simulate the system deep inside the supercooled region of the phase diagram (where fast crystallisation, slow equilibration and cavitation pose hurdles to obtaining equilibrated data). In order to obtain equilibrated data we have employed NPT parallel tempering MC simulation technique [51], in which copies of the system at different T and P are swapped periodically according to a Metropolis acceptance criterion, thereby avoiding the possibility of the system getting stuck in phase space at low temperatures (details given in the *Methods and calculations* chapter). In FIG. 3.7 we show

the TMinD obtained from maxima along isochores. There have been very few reports of density minima for any substance. Experimental and simulation observation for water were reported only recently [96, 124].

Temperature of minimum compressibility ($TMinC$): Using the NPT MD simulations we obtain the line of TMinC (*see* FIG. 3.8 *top panel*). At pressure values below $P = -3.80GPa$ system cavitates quite easily and often. Hence care was taken by performing simulations for a minimum of 10 independent samples to construct the equation of state, from which we calculate the compressibility values.

Temperature of maximum compressibility (TMC or Widom line): The value of TMC at the high pressure values ($P > -2GPa$) is obtained from FIG. 3.3. In the FIG. 3.9 we show the compressibility data from which K_T^{max} were obtained for $P < -2GPa$. As the system crosses the K_T^{max} line from high T to low T (at a chosen pressure value), the relaxation times were found increase from picoseconds to tens of nanoseconds. Nearing the locus of compressibility maxima, crystallisation of samples was also found to be frequent. The K_T values shown in FIG. 3.9 are calculated from both volume fluctuations measured in the NPT MD simulations and from derivatives of pressure from the NVT MD simulations. For pressure values below $-3.90GPa$, the system cavitates easily and hence the location of K_T^{max} at these state points were not evaluated.

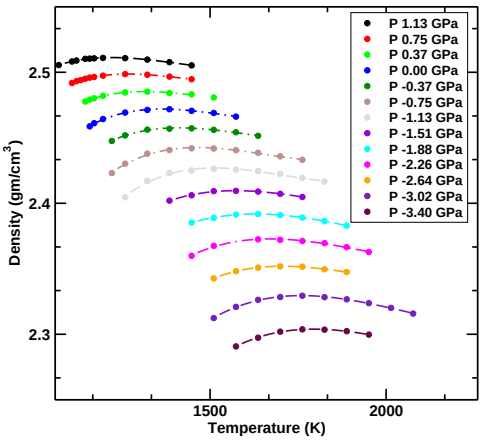

Figure 3.5: Density against temperature for different isobars from the NPT MD simulations. The temperatures associated with the maxima along each isobar defines the TMD line.

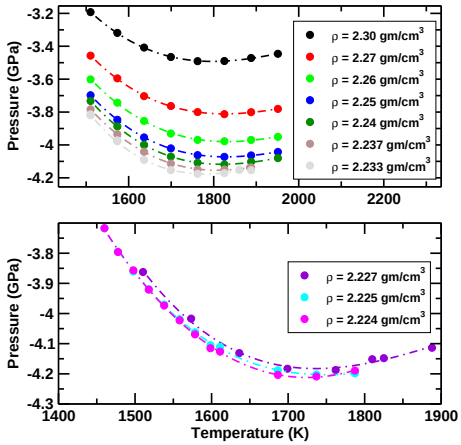

Figure 3.6: *(top panel)* Pressure against temperature for different isochores from the NVT MD simulations. The pressure and temperature values at the minimum obtained along each isochore for varying density define the TMD line in the (P, T) plane. *(bottom panel)* Isochores obtained from the NVT MD simulations at the lowest three densities. Below these densities, the system cavitates before the isochore passes through a minimum.

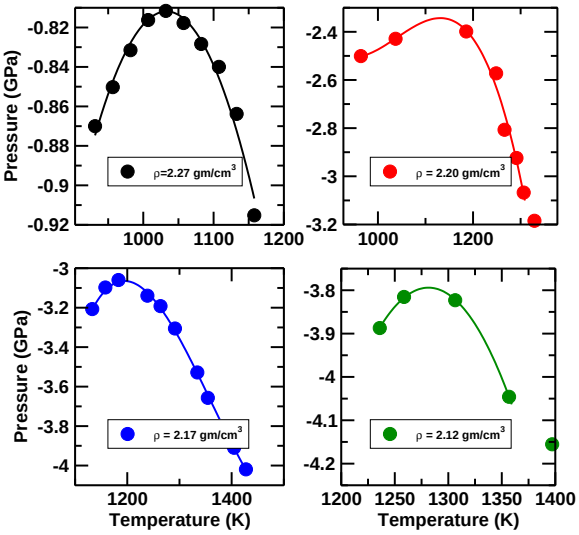

Figure 3.7: Pressure against temperature for different isochores from parallel tempering MC simulations. The location of the maxima along the isochores define the TMinD line.

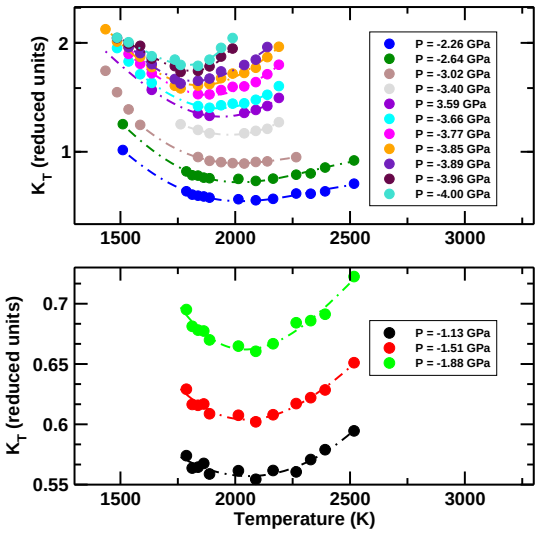

Figure 3.8: Isothermal compressibility against temperature for different isobars from NPT MD simulations. The location of the minima along the isobars define the TMinC line.

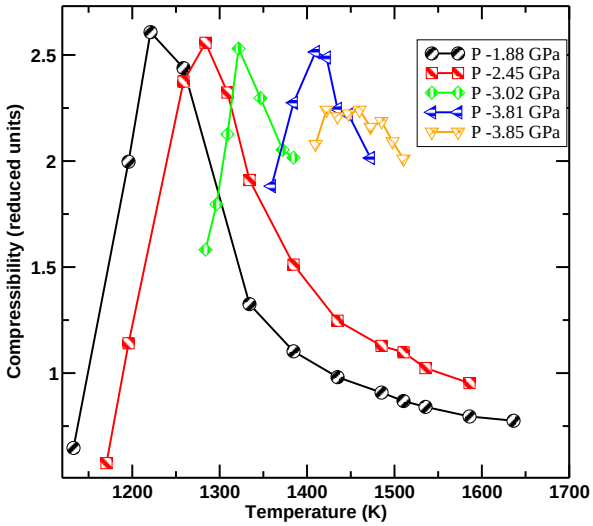

Figure 3.9: Isothermal compressibility against temperature for different isobars from NPT MD simulations. The location of the maxima along the isobars define the TMC line.

Liquid spinodal: The locus of limit of stability points which satisfy the thermodynamic condition $(\partial P/\partial V)_T = 0$ is termed as spinodal. It denotes the boundary between stable (or metastable) and unstable state points. In FIG. 3.10 we show high temperature spinodal isotherms ($T > 2200K$). These isotherms were obtained from the NVT MD simulations. For T $<$ 2200 K, cavitation was observed in the NVT simulations before the minimum along an isotherm is reached, due to which a drastic increase in the pressure was observed. In an attempt to circumvent this problem, we have performed restricted ensemble MC simulations wherein an arbitrary bound was imposed on the magnitude of the allowed density fluctuations by dividing the simulation box into a number of equal sub-cells and constraining the number of atoms in each of these sub-cells [32]. However, even in the restricted ensemble MC simulations, the system was found to cavitate occasionally, with the formation of voids across sub-cell boundaries (with each sub-cell satisfying the applied constraint on number of atoms). Hence the estimation of the spinodal at these state points were done from a quadratic extrapolation of

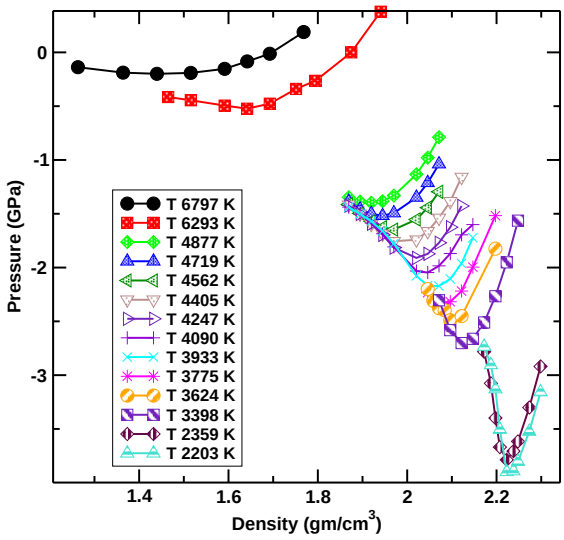

Figure 3.10: Pressure against density for high temperature isotherms ($T > 2200K$) from the NPT MD simulations. The location of the minima along the isotherms define the spinodal line.

the isotherms. The data points obtained from restricted ensemble MC simulations was fitted with a quadratic function $(p_0 + a1(\rho - \rho_0) + a2(\rho - \rho_0)^2)$, where p_0 and ρ_0 are the spinodal pressure and density values. The data and the fits are shown in FIG. 3.11.

As a further check of the spinodal estimate, we obtain the tensile limit of the liquid phase by increasing the tensile pressure on the simulation cell at different constant rates. The tensile limit line is defined as the the locus of maximum tensile stress (negative pressure) a system can withstand before it fails. At a given temperature we equilibrate the system at a high pressure value (for $T < 1510K$ at $P = -2.26GPa$ and for $T > 1510K$ at $P = 0GPa$, by performing NPT MD simulation) and then we apply a tensile pressure which increases at a specified rate. We have performed simulations at four different constant rates of change of tensile pressure ($0.1MPa/ps$, $1.0MPa/ps$, $10.0MPa/ps$, $50.0MPa/ps$). When the system reaches its limit of tensile strength, the system's density decreases drastically towards zero. In FIG.

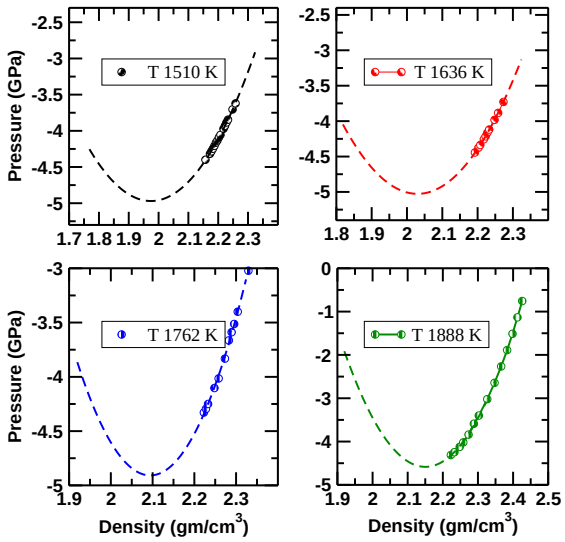

Figure 3.11: Pressure against density for low temperature isotherms ($T < 2200K$) from MD simulations. The dashed line indicate the quadratic extrapolation of the form $p_0 + a1 \times (\rho - \rho_0) + a2 \times (\rho - \rho_0)^2$ which are used to locate the spinodal.

3.12 we show the applied pressure against the measured density for a range of temperatures, from which the tensile limit line was obtained. At faster stretching rate ($10MPa/ps$) we find that the tensile limit is consistent with the spinodal estimates. For slow stretching rate ($0.1MPa/ps$) we find that the system cavitates at higher (less negative) pressure values. At an intermediate rate, ($1.0MPa/ps$) the estimated tensile limit line lies between the estimates obtained from the faster ($10MPa/ps$) and slow ($0.01MPa/ps$) stretching rates. At very high rate of change of tensile pressure ($50.0MPa/ps$), we find that the tensile limit to be below the spinodal estimates, indicating perhaps that the stretching rates are faster than microscopic relaxation time scales of the system.

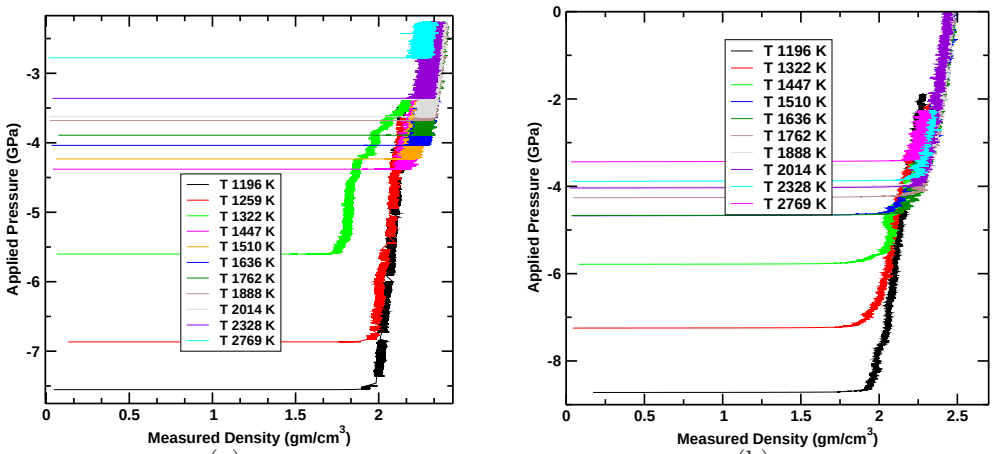

Figure 3.12: Applied pressure against measured density for different temperatures from the NPT MD simulations. The stretching rate in (a) corresponds to $0.1 MPa/ps$ and in (b) corresponds to $10.0 MPa/ps$.

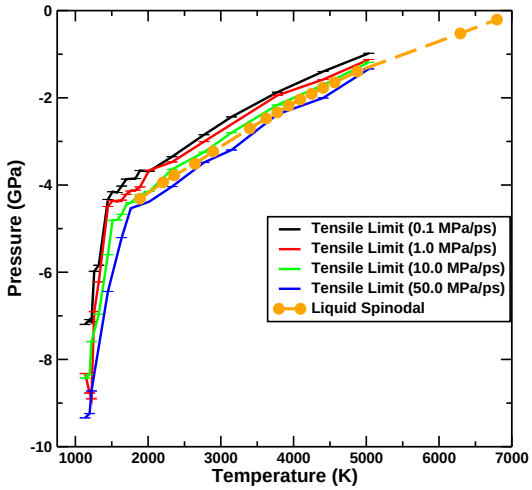

Figure 3.13: Pressure against temperature showing tensile limits obtained from different stretching rates along with the estimated spinodal line from NPT MD simulations.

In FIG. 3.13, the tensile limit obtained from different stretching rate along with the spinodal estimate is shown in the $P - T$ plane. At around $P = -4.0GPa$, the slope of the tensile limit changes to a bigger value, and based on the location of the compressibility maximum line, the states near the tensile limit change from HDL to LDL-like. In the phase diagram, the region of the slope change of the tensile limit correspond to the region where the TMD line meets the TMinD line and the TMC line meets the TMinC line. The connection between the change in slope of tensile limit to the changes in the nature of the states (HDL to LDL-like) is very interesting and needs to be investigated further.

Phase diagram: The liquid-liquid coexistence line was obtained from identifying the jumps in density for small changes in temperature isobars generated using the NPT MD simulations (*see* FIG.3.14). The complete phase behaviour of supercooled liquid silicon modeled by the SW potential is summarised in FIG. 3.15. The phase diagram includes the liquid-liquid critical point, liquid-liquid coexistence line, crystal-liquid coexistence line, liquid-gas coexistence line, the loci of TMD, TMinD, TMC and TMinC along the liquid-spinodal and tensile limit line. The estimated spinodal is monotonic in pressure *vs.* temperature T, *i.e.,* not "re-entrant" as predicted to be the case [155] if it intersects the TMD. The TMD, changes slope upon intersection with the TMinC, as analysed in [143]. Evaluating the relevant equation of state data as the TMD approaches the spinodal is particularly challenging. From available data, we can conclude that the TMinC appears to be smoothly joining with the TMC (line of compressibility maxima) that emanates from the liquid-liquid critical point. We have performed parallel tempering MC simulation below the critical temperature and pressure to recognise the line of density minima which appears to smoothly join the TMD line, as required by thermodynamic consistency.

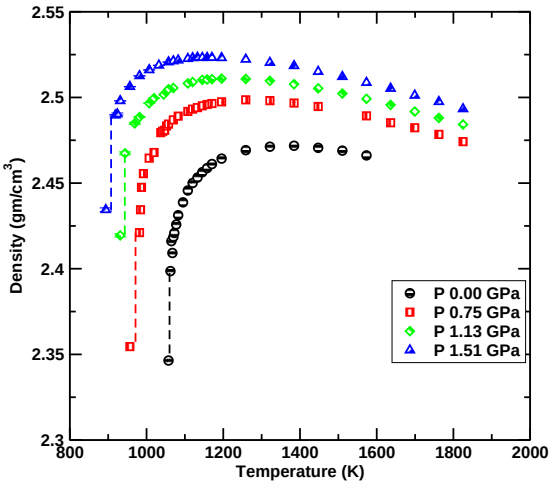

Figure 3.14: Density against temperature for four different isobars from the NPT MD simulations. The jumps in the isobars were used to identify the liquid-liquid transition line.

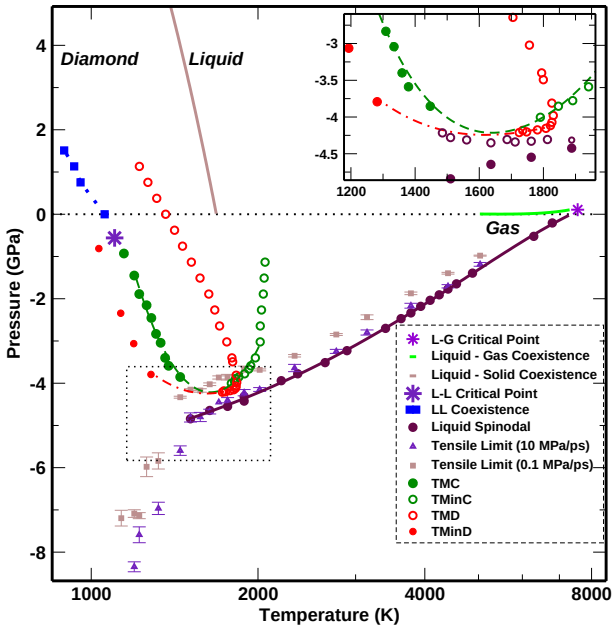

Figure 3.15: The phase diagram of supercooled liquid silicon in pressure-temperature (P, T) plane obtained from simulations. The phase diagram shows the the location of (i) the liquid-crystal phase boundary [179] - brown line, (ii) the liquid-gas phase boundary and critical point - green line and blue star, (iii) the liquid-liquid phase boundary and critical point - blue square and brown star, (iv) the liquid spinodal - black circles (v) the tensile limit - brown square (vi) the density maximum (TMD) and minimum (TMinD) lines - red open and filled circles, and (vii) the compressibility maximum (TMC) and minimum (TMinC) line - green closed and open circles. Lines joining TMD and TMinD (dot-dashed), TMC and TMinC (solid), Spinodal (black dotted line) are guides to the eye.

3.3 Summary

Using the SW potential for silicon we have performed a detailed simulation study of the supercooled phase of silicon at wide range of temperatures and pressures and we have constructed a detailed phase diagram of supercooled liquid silicon. We have identified the critical point associated with the liquid-liquid transition and the line of liquid-liquid coexistence. The interconnection between thermodynamic anomalies and liquid spinodal have been verified from our simulations. We find that the phase behaviour of silicon is similar to that of metastable water. Unlike in water, we find in silicon the TMD line approaches very close to the liquid spinodal. A careful analysis of the free energy landscape, and finite size analysis would an important study to be pursued.

In the next chapter we analyse various structural and dynamic properties of silicon.

Chapter 4

Properties of Supercooled Silicon

In this chapter we discuss structural and dynamic properties of the liquid silicon which we have analysed across the phase diagram for a wide range of temperature and pressure values. The structure of the system is quantified by the radial distribution function or the pair correlation function ($g(r)$), the coordination number (C_{nn}), the structure factor ($S(q)$) and the structural order parameters. We have calculated the diffusivity (D) from the mean square displacement (MSD), the relaxation time (τ_α obtained from the coherent intermediate scattering function ($F(q,t)$) and the viscosity (η), to characterise the dynamical properties of the system. We have also analysed the relation between the structural arrangement of atoms and the dynamics of the system and find a strong relationship between them over a wide range of temperature and pressure values. Stokes-Einstein (SE) relation, which relates the diffusion coefficient of the liquid with the shear viscosity (or the α relaxation time), is tested across the phase diagram and at low temperatures in the vicinity of onset temperature, the SE relation fails. In the phase diagram, we have recognised the location of the SE breakdown temperature for different pressure values. A hierarchy in different anomalous regions has been previously observed in the case of water [52, 139], in which it was found that the different anomalous regions (corresponding to density

(ρ), diffusivity and structural order) cascade on each other which indicates an interconnection between these anomalies. This has been studied in various other systems [38, 72, 74, 153] and the findings has been also associated with changes in the structural entropy. In our work we have carried out an analysis on similar lines, which is presented in the section entitled *Nesting of anomalies*.

We note that most of the analysis presented in the following sections are at $P = 0GPa$ and $P = -1.88GPa$, which corresponds to pressure values above and below the critical pressure in the phase diagram in (P, T) plane.

4.1 Structural Properties

4.1.1 Radial Distribution Function, Coordination Number and Structure Factor

From the analysis of the radial distribution function ($g(r)$) we can obtain information about the local structural arrangements of silicon atoms and the average coordination number. In FIG. 4.1 (a) we show the $g(r)$ calculated from the equilibrated configurations at constant pressure ($P = 0GPa$) and four different temperatures corresponding to high T liquid, high density supercooled liquid (HDL), low density supercooled liquid (LDL) and stable crystal phase of silicon. The g(r) of the crystalline phase is calculated at around $T = 1070K$ and it has periodic peaks even at large r values indicating a long range order. Since the crystal is at finite temperature, atoms will be vibrating about their mean positions and hence the g(r) peaks have finite width (which vanishes when we calculate $g(r)$ from energy minimised equilibrium configurations (also termed as inherent structure configurations) - see FIG. 4.1 (b)).

From the equilibrium liquid $g(r)$ analysis we can infer the following features: (1.) The LDL phase has a sharper first coordination shell which is more clearly separated from the second coordination shell as compared to HDL and high density phase. As the system transforms from high T liquid to HDL to LDL, the amplitude of the first peak of the $g(r)$ (at $r \sim 2.6$Å)

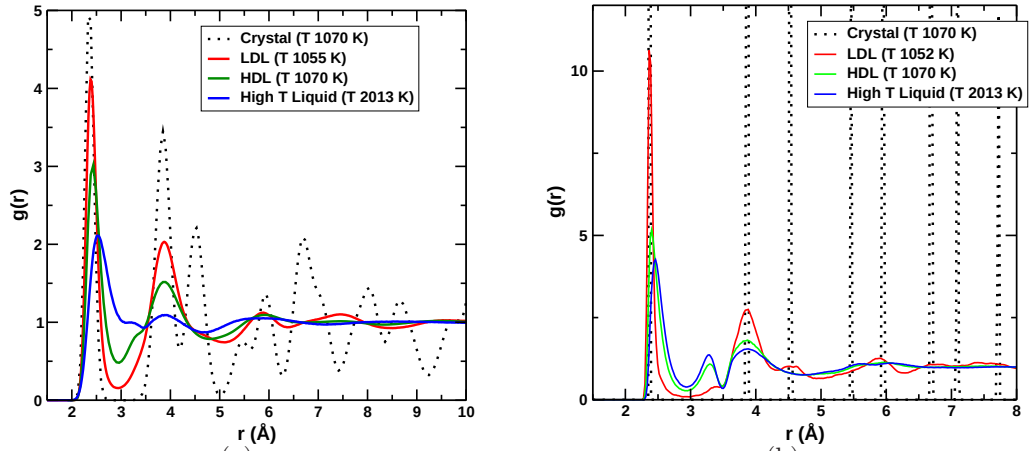

Figure 4.1: The pair correlation function $g(r)$ for crystal, low density liquid, high density liquid and high temperature liquid calculated from (a) NPT MD simulations and (b) minimised equilibrium configurations or inherent structure (IS).

increases and the peak shift towards lower values of r approaching the crystalline peak. (2.) At larger r values the liquid $g(r)$ depart significantly from the crystal $g(r)$, decaying to ideal gas $g(r)$ value of 1. (3.) As the system transform from LDL to HDL to high T liquid the coordination number changes from 4 to 5 to 6. This leads to the rearrangement of atomic positions around the first and second coordination shell, hence we find a shoulder like feature at $r \sim 3.25$Å.

The liquid $g(r)$ calculated from the minimised configurations enhances the above features. Especially in the High T liquid phase, the shoulder becomes more prominent as it is seen in FIG. 4.1 (b).

In FIG. 4.2 and FIG. 4.3 we show the $g(r)$ and the S(q) along $P = 0GPa$ and $P = -1.88GPa$ isobars respectively for a set of ten different temperatures. We have also calculated the fifth neighbour distribution $g_5(r)$ (see inset of FIG. 4.2 and FIG. 4.3), which represent the distribution of distances of a 5^{th} nearest neighbour to a chosen atom (defined in *Methods and calculations* chapter). At $P = 0GPa$ we find that the $g(r)$ profile changes in a *discontinuous* manner (see $g(r)$ for $T = 1062K$ and $T = 1055K$ in FIG. 4.2

(a)), whereas at $P = -1.88GPa$, we find a continuous evolution of structural change. These changes are more evident in the g_5(r) distribution. At $P = 0GPa$, we find g_5(r) change from from a unimodal to bimodal distribution, as the temperature changes from $T = 1062K$ to $T = 1055K$ (the liquid-liquid transition temperature for $P = 0GPa$ is at $T = 1060K$) and at $P = -1.88GPa$ we see a continuous change in the g_5(r).

The static structure factor $S(q)$ is an experimentally accessible quantity. In computer simulations we can obtain $S(q)$ either from the Fourier transform of $g(r)$ or directly by evaluating the density-density correlation function in the Fourier space. We show the evolution of $S(q)$ with varying temperatures for $P = 0GPa$ and $P = -1.88GPa$ in FIG. 4.2 (b) and FIG. 4.3 (b) respectively. We find that in the LDL phase we have two distinct peak. As the system transform to a HDL phase the amplitudes of the peak decreases and the difference in the q values corresponding to two peak decreases. In all the structure factors we have analysed, we find that at $q \to 0$ limit the S(q) has a finite value, implying that the system has a finite compressibility. We compare our results with the structure factors obtained from experiments in a later chapter (see *Applicability to real silicon* chapter).

The coordination number C_{nn} represents the number of atoms in the first coordination shell, and is calculated by integrating the $g(r)$ till its first minimum (r_c) from the relation $C_{nn} = \int_0^{r_c} 4\pi r^2 \rho g(r) dr$. The so calculated coordination number is found to be sensitive to the location of the first minimum of $g(r)$. At $P = 0GPa$ for temperatures less than $1259K$ we find $r_c \sim 2.96\mathring{A}$. But for $T > 1259K$, the minimum was found to shift towards higher values of r (FIG. 4.4 (a)). For a given temperature, with varying pressure, r_c does not to vary much (FIG. 4.4 (b)). In FIG. 4.5 we show the coordination number as a function of pressure for different temperature values. For $T < 1259K$ the coordination number was found to vary from 4.6 to 5.0 in the HDL phase, which decreases to around 4.2 in the LDL phase. At $T = 1510K$, the coordination number varies between 4.8 and 5.5. Note that in [142] and [176] the integration was performed up to the first minimum of $4\pi r^2 \rho g(r)$, rather than the g(r) directly, which leads to a small underestimate in the coordination number at high temperatures and pressures.

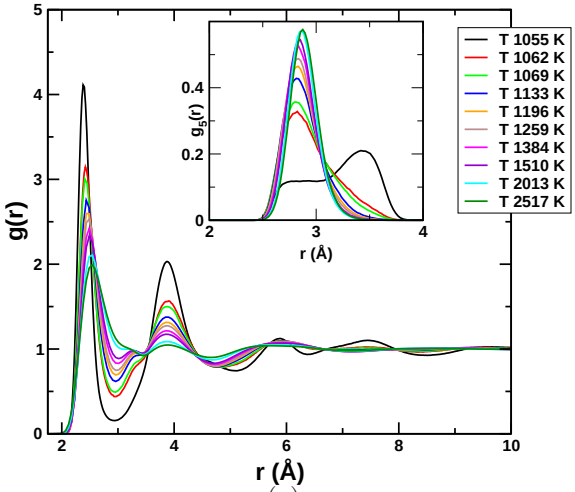

(a)

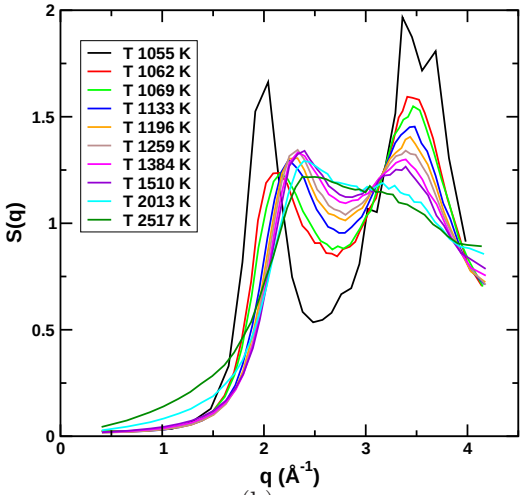

(b)

Figure 4.2: (a) The pair correlation function g(r) and (b) the structure factor S(q) for different temperatures at $P = 0GPa$. The inset in (a) shows the fifth neighbour distribution.

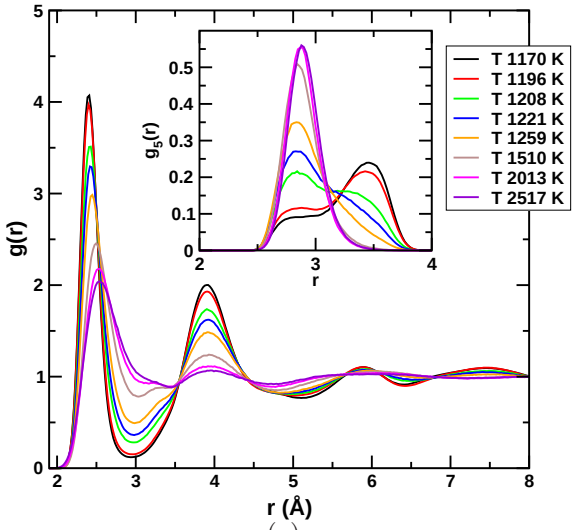

(a)

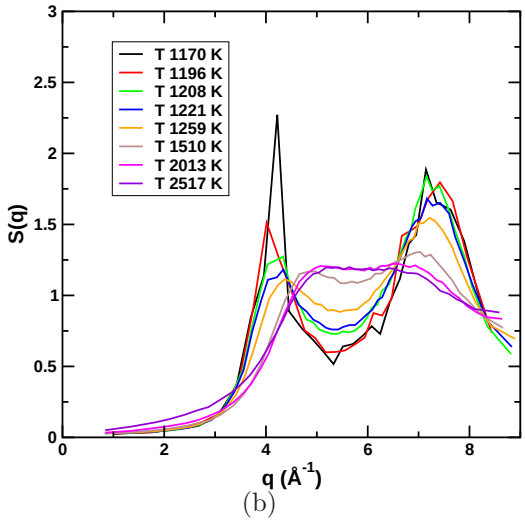

(b)

Figure 4.3: (a) The pair correlation function g(r) and (b) the structure factor S(q) for different temperatures at $P = -1.88GPa$. The inset in (a) shows the fifth neighbour distance distribution.

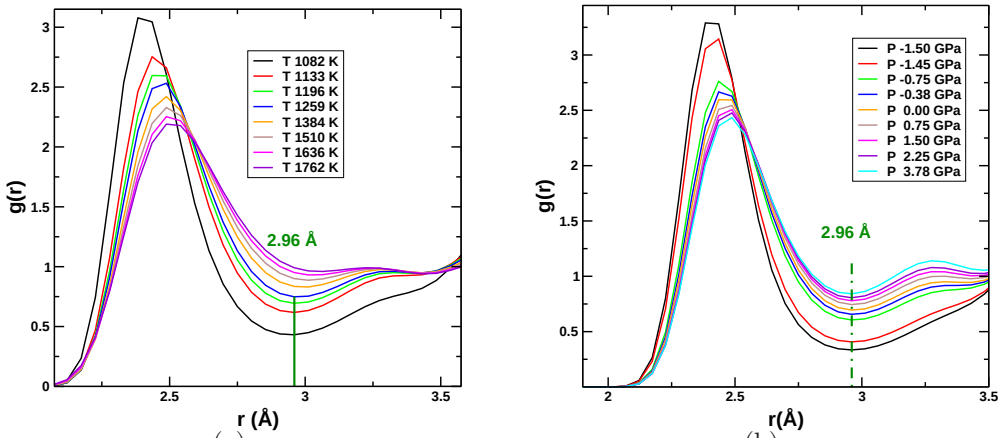

Figure 4.4: (a) The pair correlation function $g(r)$ at different temperatures for $P = 0GPa$. The position of the first minimum of $g(r)$ remains unchanged till $T < 1259K$. (b) The pair correlation function $g(r)$ at different pressures for $T = 1196K$. The position of first minimum of $g(r)$ remains fairly unchanged for a wide range of pressure values.

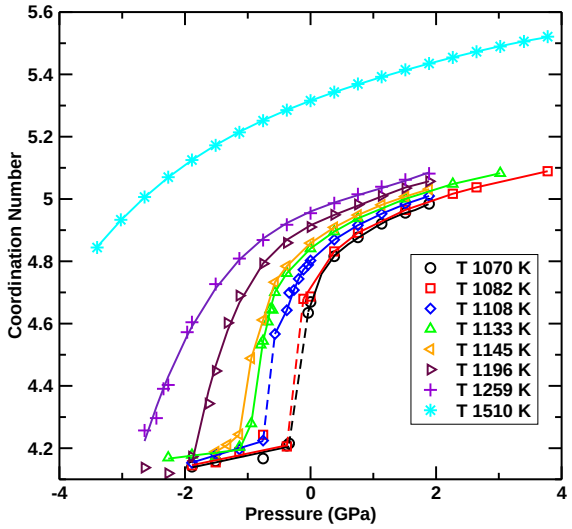

Figure 4.5: Coordination number against pressure at different temperatures. In the high density liquid (HDL) phase the coordination number varies from 4.6 to 5.4. In the low density liquid (LDL) phase the coordination number is around 4.2.

The coordination number of silicon is a much debated quantity in the literature [9, 69, 75, 84–86, 117, 180]. The large discrepancy between different experimental calculations of the radial distribution function and of the density (*see* FIG. 1.7) leads to large variations in the calculated coordination number (see *Applicability to real silicon* chapter).

4.1.2 Random Tetrahedral Network (RTN)

The g(r) analysis has shown the variation of average coordination number for different phases ($\sim$ 6 in the high T liquid phase to $\sim$ 5 in the HDL phase to ~ 4 in the LDL phase). We now focus our attention on at the local arrangement of atoms quantified by the tetrahedrality order q_{tetra} and the local bond orientational order q_3 (defined in the *Methods and calculations* chapter. These quantities measure the extent of tetrahedral environment around a chosen atom.

The tetrahedrality order is defined such that the average q_{tetra} varies between 1 (perfect tetrahedron) and 0 (gas). We show the distribution of q_{tetra} in FIG. 4.6 (a) for $P = 0GPa$. Silicon crystallises into a cubic diamond phase and hence the local arrangement of atoms is a perfect tetrahedron. This is reflected in the q_{tetra} distribution which is indeed peaked around 1. In the LDL phase we find broader q_{tetra} distribution (peaked near 1) compared to the crystal phase and in the HDL phase we find a second peak evolving at $q_{tetra} \sim 0.53$, which becomes more prominent in high T phase. The bimodal distribution of the q_{tetra} is indicative of the presence of atoms having very different local environment. When we calculated the q_{tetra} distribution of 4-coordinated atoms and of $>$ 4-coordinated atoms separately, we find two overlapping unimodal distributions (see FIG. 4.6 (b)). Since these are time-averaged distributions we can not interpret this result as co-existence of two different kinds of liquids. These are transient arrangement of tetrahedrally coordinated atoms and distorted tetrahedral or non-tetrahedral atoms.

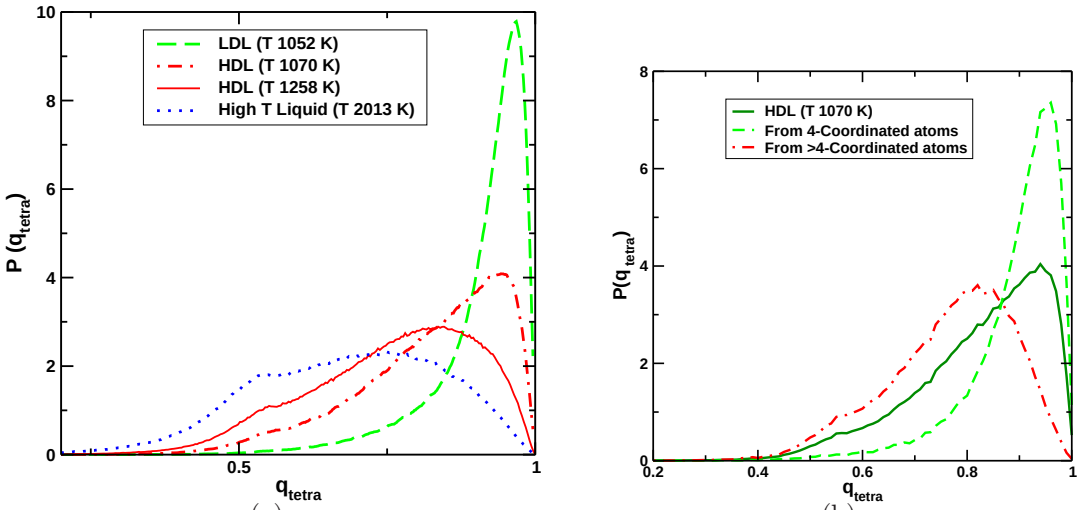

(a) (b)

Figure 4.6: (a) The distribution of tetrahedrality order distribution $P(q_{tetra})$ for four different phases at $P = 0GPa$. (b) The distribution of tetrahedrality order $P(q_{tetra})$ for $T = 1070K$ considering all atoms (dark green line), only four coordinated atoms (green line) and > 4 coordinated atoms (red line).

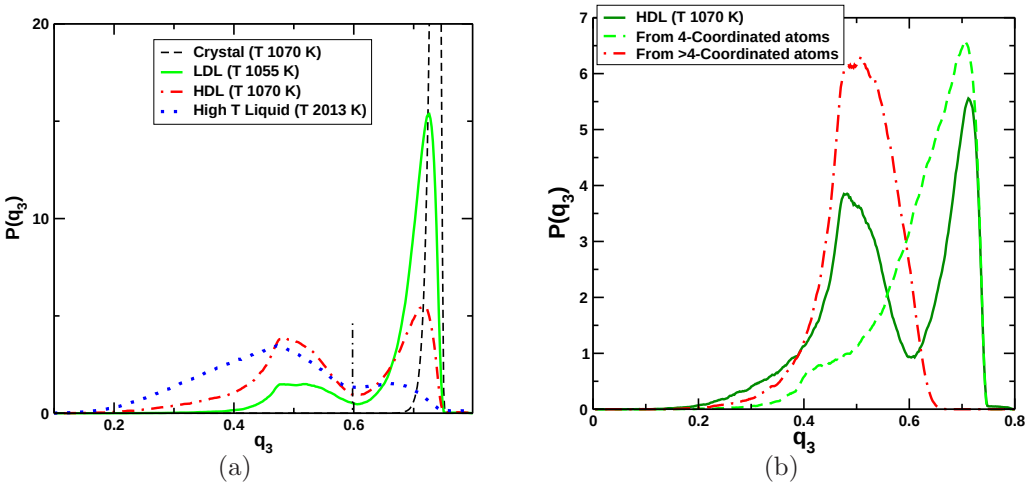

(a) (b)

Figure 4.7: (a) The distribution of local orientational order $P(q_3)$ for four different phases at $P = 0GPa$. (b)The distribution of local orientational order $P(q_3)$ for $T = 1070K$ considering all atoms (dark green line), only four coordinated atoms (green line) and > 4 coordinated atoms (red line).

The definition of the tetrahedrality order considers the first four nearest neighbours to calculate q_{tetra}, which will become ambiguous if an atom has 5 or more neighbours within the first coordination shell. Hence we calculate the local orientational order q_3 which considers all the neighbouring atoms. In FIG. 4.7 (a) we show the q_3 distribution for different phases. The q_3 takes a value of ~ 0.75 for a pure diamond crystal. The finite temperature crystal phase is indeed peaking around this value. The liquid phases show bimodal distribution in q_3, peaked at either side of $q_3 = 0.6$ value, clearly demarcating the two transient species of atoms (see FIG. 4.7 (b). We use this criterion to recognise 4-coordinated or LDL-like atom ($q_3 \geq 0.6$) and $>$ 4-coordinated or HDL-like atom ($q_3 < 0.6$).

The crystalline phase of silicon can be considered as a network of atoms having perfect tetrahedral local environment. From the q_3 distribution (as well as from the coordination number) there is a clear indication of an increase in the number of tetrahedrally coordinated atoms as we approach the LDL phase from high temperature. Hence it is interesting to look at the evolution of network of LDL-like atoms. We define a cluster of LDL-like atom using a criterion in which two atoms are connected if they are within a distance of 2.9Å(which corresponds to the distance of the first minimum of g(r)). In FIG. 4.8 we show snapshots of equilibrium configurations at various different temperature values for $P = 0GPa$ and $P = -1.88GPa$. In these snapshots, green coloured atoms are LDL-like atoms, blue coloured bonded atoms are LDL-like atoms belonging to the largest cluster in the system and the red colour represents the HDL-like atoms. In comparison with a crystal phase (see FIG. 4.9) which has an ordered network of tetrahedral atoms, the cluster of LDL-like atoms can be termed as the random tetrahedral network (RTN). For $P = 0GPa$ as the system transforms from HDL to LDL phase, we clearly observe a drastic change average size of RTN cluster. At $P = -1.88GPa$, the growth of RTN cluster is more continuous.

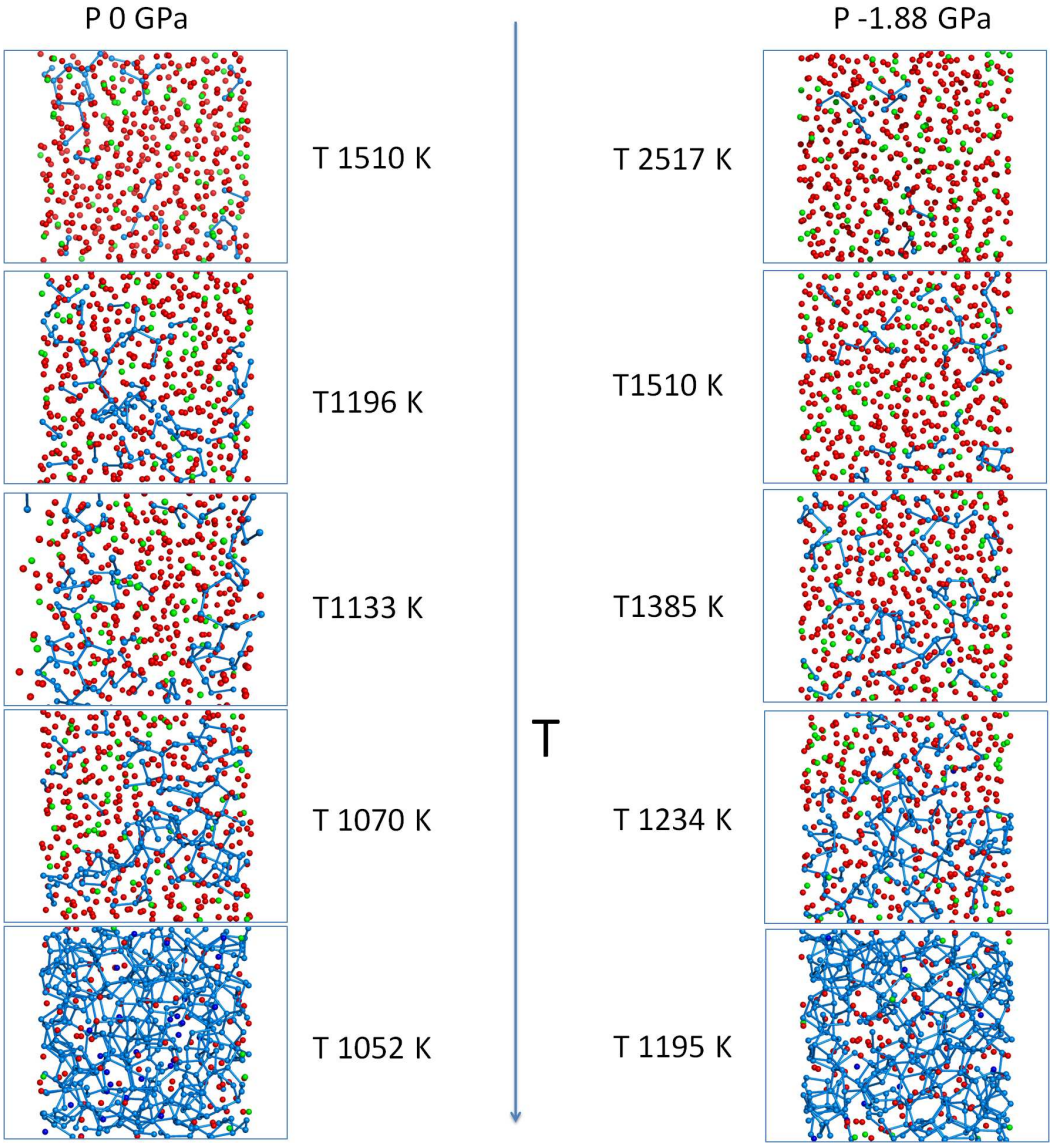

Figure 4.8: Snapshots of configurations at different temperatures obtained from NPT MD simulations. The left panel corresponds to $P = 0GPa$ and the right panel corresponds to $P = -1.88GPa$. The low density liquid, LDL-like atoms are coloured green, The bonded blue coloured atoms are LDL-like atoms belonging to the largest RTN cluster in the system and the high density liquid, HDL-like atoms are coloured red.

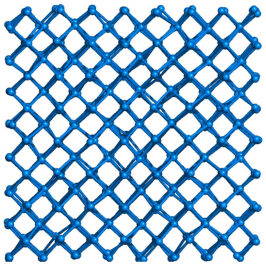

Figure 4.9: Snapshots of crystalline silicon at $P = 0GPa$ and $T = 1070K$ obtained from NPT MD simulations.

The RTN clusters are open clusters hence we can relate the presence of these cluster to the density anomaly found in liquid silicon. In FIG. 4.10 (a) we show the behaviour of average size of the largest RTN cluster as a function of temperature for three different pressure values in which two pressures $P = 0.75GP$, $P = 0GPa$ and $P = -1.88GPa$. The vertical solid line in the figure indicated the temperature of density maxima. We find that at all pressure value, at high temperatures, size of the largest RTN cluster is less than 3% of the system size (around 15 atoms in the system size of 512 atoms) and the system shows normal behaviour in density. As the RTN cluster size becomes greater 10% of the system size, the system's density decreases with decrease in temperature, showing an anomalous behaviour. Instead of moving along an isobar, if we decrease the pressure sitting at one particular temperature, even then the above argument should hold good, which is what we find, as shown in FIG. 4.10 (b). We show in FIG. 4.11 the cluster size distribution of RTN atoms along (a) an isobar and (b) an isotherm. At high temperatures (keeping pressure constant) and at high pressures (keeping temperature constant) we find stretched exponential decay in cluster size distribution. In the region of density anomaly, we find a distinctly peaked distribution, which is indicating at existence of an *indissoluble* RTN cluster.

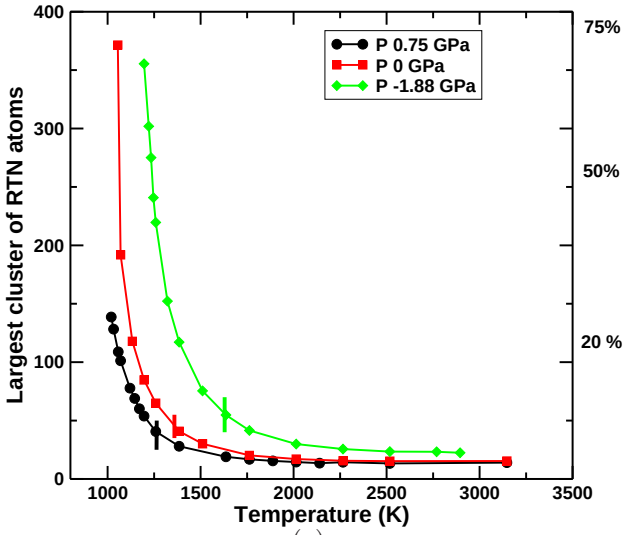

(a)

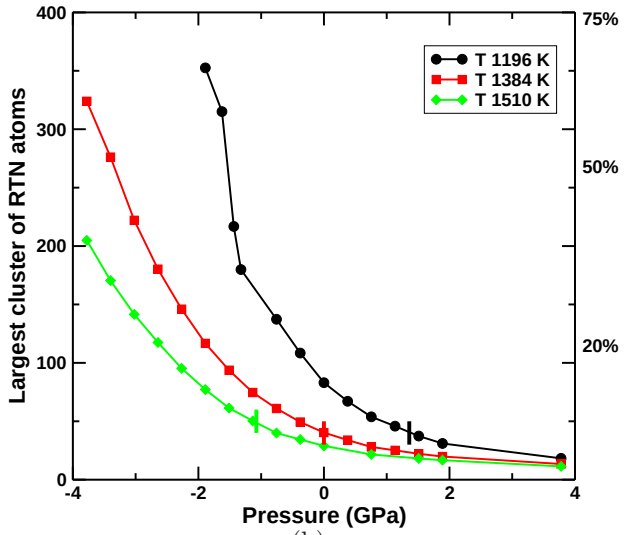

(b)

Figure 4.10: (a) Average cluster size of RTN atoms as a function of temperature for three different pressures. (b) Average cluster size of RTN atoms as a function of pressure for three different temperatures. The vertical bold line represents the temperature corresponding to density maxima.

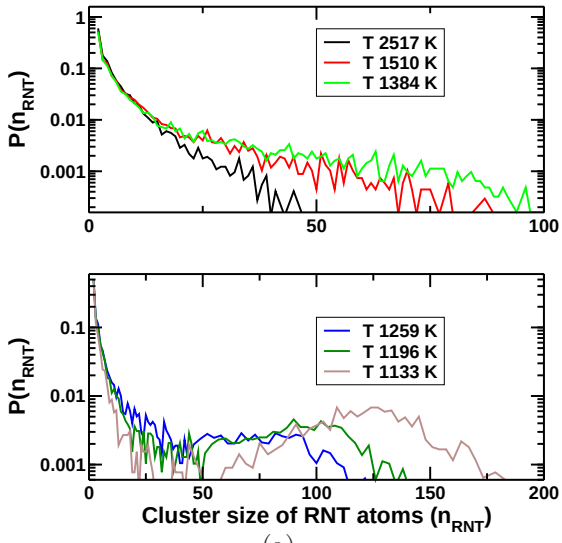

(a)

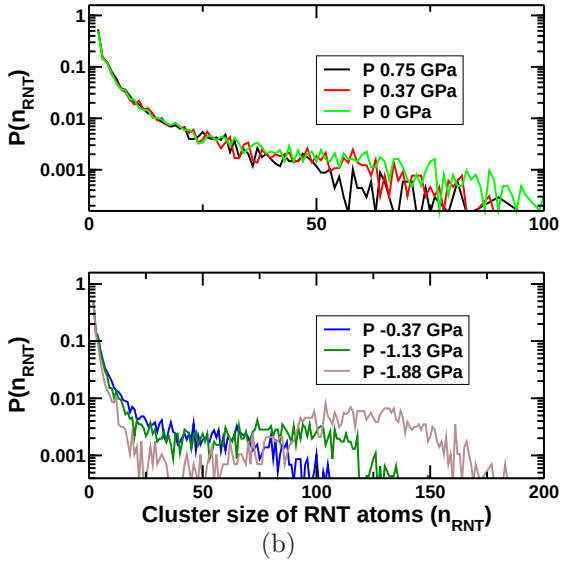

(b)

Figure 4.11: RTN cluster size distribution along (a) $P = 0GPa$ isobar for different temperatures and (b) $T = 1384K$ isotherm for different pressures. At high temperatures and high pressures RTN cluster size distribution shows a stretched exponential decay (top panel in (a) and (b)). In the region of density anomaly we find a distinctly peaked distribution, which is indicating at existence of an *indissoluble* RTN cluster.

4.2 Dynamic Properties

Mean Square Displacement and Diffusivity

The mean square displacement (MSD) is a measure of the average distance an atom travels within a given time period. The slope of the MSD in the long time regime gives the coefficient of diffusion or diffusivity, which is a measure of average mobility of an atom in the system. In FIG. 4.12 we show MSD for different temperatures at $P = 0GPa$ and $P = -1.88GPa$. At all temperatures we find a ballistic regime at the initial time period followed by a caging regime and a diffusive regime at the long time interval. We find that the caging regime is bigger in the LDL phase as well as in the vicinity of locus of compressibility maxima or the Widom line. In the LDL phase we also observe a maximum in the MSD (at the crossover from the ballistic to the caging regime), which has been related to the Boson peak [7], a feature in the short time dynamics. The slope of the MSD in the diffusive regime gives us the diffusivity of the system. In FIG. 4.13 we show the temperature dependent of diffusivity for $P = 0GPa$ and $P = -1.88GPa$ and we find a crossover from an Arrhenius to a non-Arrhenius behaviour in the T dependence of diffusivity. In FIG. 4.14 (a) we show the pressure dependence of D for a range of temperatures above and below the critical temperature. We find that as the liquid transforms from HDL to LDL, the diffusivity change by two orders of magnitude. Also with the decrease in compression or pressure we find that D is decreasing, which is an anomalous behaviour. Similar feature has been reported in water and silica [52,153]. At a higher pressure value diffusivity goes through a maximum and return to the normal behaviour as we show in FIG. 4.14 (b) for $T = 1259K$.

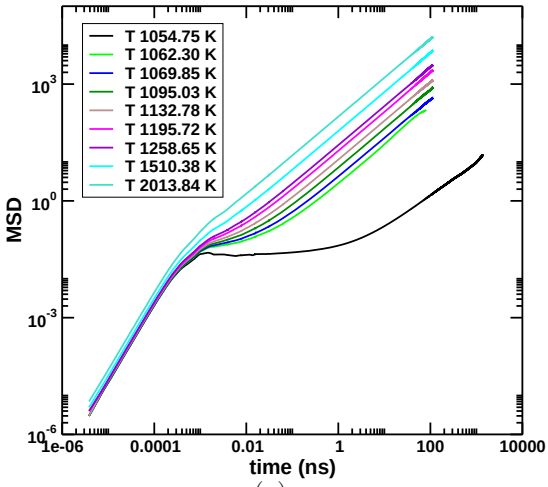

(a)

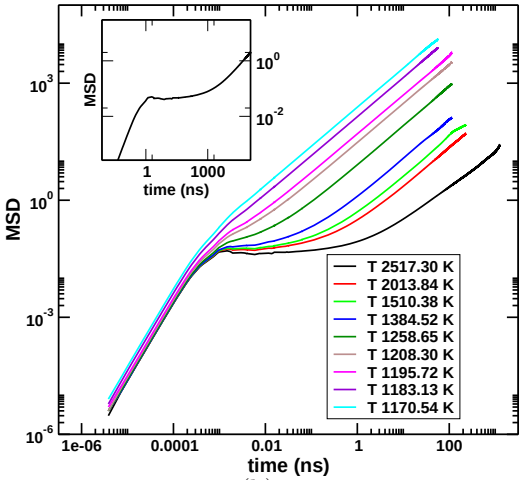

(b)

Figure 4.12: The mean square displacement (MSD) as a function of time for (a) $P = 0GPa$ and (b) $P = -1.88GPa$ obtained from NPT MD simulations. The inset of (b) show the maximum in the MSD at the crossover from the ballistic to the caging regime.

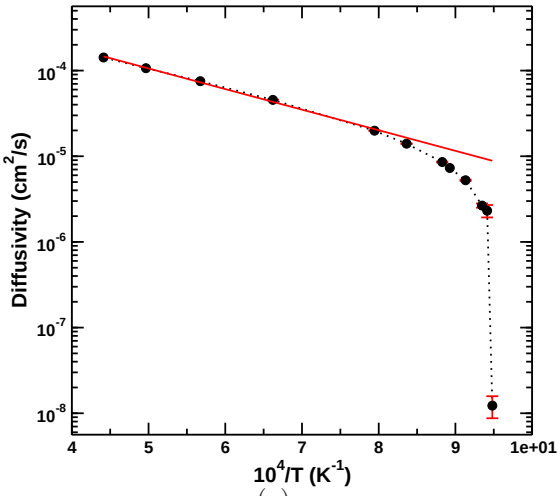

(a)

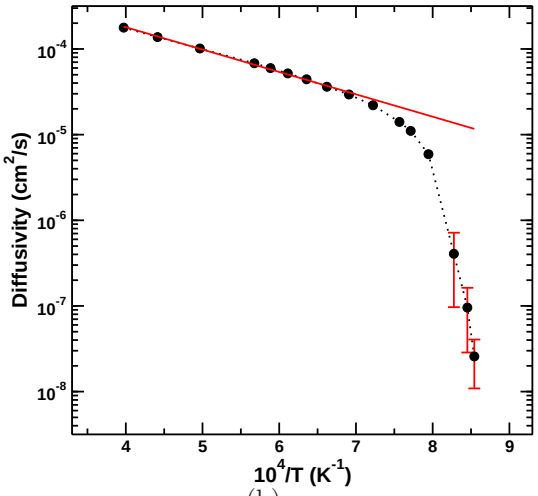

(b)

Figure 4.13: The diffusivity (D) of the system (calculated from the mean square displacement) as a function of inverse temperature for (a) $P = 0GPa$ and (b) $P = -1.88GPa$ obtained from NPT MD simulations. Diffusivity changes from an Arrhenius to a non-Arrhenius behaviour at both pressure values.

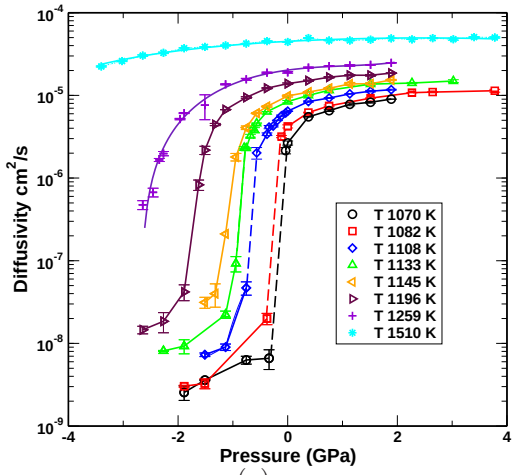

(a)

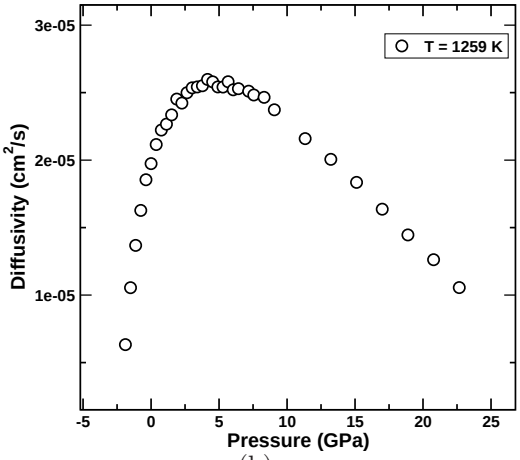

(b)

Figure 4.14: (a) Diffusivity (D) against pressure for different temperatures. Diffusivity decreases with decrease in pressure. (b) Diffusivity against pressures for $T = 1259K$. Diffusivity goes through a maximum at around $4.5GPa$.

Structural Relaxation Time

For further understanding of the dynamics of the system we have calculated the intermediate scattering function $F(q,t)$ for the wave vector k corresponds to the first peak of the static structure factor [37]. In FIG. 4.15 we show the behaviour of $F(q,t)$ at $P = 0GPa$ and $P = -1.88GPa$. As we lower the temperature, approaching the liquid-liquid transition line at $P = 0GPa$ and the Widom line at $P = -1.88GPa$, we find a two step relaxation process. We find a ballistic regime at short time which is followed by a plateau in the intermediate time window, which corresponds to β relaxation regime. The time window in which the $F(q,t)$ decays to zero corresponds to the α relaxation regime. We also find that with the lowering of the temperature the decay of $F(q,t)$ changes from exponential to stretched exponential, with the exponent varying from 1.0 to 0.5.

We define the α relaxation time (τ_α), also termed as the structural relaxation time or just the relaxation time, as the time at which the $F(q,t)$ decays by a factor of e. In FIG. 4.16, we show τ_α as a function of inverse temperature at $P = 0GPa$ and $P = -1.88GPa$. Similar to diffusivity, we find a crossover from an Arrhenius to a non-Arrhenius behaviour in the T dependence of relaxation time. In FIG. 4.16 we show the relaxation times as a function of pressure for three different temperatures values. As system goes from high T liquid to HDL to LDL, the relaxation time varies from ps to hundreds of ns.

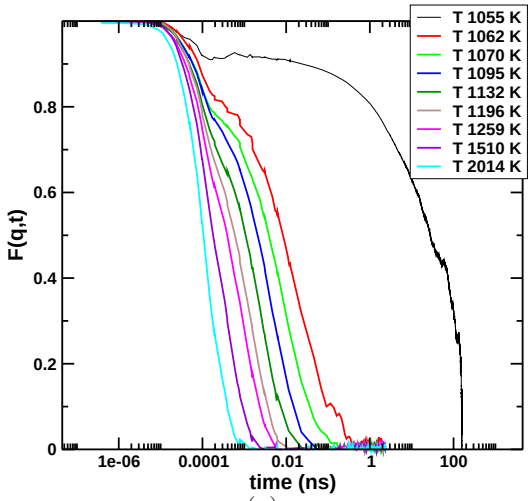

(a)

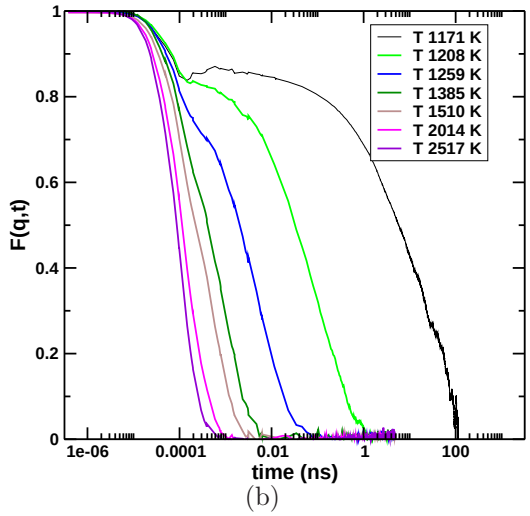

(b)

Figure 4.15: The intermediate scattering function $F(q,t)$ as a function of time for (a) $P = 0GPa$ and (b) $P = -1.88GPa$ calculated from NPT MD simulations. We note that at low temperatures ($T = 1055K$ at $P = 0GPa$ and $T1171K$ at $P = -1.88GPa$) data may not be well equilibrated.

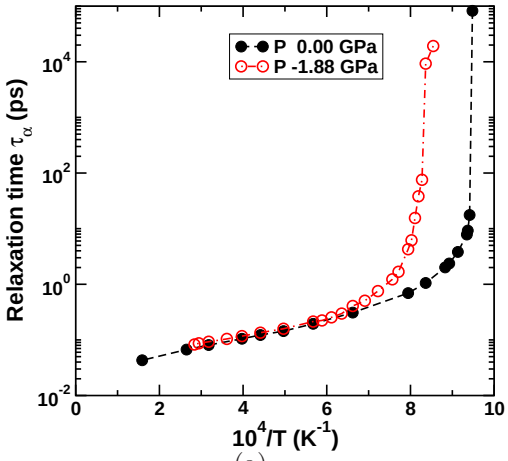

(a)

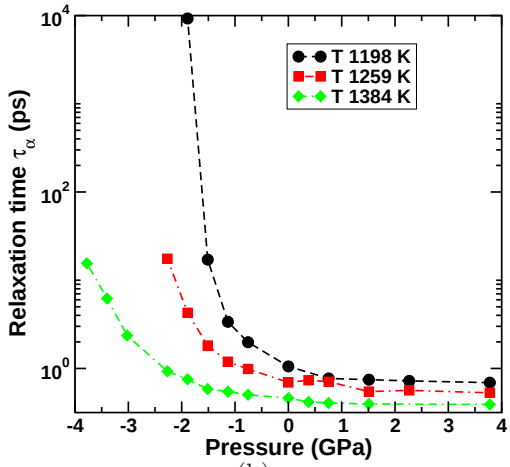

(b)

Figure 4.16: (a) Relaxation time (τ_α) against inverse temperature at $P = 0GPa$ and $P = -1.88GPa$. An Arrhenius to a non-Arrhenius behaviour in relaxation times is found in both pressure values (b) Relaxation time against pressure at $T = 1198K$, $T = 1259K$ and $T = 1384K$.

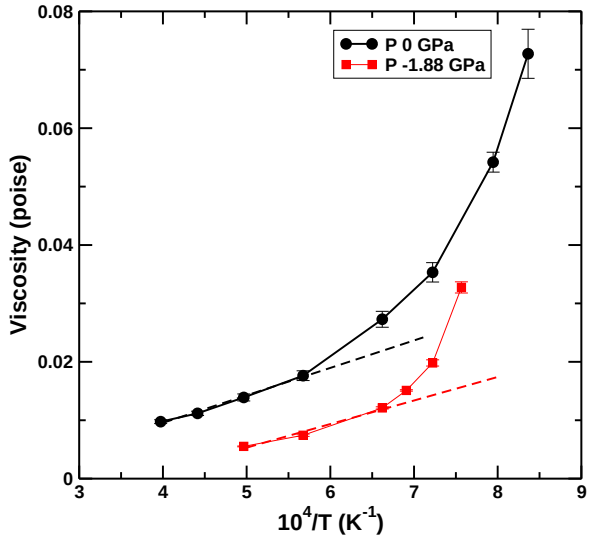

Figure 4.17: The viscosity of the system as function of inverse temperature for $P = 0GPa$ and $P = -1.88GPa$ obtained from NPT MD simulations. Dotted lines suggesting an Arrhenius behaviour of viscosity at high temperatures.

Viscosity

Viscosity is a measure of the rate of dissipation of energy per unit volume per unit shear rate. Physically it a measure of the momentum transfer in a field perpendicular to the direction of flow of liquid. In order to compute the viscosity we first calculate the stress auto-correlation function at a chosen state point using the LAMMPS MD package [121]. We integrate the stress auto-correlation function (*see* Methods and calculations chapter) to obtain the viscosity of the system. In FIG. 4.17 we show the viscosity as a function of inverse temperature calculated for $P = 0GPa$ and $P = -1.88GPa$. We find a crossover from an Arrhenius to a non-Arrhenius behaviour in the T dependence of viscosity, similar to other two dynamical quantities we have measured.

Even though not very sharp, we do find a crossover from an Arrhenius to a non-Arrhenius temperature dependence in all three measure of dynamical property. The temperature (T_{onset}) associated with this crossover is termed

as the onset of slow dynamics. To obtain a good estimate of T_{onset} we can define a temperature dependent *activation energy* following the REF. [140] as

$$E(T)/E_0 = k_B T ln(D/D_0) \tag{4.1}$$

where E_0 and D_0 is obtained from an Arrhenius fit to the high T data, D is the dynamical quantity which can be either diffusivity, relaxation time or viscosity. The onset temperature is obtained from 1% to 5% (in diffusivity data) or 5 to 15% (in relaxation time data) deviation from the high temperature value of 1. This change reflects as large error bars in the estimation of the onset temperature. In FIG. 4.18 where we show the $E(T)$ obtained from diffusivity and relaxation time against temperature. In FIG. 4.22 we show the locus of onset temperature obtained from above protocol in phase diagram of supercooled silicon.

We next discuss our study related to the breakdown of Stokes-Einstein relation in supercooled liquid silicon.

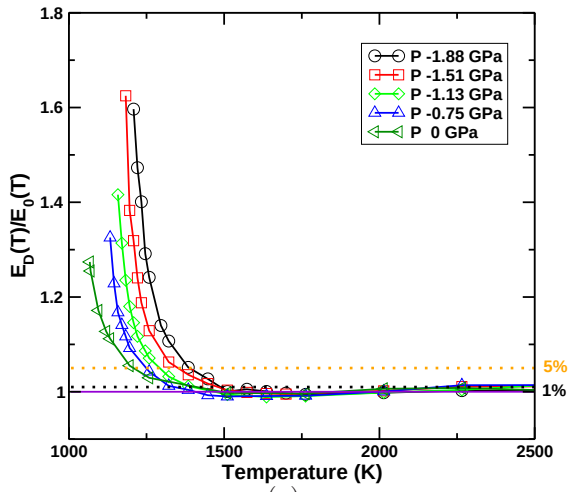

(a)

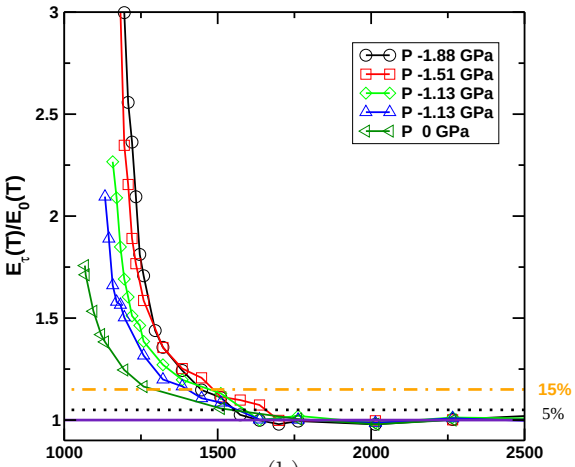

(b)

Figure 4.18: The temperature dependent *activation energy* obtained from (a) diffusivity and (b) relaxation time. We define a 5% deviation in diffusivity data or a $5-15\%$ deviation in relaxation time data, from the constant high temperature value marks the onset of slow dynamics.

4.3 Stokes-Einstein Breakdown

The diffusion coefficient is connected to the the viscosity of the system by the Stokes-Einstein (SE) relation given by

$$D = \frac{mk_B}{6\pi R}\frac{T}{\eta} \tag{4.2}$$

where k_B is the Boltzmann constant, η is the viscosity and R is the hydrodynamic radius. Even though originally the above relation was derived for the probe particle which are much bigger than the solvent particles, the relation has been found to hold good even for the case of self-diffusion coefficient (where both the probe and solvent particles are of same size) [49]. Assuming that we can avoid crystallisation, the viscosity (and the relaxation time) of the liquid increasing with the decrease in temperature. At these low temperatures, many experimental and simulation work ([19, 29, 188] and references within) have shown a breakdown in the SE relation. The Eq. 4.2 can be rewritten as

$$\frac{D\eta}{T} = const. \tag{4.3}$$

An increase in the above ratio with the decrease in temperature is termed as the breakdown in SE relation. It has been empirically observed that a *fractional* SE relation $D \propto (\eta/T)^{-\xi}$ holds good for temperatures below which SE relation fails. The exponent ξ, reported in various literature, normally varies between 0.7 and 0.8 ([19] and references with in). Note that $\xi = 1$ if the SE relation is valid.

In this section we test the validity SE relation in the liquid silicon and recognise the locus of SE breakdown temperature at different pressure values. We note that the viscosity of the system is proportional to the relaxation time [47] and hence we can use τ_α in place of η (since calculation of viscosity is computationally expensive compared to $F(q,t)$, from which we obtain τ_α).

In FIG. 4.19 we show plot of relaxation time against the viscosity for $P = 0GPa$ and we find that to a good approximation they are proportional to each other. Hence in rest of our analysis in this section, we have used τ_α in place of η. In the FIG. 4.20 we show the SE ratio (defined in Eq. 4.2)

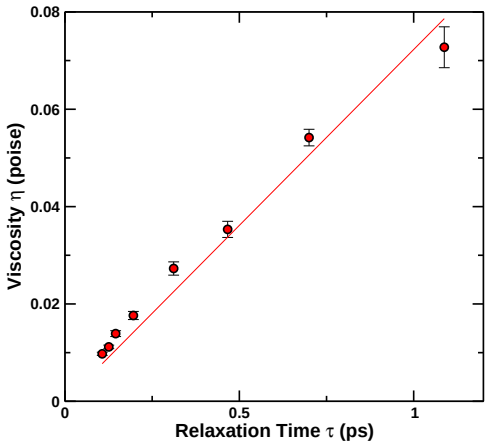

Figure 4.19: Viscosity calculated from stress auto-correlation function against the structural relaxation time obtained from $F(q,t)$ for $P = 0GPa$. Viscosity is proportional to the relaxation time.

as a function temperature for five different pressure values. We find that at high temperatures the SE ratio is indeed constant and hence the liquid follow the SE relation. With the lowering of temperature, an increase in the SE ratio is clearly seen indicating a breakdown of the SE relation. In the FIG. 4.21 we show the plot of D against τ_α/T for $P = 0GPa$, $P = -1.13GPa$ and $P = -1.88GPa$. We find that the slope ξ distinctly change from -1 (at high temperatures) to a value varying between 0.76 and 0.71 for different pressures. The temperature associated with the cross over from $\xi = 1$ to $\xi < 1$ is recognised as the SE breakdown temperature. In FIG. 4.22 we show the locus of SE breakdown temperature. We notice that the the locus SE breakdown temperature is near to the density maxima line and the locus onset temperature. We note that below the density maxima line the system contains clusters RTN atoms which have low mobility compared to HDL atoms. Further analysis is required to understand the role of RTN cluster in the SE breakdown.

A feature of the low temperature liquid which has often been associated with the breakdown of the SE relation is dynamic heterogeneity in the system, which refers to spacially correlated heterogeneous dynamics. The diffusivity

of the system is determined by the high mobility particles, whereas the viscosity is determined by the low mobility particles [157]. The work of Kevilson and Tarjus [164] argues that these domains of different mobility particles can lead to breakdown in the SE relation. In network forming liquids like water, dynamic heterogeneity is found increase approaching the Widom line and hence the onset of SE breakdown is associated with the Widom line [87]. Dynamic heterogeneity in a system can be quantified in various ways. The heterogeneity associated with the relaxation dynamics can be quantified by measuring the dynamic susceptibility χ_4, which is a defined as the variance in the density-density correlation function (*e.g.* $F_s(q,t)$) [169] and is given by

$$\chi_4(t) = N\left(< F_s(q,t)^2 > - < F_s(q,t) >^2\right) \tag{4.4}$$

The $\chi_4(t)$ is maximum at a time proportional to the α-relaxation time and the χ_4 value corresponding to the maximum is a measure of the number of particles involved in correlated motion.

Another measure of dynamic heterogeneity given in terms particle displacements is the non-Gaussian parameter α_2 [127] which is defined as

$$\alpha_2(t) = \frac{3}{5}\frac{< \mathbf{r}^4(t) >}{< \mathbf{r}^2(t) >^2} - 1 \tag{4.5}$$

where $< \mathbf{r}^2 >$ is the mean square displacement and $< \mathbf{r}^4(t) >$ is given by

$$< \mathbf{r}^4(t) >= (1/N)\left\langle \sum_{i=1}^{N} |r_i(t) - r_i(0)|^4 \right\rangle$$

The non-Gaussian parameter is a measure of the departure of the particle displacement distribution from the Gaussian distribution.

In FIG. 4.23 and 4.24 we show plot of χ_4 and α_2 for $P = -1.88GPa$ as a function of time for temperatures varying from high T to temperatures crossing the Widom line. The peak amplitude of the χ_4 appears to decrease up on crossing the Widom temperature ($T_w = 1221K$), whereas the peak amplitude α_2 is monotonically increasing. At very high T values, we find that

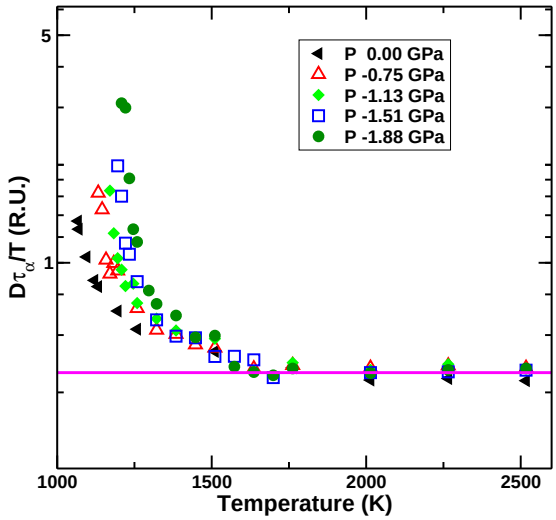

Figure 4.20: The Stokes-Einstein ratio $D\tau_\alpha/T$ against the temperature for different isobars. At high temperatures the ratio is constant. A deviation from the constant value indicates at a breakdown of SE relation.

the peak amplitude of χ_4 is found to increase again. Further analysis of these interesting features in different measures of heterogeneity would shed light on the decoupling between τ_α and D and hence provide better understanding of SE breakdown phenomenon.

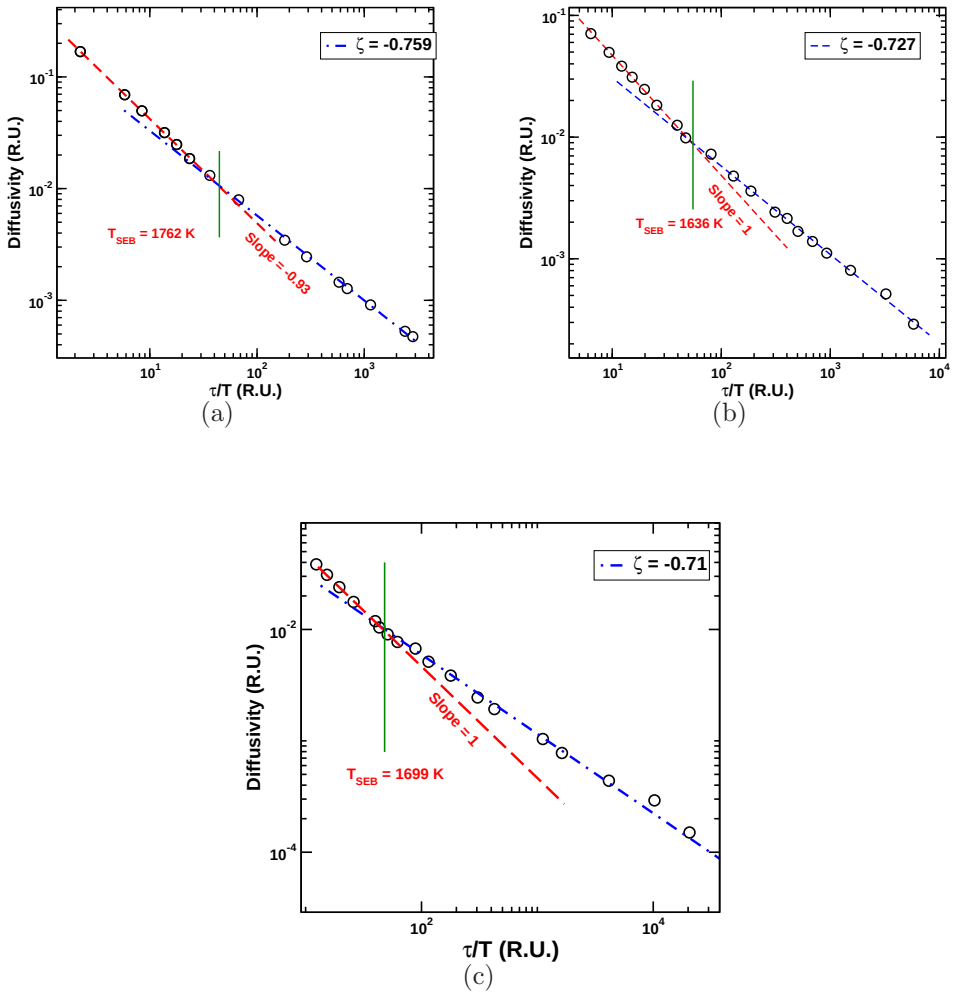

Figure 4.21: Diffusivity against τ_α/T show for three different pressure values. (a) $P = 0GPa$ (b) $P = -1.13GPa$ and (c) $P = -1.88GPa$. Stokes-Einstein relation is valid at high temperatures and hence fractional Stokes-Einstein (FSE) exponent is around 1. At low temperature the FSE exponent varies from 0.759 to 0.71. The vertical green line indicates the SE breakdown temperature.

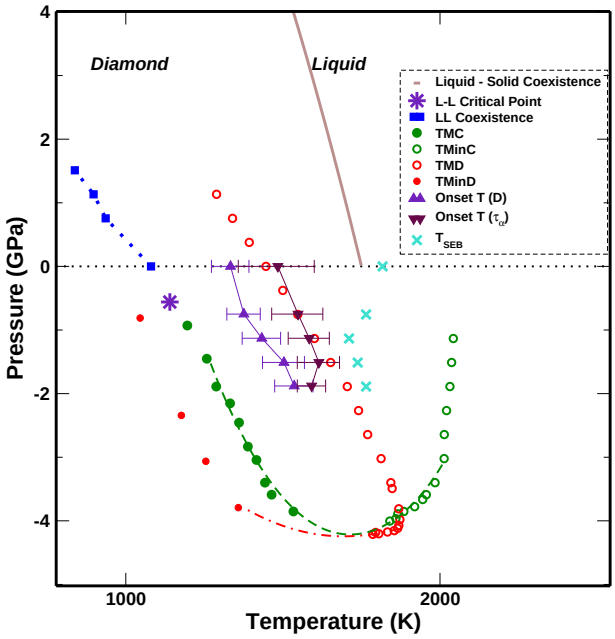

Figure 4.22: The phase diagram of liquid silicon in (P, T) plane showing the onset temperature estimates obtained from diffusivity and relaxation time along with the locus of Stokes-Einstein breakdown temperature.

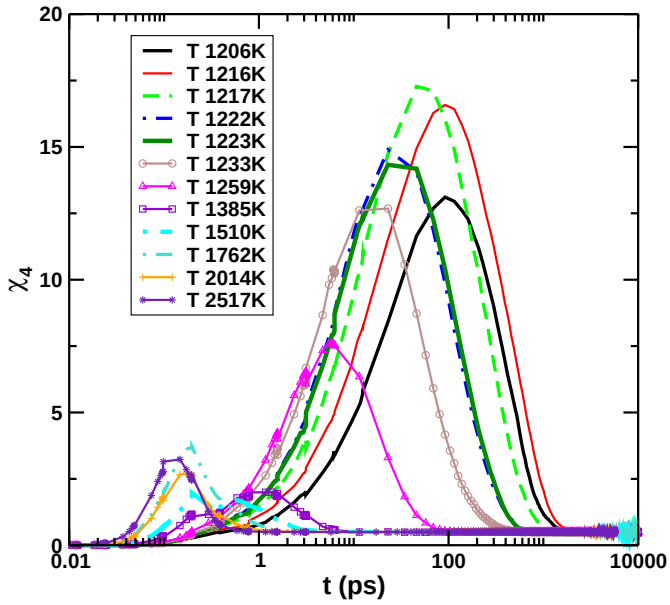

Figure 4.23: Dynamic susceptibility χ_4 ($q = 2.14\text{Å}^{-1}$) calculated at $P = -1.88GPa$ for different temperatures varying from high T liquid state to temperatures crossing the Widom line ($T_w = 1221K$).

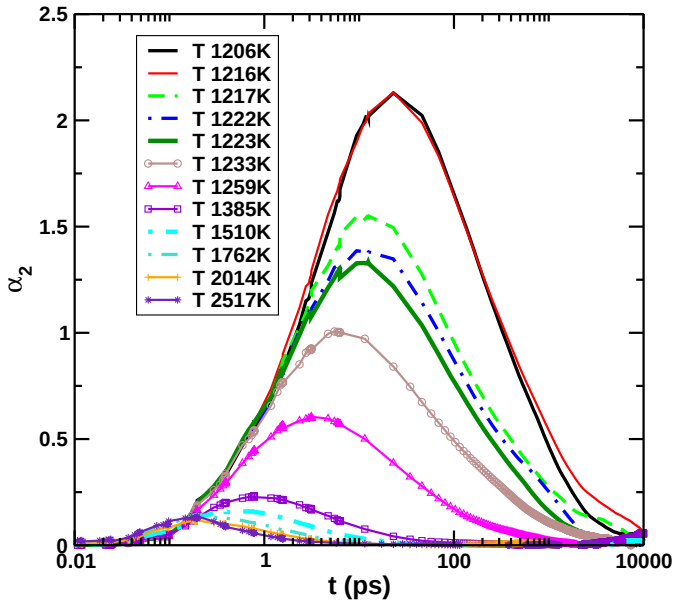

Figure 4.24: non-Gaussian parameter α_2 calculated at $P = -1.88GPa$ for different temperatures varying from high T liquid state to temperatures crossing the Widom line ($T_w = 1221K$).

4.4 Relationship between Structure and Dynamics

From the data of the coordination number and the diffusivity, it is evident at a qualitative level that the diffusivity in silicon is correlated with coordination number, with higher coordination number corresponding to larger diffusivity. We show that the diffusivity depends quite strongly on coordination number and has only a weak temperature dependence (*see* FIG. 4.25). Scaling the diffusivity to its value at a fixed C_{nn} in the HDL phase for different temperatures, a remarkable data collapse is obtained that spans two distinct phases, a wide range of temperature and pressure, and four decades of change in diffusivity (*see inset* of 4.25). The resulting master curve was found to fit well to a *Vogel-Fulcher-Tammann* (VFT) form, $D(C_{nn}) = D_0\ exp(-\frac{A}{C_{nn}-n_0})$ with $n_0 = 3.86$, and also to a power law $D(n) = D_0(n-n_0)^3$, with $n_0 = 4.06$. These results suggest that the mobility of atoms is strongly tied to the presence of coordination larger than four, and that regions of higher coordination number act as "defects" that promote faster rearrangements of atomic positions. This observation is consistent with previous analysis of the role of bifurcated bonds or the fifth neighbour in determining molecular mobility in water [149, 150], though seen here for a remarkably wide temperature and pressure range. Note that the role of RTN cluster in the context of dynamical properties needs to be investigated and it is not included in this thesis.

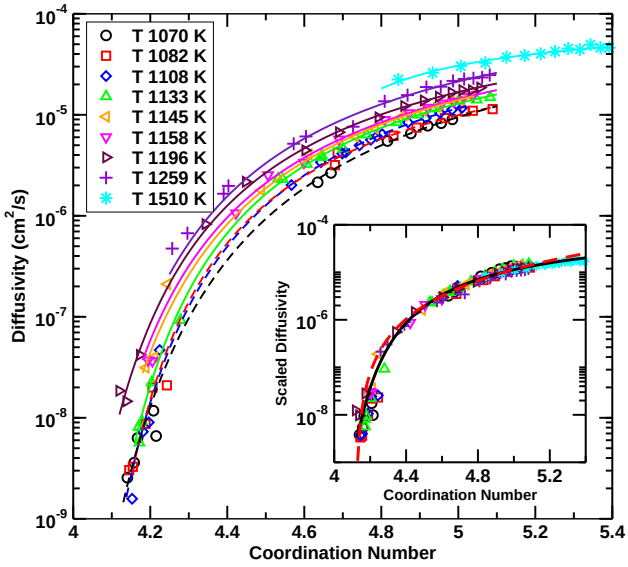

Figure 4.25: Diffusivity (D) against coordination number (C_{nn}) at different temperatures. Lines through the data points are guides to the eye, and highlight the remarkably similar dependence of D on C_{nn} at all temperatures, including those below the critical temperature, where both D and C_{nn} change discontinuously. ($Inset$) Diffusivity (scaled to match at $C_{nn} = 4.8$) versus C_{nn}, showing data collapse. The solid line is a Vogel-Fulcher-Tammann (VFT) fit, with a C_{nn} of vanishing diffusivity = 3.86. The dashed line is a power law fit, with a coordination number of vanishing diffusivity = 4.06.

4.5 Nesting of Anomalies

Anomalous behaviour in tetrahedral liquids has been explored in terms of thermodynamic consistency and phase behaviour (as we have already discussed in the preceding chapters). Some of these anomalies, found in network forming liquids like water and silica, has also been studied in terms of underlying structural properties [38,52,72,74,152,153,172]. Network forming liquids have locally ordered structures, which can be analysed using structural order parameters. We have already discussed in the earlier parts of this chapter two such order parameters, q_{tetra} and q_3, which measure the orientation of neighbours surrounding a reference atom. Another measure of structural order is associated with the inter-atomic distances, which is termed as the *translational order* (t_{trans}). The t_{trans} measures the degree to which neighbours of an atom are organised at preferred distances rather than randomly distributed.

A computer simulation study of water (modeled by SPC/E potential) carried out by Errington and Debenedetti [52] looked at the behaviour of above mentioned structural orders and we put down salient points from their work below.

1. The tetrahedrality order q_{tetra} and the translational order parameter q_{trans} were calculated for a range of density and temperature.

2. The distribution of q_{tetra} was found to be bimodal and with decrease in temperature (keeping density fixed) the peak of the distribution at high q_{tetra} value increased at the expense of low q_{tetra} peak.

3. At a given temperature, starting at low densities, average values of q_{tetra} and t_{trans} increased with increase in compression -termed as structurally normal region- till a maximum in tetrahedrality order was reached.

4. With further increase in compression, both the order parameters decreased -termed as the structurally anomalous region- till t_{trans} goes through a minimum (after which, continued compression increased t_{trans} without much change in the trend of q_{tetra}).

5. The structurally anomalous region is demarcated by a maximum in q_{tetra} at low pressure (low density) and by a minimum in t_{trans} at high pressure (high density) (see Fig. 4.26 (a)).

6. In the structurally anomalous region the two order parameters were found to be strictly correlated with each other (for particular value of q_{tetra} there is an associated unique value of t_{trans}).

7. The loci of structural order extrema (q_{tetra} maxima and t_{trans} minima) was found in the (T, ρ) plane. Interestingly the loci of structural order extrema was found to be enclosing the region of diffusivity anomaly (demarcated by the loci of diffusivity maxima at the high density and diffusivity minima at the low density), which in turn enclosed the region of density anomaly (demarcated by the loci of density maxima).

In the Fig. 4.26 (b) we show the *nesting* of anomalous regions in the (T, ρ) plane as well as in the (P, T) plane for the case of water.

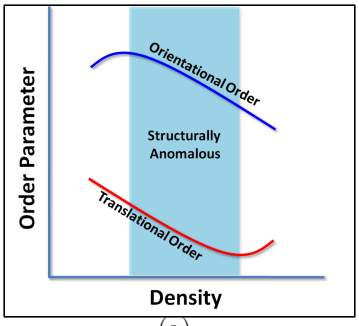

(a)

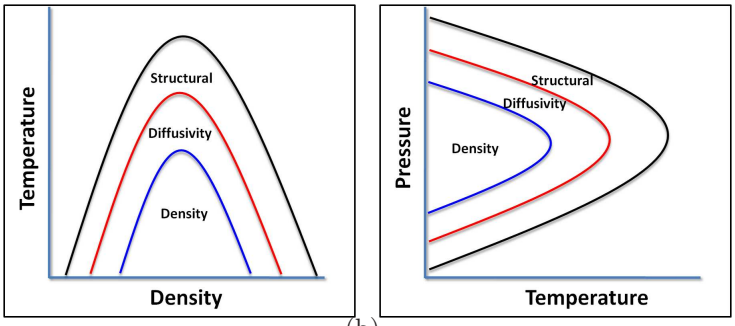

(b)

Figure 4.26: (a) The schematic phase diagram showing the structurally anomalous region for a fixed temperature bounded by tetrahedrality order maxima at low density and translational order minima at high density (b) The schematic phase diagram showing the regions of structural, diffusivity and density anomalies in (T, ρ) plane (left panel) and in (P, T) plane (right panel).

A similar analysis was carried out by Shell *et al* [153] for a model of silica. Even though most feature were akin to that of water there were two exceptions. Firstly in the structural anomalous region, the correlation between the two order parameters was not as tight as in the case of water and secondly, the hierarchy in the cascading of anomalous region was different. The loci of diffusivity extrema enclosed the structurally anomalous regions in the (T, ρ) plane.

We now present our analysis of supercooled liquid silicon.

4.5.1 Results

We have performed calculations of translational order (t_{trans}), tetrahedrality order parameter (q_{tetra}), local orientational order parameter (q_3), excess entropy S_2, diffusivity D and density ρ over a temperature range varying between $T = 1070K$ and $T = 6300K$ and pressure range varying between $P = -3.7GPa$ and $P = 15.0GPa$. We begin with the behaviour of structural order parameters.

Behaviour of Structural Order Parameters

In FIG. 4.27 and FIG. 4.28 we show t_{trans} and q_{tetra} as function of density and pressure respectively for different temperatures. As we lower the density (or pressure) the translational order goes through a minima indicating at beginning of anomalous behaviour. For temperatures greater than $T = 2517K$ we encounter the liquid spinodal (and the system cavitates). Therefore we do not find a minimum in t_{trans} for there temperatures. Curiously at very high temperatures, $T > 5000K$ we once again find that the t_{trans} goes through a minima. The tetrahedrality order parameter increases with the decrease in density (or pressure) for $1145K < T < 3147K$ and we do not find a maximum in q_{tetra} which marks the end of the anomalous region, in this range of temperature. We do find normal behaviour in q_{tetra} at very high temperatures ($T > 3776K$). At high temperatures (and low density / pressure) we encounter the liquid spinodal and at very low temperature (and low density / pressure) the system's dynamics slow and crystallisation rates are high,

which hinders our attempt to obtain q_{tetra} maximum. In FIG. 4.29 we show the parametric plot of t_{trans} *vs* q_{tetra}. Similar to water [52], we find that in the region of structural anomaly, there is tight correlation between the two order parameters.

We also find a re-entrant feature for temperature ranging between $T = 1145K$ and $T = 2130K$ at high compressions (which in FIG. 4.28 is seen as a minima at high density (pressure) values). This indicates an increase in tetrahedrality order, which is unexpected, since the coordination number at these states points is around 6. We believe this is an artifact from the definition of tetrahedrality order parameter. While calculating the q_{tetra} we consider the first four nearest neighbour, which becomes ambiguous if the first coordination shell has around more than 5 atoms at equal distances from a reference atom. To verify this we have calculated the local orientational order parameter q_3 which considers all the neighbours within the first coordination shell. In FIG. 4.30 (a) we show the parametric plot of t_{trans} *vs* q_3, which clearly shows that at high compressions the q_3 values remains fairly unchanged. But the tight correlation between the two order parameter is absent. When we calculate the q_3 order parameter by considering only the first four nearest neighbour, we should get back features of q_{tetra}, which we indeed find (see FIG. 4.29 (b)). We note that in silica, Shell *et al* [153] do find a similar result and in their work they use tetrahedrality order parameter considering six nearest neighbours.

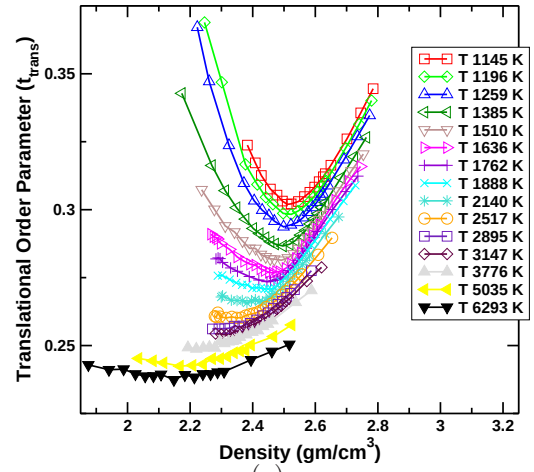

(a)

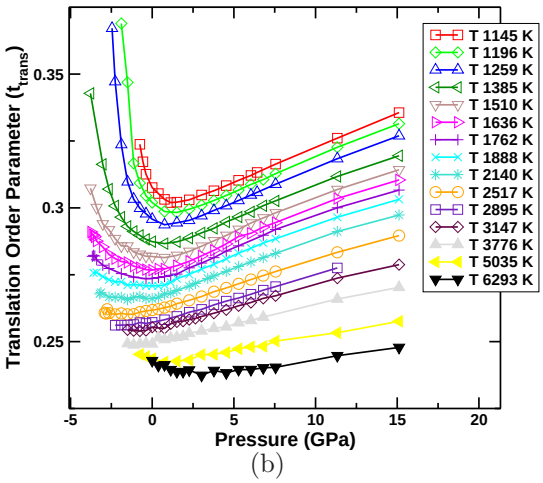

(b)

Figure 4.27: The average translational order t_{trans} as a function of (a) density and (b) pressure for different temperatures obtained from NPT MD simulations. At low pressures and densities, the translational order goes through a minimum indicating at beginning of structural anomalous region.

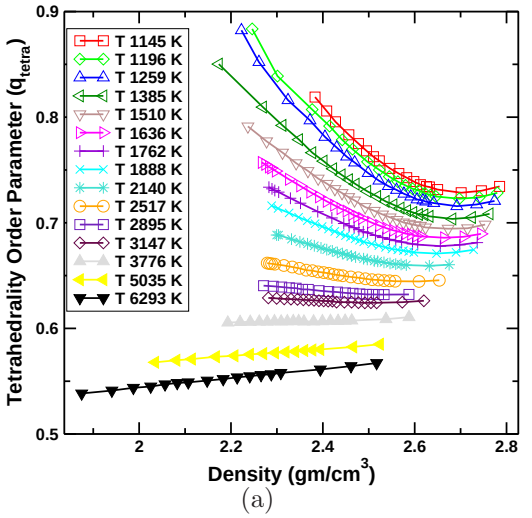

(a)

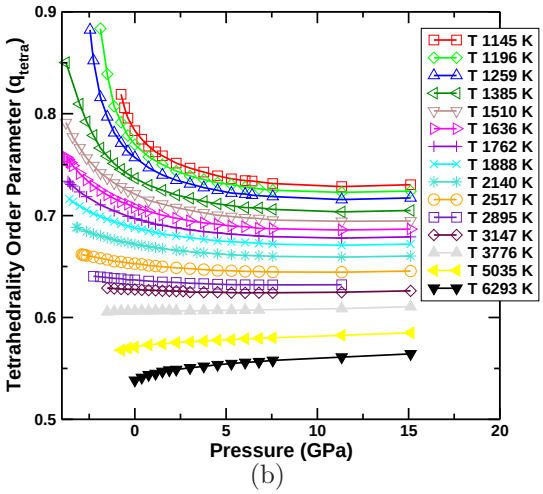

(b)

Figure 4.28: The average tetrahedrality order q_{tetra} as a function of (a) density and (b) pressure for different temperatures obtained from NPT MD simulations.

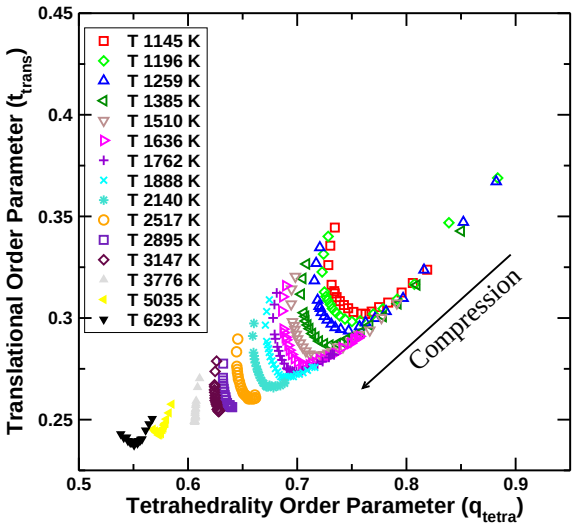

Figure 4.29: Parametric plot of translation order against the tetrahedrality order for different temperatures obtained from NPT MD simulations. The arrow mark represents the direction of increase in compression for each temperature.

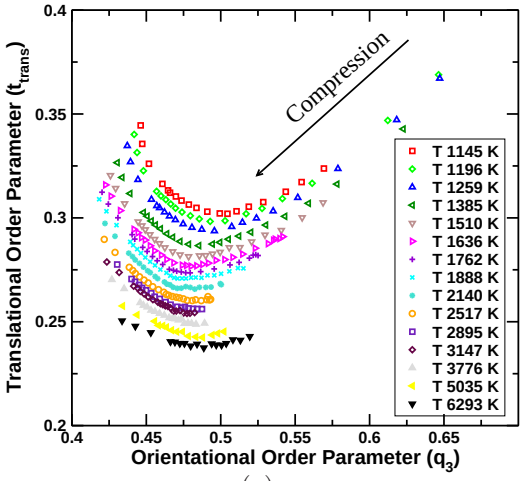

(a)

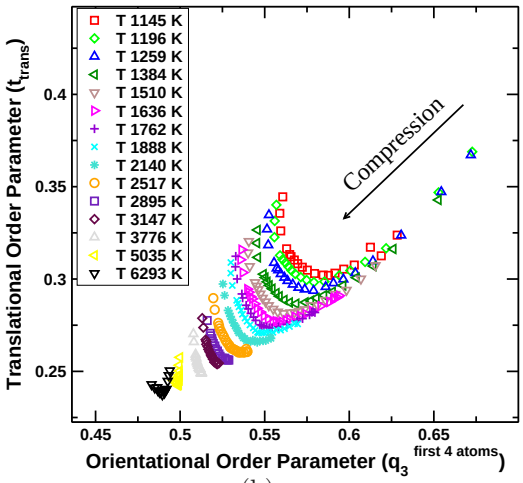

(b)

Figure 4.30: Parametric plot of translation order parameter against the (a) local orientational order parameter and (b) local orientational order parameter calculated from first four neighbours for different temperatures obtained from NPT MD simulations. The arrow mark represents the direction of increase in compression for each temperature.

Anomaly in Diffusion Coefficient

The anomalous behaviour in diffusion is characterised by increase in diffusivity with an increase in pressure or density. FIG. 4.31 we show diffusivity as a function of density and pressure for different temperatures. The isotherms ranging between $T = 1145K$ and $T = 2895K$ shows a maxima in diffusivity, hence dividing the region of anomalous and normal behaviour in D. For $T > 3000K$ we encounter the liquid spinodal and hence we do not find anomalous diffusivity for these isotherms. The locus of diffusivity maxima defines the beginning of the anomalous region in phase diagram. The locus of diffusivity minima (which we has not found this in our study) marks the lower bound of anomalous region and is expected to be found at low temperatures where system's dynamics slow and crystallisation rates are high.

In FIG. 4.32 and FIG. 4.33 we show the *nesting* of different anomalous regions in (T, ρ) and (P, T) planes respectively. The cascading of different region of anomaly is similar to that of silica - region structural anomaly enclose the region of dynamic anomaly which in turn enclose the region of thermodynamic anomaly.

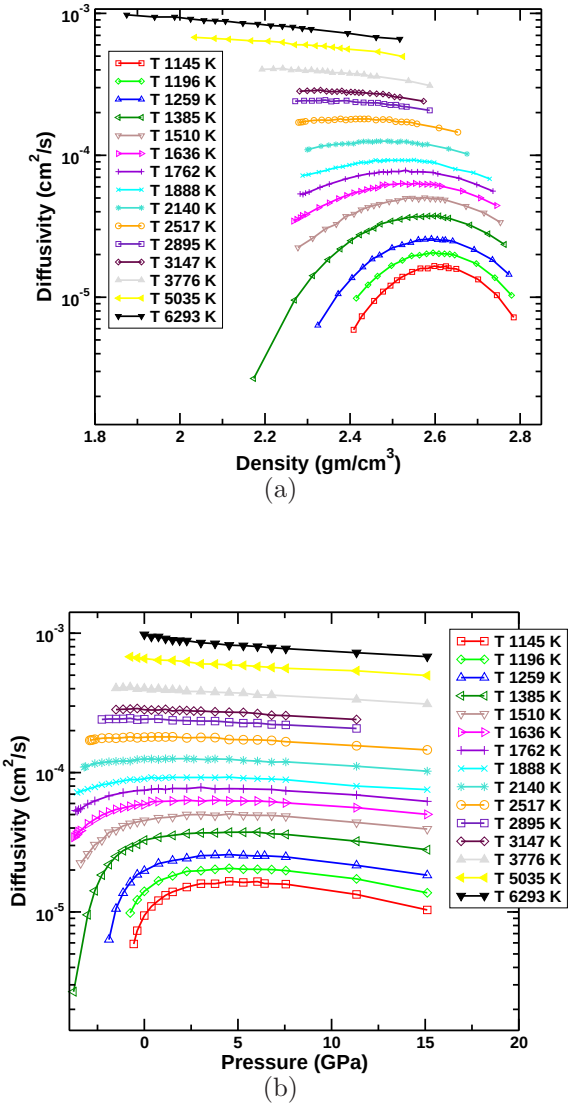

(a)

(b)

Figure 4.31: The diffusivity as a function of (a) density and (b) pressure for different temperatures obtained from NPT MD simulations.

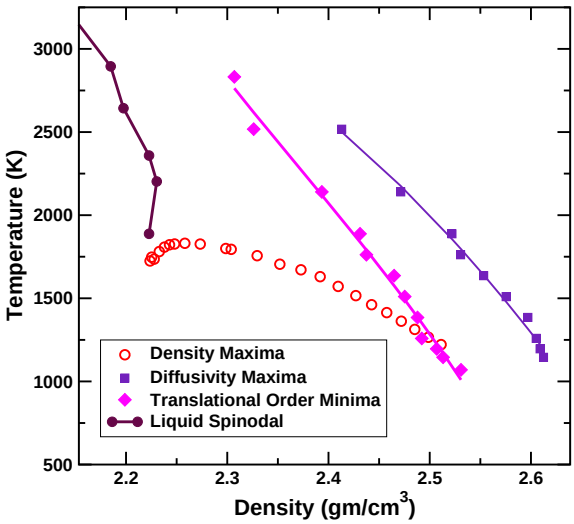

Figure 4.32: The phase diagram of liquid silicon in (T, ρ) plane showing the loci of density maxima, translational order minima and diffusivity maxima along with the liquid spinodal.

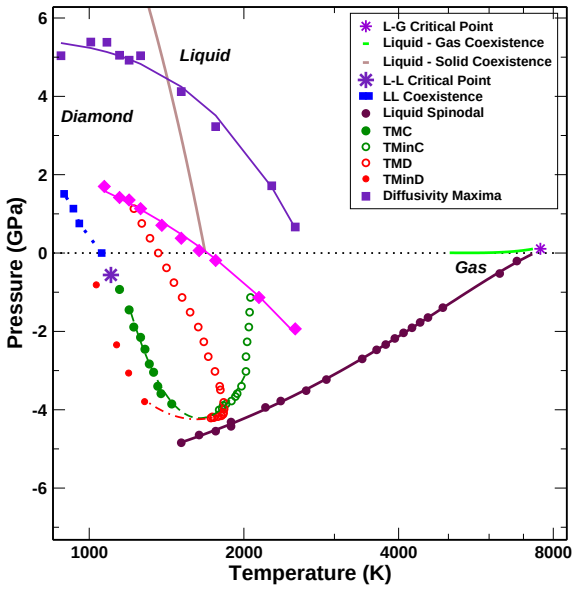

Figure 4.33: The phase diagram of liquid silicon in (P, T) plane showing the loci of density maxima, translational order minima and diffusivity maxima along other features of the phase diagram.

Excess Entropy

The feature of nesting of anomalous regions has been related to the two-body excess entropy [53, 172]. The Excess entropy, $S_x = S - S_{id}$, where S is the total entropy of the system and S_{id} is the entropy of an ideal gas system, can be calculated from the multi-particle correlation function truncated at the two-body term [16, 119] and is given

$$S_2/k_B = -2\pi\rho \int dr\{g(r)ln(g(r)) - [g(r) - 1]\}r^2 dr \tag{4.6}$$

where $g(r)$ is the pair correlation function, ρ is the number density and k_B is the Boltzmann constant. The S_2 entropy is zero for an ideal gas and infinity for a crystal. The S_2 entropy has been found to match reasonably well with the total excess entropy (S_x) [53]. In the following discussion we look at the relation between excess entropy and translational order, density and diffusivity.

Translational order and S_x: The excess entropy by definition ($S_x = S - S_{id}$) characterise the reduction in the accessible states relative to an ideal gas, due to the inter-particle correlation. Hence we can vaguely associate the in increase in translation order to decrease in the excess entropy [53]. Inside the region of structural anomaly, the translational order decreases with increase in density and hence the criterion to observe a structural anomaly can be written in terms of $ln(\rho)$ as $\partial S_x/\partial ln(\rho)|_T > 0$.

Density and S_x: To associate the excess entropy with the density we consider the following thermodynamic relation [100]

$$\left.\frac{\partial\rho}{\partial T}\right|_P = \rho^2 \left.\frac{\partial\rho}{\partial P}\right|_T \left.\frac{\partial S}{\partial\rho}\right|_T \tag{4.7}$$

where S is the total entropy of the system. The condition for density anomaly is that $\partial\rho/\partial T|_P$ should be greater than zero. Since the compressibility is a positive definite quantity for an equilibrium system, we can deduce from the

above equation that for system showing density anomaly should satisfy the condition $\partial S/\partial T|_P > 0$. We know $S_x = S - S_{id}$, where $S_{id} = -ln(\rho) + C(T)$ and $C(T)$ is temperature dependent constant. By taking a partial derivative w.r.t $ln(\rho)$ of S_x at a constant temperature we get

$$\left.\frac{\partial S_x}{\partial ln(\rho)}\right|_T = \left.\frac{\partial S}{\partial ln(\rho)}\right|_T + 1 \tag{4.8}$$

From the above equation we can infer that to observe a density anomaly, $\partial S_x/\partial ln(\rho)|_T$ should be greater than 1.

Diffusivity and S_x: Even though there is no rigorous thermodynamic relation which associates the diffusivity and S_x, there are scaling relations obtained empirical observations. One of the earliest proposal was by Rosenfeld [133] in which the reduced diffusion coefficient (D^*) is related to the excess entropy S_x as

$$D^* = a_D \; exp\left(\frac{b_D S_x}{N k_B}\right) \tag{4.9}$$

where $D^* = D\rho^{1/3}/(k_B T/m)^{1/2}$, D is the diffusion constant, m is the mass of the system, N is the number of particles, k_B is the Boltzmann constant, a_D and b_D are system dependent constant (which takes the values 0.6 and 0.8 respectively for system interacting with pair-potential like hard-sphere, soft-sphere and Lennard-Jones). Taking the partial derivative of Eq. 4.9 w.r.t $ln(\rho)$ we get

$$\left.\frac{\partial S_x}{\partial ln(\rho)}\right|_T = \frac{C}{3b_D} \tag{4.10}$$

where $C = 1{+}3\left.\frac{\partial ln(D)}{\partial ln(\rho)}\right|_T$. Hence the criterion to observe a diffusivity anomaly in the system would be $\partial S_x/\partial ln(\rho)|_T > c$, where c is a positive quantity which is system dependent.

We now present our analysis of excess entropy in the context of density and structural anomaly. To begin with we look at the relation between S_2 entropy and structural anomaly.

Excess entropy and structural anomaly: In FIG. 4.34 (a) we show S_2 entropy as a function of density for different temperatures and we find that at low densities the S_2 entropy has a positive slope hence we expect that these state points should correspond to the region of anomaly in translational order and the locus of S_2 maxima should correspond to the beginning region of structural anomaly. In FIG. 4.34 (b) we show the locus of S_2 maxima and the locus of translational order parameter (q_{tetra}) minima, which agree well with each other.

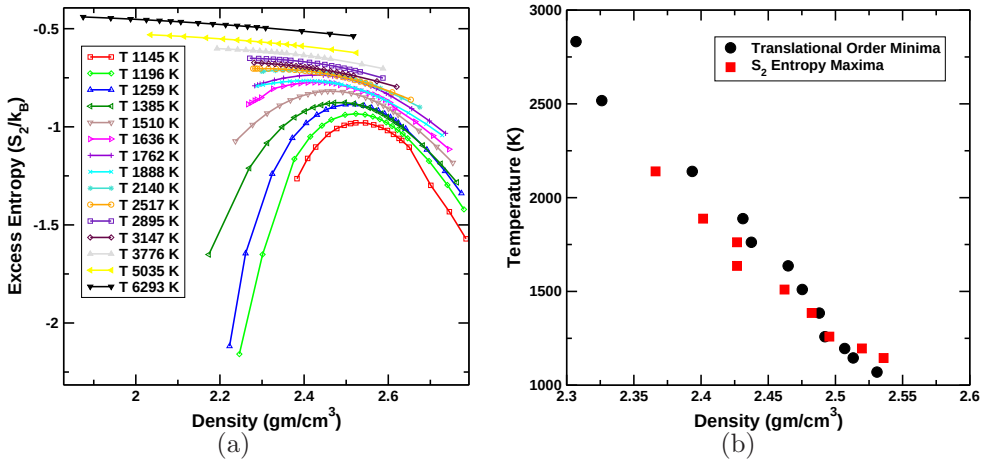

Figure 4.34: (a) The pair-correlation excess entropy (S_2) as a function of density for different temperatures. (b) The locus of pair-correlation excess entropy (S_2) maxima and the locus translational order (t_{trans}) minima in the (T, ρ) plane.

Excess entropy and density anomaly: To observe a density anomaly the criterion that has to be satisfied by S_2 entropy is $\Sigma_x \equiv \partial S_x / \partial ln(\rho)|_T > 1$. In FIG. 4.35 we show Σ_x as function of ρ for different temperatures. We extract the density corresponding to $\Sigma_x = 1$ at each temperature and locus of these points is expected to follow the locus of density maxima and we do find that to be the case (see FIG. 4.35 (b)).

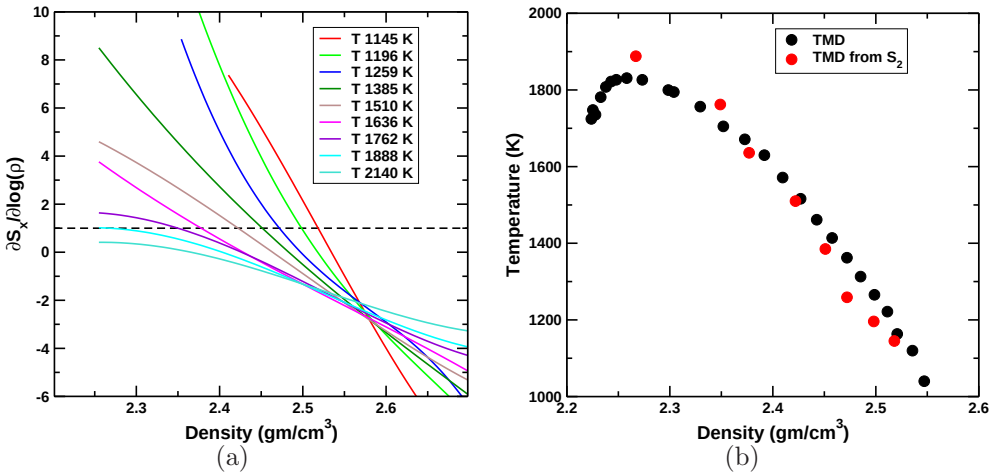

Figure 4.35: (a) Σ_x, the derivative of pair-correlation excess entropy (S_2) w.r.t $\ln(\rho)$ as a function of density for different temperatures. (b) The locus of points satisfying $\Sigma_x = 1$ and the locus of density maxima in the (T, ρ) plane.

4.6 Summary

In this chapter we analysed the changes in structural and dynamical properties as the system evolves from high T liquid to HDL to LDL phase. We found that the structure plays a very important role in determining the dynamics. A sufficiently large cluster of bonded LDL atoms (recognised as random tetrahedral networking forming atoms) is formed near locus of density maxima. The RTN cluster is found to grow with the decrease in temperature and this tetrahedral network spans the whole system approaching the LLT line and the Widom line. We find that at low temperatures the system show breakdown in Stokes-Einstein relation. The Stokes-Einstein breakdown temperature is found to be in the vicinity of density maxim and the onset temperature. Most of the computer simulation literature on the SE relationship assumes that the structural relaxation time or the α-relaxation time (τ_α), calculated from $F(q,t)$ at q corresponding to the first peak of structure factor, is proportional to viscosity. The validity of this assumption needs to be carefully analysed, by studying τ_α at various q values. We have analysed the link between the thermodynamic, dynamic and structurally anomalous region and found a nesting of anomalous regions in the phase diagram. Unlike in water and more like in silica we find that the region of structural anomaly and thermodynamic anomaly lie with in the region of dynamic anomaly.

Chapter 5

Crystal Nucleation

In the previous chapters we have looked at various aspects of the metastable liquid phase of silicon. The metastability related to stretching of the liquid (or negative pressure liquid) ends at the spinodal, as we have already discussed in the context of phase behaviour. The eventual fate of a metastable liquid upon continued undercooling is the stable crystal phase. The process of nucleation of liquid silicon to a cubic diamond crystal phase is the topic of this chapter.

Upon lowering the temperature below the T_m (the melting temperature) the difference in chemical potential $\Delta\mu$ between the crystal and the liquid phase increases and from classical nucleation theory (CNT) we know that the nucleation barrier decreases monotonically. Hence the system is prone to crystallisation at deeper undercooling. The CNT predictions are based on the fact that the nucleation process is a single step process, in which the parent metastable phase transforms into new stable phase. The formation of a stable critical nucleus from a liquid state involves change in density as well as the structure. During the nucleation process the change in these two order parameters may occur simultaneously, in which case we would observe a single-step process. Recently many simulations and theories [58,161,177,186] have suggested a multi-step mechanism of crystal nucleation in which the density fluctuations precedes the fluctuations associated with structure. The work of ten Wolde and Frenkel [186] on globular proteins (modeled by a

generalised Lennard-Jones potential) found that the metastable liquid-liquid critical point separates out the contribution of density fluctuation and structural fluctuation to the crystal nucleation process. Close to the critical point it was found that a crystal nucleus of critical size formed within a nucleus of dense liquid. Away from the liquid-liquid critical point a single-step nucleation process was observed, wherein a critical nucleus directly formed from the parent liquid phase.

Crystal nucleation process, can also be influenced by pre-structured liquid phases, as some recent work suggest [64, 92]. A pre-structured liquid is a phase which has local structural arrangement similar to the local structure of crystal. Ghiringhelli *et al.* [64], looking at the nucleation process in carbon (a locally tetrahedral crystal), found that with the change in local coordination of the liquid from threefold to fourfold the nucleation rates increased by many orders of magnitude. The free-energy cost to create a diamond-liquid interface was found to be lower in the fourfold than in the threefold liquid.

In our work, as discussed in the previous chapters, we have shown existence of a liquid-liquid critical point ($LLCP$) in supercooled phase of silicon. Also in our study we find that approaching the liquid-liquid critical point and the Widom line the system predominantly contains four-folded RTN atoms whose local structure is similar to that of a crystal. Hence it is interesting to understand how different is the nucleation process in a HDL phase away from the LLCP, where the system is predominantly five-folded, as compared to the nucleation process approaching the LLCP from high temperatures, where number of four-folded atoms steadily increases. To address this question we analyse the spontaneously crystallising run and also compute free energy difference (ΔG) across various state points in the phase diagram. We begin this chapter with a discussion of computational details related to the recognising of crystal phase and calculation of ΔG.

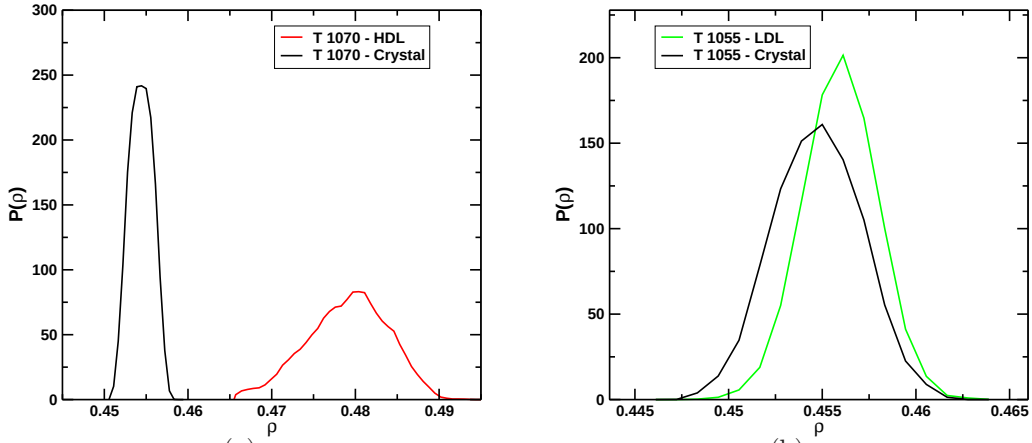

(a) (b)

Figure 5.1: Distribution of density comparing (a) high density liquid (HDL) and crystal phase and (b) low density liquid (LDL) and crystal phases.

5.1 Computation of Crystal Nucleation Barrier

In order to compute the free energy barrier we need to define a reaction coordinate (or an order parameter), which can distinguish between the liquid phase of silicon and the cubic diamond crystal phase. The structural order of the liquid phase invariably differs from that of a crystal. Density on the other hand can be similar as we show in FIG. 5.1. The bond orientational order introduced by Steinhardt *et al.* can capture the changes in structural arrangements of the atoms effectively and hence has been used in previous crystal nucleation studies ([12, 166] and references within) efficiently. As discussed in the chapter on *Methods and calculations* one can define both global as well as local orientational orders. But the global orientational order was found in a previous study to have issues related to overestimation of critical nucleus size [165] and also had dependence of system size [93]. In our study we use a global order parameter is defined by a local orientational order as prescribed in the work of ten Wolde [166] and Auer [12]. We elaborate the details of order parameter next.

5.1.1 Identification of Crystalline Nucleus

The local bond orientational order $q_l(i)$ is given by

$$q_l(i) = \left(\frac{4\pi}{2l+1} \sum_{m=-l}^{l} |q_{lm}(i)|^2 \right)^{(1/2)} \tag{5.1}$$

where $q_{lm}(i)$ is defined as

$$q_{lm}(i) \equiv \frac{1}{N_n(i)} \sum_{j=1}^{N_n(i)} Y_{lm}(\hat{r}_{ij}) \tag{5.2}$$

where $N_n(i)$ is the number of neighbouring atoms which are within a distance of 2.9 Åfrom a reference atom i (*see* FIG. 4.1), $Y_{lm}(\hat{r}_{ij}) \equiv Y_{lm}(\theta_{ij}, \phi_{ij})$ are the spherical harmonics calculated along the vector $\hat{r}_{ij}$ between the atoms i and j, θ_{ij} and ϕ_{ij} represent the polar and azimuthal angles respectively. In FIG. 5.2 we show local orientational order distribution obtained from isobaric-isothermal (NPT) molecular dynamics (MD) simulations of liquid and crystal phases. We find that in both q_3 and q_6 distribution there is an overlap in the distributions of liquid and crystal. To enhance this separation we calculate the correlation function between the q_l vectors of the two neighbouring atoms i and j as

$$q_l(i).q_l(j) \equiv \sum_{m=-l}^{m=l} q_{lm}(i).q_{lm}(j)^* \tag{5.3}$$

Physically this means that if the local environment of atom i and j are similar then the two environments will be correlated. The distribution of the correlation function for $l = 3$ and $l = 6$ is shown in FIG. 5.3. We find that both q_3 and q_6 differentiate the phases to a similar resolution. In our work we have used q_3 to recognize the crystal-like atom. An atom i is crystal-like atom if $q_3(i).q_3(j) < -0.23$ (*see* 5.3 (a)). In addition to this we also apply a second criterion by defining a threshold number of connections a crystal-like atom should have with its neighbours crystal-like atoms. From FIG. 5.4 we

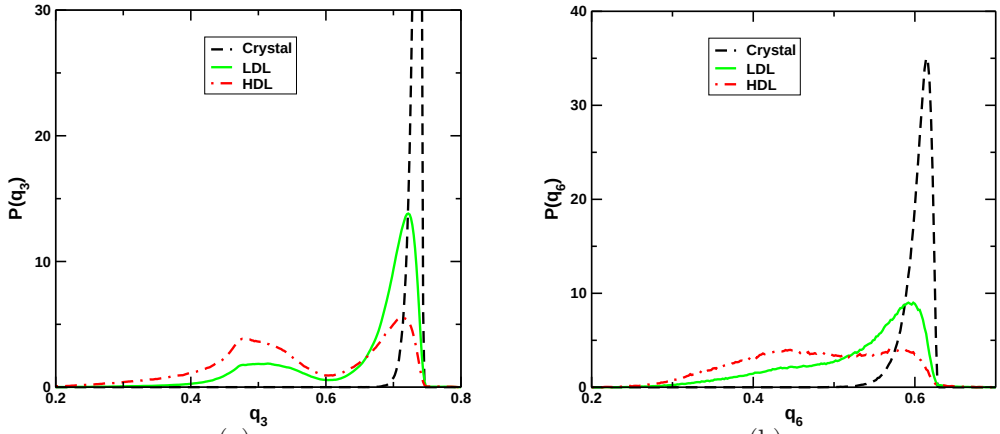

Figure 5.2: Distribution of local orientational order (a) q_3 and (b) q_6 for high density, low density and crystal phases.

define that every crystal-like atom should be connected with minimum 3 other crystal-like atoms. Finally to identify a crystalline nucleus we define that two crystal-like atoms belong to the same nucleus if the distance between them is $\leq$ 3.77 Å(cut-off of the two-body part of the Stillinger-Weber potential). The size of largest crystalline nucleus (n_0) in the system is used as the order parameter for the free energy computation at high temperature and pressure values away from the Widom line.

Next we discuss the umbrella sampling MC method used to compute the free energies. We also discuss the issues related to using n_0 as the order parameter to compute ΔG at low temperatures and pressures near the Widom line.

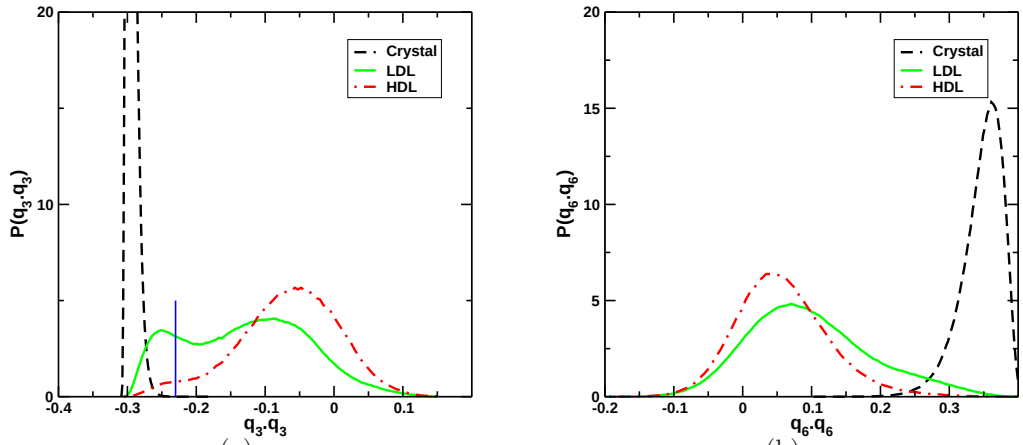

Figure 5.3: Distribution of (a) $q_3(i).q_3(j)$ and (b) $q_6(i).q_6(j)$ correlation for high density, low density and crystal phase. Any atom is considered crystal-like if $q_3(i).q_3(j) < -0.23$.

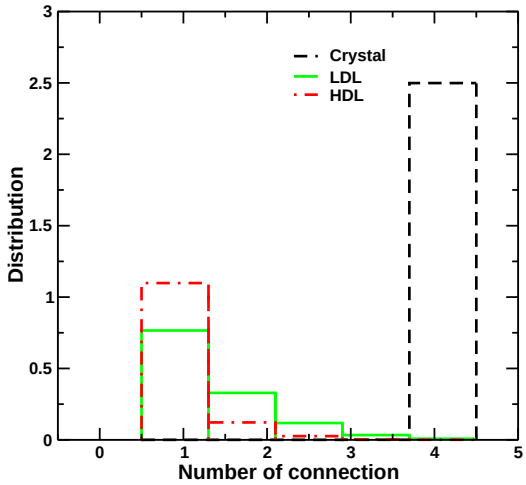

Figure 5.4: Typical distribution of number of connections per atom in high density, low density and crystal phases

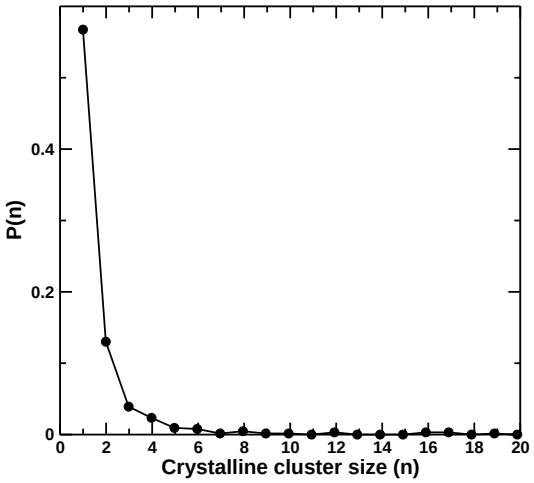

Figure 5.5: Equilibrium distribution of crystalline nuclei obtained from NPT MD simulation at $T = 1080K$ and $P = 0GPa$.

5.1.2 Gibbs Free Energy Barrier - Order Parameter and System Size

The nucleation free energy barrier can be computed from the equilibrium distribution of crystalline nuclei $P(n) = N(n)/N$, where $N(n)$ represent number of nuclei consisting of n crystalline atoms and N is the total number of liquid-like atoms in the system. The free energy difference $\Delta G(n)$ is related $P(n)$ by

$$\Delta G(n) = -k_B T ln[P(n)] \tag{5.4}$$

The $P(n)$ as obtained from an NPT MD simulation (which has not spontaneously crystallised) at $T = 1080K$ and $P = 0GPa$ is shown in FIG. 5.5, which clearly illustrates that the formation of large crystalline nucleus is less probable. Even in cases of a crystallising runs, the statistical accuracy with which we determine the $\Delta G(n)$ at bigger nucleus size will be very poor. In order to sample larger nucleus sizes with better sampling we have employed the umbrella sampling MC technique introduced by Torrie and Valleau [171].

The basic idea behind the umbrella sampling MC technique is to bias

the simulation to sample the configurations of interest (for which the Boltzmann factor is small). In our study we need to sample configurations of specified nucleus sizes. In a conventional MC simulation we generate configurations such that the distribution of the configuration will be proportional to $exp(-\beta E(r^N))/Z$, where $E(r^N)$ is the Hamiltonean of the system. In a umbrella sampling MC by modify the Hamiltonean by adding a bias potential and generate configurations having specified nucleus size. The average number of nucleus size n in a biased ensemble can be written as

$$< N(n) >_{NPT} = \frac{\left\langle N(n)/W(\mathbf{r}^N)\right\rangle_W}{\left\langle W(\mathbf{r}^N)\right\rangle_W} \sim \frac{\sum[N(n)/W(\mathbf{r}^N)]}{\sum W(\mathbf{r}^N)} \tag{5.5}$$

where the summation is over all the measured configuration in the biased ensemble. Note that when the nucleus formations are rare it can been shown [134] that $P(n) = P(n_0)$, where n_0 is the size of the largest crystalline nucleus. This is a valid approximation when the critical nucleus sizes are big and the free energy barriers are large.

The distribution obtained from umbrella sampling is in a biased ensemble. Since $P_{bias}(n_0) = exp(-(\Delta G(n_0) + W(n_0))/(k_B T))$, where $P_{bias}(n_0)$ is the nucleus size distribution in a biases ensemble, $\Delta G(n_0)$ is the free energy difference, and $W(n_0)$ is the bias potential, we can easily unbias the distribution using the relation

$$P(n_0) \equiv exp(-\Delta G(n_0)/(k_B T)) = -P_{bias}(n_0) exp(W(n_0)/(k_B T)) \tag{5.6}$$

We perform umbrella sampling MC simulation at different n_0 values using a harmonic bias potential and in the FIG. 5.6 (a) and (b) we show the biased and unbiased distribution respectively. The free energy difference $\Delta G(n_0)$ computed from above expression will be accurate up to a constant term (note that we do not know the denominator $\sum W(\mathbf{r}^N)$ in the Eq. 5.5). In order to obtain the missing constant, we fit the $\Delta G(n_0)$ estimates obtained from simulations performed at different windows of n_0 to a single polynomial

of n_0. This can be done by a least square fit, by minimising

$$\chi = \sum_{n=1}^{N_w} \sum_{d=1}^{N_d} \left[\Delta G_d(n) - \sum_{i=1}^{p} (a_i n^i) - b_n \right] \tag{5.7}$$

where N_w is the total number of windows of n_0, N_d is the total number of data points in each window of n_0, p is the order of the polynomial with coefficients a_i, which is same for all the windows and b_n, which will give us the missing constant. From CNT we know that $\Delta G(n) = -a_0 n + a_1 n^{2/3}$. Hence we have used a polynomial of the form $a_0 n + a_1 n^{2/3} + a_2 n^2 + a_3 n^3 \cdots$.

We next discuss the choise of bias potential and the issues related to the use of largest crystalline nucleus as the order parameter.

Bias Potential and Choice of Order Parameter

Harmonic bias potential: A bias potential which is a harmonic function of size of the largest crystalline nucleus is found to be a good choice in many of the previous work ([13,94,134,165] and references within). The harmonic bias potential $W(n_0)$ is defined as

$$W(n_0) = (k/2)(n_1(\mathbf{r}^N) - n_0(\mathbf{r}^N))^2 \tag{5.8}$$

The constant k is chosen such that the $P(n_0)$ obtained at different windows of n_0 have sufficient overlap (which is necessary for better polynomial fitting). We found that $k = 0.02\epsilon$ is a good choice for all the state points at which we performed the free energy computation.

In our simulation using the harmonic bias potential we came across various issues related to second crystalline nucleus growth which we summarise below:

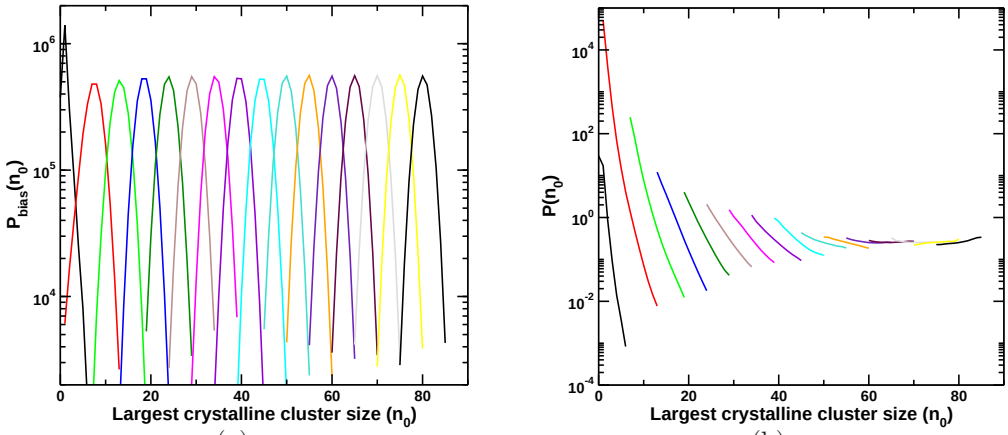

(a) (b)

Figure 5.6: Distribution of size of largest nucleus size (n_0) obtained from umbrella sampling MC simulation using the SW potential for silicon at $T = 1221K$ and $P = 0GPa$. (a) with bias potential and (b) after removing contribution of bias potential.

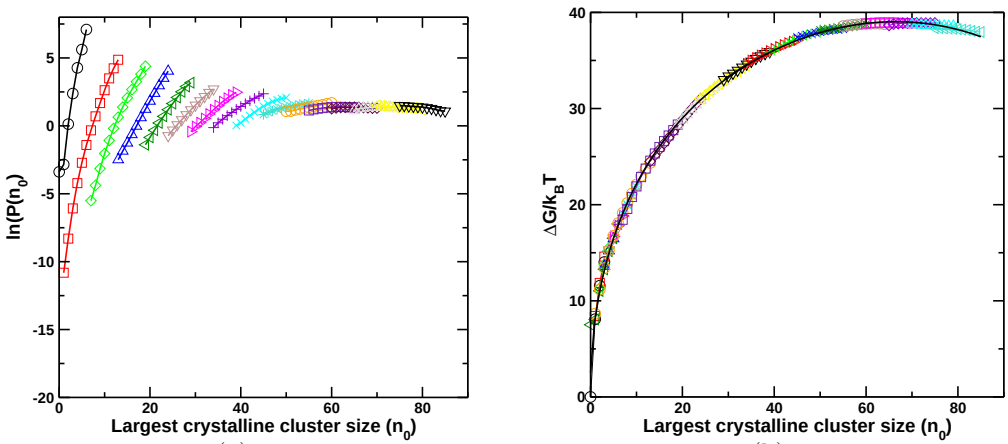

(a) (b)

Figure 5.7: (a) The free energy difference $\Delta G(n_0)/k_BT$ obtained from taking logarithm of unbiased n_0 distribution. (b) $\Delta G(n_0)/k_BT$ after fitting the free energy data from different windows to a single polynomial (Note that to fit a polynomial we have also included the data obtained from umbrella sampling using hard wall bias potential).

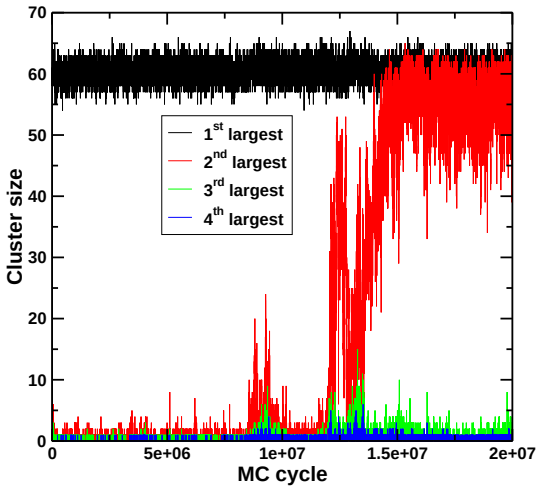

Figure 5.8: Crystalline nucleus size as a function of MC cycle obtained from umbrella sampling MC simulation in the $n_0 = 60$ window using SW potential for silicon at $T = 1259K$ and $P = 0GPa$. The second nucleus growth (red) was observed approaching the critical nucleus size of ~ 90.

1. Crystal nucleus size of $60 - 90$ atoms: In umbrella sampling MC simulations performed with a system size of 4000 atoms, we observed that approaching the critical nucleus size the system contained more than one largest nucleus (*see* FIG. 5.8). This issue was resolved by performing parallel tempering MC simulation (explained in later subsection) wherein we swapped two replicas having different largest nucleus size.

2. Crystal nucleus size of $\sim$ 20 atoms: In these cases the assumption $P(n) = P(n_0)$ is no longer valid. Hence umbrella sampling simulation using a hard wall bias potential in which we build the distribution by including nucleus of all sizes (*explained below*).

3. Post critical nucleus: Crossing the critical nucleus size the free energy for formation of nucleus decreases. Hence we observe formation of multiple nucleus of n_0. This issue was resolved by performing umbrella sampling simulation using a hard wall bias potential.

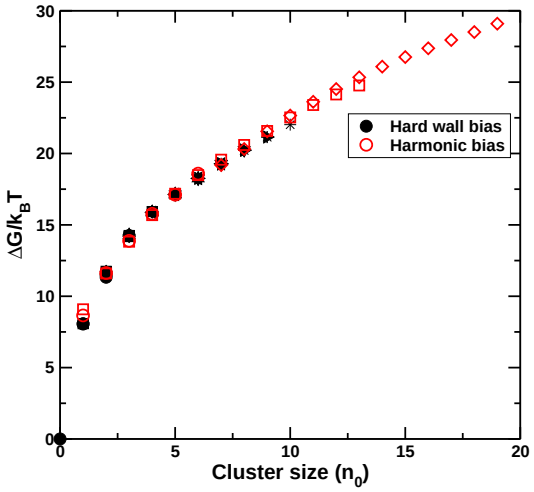

Figure 5.9: Comparison of free energy difference (ΔG) obtained from hard wall bias potential and harmonic bias potential in umbrella sampling MC simulation using SW potential for silicon at $T = 1221K$ and $P = 0GPa$.

Hard wall bias potential: When the formation of a crystalline nucleus is no longer a rare event the assumption $P(n) = P(n_0)$ breaks down [134]. Hence we have calculate the distribution of nuclei instead of largest nucleus distribution. In these cases we apply a hard wall bias potential and obtain distribution of all the nuclei in the system whose size vary between the bounds specified in the bias potential. The hard wall bias potential is defined as

$$\begin{aligned} \delta(n_1) &= 0 \text{ if } n_0^l \leq n_1 \leq n_0^h \\ &= \infty \text{ otherwise} \end{aligned} \tag{5.9}$$

We have compared the $\Delta G(n_0)$ from both the bias potential at states point where the harmonic potential works well and we find that both methods match with each other (*see* 5.9).

System Size Dependence

The free energy barrier and the critical nucleus size are intensive quantities and hence should not depend on the system size. In simulations, since we

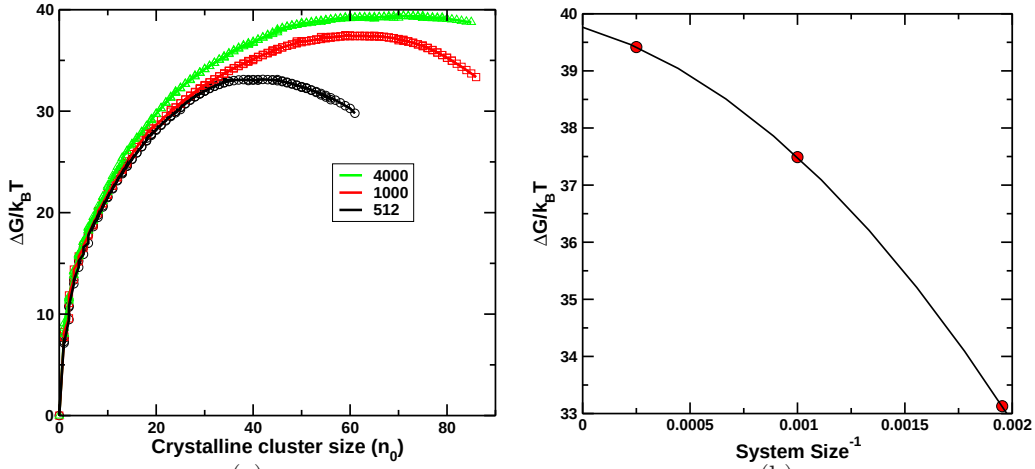

Figure 5.10: Free energy barrier (ΔG) computed for different system sizes ($T = 1221K$ and $P = 0GPa$).

apply a periodic boundary condition, care has to be taken while choosing the system size, because the periodic image of large crystalline nucleus can affect the procedure of identification of crystalline atom. We explain this point with an example taken from our simulation. In the HDL phase the typical density is around $\rho \sim 0.5\sigma^{-3}$, where σ is the diameter of the atom and in a crystalline phase $\rho \sim 0.45\sigma^{-3}$. If we the system size is 512 atoms, the cubic simulation box will have a length $l \sim 10\sigma$. For a crystal nucleus size is around 80 atoms, the diameter of the nucleus is $\sim 7\sigma$, which larger than $l/2$ and hence the periodic image will influence the environment of the atoms in the original simulation box. In FIG. 5.10 (a) we show the free energy computed at $T = 1221K$ (27% undercooling) and $P = 0GPa$ for three different sizes of the system (512, 1000 and 4000) atoms. In FIG. 5.10 (b) we show the free energy barrier as function of inverse system size. By extrapolating the inverse system size to zero, we find that 4000 atoms is the right system size for the state point we are interested to compute free energies.

5.1.3 Umbrella Sampling with Parallel Tempering

At state points approaching the Widom line, the dynamics of the system becomes very slow and relaxation times are big. Hence along with the umbrella sampling we also implement parallel tempering scheme. Note that we can perform parallel tempering in temperature, pressure and also in the order parameter (n_0). Since we are interested in computing free energies along isobars, we perform replica swap between nearest two temperature windows and nearest two n_0 windows in the same temperature window as illustrated in the FIG. 5.11. The acceptance criterion for the n_0 swap is given by

$$\begin{aligned} acc((1, n_0^{(1)}, T_1), (2, n_0^{(2)}, T_2)) &\rightarrow ((2, n_0^{(1)}, T_1), (1, n_0^{(2)}, T_2))) \\ &= min(1, exp(-\beta(W_n - W_o))) \end{aligned} \tag{5.10}$$

where $W_n = 0.5k^{(1)}(n_1^{(1)} - n_0^{(1)})^2 + 0.5k^{(2)}(n_1^{(2)} - n_0^{(2)})^2$ and $W_o = 0.5k^{(1)}(n_1^{(2)} - n_0^{(1)})^2 + 0.5k^{(2)}(n_1^{(1)} - n_0^{(2)})^2$. The superscripts within braces represent the replica index. The swap frequency for temperature was chosen such that the system spends at least an amount of time corresponding to the mean square displacement of $1\sigma^2$ at the highest temperature and for the n_0 swap we chose a swap frequency such that the system get enough time to change its largest nucleus size to the applied n_0.

We summarise the entire umbrella sampling procedure below.

1. For an given temperature (T), pressure (P) we perform normal MC simulation in NPT ensemble.

2. Every MC step, we perform the umbrella sampling move for a given nucleus size value of n_0 which involves

   (a) Recognising largest crystalline nucleus size recognized (n_1).

   (b) Calculating the change in bias potential energy $W(n_1) - W(n_0)$ and invoking the Metropolis acceptance criterion.

3. Every T_{swap} MC steps we perform the parallel tempering in T.

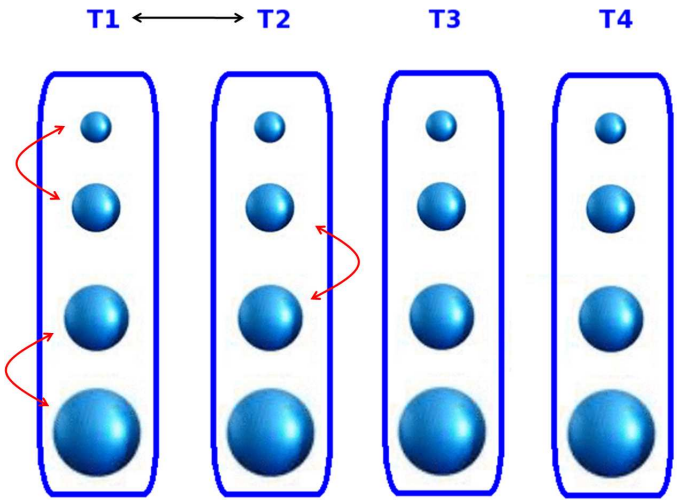

Figure 5.11: Illustration of parallel tempering scheme. The arrows indicate the swap between nearest two temperature windows and nearest two n_0 windows.

4. Every $n0_{swap}$ MC steps we perform the parallel tempering in n_0.

5. After the equilibration run, we obtain the nucleus size distribution ($P_{bias}(n_0)$) from the production run. (*Implementation note:* One has to use *long int* data type for an array which stores the nucleus size distribution).

6. We then unbias the distribution and obtain the free energy at different windows of n_0.

7. In the end we fit a single polynomial for different windows of n_0 and obtain the complete $\Delta G(n_0)$ profile from which we recognise the free energy barrier $\Delta G(n_0^*)$ and critical nucleus size n_0^*.

Note that in the cases where we have to perform simulations at large crystalline nucleus, the initial configuration is seeded with a sufficiently big crystalline nucleus.

We now discuss our results, starting with an analysis of spontaneous crystallising runs.

5.2 Spontaneous Crystallising Runs

From the exhaustive MD simulations which we have performed during the course of our study of phase diagram of supercooled liquid silicon we have obtained statistics related to how often a system crystallises. We find that the system is prone to crystallisation in the vicinity of liquid-liquid critical point ($LLCP$) and the Widom line. Also we find that the crystallisation process in HDL is markedly different from LDL phase. We elaborate these observation below.

We have considered state points that belong to $P = 0GPa$ and analyse the MD configurations at different temperatures. We can pick out a crystallising samples looking at the drop in energy as a function of MD time step and by counting the number of crystalline atoms in the system. All our analysis were done on the system having a size of 512 atoms. Our observations are as follows:

1. In the HDL phase, uptill 35% undercooling ($T = 1095K$), we do not find any of the 5 independent MD simulations (which were all run for a minimum duration of $22ns$) to show any signature of crystallisation. In fact in these samples we find very few crystalline atoms. At a slightly lower temperature $T = 1080K$ we find that 50% (8 out of 16) of our samples crystallised, with in a duration of run ranging between $2ns$ and $22ns$. At $T \sim 1060K$ all the 35 independent samples crystallised with in a duration of run ranging between $2ns$ to $13ns$ (*see* FIG. 5.12 - corresponds to HDL phase at $T = 1080K$).

2. In the LDL phase ($T = 1055K$) we have performed around 50 independent runs. A few samples (~ 20) show clear indication of crystallisation with a few ns. In the rest of the samples it is difficult to decide whether the system has crystallised or not, since we find in these samples, a considerably large crystalline nucleus ($\sim 30\%$ of the system size) which appears *arrested* and did not grow in the simulation time we looked at ($100ns$ to $200ns$)(*see* FIG. 5.13).

At positive pressure value $P = 0.75GPa$ we do not find any crystallising

sample in the temperature range (till $T = 755K$) we have performed simulation.

Now we consider the $P = -1.88GPa$ isobar, which is below the critical pressure. Along this isobar for $T \geq 1258K$ we find that none of the 8 samples (each run for minimum of $22ns$) crystallised. Approaching the Widom line from high temperature we find that all our 40 samples crystallised (duration of run ranging between $5ns$ and $25ns$). At the low temperature side of Widom line we find similar trends as that of LDL phase at $P = 0GPa$. These observations are consistent for the rest of the isobars below the critical pressure.

To understand these observations we calculate the ΔG along different paths in the phase diagram. Understanding the influence of various features in the phase diagram on the crystal nucleation process becomes complicated as these features are closely related to each other. For example with undercooling along an isobar, the $\Delta\mu$ increase, the coordination number decreases and the compressibility increases. In our study we have computed ΔG following four different paths in the phase diagram, which are (1.) Changing compressibility and keeping coordination number fixed at a fairly larger than the tetrahedral coordination. (2.) Changing the coordination number and keeping the compressibility fixed, (3.) Along an isobar crossing the Widom line and (4.) Along different isobars approaching the Widom line from high temperature. In the FIG. 5.14 we show the state points where we compute the free energy employing the umbrella sampling Monte Carlo simulation.

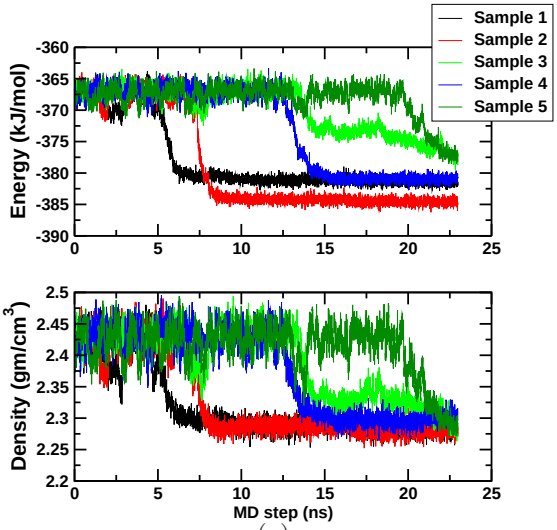

(a)

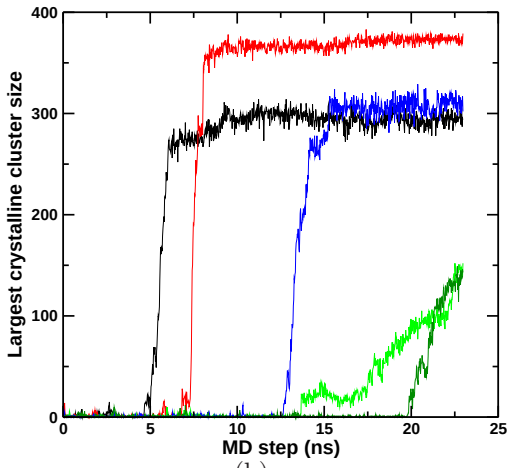

(b)

Figure 5.12: (a) Total energy (top panel) and density (bottom panel) of the system as a function of MD time step. (b) largest crystalline nucleus as a function of MD time step. Each color represent an independent NPT MD simulation run performed at $T = 1080K$ and $P = 0GPa$ using the SW potential for silicon. As the system transform into a crystal phase, a jump in energy to a lower value is detected, along with an increase in crystalline nucleus size. The crystallisation time vary from $5ns$ to $20ns$. All the samples show fairly sharp increase in the crystal growth.

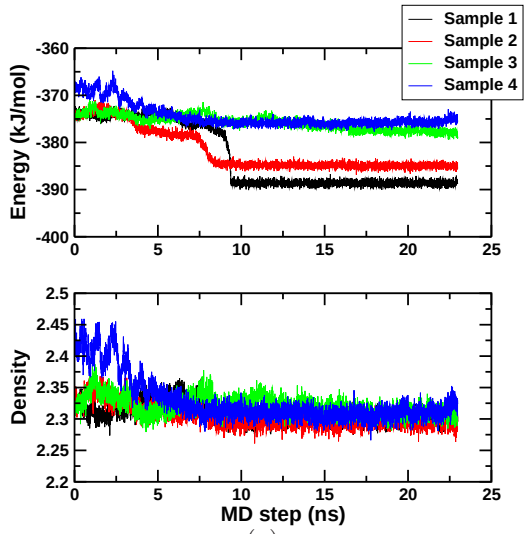

(a)

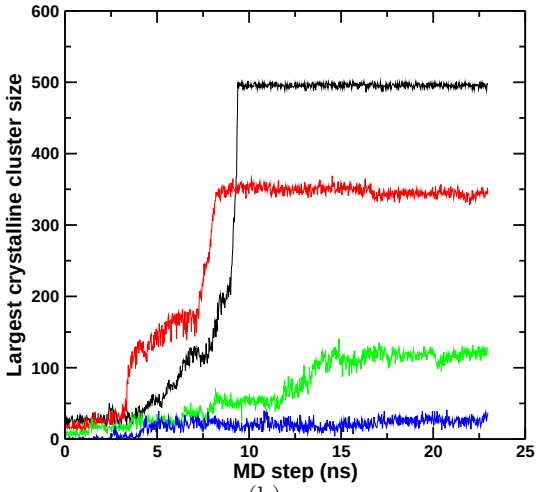

(b)

Figure 5.13: (a) Total energy (top panel) and density (bottom panel) of system, (b) largest crystalline nucleus as a function of MD time step. Each color represent an independent NPT MD simulation run performed at $T = 1055K$ and $P = 0GPa$ using the SW potential for silicon. As the system transform into a crystal phase, a jump in energy to a lower value is detected, along with an increase in crystalline nucleus size. Even though all the samples show signature of crystallisation, we find a big difference in the extent of crystal growth. Note that in all the samples the density of LDL phase is similar to that of crystal.

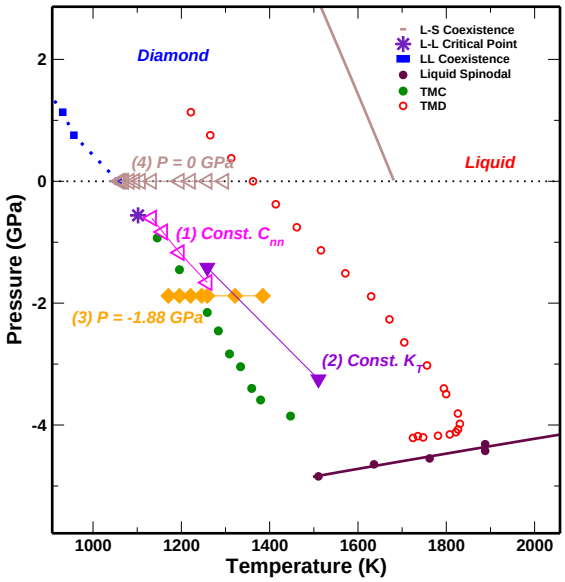

Figure 5.14: The phase diagram of liquid silicon in (P, T) plane depicting the state points where we have computed the free energy barrier. (1) magenta triangles are state points where the coordination number is constant ($C_{nn} = 4.66$), (2) two violet triangles represents state points where compressibility is constant ($K_T = 1.5$ reduced units), (3) orange diamonds are state points where $P = -1.88GPa$ and (4) brown triangles represent state points where $P = 0GPa$.

5.3 Free Energy and Compressibility

We have chosen state points in the HDL region of phase diagram, such that the coordination number remains constant as the compressibility increases. We have chosen a coordination number of $C_{nn} = 4.66$, a fairly larger than the tetrahedral coordination so that we can analyse the effect of density fluctuations on the free energy barrier. We find that all these state points sit parallel to Widom line. In the FIG. 5.15 we show the free energy difference ΔG as a function of order parameter n_0. As we approach the critical point, the compressibility increases and the free energy barrier decrease to around $10k_BT$. The critical nucleus size change from 35 atoms to less than 10 atoms (in the vicinity of LLCP).

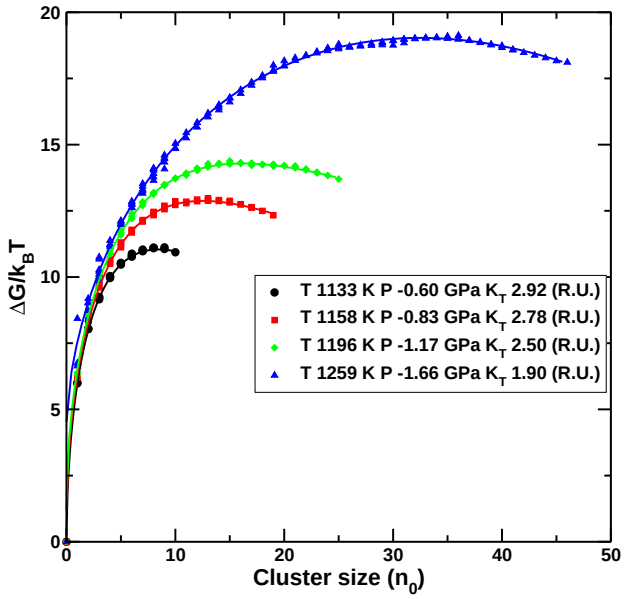

Figure 5.15: Free energy difference $\Delta G/k_BT$ against the nucleus size obtained from NPT umbrella sampling MC simulation. At all the state points, the coordination number is same ($C_{nn} = 4.66$), but the compressibility is decreasing monotonically with temperature and pressure.

We next look at the effect of local coordination number on the free energy barrier keeping the compressibility fixed.

5.4 Free Energy and Coordination Number

Keeping the compressibility fixed we try to find the effect of coordination number on ΔG of the system. We chose the compressibility value such that the difference in the coordination number is largest. In the FIG. 5.16 (inset) we show the dependence of compressibility on the pressure for two isotherms $T1259K$ and $T1510K$. The symbols represent the state points where the compressibility is constant and the coordination number varies by 3%. In the FIG. 5.16 (main panel) we show the corresponding change in the free energy, where in we find a dramatic change in the free energy barrier and

critical nucleus size as we approach the smaller coordination number. Since the temperature difference is around $250K$,we should expect a big change in chemical potential difference $\Delta\mu$, hence it is inconclusive whether the effect is due to the change in local structure.

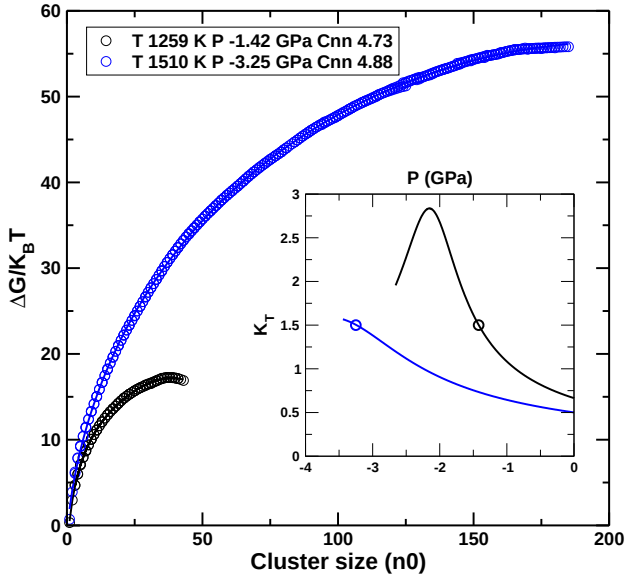

Figure 5.16: Free energy difference $\Delta G/k_BT$ against the nucleus size obtained from NPT umbrella sampling MC simulation. At both the state points, the compressibility is fixed ($K_T = 1.5$ reduced units), but the coordination number changes by 3%.

We next look at the change in ΔG across the Widom line at $P = -1.88GPa$ isobar.

5.5 Free Energy across the Widom Line at $P = -1.88GPa$

In the previous two cases we restricted our analysis in the HDL phase. We now analyse the change in ΔG as we go from high T liquid to low T liquid

crossing the compressibility maxima line or the Widom line. We fix the pressure at $P = -1.88GPa$ and vary the temperature from $T = 1385K$ to $T = 1171K$ (*see* FIG. 5.14). The compressibility maxima is at $T \sim 1230K$. At the low temperature state points we have performed around 150 million parallel tempering MC cycles. We show our results in FIG. 5.17. We find that free energy barrier decreases monotonically as we go from high T liquid to low T liquid. In the low temperature side of Widom line, the free energy barrier changes by $2k_BT$ for a $50K$ change in temperature. Also the free energy barrier shows a broader peak. At the high temperature side, we find that for a similar change in temperature, the free energy barrier changes by $10k_BT$.

We next look at the behaviour of $\Delta G(n)$ along $P = 0GPa$ approaching the vicinity of critical point.

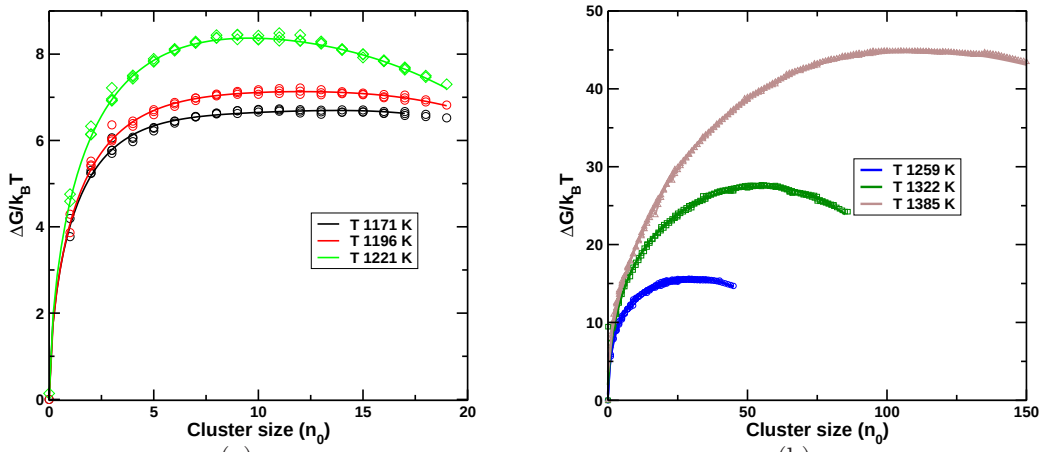

(a) (b)

Figure 5.17: Free energy difference $\Delta G/k_BT$ against the nucleus size obtained from NPT umbrella sampling MC simulation at $P = -1.88GPa$. (a) Low temperature side of Widom line (b) High temperature side of Widom line.

5.6 Free Energy along $P = 0GPa$

Keeping the pressure constant at $P = 0GPa$, starting from $T = 1296K$ ($\sim$ 23% undercooling) to $T = 1059.8K$ ($\sim$ 37% undercooling) we have calculated the ΔG as a function of crystal nucleus size n_0 (*see* FIG. 5.18). We find that the barrier at the highest temperature is around $60k_BT$ which decreases to around $8k_BT$ in the vicinity of LLT. The critical nucleus size changes from around 140 atoms to less then 10 atoms (*see* FIG. 5.19). For $T <= 1082K$, free energy barrier shows a broader peak which are evidently different from high temperature free energy profiles. We note that from the MD simulation statistics we find that the system crystallise more often for $T \leq 1080K$. It is just an observation and we can not conclude much from this since we lack good statistics of crystallising MD runs.

We make an attempt to compare these results with the CNT predictions. According to CNT the free energy barrier and the critical nucleus is given by

$$\begin{aligned} \Delta G(n_0^*) &= \frac{16\pi}{3}\left(\frac{v'\sigma^{3/2}}{(-\Delta\mu)}\right)^2 \\ n_0^* &= \frac{32\pi}{3}\left(\frac{(v')^{2/3}\sigma}{(-\Delta\mu)}\right)^3 \end{aligned} \tag{5.11}$$

where v' is the volume of the critical nucleus, σ is the surface free energy. To make a proper comparison we need v', σ and $\Delta\mu$. We have used the $\Delta\mu$ from the work of Broughton and Li [24] and the other variables v' and σ are unknown, which we get as fit parameter from the plot of (a) $ln(n_0^*)$ against $ln(-\Delta\mu)$ and (b) $ln(\Delta G(n_0^*)$ against $ln(-\Delta\mu)$. From the CNT we expect the slope of the curve (a) to be 3 and from (b) to be 2. In the FIG. 5.20 we find that no region of the curve follows CNT, which can be due to the fact that we are assuming that both v and σ varies linearly with temperature.

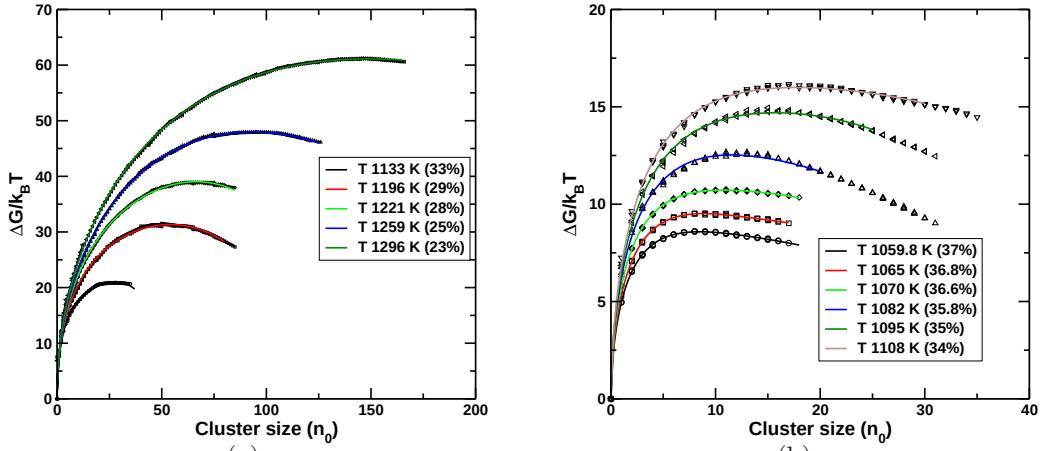

Figure 5.18: Free energy difference $\Delta G/k_BT$ against the nucleus size obtained from NPT umbrella sampling MC simulation at $P = 0GPa$. (a) $\Delta G(n_0)$ for $T \geq 1296K$ (b) $\Delta G(n_0)$ for $T \leq 1108K$.

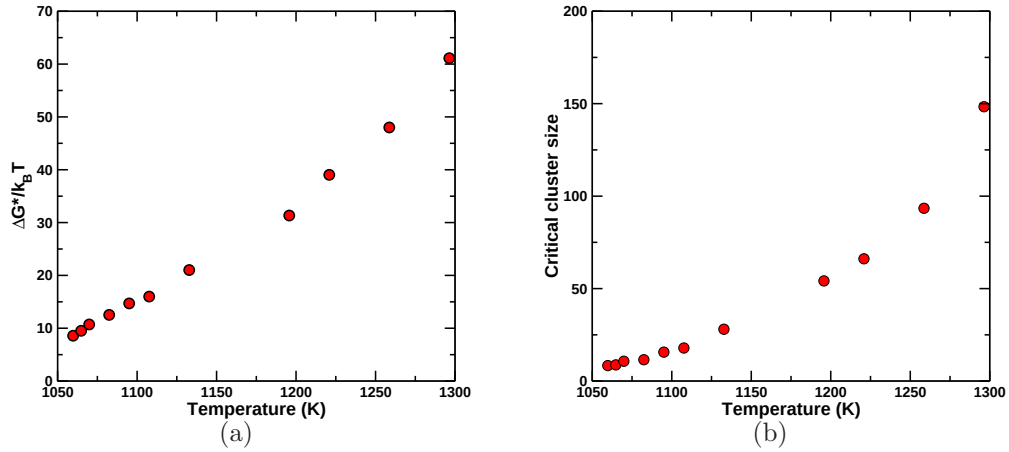

Figure 5.19: (a) Free energy barrier $\Delta G(n_0^*)$ and (b) Critical nucleus size n_0^* as a function of temperature for $P = 0GPa$.

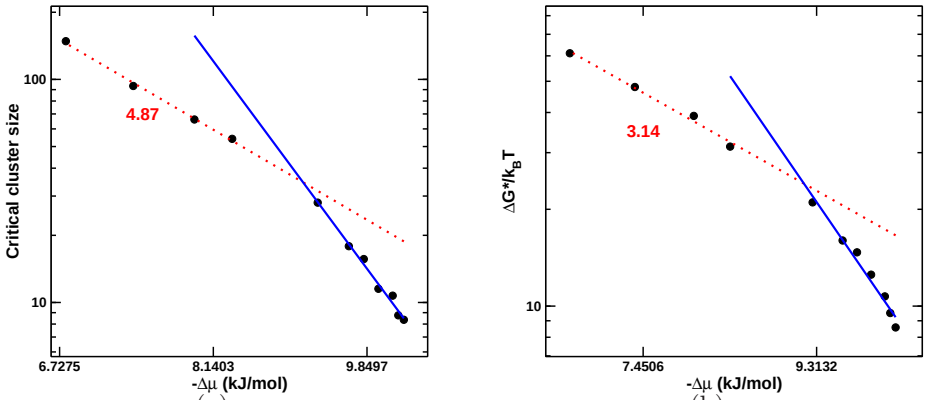

Figure 5.20: Comparison of CNT prediction. The $\Delta\mu$ estimates for $P = 0GPa$ were obtained from Broughton and Li [24]. The solid lines are CNT fit lines.

5.7 Free Energy across the Phase diagram

We now present our results of free energy computation across the whole phase diagram for pressure values ranging from from $0.75GPa$ to $-3.02GPa$ and temperature values ranging from $1000K$ to $1450K$. In FIG. 5.21, 5.22, 5.23, 5.24, 5.25, 5.26 we show the ΔG computed for $P = 0.75GPa$, $-0.60GPa$, $-1.13GPa$, $-1.51GPa$, $-2.64GPa$, $-3.02GPa$ respectively. At all the pressure values below the critical pressure we find that the the free energy barrier decreases monotonically as we approach the Widom line from high temperature. In the FIG. 5.27 we show free energy barrier and critical nucleus size as a function of temperature for different pressure values, from which we extract the *iso-free energy barrier* lines and *iso-critical nucleus size* lines (*see* FIG. 5.28). These results suggest that within the accuracies of our computation there is no particular change in the free barrier or the critical nucleus size near the liquid-liquid critical point. According to the CNT prediction the $\Delta G(n_0^*) \propto (n_0^*)^{(2/3)}$. Interestingly we do find this relation to be valid for a wide range of data as shown in the FIG. 5.29 where we have plotted scaled data of free energy barrier $\Delta G(n_0^*)$ against the critical nucleus n_0^* (Choosing a high temperature free energy value reference we have scaled was done by hand).

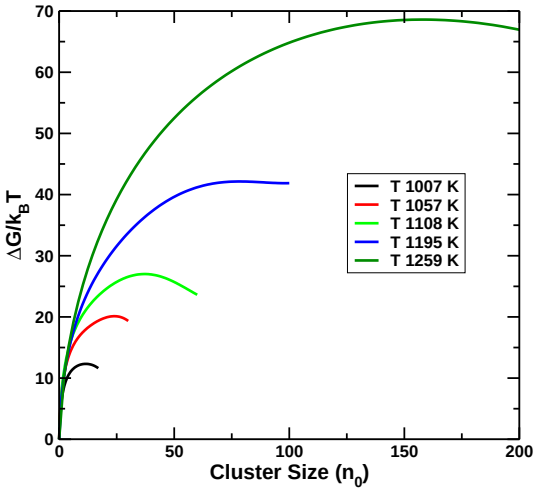

Figure 5.21: Free energy difference $\Delta G(n_0)$ against the nucleus size (n_0) obtained from NPT umbrella sampling MC simulation along the $P = 0.75GPa$ isobar.

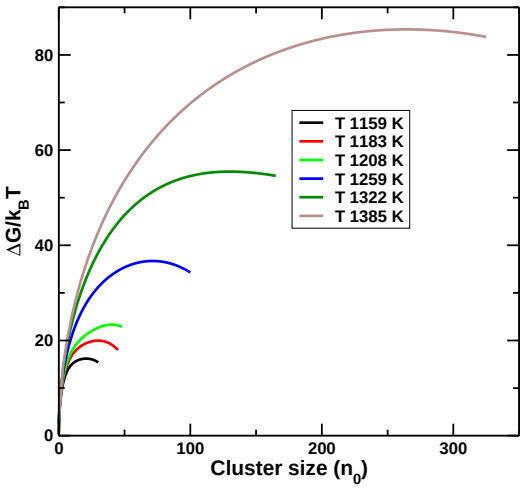

Figure 5.22: Free energy difference $\Delta G(n_0)$ against the nucleus size (n_0) obtained from NPT umbrella sampling MC simulation along the $P = -0.60GPa$ isobar.

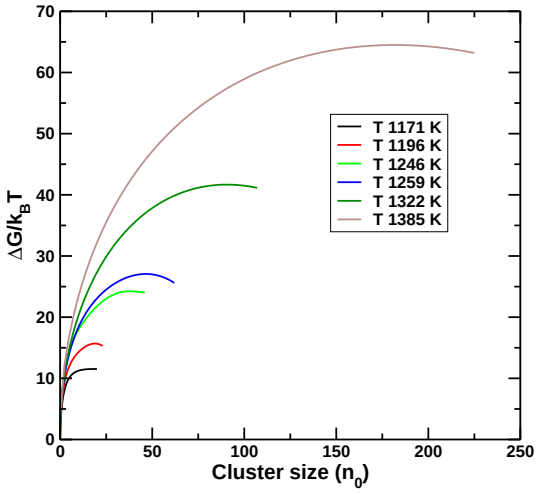

Figure 5.23: Free energy difference $\Delta G(n_0)$ against the nucleus size (n_0) obtained from NPT umbrella sampling MC simulation along the $P = -1.13GPa$ isobar.

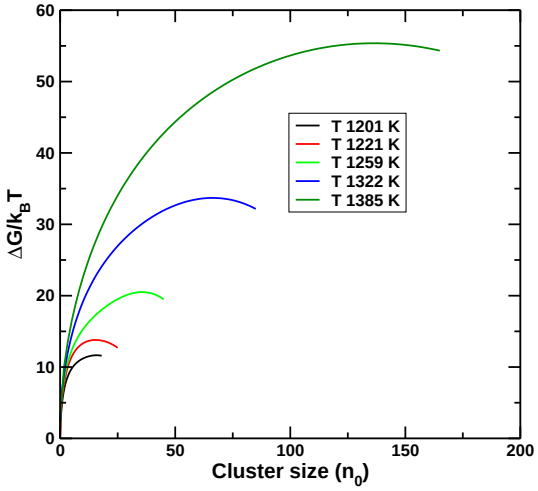

Figure 5.24: Free energy difference $\Delta G(n_0)$ against the nucleus size (n_0) obtained from NPT umbrella sampling MC simulation along the $P = -1.51GPa$ isobar.

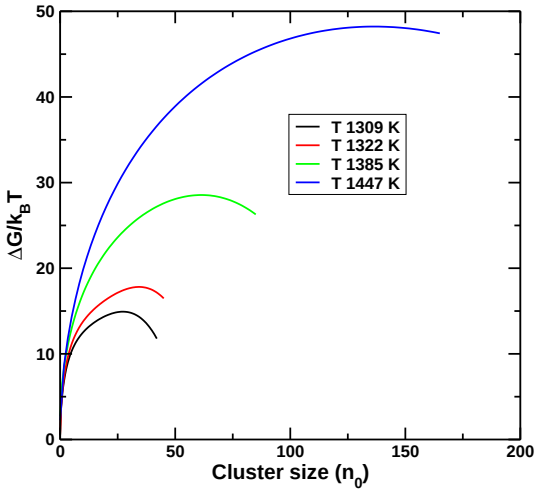

Figure 5.25: Free energy difference $\Delta G(n_0)$ against the nucleus size (n_0) obtained from NPT umbrella sampling MC simulation along the $P = -2.64GPa$ isobar.

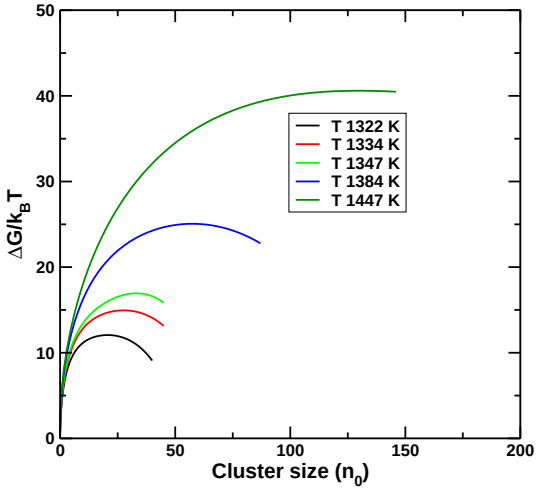

Figure 5.26: Free energy difference $\Delta G(n_0)$ against the nucleus size (n_0) obtained from NPT umbrella sampling MC simulation along the $P = -3.02GPa$ isobar.

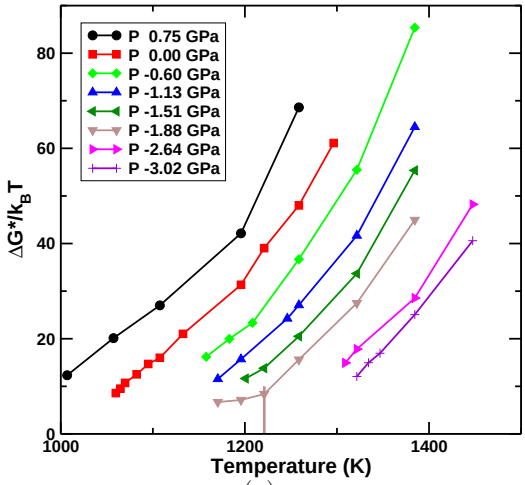

(a)

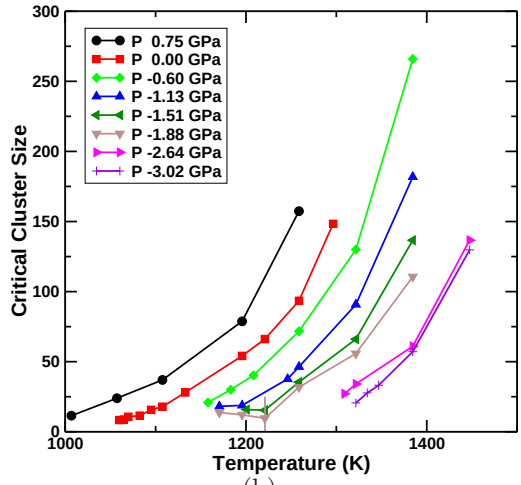

(b)

Figure 5.27: (a) Free energy barrier $\Delta G(n_0^*)$ and (b) Critical nucleus size n_0^* as a function of temperature for eight different isobars.

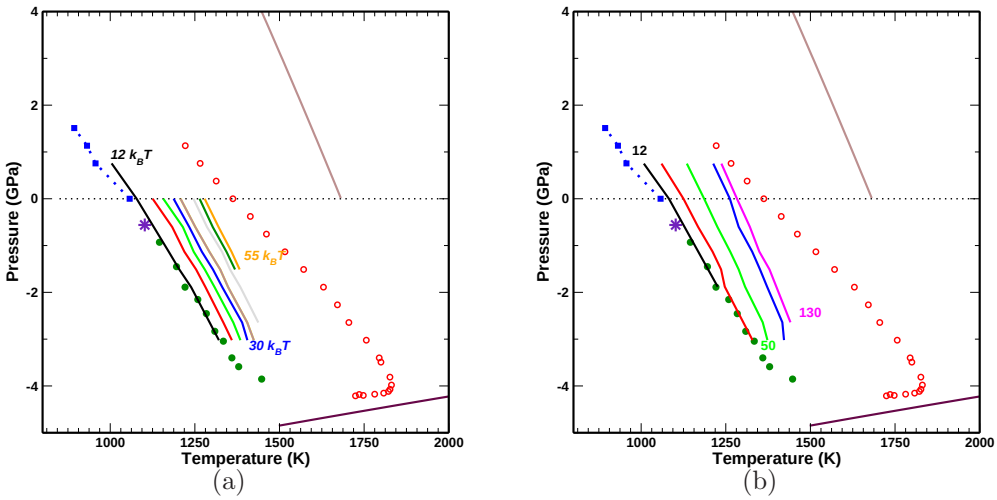

Figure 5.28: Phase diagram of silicon in (P, T) plane showing (a) the constant free energy barrier lines and (b) the constant critical nucleus size lines

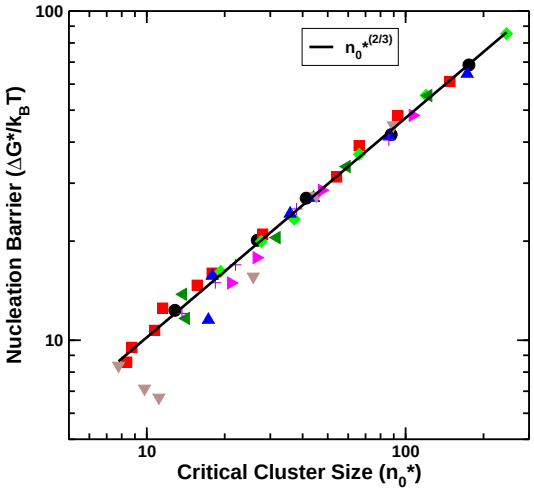

Figure 5.29: Free energy barrier $\Delta G/k_BT$ against the critical nucleus obtained across the phase diagram. Choosing a high temperature free energy value as reference we have scaled the rest on the data on to that value by hand.

5.8 Nucleation Mechanism

In this section we perform detailed analysis of local structural and density changes as the system transform from liquid to crystal state. We have analysed the NPT MD runs as well as the NPT umbrella sampling MC runs.

5.8.1 Analysis of spontaneously crystallising runs

In the earlier section we discussed to some extent crystallising MD configurations, where in we looked at the change in energy, density and size of largest crystal nucleus as a function of MD time step. We extend the analysis and recognize, along with largest crystal nucleus (which we represent by blue color in all plots), number of other crystalline atoms (orange), number of 5-coordinated atoms or atoms with $q_3 < 0.6$ (red), number of 4-coordinated atoms or atoms with $q_3 \geq 0.6$ (green) and number of random tetrahedral network forming atoms or RTN atoms (magenta). The state points chosen for analysis are along $P = 0GPa$ isobar and for $T = 1055K$, corresponding to the LDL phase, $T = 1065K$, corresponding to the HDL phase and $T = 1080K$, corresponds to the highest T at which we find spontaneous crystallisation.

$T = 1055K$, $P = 0GPa$: We begin with the analysis of $T = 1055K$ isotherm, at which the critical nucleus is around $5 - 6$ atoms. In the FIG. 5.13 (a) we show change in energy and density for five different samples, out of which we have chosen *sample 1* and *sample 3* to analyse. In case of *sample 1* we find a sharp jump in the energy of the system as system crystallise. The *sample 3* has not completely crystallised but we find steady increase in the number of crystalline atoms (*see* FIG. 5.13 (b)). In FIG. 5.30 we show the evolution of number of atom belonging to different local environment as the system crystallise and we summarise our observations below.

1. In both the samples, number of crystalline atoms (orange) not belonging to the largest crystalline nucleus is small in number.

2. A majority of 4-coordinated atoms (green) are part of RTN cluster

(magenta).

3. In the *sample 1* we find that as the number of crystalline atoms begin to increase (MD time step $t < 10ns$) the number of RTN atoms decreases but the number of 5-coordinated atoms remains fairly constant. For $t > 10ns$, the number of crystalline atoms increase very steeply as number of both 4-coordinated and 5-coordinated atoms decrease.

4. In the *sample 3* we find that the crystallisation in the system is very slow. Like in *sample 1*, number of crystalline atoms increase with the decrease in number of RTN atoms, during which number of 5-coordinated atoms do not change much. For $t > 15ns$ we find that there is no change in the number of RTN atoms and the crystallisation process almost stops at this point.

$T = 1065K$, $P = 0GPa$**:** At this state point the critical nucleus has around 8 atoms. In the FIG. 5.31 we show the change in energy and density for two different samples which we are going analyse. In the *sample 1* we find a step-like feature in the total energy of the system as the system crystallise and in the *sample 2* we find that the system does not crystallise even though the largest crystalline nucleus is bigger then the critical nucleus. In the FIG. 5.32 we show the evolution of different types of atoms as the system crystallise and we summarise our observations below.

1. Similar to the case of $T = 1055K$ we find that most of the 4-coordinated atoms belong to the RTN cluster.

2. In the *sample 1*, below $t = 12ns$ we find number of 5-coordinated as well as RTN atoms remain fairly unchanged and number of crystalline atoms are small in number (around 8-10). Between $t = 12nsand15ns$, we see decrease in 5-coordinated atoms and increase in number of RTN and crystalline atoms. For $t > 17ns$ we find a sharp decrease in number of RTN and 5-coordinated atoms resulting in drastic increase in the size of crystalline nucleus.

3. In the *sample 2*, we again observe at the initial stage of crystallisation ($t < 15ns$, decrease in number of 5-coordinated atoms and increase in number of RTN and crystalline atoms. But at later stages the number of RTN atoms remain constant and the crystallise nucleus seizes to grow.

$T = 1080K$, $P = 0GPa$**:** At this state point the critical nucleus is around 12 atoms. In the FIG. 5.12 we show change in energy and density for different samples among which we have chosen *sample 1* and *sample 3* to analyse. In the FIG. 5.33 we show the evolution of different types of atoms as the system crystallise and we summarise our observations below.

1. Similar to the previous two cases we find that most of the 4-coordinated atoms belong to the RTN cluster.

2. In *sample 1* we find that a sharp decrease in 5-coordinated atoms results in a sharp increase the size of the crystalline nucleus, as the RTN atoms remains constant.

3. In *sample 3* at around $13ns$, we find that the number of 5-coordinated atoms decreases as the the number of RTN atoms increase. We also find a small increase in crystalline atoms. For $t > 17ns$ the number of RTN atoms remain constant, but as the number of 5-coordinated atoms decrease the crystalline nucleus grows slowly.

From the above analysis of spontaneously crystallising MD runs we find that that even though the size of critical nucleus is of the order of few atoms the system continuos to state in liquid state. The role of RTN atoms seems to be important since we find in all the spontaneously crystallising state points the rate of crystallisation distinctly depends on how fast the RTN cluster shrinks.

All spontaneously crystallised samples belong to deeply undercooled state point. To understand the precise role of RTN cluster we also need to analyse the high temperature crystallising runs. Since we do not have any spontaneously crystallising sample in the duration of run we have simulated, we

have to seed the high temperature samples with crystalline nucleus of size larger than the critical size. Instead we analyse umbrella sampling MC configurations at various stages of nucleation process.

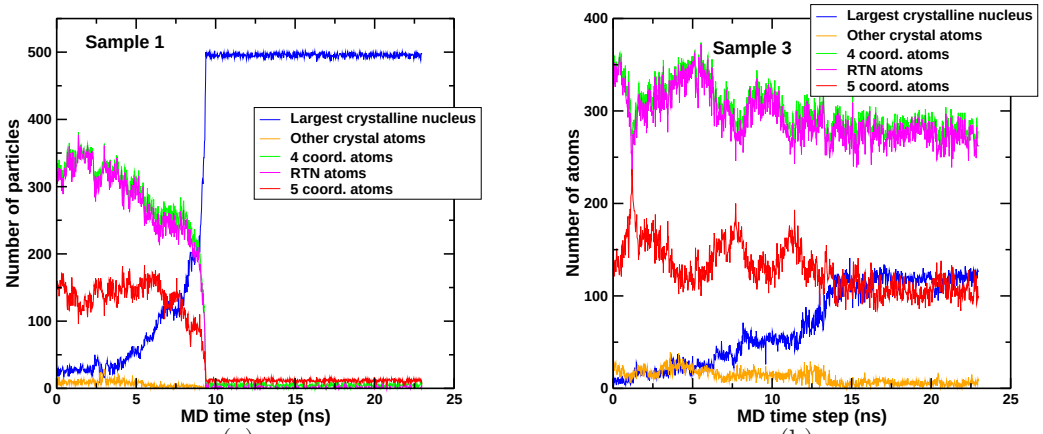

Figure 5.30: Evolution of different kinds of atoms in two different samples (a) and (b) as the system at $T = 1055K$ and $P = 0GPa$ crystallise. Blue represents the atoms belonging to the largest crystalline nucleus, orange represents other crystalline atoms (orange), red represents 5-coordinated atoms or liquid atoms with $q_3 < 0.6$, green represents 4-coordinated atoms or liquid atoms with $q_3 \geq 0.6$ and magenta represents random tetrahedral network forming atoms or RTN atoms.

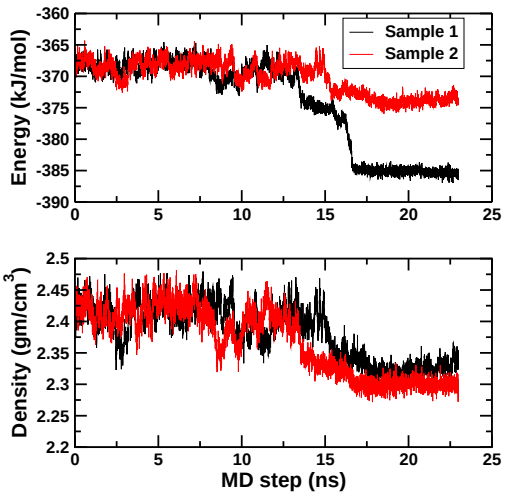

Figure 5.31: (a) Total Energy (top panel) and density (bottom panel) of system as a function of MD time step from two independent NPT MD simulation runs performed at $T = 1065K$ and $P = 0GPa$. As the system transform into a crystal phase, a jump in energy to a lower value is detected.

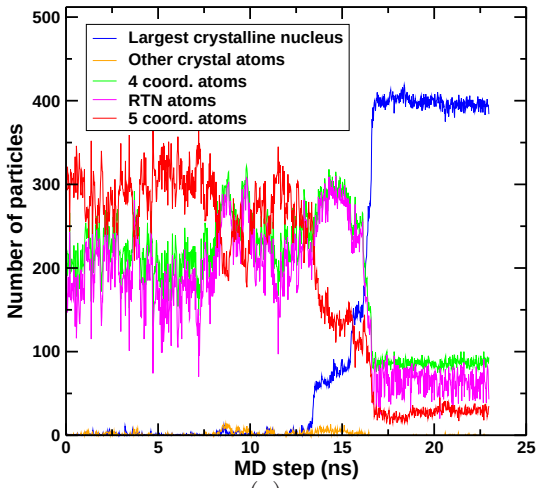

(a)

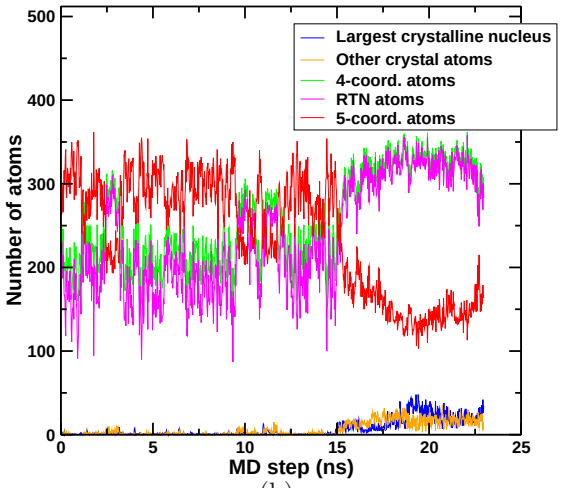

(b)

Figure 5.32: Evolution of different kinds of atoms in two different samples (a) and (b) as the system at $T = 1065$ and $P = 0GPa$ crystallise. Blue represents the atoms belonging to the largest crystalline nucleus, orange represents other crystalline atoms (orange), red represents 5-coordinated atoms or liquid atoms with $q_3 < 0.6$, green represents 4-coordinated atoms or liquid atoms with $q_3 \geq 0.6$ and magenta represents random tetrahedral network forming atoms or RTN atoms.

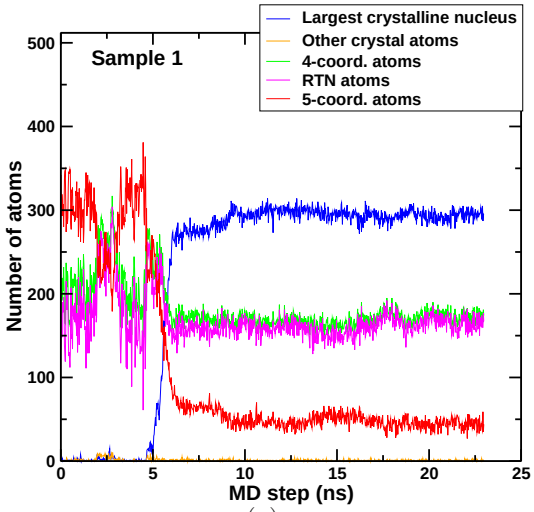

(a)

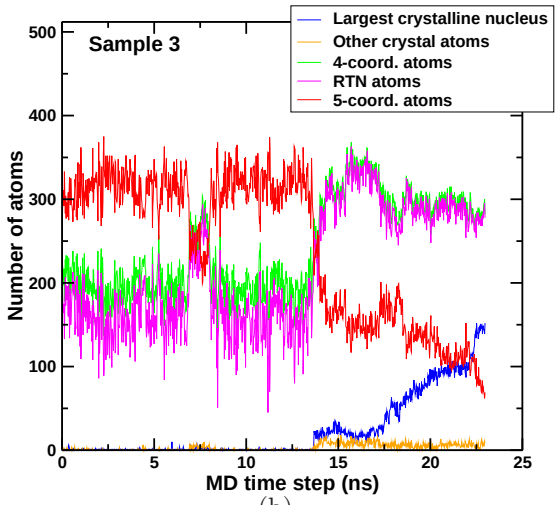

(b)

Figure 5.33: Evolution of different kinds of atoms in two different samples (a) and (b) as the system at $T = 1080$ and $P = 0GPa$ crystallise. Blue represents the atoms belonging to the largest crystalline nucleus, orange represents other crystalline atoms (orange), red represents 5-coordinated atoms or liquid atoms with $q_3 < 0.6$, green represents 4-coordinated atoms or liquid atoms with $q_3 \geq 0.6$ and magenta represents random tetrahedral network forming atoms or RTN atoms.

5.8.2 Analysis of Umbrella Sampling Runs

Using the umbrella sampling MC configurations we have analysed the change in local density in the surrounding regions of the crystalline nucleus. Since in an umbrella sampling MC scheme we can bias the system to sample a particular size of the crystalline nucleus we can obtain better statistics of quantities which were analysed in the previous section, at different stages (pre-critical, critical and post-critical) crystallisation process. Note that all the umbrella sampling MC simulations were performed with a system size of 4000 atoms.

To perform local density analysis we first recognize the center of mass of the largest crystalline nucleus and the boundary of the of the crystalline nucleus. We assume the crystalline nucleus to be spherical and define the boundary as the distance between the centre of mass and the farthest crystalline atom in the nucleus. We count the number of crystalline atoms (n_c), LDL atoms (n_{ldl}) and HDL atoms (n_{hdl}) within a shell of volume dV at a distance r from the center of mass and hence obtain local density as

$$\begin{aligned} \rho_c &= n_c/dV \\ \rho_{ldl} &= n_{ldl}/dV \\ \rho_{hdl} &= n_{hdl}/dV \end{aligned} \tag{5.12}$$

Spontaneously crystallised samples we analysed were at state points corresponding to $T = 1055K$, $T = 1080K$ and $T = 1080K$ along $P = 0GPa$ isobar. We now analyse $T = 1108K$ and $T = 1196K$ along $P = 0GPa$ isobar.

We now discuss the results from the local density analysis for $T = 1108K$ and $P = 0GPa$. At this state point the critical nucleus size is around 17-20 atoms and 30% of the system contains 4-coordinated or LDL atoms. The local density analysis is performed for configuration having crystal nucleus of size 9, 20 and 26 atoms. In FIG. 5.34 (a) we show local LDL density (*top panel*) and local HDL density (*bottom panel*) as a function of distance from the center of crystalline nucleus. The orange line in corresponds to the

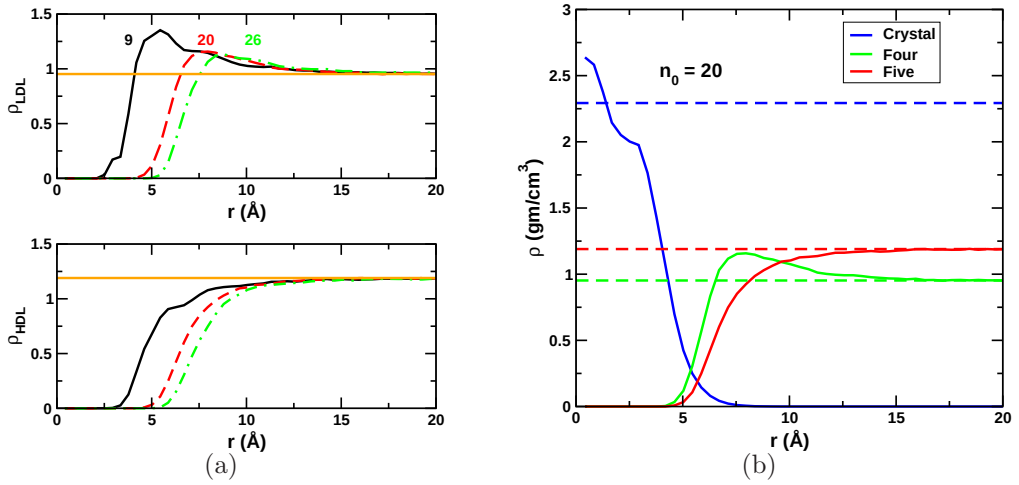

Figure 5.34: (a) Local LDL density (*top panel*) and local HDL density (*bottom panel*) as a function of distance from the center of crystalline nucleus at $T = 1108K$ and $P = 0GPa$ for different n_0 values. (b) Local density of crystalline, LDL and HDL atoms as a function of distance from the center of crystalline nucleus at $T = 1108K$ and $P = 0GPa$ at $n_0 = 20$.

equilibrium density of respective atoms. We find that at all state of crystallisation an excess in local density of LDL atoms near the boundary of the crystalline nucleus. But this wetting layer of LDL atoms starts diminishing as the crystalline nucleus size grow. In FIG. 5.34 (b) we show the local density for all the crystal, LDL and HDL atoms at $n_0 = 20$.

In FIG. 5.35 we show the local density analysis for $T = 1196K$ and $P = 0GPa$. At this state point the critical nucleus size is around 50 atoms and 25% of the system contains 4-coordinated or LDL atoms. At this state point the wetting layer of LDL atoms seems to persist at all stages of nucleation.

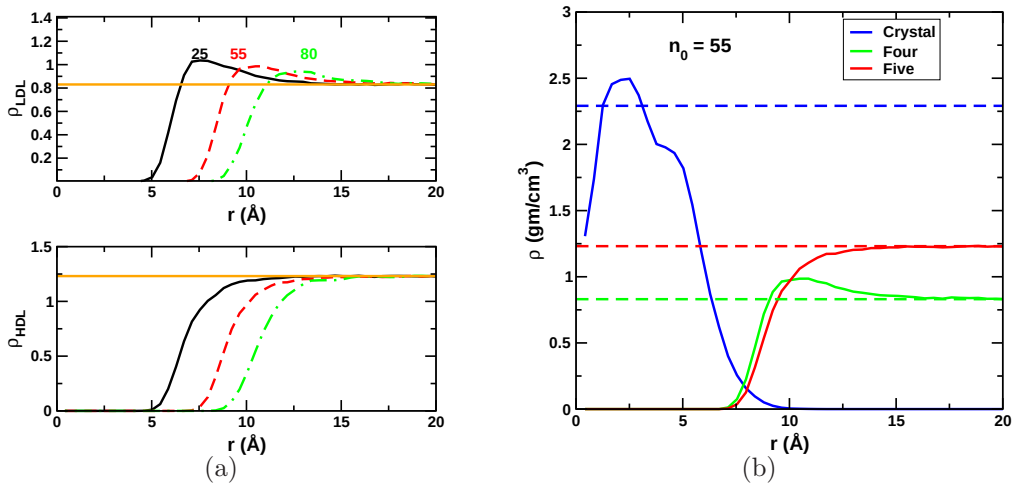

Figure 5.35: (a) Local LDL density (*top panel*) and local HDL density (*bottom panel*) as a function of distance from the center of crystalline nucleus at $T = 1195K$ and $P = 0GPa$ for different n_0 values. (b) Local density of crystalline, LDL and HDL atoms as a function of distance from the center of crystalline nucleus at $T = 1195K$ and $P = 0GPa$ at $n_0 = 55$.

5.9 Summary

In this chapter we have studied the crystal nucleation process in supercooled silicon. From the crystal nucleation barrier calculated across various state point in the phase diagram we find that in the vicinity of LLCP and the Widom line, separating out the influence of density fluctuations and structural arrangement on the nucleation barrier is not possible. Approaching the LLCP and the Widom line from high temperature, we find that the nucleation barrier is of the order of $10k_BT$ and the critical nucleus size is around 10-15 atoms. At the low temperature side of the Widom line, nucleation barrier is of the order of $7k_BT$ and the critical nucleus size is around 7-10 atoms. Analysis of spontaneously crystallising sample at these state points reveal very interesting fact related to the growth of the crystal nucleus. Even though size of critical nucleus is of the order of few atoms the system continuos to be in liquid state due to the presence of RTN cluster. The role of RTN atoms is important as crystallisation rate distinctly depend on the how fast the RTN cluster melts. Local density analysis at moderately high temperatures reveal a wetting layer of LDL atoms surrounding the crystalline nucleus.

Chapter 6

Applicability to Real Silicon

The supercooled phase of silicon has been extensively studied in the past three decades and a vast amount of knowledge has come from computer simulations using the classical Stillinger-Weber (SW) model potential, although there have also been many *ab initio* simulations performed in recent years. Any model interaction potential is parameterised so as to reproduce certain experimentally known properties like phase transition temperature, crystalline structure *etc* and hence it is difficult for a single empirical interaction potential to reproduce a wide range of properties in different phases of matter. Unlike empirical interaction potentials, in *ab initio* simulations the effective atomic interactions are obtained on the fly from quantum mechanical calculations such as Density Functional Theory (DFT) and hence free of parameterisation, although not free of errors arising from necessary approximations involved in such calculations. But, *ab initio* simulations are computationally very expensive and hence it is difficult to access large system sizes and time scales using them. These shortcomings becomes a real bottleneck when one needs to study systems at low temperatures or near a critical point, as is the case with supercooled silicon. Relaxation times increase with the lowering of temperature and also with the approach to a critical point. The spatial correlation in the system increases with the approach to a critical point which makes it necessary to study larger system sizes (though we

must mention that this shortcoming also applies to much of the classical simulation results presented in our work). In the studies involving supercooled phases we have to also confront the issue of crystallisation. Since crystallisation is inherent to a supercooled phase, it is not a feature that can be easily eliminated without introducing artefacts in the sampling. Hence, it may be necessary to perform simulations of multiple independent samples to obtain reasonable information on the metastable states. Given these considerations, in the case of silicon, one must of necessity perform some of the simulations using a classical empirical potential such as the SW potential. It is therefore interesting to see to what extent the liquid state properties evaluated using the SW potential agree with the available first principles and experimental properties.

In this chapter we carry out such a comparison of various properties obtained in the simulations using the SW potential with the available experimental as well as *ab initio* and other model potential results. These comparisons allow us to understand to what extent the SW silicon results are applicable to real silicon. We note that a previous work by Balamane *et al.* [15] compare six different empirical potentials for silicon looking at various properties at $T = 0K$, but very little focus was given to the liquid state of silicon.

The Stillinger-Weber potential is one of the best model potentials for studying the liquid and supercooled liquid phases of silicon, since the parameters of the model potential are chosen explicitly to predict the structural properties of real liquid silicon. However, whether the model faithfully captures temperature as well as pressure variations of thermophysical, structural and dynamic properties is unclear, and one should expect that the results obtained from the simulation will be sensitive to the model parameters. Beaucage and Mousseau [17], based on their study in which they modify the strength of the three body potential (λ), interrogate the finding of a liquid-liquid transition (LLT) in supercooled liquid silicon using the SW potential. In this context, these authors make the following two observations from their simulation (1.) At negative pressures (authors report at $P = -2GPa$) the

system does not show a first order liquid-liquid transition but instead a second order transition is observed (2.) For a small increase in λ (by 5%) the LLT disappears or totally gets hidden by crystallisation. Hence these authors claim that the nature of the transition in SW silicon is highly sensitive to model parameters and therefore no strong claims can be made for what must happen in real silicon based on simulations of the SW potential. From the phase diagram of supercooled liquid silicon which we discussed in detail in previous chapters, it is clear that there is no phase transition at $P = -2GPa$, and examination of well equilibrated data does not reveal any second derivative singularity to suggest a second order transition. In fact the observations like dramatic change in coordination number and diffusivity these authors make is due the crossing of Widom line from high T to low T along the $P = -2GPa$ isobar. Regarding the second point raised by these authors, it is clear that a change in model parameters will change the phase diagram. Importantly, a shift by 5% in the value of λ changes the LLT temperature to higher values [111], to about $T = 1390K$ at which Beaucage and Mousseau see crystallisation. In our work (*Crystal Nucleation* chapter) we show that the crystal nucleation barrier and the size of critical nucleus decreases dramatically when the transition boundary to the low density liquid (LDL) is crossed. Hence it is not surprising that crystallisation is observed at an elevated temperature compared to the normal SW parameters. In the FIG. 6.1 we have shown the phase diagram of supercooled silicon (including the LLT points [111], the density maxima and compressibility maxima at zero pressure) for two different values of λ (20.5 and 21.5) along with $\lambda = 21.0$ (for silicon). With a small increase in λ the phase diagram shift towards the high temperature (and higher pressure) but the salient features of the phase diagram do not change. In the FIG. 6.2 we show the change in density with temperature for different values of λ. A detailed work on change in nucleation rates with strengthening or weakening of λ will shed more light on what Beaucage and Mousseau observe, but clearly, the qualitative features of the phase diagram including the LLT remain intact even with a change in parameters.

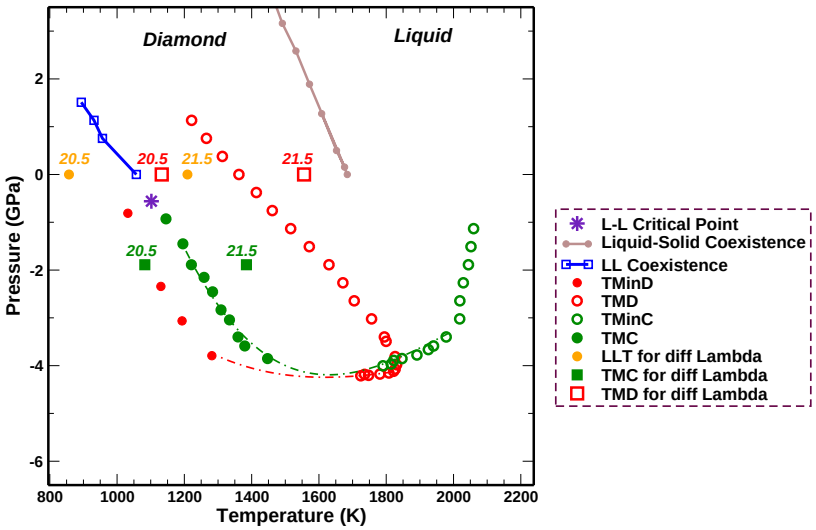

Figure 6.1: Phase diagram of supercooled silicon (in PT plane) at $\lambda = 20.5, 21.0(Si)$ and 21.5 from MD simulations using the SW potential. The liquid-liquid transition data [111] are shown in orange circles, the density maxima point are shown in bold red squares and compressibility maxima points are shown in bold opaque green squares. The values of λ are stated over the symbols.

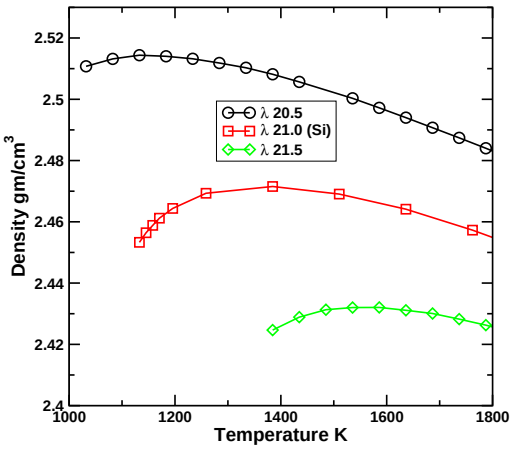

Figure 6.2: Density against temperature for three different values of λ from NPT MD simulations using the SW potential.

To evaluate the reliability of the SW potential for silicon, we examine the extent to which there is an agreement between the properties obtained from SW silicon and from experiments or first principles simulations. Such a comparison is made here on the basis of an extensive literature search of experiments, first principles simulations and other empirical potential simulations performed on liquid silicon. We compare results for density (ρ), structure factor ($S(q)$), radial distribution function ($g(r)$), diffusivity (D) and viscosity (η) obtained from various reports with the SW silicon data.

Before we go in to the details we would like to mention that the criterion for choosing the simulation works for the comparison is solely based on the reported temperature range ($T = 1100K$ to $1700K$).

Density: We have extracted the densities at normal pressure from the experimental reports of Langen *et al.* (1998) [91], Egry (1999) [50], Sato *et al.* (2000) [145], Rhim (2000) [130], Higuchi *et al.* (2005) [69], Inatomi *et al.* (2007) [73] and Watanabe *et al.* (2007) [182]. We have used the simulation data reported by Keblinski *et al.* (2002) [81] using the environment dependent interaction potential, Morishita (2006) [117] using *ab initio* simulation and Timonova *et al.* (2010) [104] using the MEAM potential. We show the comparison of densities from different reports in FIG. 6.3 and we infer the following points:

1. The differences within different experimental values of density are large. All the experiments (within error bar) show monotonically increasing density with decrease in temperature till the lowest reported temperature of measurement [130] and hence density anomaly is not yet experimentally verified.

2. The SW potential considerably underestimates the densities. However it is comparatively better than other estimates from other classical empirical potentials [81, 104]. The density maximum as predicted by SW potential at zero pressure is at $T = 1350K$. The EDIP simulations estimate for the density maximum is $T = 1300K$ and the MEAM potential estimates at $T = 2500K$.

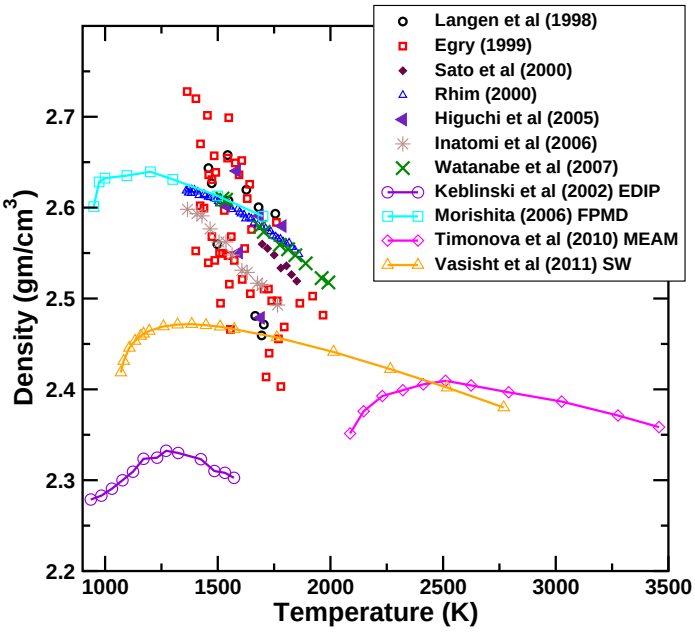

Figure 6.3: Compilation of density against temperature from different experiments and simulations. The experimental data are represented by symbols and the simulation data are represented by line and symbol. [From Langen *et al.* [91], Egry [50], Sato *et al.* [145], Rhim [130], Higuchi *et al.* [69], Inatomi *et al.* [73] and Watanabe *et al.* [182], Keblinski *et al.* [81], Morishita [117] and Timonova *et al.* [104] with permission.]

3. Estimates of density from *ab initio* simulations compare better with the experimentally measured values. The density maximum as predicted by FPMD simulation is at $T = 1200K$.

Structure factor $S(q)$ and Pair correlation function $g(r)$: In experiments S(q) is measured using various scattering techniques. The Fourier transform of S(q) yields g(r). From our literature search we find that agreement between experiments and simulations is as good (or bad) as the agreement between different experiments. We also find that agreement between experiments and MD simulations using the SW potential is as good as between experiments and first principles simulations. A detailed comparison of S(q) and g(r) is discussed below.

At normal pressures, experimental investigations have measured S(q) down to $1382K$ [84] and not below. For $T = 1382K$ we compare the SW simulation data with the experimental data extracted from Kim *et al.* (2005) [84]. Between $T = 1447K$ to $1667K$ we compare the SW simulation data with experimental data extracted from Waseda *et al.* (1995) [181], Ansell *et al.* (1998) [9], Kimura *et al.* (2001) [85], Jakse *et al.* (2003) [75], Higuchi *et al.* (2005) [69], Kim *et al.* (2005) [84], Watanabe *et al.* (2007) [182], Krishnan *et al.* (2007) [86]. Comparison with FPMD and other empirical potential simulations is made from the data extracted from Jakse *et al.* (2003) [75], Morishita (2006) [117], Wang *et al.* (2011) [180] and Colakogullari *et al.* (2011) [27].

We show the comparison of S(q) obtained from SW simulation and experiments in the FIG. 6.4. and comparison between different simulations is shown in the FIG. 6.5. We use the recent experimental S(q) of Krishnan *et al.* (2007) [86] as a reference for comparing with different simulations results. Following are our observations.

1. The differences in S(q) among different experimental reports as well as among different FPMD simulations are significant.

2. Even though all the experimental data (except Ansell *et al.* [9] at T 1542 K) show similar trends, we find a noticeable difference in the amplitudes of S(q). The trend captured by *ab initio* simulations is similar to that of SW simulations.

3. The feature of split peaks is seen in both *ab initio* and SW simulation. But in comparison with experiments, it seems that *ab initio* simulation

captures better the first peak and the SW potential captures better the second peak of S(q).

4. The minima and maxima of $S(q)$ for $q > 4$ Å^{-1} is well captured by the SW potential.

5. The ratio of the first peak to the second peak is better captured by SW potential than by the *ab initio* simulations.

We now focus on radial distribution function obtained from experiments and simulations (shown in FIG. 6.6 and 6.7) and note the following points:

1. The most noticeable feature is the difference in the first minimum of g(r) within different experiments. The coordination number is very sensitive to the location of the first minimum of g(r). The results from Jakse *et al.* [75] and Krishnan *et al.* [86] are consistent with each other and shows the minimum of g(r) at around 3.3Å. The results from Kim [84] shows the minimum is at around 3Å.

2. Both *ab initio* and SW simulations have the first minimum of g(r) at around 3Å(except for Wang *et al.* [180] which shows the first minimum of g(r) at 3.3Å).

3. The second important difference is in the amplitude of the first peak of g(r). Both *ab initio* and SW simulations have similar amplitudes of and are bigger than the observed amplitudes in experiments.

4. The intermediate peak between the first and the second prominent peak of g(r) as reported by Kim [84] is not found in the experiments of Jakse [75] and Krishnan [86]. But it is a prominent feature in both *ab initio* and SW simulations.

5. For $r > 3.5$Å(second and higher peaks), the g(r) from SW simulations compare better with the results of Kim *et al.* [84] than the *ab initio* results. Results from SW and *ab initio* simulations are less consistent with the experimental results reported by Jakse [75] and Krishnan *et al.* [86].

A comparison of S(q) and g(r) at $T = 1328K$, the lowest temperature experimentally achieved [84], is shown in FIG. 6.4 (a) and 6.6 (a). We find that even though there are differences in the amplitudes of the peaks of S(q) and g(r), the SW potential captures all the salient features found in the experimental results of Kim *et al.* [84].

High pressure S(q) and g(r): In FIG. 6.8 and FIG. 6.9 we compare the SW simulation data with experimental S(q) and g(r) [57] at three different high pressure values at $T = 1737K$. We find that at $P = 4GPa$, the SW simulation data compare reasonably well with experimental data. But at around $P = 14GPa$ the SW potential fails to capture the experimental S(q) and g(r).

From the above comparisons we find that there are noticeable differences between the structural properties (characterised by S(q) and g(r)) obtained in different experiments as well as from different simulations. We find from the comparison of simulation results with experiments, that the SW potential does as good a job as the *ab initio* simulations. At high pressure values ($P \sim 14GPa$) the SW potential fails to capture the details of experimental S(q) and g(r).

Coordination number: The coordination number C_{nn} is calculated by integrating the $g(r)$ till its first minimum (r_c) using the equation $C_{nn} = \int_0^{r_c} 4\pi r^2 \rho g(r) dr$. Hence the most important inputs that goes into the calculation of the C_{nn} are r_c and density of the liquid. The differences in g(r) and densities between the experiments and simulations will reflect in the differences we find in the calculated C_{nn} as it can seen in the FIG. 1.7. To illustrate how much the coordination numbers from the SW potential are affected by the underestimation of density, we have also shown (*see* FIG. 1.7) the coordination numbers calculated using the densities obtained from the experimental density values (Rhim *et al.* [130]).

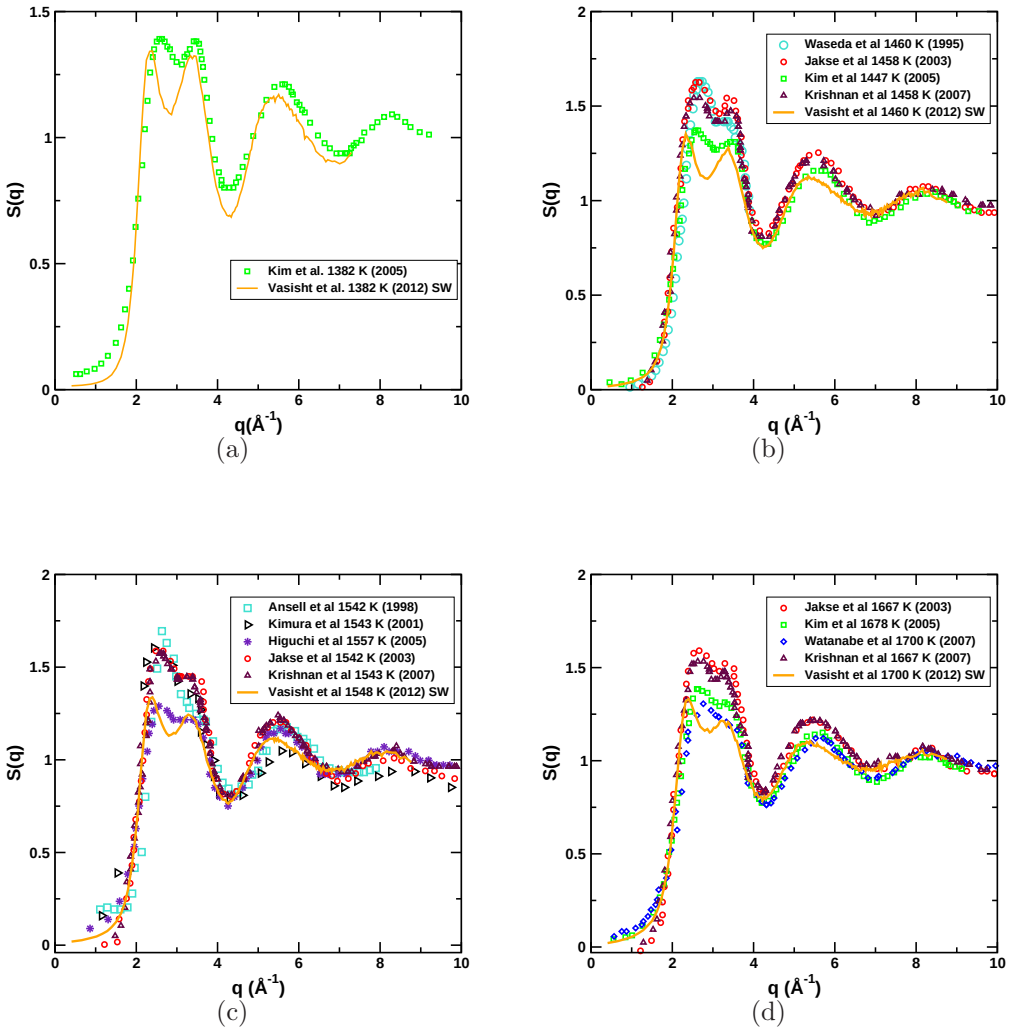

Figure 6.4: Comparison of the structure factor S(q) from NPT MD simulations using the SW potential and from experiments at four different temperatures, $T = 1382K$, $T \approx 1455K$, $T \approx 1550K$ and $T \approx 1770K$. [From Waseda *et al.* [181], Ansell *et al.* [9], Kimura *et al.* [85], Jakse *et al.* [75], Higuchi *et al.* [69], Kim *et al.* [84], Watanabe *et al.* [182], Krishnan *et al.* [86] with permission.]

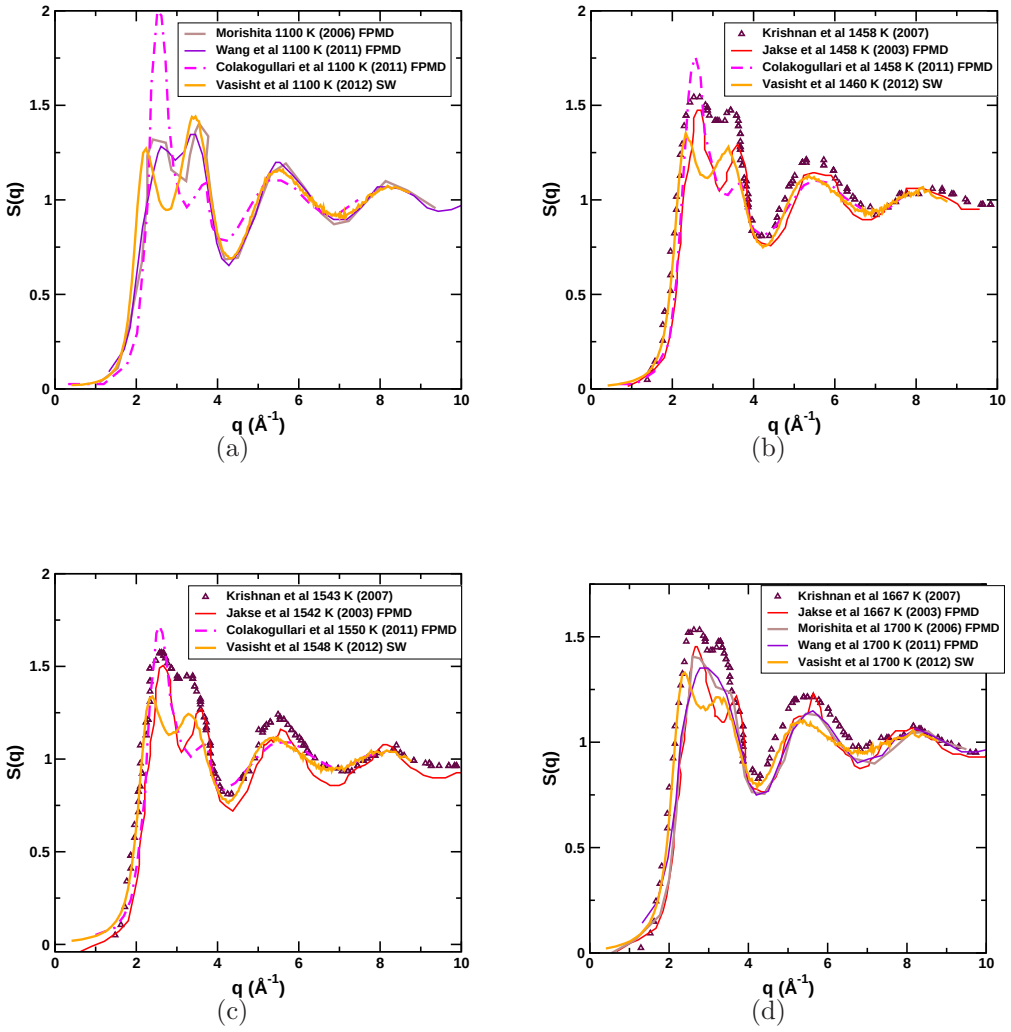

Figure 6.5: Comparison of the structure factor S(q) from different simulation works at four different temperatures, $T = 1100K$, $T \approx 1455K$, $T \approx 1550K$ and $T \approx 1700K$. We also show the recent experimental S(q) measurements for comparison purposes. [From Krishnan *et al.* [86], Jakse *et al.* [75], Morishita [117], Wang *et al.* [180] and Colakogullari *et al.* [27] with permission.]

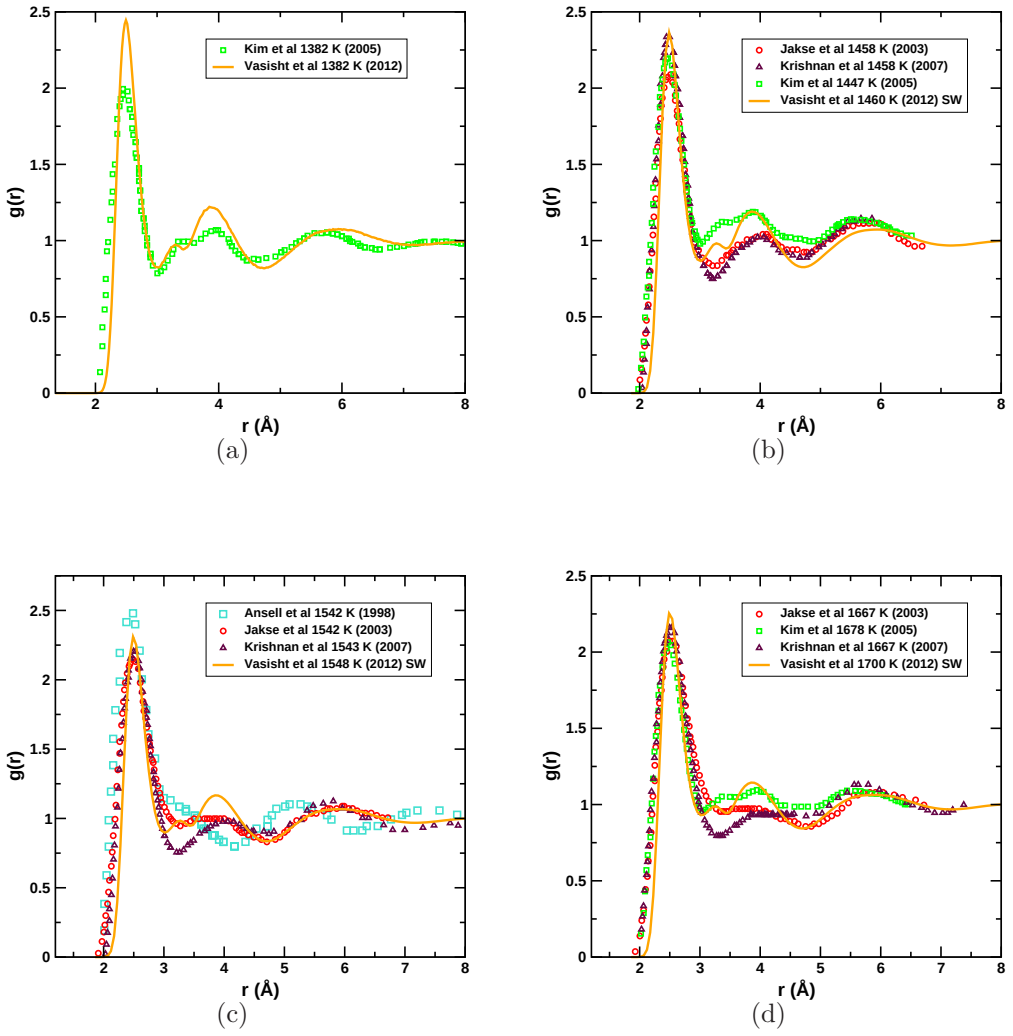

Figure 6.6: Comparison of the pair correlation function g(r) from NPT MD simulations using the SW potential and from experiments at four different temperatures, $T = 1382K$, $T \approx 1455K$, $T \approx 1550K$ and $T \approx 1770K$. [From Ansell *et al.* [9], Jakse *et al.* [75], Kim *et al.* [84], Krishnan *et al.* [86] with permission.]

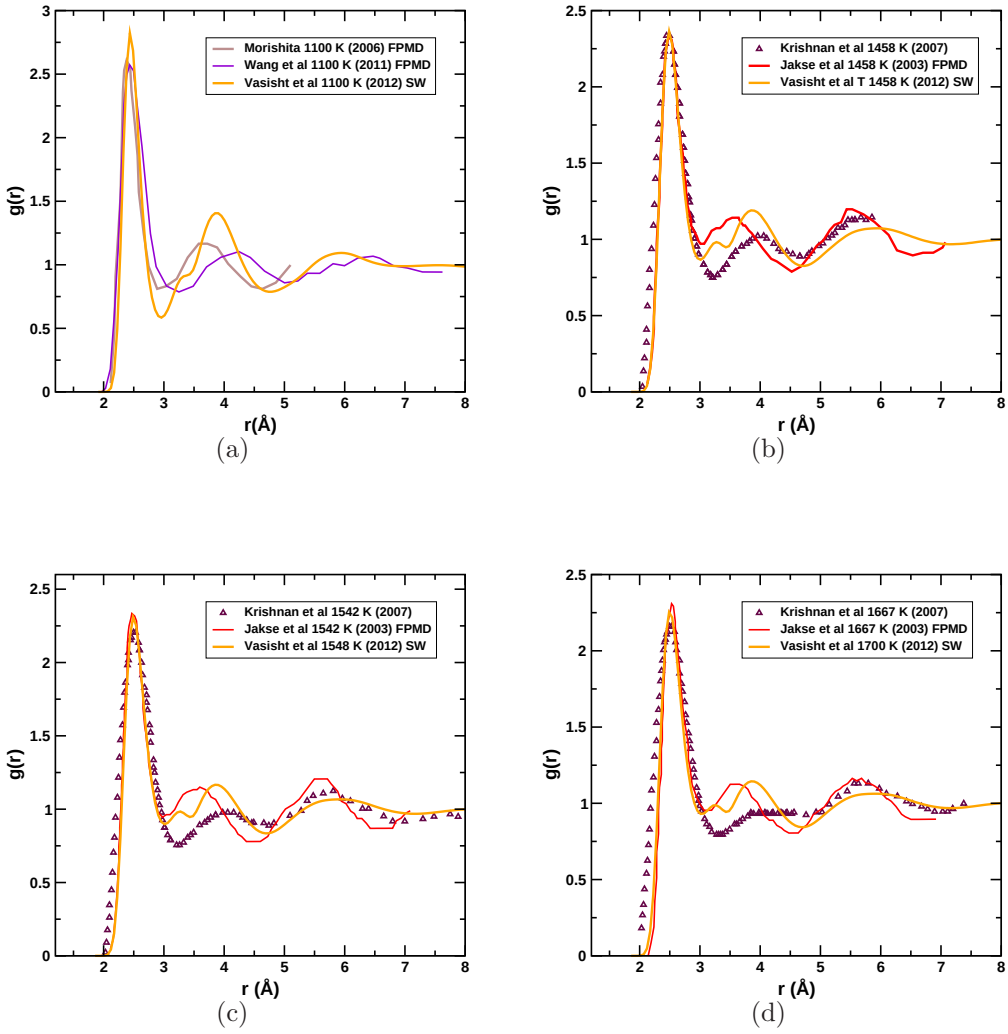

Figure 6.7: Comparison of the pair correlation function g(r) from different simulation works at four different temperatures, $T = 1100K$, $T \approx 1455K$, $T \approx 1550K$ and $T \approx 1700K$. We also show the recent experimental g(r) measurements for comparison purposes. [From Krishnan *et al.* [86], Jakse *et al.* [75], Morishita [117], Wang *et al.* [180] and Colakogullari *et al.* [27] with permission.]

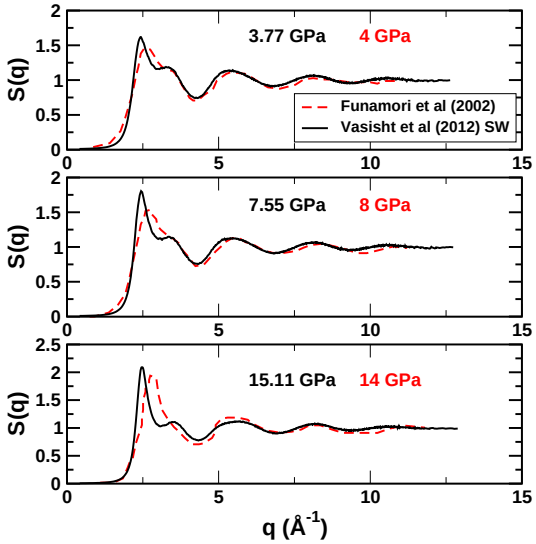

Figure 6.8: Comparison of the structure factor S(q) from NPT MD simulations using the SW potential with the experimental data at high pressure values for $T = 1737K$. [From Funamori *et al.* [57] with permission.]

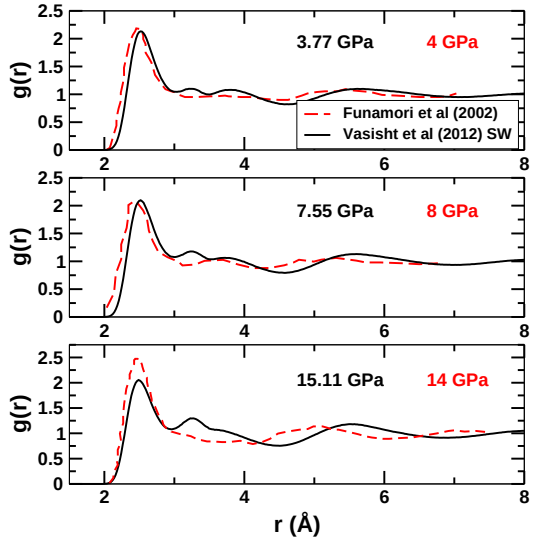

Figure 6.9: Comparison of the pair correlation function g(r) from NPT MD simulations using the SW potential with the experimental data at high pressure values for $T = 1737K$. [From Funamori *et al.* [57] with permission.]

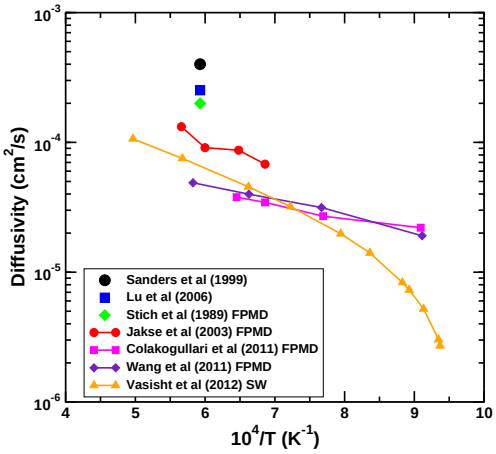

Figure 6.10: Compilation of Diffusivity against inverse temperature as reported by different experimental reports, first principle MD (FPMD) simulations along with the simulation results using the SW potential. [From Stich *et al.* [173], Jakse *et al.* [75], Colakogullari *et al.* [27], Wang *et al.* [180], Sanders *et al.* [136], Lu *et al.* [98] with permission.]

Diffusivity and Viscosity: In the FIG. 6.10 we show the comparison of temperature dependence of diffusivity (at normal pressure) reported by various simulation and experimental reports. We could only find experimental report of diffusivity at T_m (Sanders *et al.* [136] and Lu *et al.* [98]) and we show them in our comparison. The FPMD data was extracted from the reports of Stich *et al.* [173], Jakse *et al.* [75], Colakogullari *et al.* [27] and Wang *et al.* [180]. From our comparison we find that only FPMD simulation of Stich *et al.* [173] predict the diffusivity close to the experimental data. All other FPMD as well as SW simulation estimates of diffusivity (at T_m) is smaller than the experimental value. We find that the SW simulation data is comparable with the FPMD data only down to $T = 1250K$.

In the FIG. 6.11 we compare the experimentally determined viscosity values with that of the SW potential estimates. The experimental data was extracted from the report of Rhim *et al.* [130] (in which we also find the viscosity data of Sasaki *et al.* and Sato *et al.*). Similar to diffusivity we find that SW under estimates the η compared to experimental values.

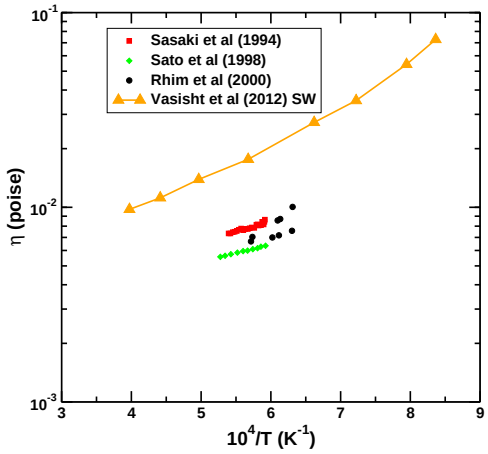

Figure 6.11: Compilation of Viscosity against inverse temperature as reported by different experimental reports along with the simulation results using the SW potential. [From Rhim *et al.* [130] with permission.]

6.1 Summary

In this section, we have compared thermodynamic (density), structural and dynamical properties of liquid silicon, obtained from various reports from experiments, first principle simulations and other model potential simulations with our data obtained from simulations using the SW potential for silicon. We find that the SW potential, while displaying significant differences with experimental data for the quantities we have discussed here, does so within deviations that are comparable to the spread between different experimental results, and these differences are comparable to those displayed by first principles simulation results. For the different quantities compared the summary of observations are as follows:

1. There are noticeable differences in structure factors and radial distribution functions reported by different experimental groups.

2. The density values reported by different experimental groups have a variation of about 10%.

3. The coordination numbers calculated are very sensitive to the location

of the first minima of g(r) and the density. There is a large spread in the coordination numbers reported by different experimental groups, between 5 and 6.5.

4. The first principles simulation estimates of S(q), g(r) and diffusivity do not show any better agreement with experiments than SW simulations.

5. The SW potential underestimates the density by 5%, which leads to lower estimates of the coordination number by 4%. Even then these numbers are within the error bars of reported experimental data.

6. The SW potential estimates of diffusivity (which is comparable to the first principle simulations) is approximately a factor of 4 less than the experimental value and viscosity is approximately a factor of 3 higher than the experimental value.

It is evident that the most significant shortcoming of the SW potential appears to be in the estimates of the density. Given the detailed understanding of the SW potential, it may be interesting to fine tune the potential by varying the strength of the three body interactions and the range of interactions, which is a useful future direction to pursue.

Chapter 7

Conclusions

We present in this chapter the main conclusion drawn from our studies on the phase behaviour of supercooled liquid silicon. In our study we have primarily focused on three topics of interest namely (1.) liquid-liquid transition, critical point and phase behaviour, (2.) structural and dynamic properties and (3.) crystal nucleation.

The phase behaviour of supercooled liquid silicon studied in *chapter 3*, we provide an evidence for existence of liquid-liquid critical point associated with the liquid-liquid transition. We chart out the complete phase diagram of supercooled liquid silicon which includes (a) liquid-liquid coexistence line (LLT), (b) liquid-liquid critical point, (c) loci of density extrema, (d) loci of compressibility extrema and (e) liquid spinodal. We find that the phase behaviour of silicon is very similar to that of water. This similarity in the phase behaviour is interesting for the fact that both liquids belong to the class of network forming liquids. A careful analysis of the free energy landscape, and finite size analysis would an important study to be pursued.

An elaborate analysis of structural and dynamical properties of liquid and supercooled liquid silicon presented in the *chapter 4* provides insights into the evolution of the liquid as we go deeper in to the metastable region. Approaching the LLT line or the Widom line from the high temperature liquid state, change the system's coordination number from 6 in the high T liquid to 5 in the high density supercooled liquid to 4 in the low density supercooled liquid

(LDL) is observed. From the analysis of dynamical properties including diffusivity, relaxation time and viscosity in the same range of temperatures, we find that the dynamics of the system changes by four order of magnitude. We find a strong correlation between the local structural arrangement (quantified by coordination number) and the dynamics of the system. Analysis of local structural order reveals formation of Random Tetrahedral Network (RTN) of low density liquid atoms. The cluster of RTN atoms grows with lowering of temperature and spans the whole system approaching the LLT line or the Widom line. The presence of RTN clusters leads to anomalous behaviour in density. We also show that in silicon there is a hierarchy in thermodynamic, dynamic and structural region of anomaly, similar to silica and water. Our study of the breakdown of the Stokes-Einstein relation shows that the locus the breakdown temperature is closely related to the onset of slow dynamics in the system and also the growth of RTN clusters. Analysis of local dynamics within the RTN clusters would shed more light on the SE relation and its breakdown.

Analysis of the crystal nucleation barriers and the mechanism of nucleation presented in the *chapter 5* looked at crystallisation process in supercooled silicon. Employing the umbrella sampling MC simulation, nucleation free energy barriers were computed across the phase diagram. The free energy barrier varies from around $60k_BT$ at the around 23% undercooling to $7-10k_BT$ at around 37% undercooling. In the same range of undercooling the critical nucleus size was found to vary between 150 atoms to $7-15$ atoms. Up on approaching the liquid-liquid critical point or the Widom line from the high temperature, the nucleation barrier is found to be of the order of $10k_BT$ and critical nucleus size is of the order of $10-15$ particles. Analysis of nucleation mechanism in the spontaneously crystallising samples as well as the umbrella sampling configurations reveal a preliminary evidence of two step nucleation process in high density liquid phase (HDL). Obtaining free energy barrier associated with LDL to crystal and HDL to crystal transformation along with free energy landscape as a function of two order parameters (density and structural order) would provide a clear evidence for two step nucleation in supercooled silicon.

Bibliography

[1] Aasland, S. & McMillan, P. F. 1994 Density-driven liquid-liquid phase separation in the system $AI_2O_3 - Y_2O_3$ *Nature* **369**, 633–636.

[2] Abascal, J. L. F. & Vega, C. 2010 Widom line and the liquid-liquid critical point for the TIP4P/2005 water model *The Journal of Chemical Physics* **133(23)**, 234502.

[3] Allen, R., Warren, P. & Ten Wolde, P. 2005 Sampling rare switching events in biochemical networks *Physical Review Letters* **94(1)**, 18104.

[4] Angell, C. 2008 Insights into phases of liquid water from study of its unusual glass-forming properties *Science* **319(5863)**, 582.

[5] Angell, C., Borick, S. & Grabow, M. 1996 Glass transitions and first order liquid-metal-to-semiconductor transitions in 4-5-6 covalent systems *Journal of Non-Crystalline Solids* **205207, Part 2(0)**, 463 – 471.

[6] Angell, C. A., Bressel, R. D., Hemmati, M., Sare, E. J. & Tucker, J. C. 2000 Water and its anomalies in perspective: tetrahedral liquids with and without liquid liquid phase transitions *Physical Chemistry Chemical Physics (Incorporating Faraday Transactions)* **2**, 1559–1566.

[7] Angell, C. A., Poole, P. H. & Shao, J. 1994 Glass-forming liquids, anomalous liquids, and polyamorphism in liquids and biopolymers *Il Nuovo Cimento D* **16(8)**, 993–1025.

[8] Angell, C. A., Sichina, W. J. & Oguni, M. 1982 Heat capacity of water at extremes of supercooling and superheating *The Journal of Physical Chemistry* **86(6)**, 998–1002.

[9] Ansell, S., Krishnan, S., Felten, J. & Price, D. 1998 Structure of supercooled liquid silicon *Journal of Physics: Condensed Matter* **10**, L73.

[10] Aptekar, L. I. Phase transitions in noncrystalline germanium and silicon in *Soviet Physics Doklady* vol. 24 1979.

[11] Ashwin, S. S., Waghmare, U. V. & Sastry, S. 2004 Metal-to-Semimetal transition in supercooled liquid silicon *Physical Review Letters* **92(17)**, 175701.

[12] Auer, S. 2002 Quantitative prediction of crystal nucleation rates for spherical colloids: A computational study *Ph.D. Thesis* .

[13] Auer, S. & Frenkel, D. 2001 Prediction of absolute crystal-nucleation rate in hard-sphere colloids *Nature* **409(6823)**, 1020–1023.

[14] Bagley, B. G. & Chen, H. S. A calculation of the thermodynamic first order amorphous semiconductor to metallic liquid transition temperature in *American Institute of Physics Conference Series* vol. 50 of *American Institute of Physics Conference Series* 1979.

[15] Balamane, H., Halicioglu, T. & Tiller, W. A. 1992 Comparative study of silicon empirical interatomic potentials *Physical Review B* **46**, 2250–2279.

[16] Baranyai, A. & Evans, D. J. 1989 Direct entropy calculation from computer simulation of liquids *Physical Review A* **40**, 3817–3822.

[17] Beaucage, P. & Mousseau, N. 2005 Liquid liquid phase transition in Stillinger Weber silicon *Journal of Physics: Condensed Matter* **17**, 2269–2279.

[18] Beaucage, P. & Mousseau, N. 2005 Nucleation and crystallization process of silicon using the stillinger-weber potential *Physical Review B* **71(9)**, 094102.

[19] Becker, S., Poole, P. & Starr, F. 2006 Fractional stokes-einstein and debye-stokes-einstein relations in a network-forming liquid *Physical Review Letters* **97(5)**, 55901.

[20] Beye, M., Sorgenfrei, F., Schlotter, W. F., Wurth, W. & Fhlisch, A. 2010 The liquid-liquid phase transition in silicon revealed by snapshots of valence electrons *Proceedings of the National Academy of Sciences* **107(39)**, 16772–16776.

[21] Biswas, R. & Hamann, D. 1985 Interatomic potentials for silicon structural energies *Physical Review Letters* **55(19)**, 2001–2004.

[22] Bolhuis, P., Chandler, D., Dellago, C. & Geissler, P. 2002 Transition path sampling: Throwing ropes over rough mountain passes, in the dark *Annual Review of Physical Chemistry* **53(1)**, 291–318.

[23] Borick, S. S., Debenedetti, P. G. & Sastry, S. 1995 A lattice model of network-forming fluids with orientation-dependent bonding: equilibrium, stability, and implications for the phase behavior of supercooled water *The Journal of Physical Chemistry* **99(11)**, 3781–3792.

[24] Broughton, J. Q. & Li, X. P. 1987 Phase diagram of silicon by molecular dynamics *Physical Review B* **35**, 9120–9127.

[25] Brovchenko, I. & Oleinikova, A. 2008 Multiple phases of liquid water. *ChemPhysChem A European Journal Of Chemical Physics And Physical Chemistry* **9(18)**, 2660–2675.

[26] Brown, D. & Clarke, J. H. R. 1984 A comparison of constant energy, constant temperature and constant pressure ensembles in molecular dynamics simulations of atomic liquids *Molecular Physics* **51**, 1243–1252.

[27] Çolakogullari, M., Dalgiç, S., González, L. E. & González, D. J. 2011 An investigation of the local structure and dynamic properties of undercooled liquid silicon using the orbital-free ab-initio molecular dynamics method *European Physical Journal Special Topics* **196**, 45–52.

[28] Chen, H. S. & Turnbull, D. 1969 Specific heat and heat of crystallization of amorphous germanium *Journal of Applied Physics* **40**, 4214–4215.

[29] Chen, S., Mallamace, F., Mou, C., Broccio, M., Corsaro, C., Faraone, A. & Liu, L. 2006 The violation of the stokes–einstein relation in supercooled water *Proceedings of the National Academy of Sciences* **103(35)**, 12974.

[30] Cook, S. J. & Clancy, P. 1993 Comparison of semi-empirical potential functions for silicon and germanium *Physical Review B* **47**, 7686–7699.

[31] Correa, A., Bonev, S. & Galli, G. 2006 Carbon under extreme conditions: phase boundaries and electronic properties from first-principles theory *Proceedings of the National Academy of Sciences* **103(5)**, 1204.

[32] Corti, D. & Debenedetti, P. 1994 A computational study of metastability in vapor–liquid equilibrium *Chemical Engineering Science* **49(17)**, 2717–2734.

[33] Cuthbertson, M. J. & Poole, P. H. 2011 Mixture like behavior near a liquid-liquid phase transition in simulations of supercooled water *Physical Review Letters* **106(11)**, 115706.

[34] Daisenberger, D., Deschamps, T., Champagnon, B., Mezouar, M., R., Q. C., Wilson, M. & McMillan, P. F. 2011 Polyamorphic amorphous silicon at high pressure: Raman and spatially resolved x-ray scattering and molecular dynamics studies *The Journal of Physical Chemistry B* **115(48)**, 14246–14255.

[35] Daisenberger, D., Wilson, M., McMillan, P. F., Quesada Cabrera, R., Wilding, M. C. & Machon, D. 2007 High-pressure X-ray scattering and computer simulation studies of density-induced polyamorphism in silicon *Physical Review B* **75(22)**, 224118.

[36] D'Antonio, M. C. & Debenedetti, P. G. 1987 Loss of tensile strength in liquids without property discontinuities: A thermodynamic analysis *The Journal of Chemical Physics* **86**, 2229–2235.

[37] De Gennes, P. G. 1959 Liquid dynamics and inelastic scattering of neutrons *Physica* **25(7-12)**, 825–839.

[38] de Oliveira, A. B., Franzese, G., Netz, P. A. & Barbosa, M. C. 2008 Waterlike hierarchy of anomalies in a continuous spherical shouldered potential *The Journal of Chemical Physics* **128(6)**, 064901.

[39] Deb, S. K., Wilding, M., Somayazulu, M. & McMillan, P. F. 2001 Pressure-induced amorphization and an amorphous-amorphous transition in densified porous silicon *Nature* **414**, 528–530.

[40] Debenedetti, P. *Metastable liquids: concepts and principles* Physical Chemistry Princeton University Press, 1996.

[41] Debenedetti, P. & DAntonio, M. 1986 On the nature of the tensile instability in metastable liquids and its relationship to density anomalies *The Journal of Chemical Physics* **84**, 3339.

[42] Debenedetti, P. G. 2003 TOPICAL REVIEW: Supercooled and glassy water *Journal of Physics: Condensed Matter* **15**, 1669.

[43] Debenedetti, P. G. & D'Antonio, M. C. 1988 Stability and tensile strength of liquids exhibiting density maxima *AIChE Journal* **34**, 447–455.

[44] Desgranges, C. & Delhommelle, J. 2011 Role of liquid polymorphism during the crystallization of silicon *Journal of the American Chemical Society* .

[45] Donovan, E. P., Spaepen, F., Turnbull, D., Poate, J. M. & Jacobson, D. C. 1983 Heat of crystallization and melting point of amorphous silicon *Applied Physics Letters* **42**, 698–700.

[46] Donovan, E. P., Spaepen, F., Turnbull, D., Poate, J. M. & Jacobson, D. C. 1985 Calorimetric studies of crystallization and relaxation of amorphous Si and Ge prepared by ion implantation *Journal of Applied Physics* **57**, 1795–1804.

[47] Dyre, J. 2006 Colloquium: The glass transition and elastic models of glass-forming liquids *Reviews of Modern Physics* **78(3)**, 953–972.

[48] E.G., P. & O.I., B. 1992 Pressureinduced amorphous phases *Materials Science Reports* **8(4)**, 147 – 191.

[49] Egelstaff, P., Egelstaff, P., Egelstaff, P. & Physicist, G. *An introduction to the liquid state* vol. 162 Academic Press London, 1967.

[50] Egry, I. 1999 Structure and properties of levitated liquid metals *Journal of Non-Crystalline Solids* **250**, 63–69.

[51] Ekdawi-Sever, N., Conrad, P. & de Pablo, J. 2001 Molecular simulation of sucrose solutions near the glass transition temperature *The Journal of Physical Chemistry A* **105(4)**, 734–742.

[52] Errington, J. & Debenedetti, P. 2001 Relationship between structural order and the anomalies of liquid water *Nature* **409(6818)**, 318–321.

[53] Errington, J. R., Truskett, T. M. & Mittal, J. 2006 Excess-entropy-based anomalies for a waterlike fluid *The Journal of Chemical Physics* **125(24)**, 244502.

[54] Findenegg, G., Jahnert, S., Akcakayiran, D. & Schreiber, A. 2008 Freezing and melting of water confined in silica nanopores *ChemPhysChem A European Journal Of Chemical Physics And Physical Chemistry* **9(18)**, 2651–2659.

[55] Franzese, G., Marqués, M. & Stanley, H. E. 2003 Intramolecular coupling as a mechanism for a liquid-liquid phase transition *Physical Review E* **67(1)**, 011103.

[56] Frenkel, D. & Smit, B. 2002 Understanding molecular simulation, 2nd Ed. *Academic press* .

[57] Funamori, N. & Tsuji, K. 2002 Pressure-induced structural change of liquid silicon *Physical Review Letters* **88(25)**, 255508.

[58] Galkin, O. & Vekilov, P. 2000 Control of protein crystal nucleation around the metastable liquid–liquid phase boundary *Proceedings of the National Academy of Sciences* **97(12)**, 6277–6281.

[59] Ganesh, P. & Widom, M. 2009 Liquid-liquid transition in supercooled silicon determined by first-principles simulation *Physical Review Letters* **102(7)**, 075701.

[60] Ganesh, P. & Widom, M. 2011 First-principles coexistence simulations of supercooled liquid silicon *Journal of Non-Crystalline Solids* **357**, 442–445.

[61] Garcez, K. M. S. & Antonelli, A. 2011 Pressure effects on the transitions between disordered phases in supercooled liquid silicon *The Journal of Chemical Physics* **135(20)**, 204508.

[62] Gasser, U., Weeks, E., Schofield, A., Pusey, P. & Weitz, D. 2001 Real-space imaging of nucleation and growth in colloidal crystallization *Science* **292(5515)**, 258–262.

[63] Ghiringhelli, L. M. & Meijer, E. J. 2007 Simulating the phosphorus fluid liquid phase transition up to the critical point *Journal of Physics: Condensed Matter* **19**, 6104.

[64] Ghiringhelli, L. M., Valeriani, C., Meijer, E. J. & Frenkel, D. 2007 Local structure of liquid carbon controls diamond nucleation *Physical Review Letters* **99(5)**, 055702.

[65] Glosli, J. & Ree, F. 1999 Liquid-liquid phase transformation in carbon *Physical Review Letters* **82(23)**, 4659–4662.

[66] Hansen, J. & McDonald, I. *Theory of simple liquids* Academic press, 2006.

[67] Harrington, S., Poole, P. H., Sciortino, F. & Stanley, H. E. 1997 Equation of state of supercooled water simulated using the extended simple point charge intermolecular potential *The Journal of Chemical Physics* **107**, 7443–7450.

[68] Hedler, A., Klaumünzer, S. L. & Wesch, W. 2004 Amorphous silicon exhibits a glass transition *Nature Materials* **3**, 804–809.

[69] Higuchi, K., Kimura, K., Mizuno, A., Watanabe, M., Katayama, Y. & Kuribayashi, K. 2005 Precise measurement of density and structure of undercooled molten silicon by using synchrotron radiation combined with electromagnetic levitation technique *Measurement Science and Technology* **16**, 381–385.

[70] Higuchi, K., Kimura, K., Mizuno, A., Watanabe, M., Katayama, Y. & Kuribayashi, K. 2007 Density and structure of undercooled molten silicon using synchrotron radiation combined with an electromagnetic levitation technique *Journal of Non-Crystalline Solids* **353**, 2997–2999.

[71] Holten, V., Bertrand, C. E., Anisimov, M. A. & Sengers, J. V. 2012 Thermodynamics of supercooled water *The Journal of Chemical Physics* **136(9)**, 094507.

[72] Hujo, W., Shadrack Jabes, B., Rana, V. K., Chakravarty, C. & Molinero, V. 2011 The rise and fall of anomalies in tetrahedral liquids *Journal of Statistical Physics* **145**, 293–312.

[73] Inatomi, Y., Onishi, F., Nagashio, K. & Kuribayashi, K. 2007 Density and thermal conductivity measurements for silicon melt by

electromagnetic levitation under a static magnetic field *International Journal of Thermophysics* **28**, 44–59.

[74] Jabes, B., Agarwal, M. & Chakravarty, C. 2010 Tetrahedral order, pair correlation entropy, and waterlike liquid state anomalies: Comparison of geo with bef, sio, and ho *The Journal of Chemical Physics* **132**, 234507.

[75] Jakse, N., Hennet, L., Price, D., Krishnan, S., Key, T., Artacho, E., Glorieux, B., Pasturel, A. & Saboungi, M. 2003 Structural changes on supercooling liquid silicon *Applied Physics Letters* **83**, 4734.

[76] Jakse, N. & Pasturel, A. 2007 Liquid-liquid phase transformation in silicon: Evidence from first-principles molecular dynamics simulations *Physical Review Letters* **99(20)**, 205702.

[77] Jakse, N. & Pasturel, A. 2008 Dynamic aspects of the liquid-liquid phase transformation in silicon *The Journal of Chemical Physics* **129(10)**, 104503.

[78] Jakse, N., Pasturel, A., Sastry, S. & Angell, C. A. 2009 Response to "Comment on 'Dynamic aspects of the liquid-liquid phase transformation in silicon' " [J. Chem. Phys. 130, 247102 (2009)] *The Journal of Chemical physics* **130(24)**, 247103.

[79] Karki, B. B., Bhattarai, D. & Stixrude, L. 2007 First-principles simulations of liquid silica: Structural and dynamical behavior at high pressure *Physical Review B* **76(10)**, 104205.

[80] Katayama, Y., Mizutani, T., Utsumi, W., Shimomura, O., Yamakata, M. & Funakoshi, K.-I. 2000 A first-order liquid-liquid phase transition in phosphorus *Nature* **403**, 170–173.

[81] Keblinski, P., Bazant, M., Dash, R. & Treacy, M. 2002 Thermodynamic behavior of a model covalent material described by

the environment-dependent interatomic potential *Physical Review B* **66(6)**, 064104.

[82] Kelton, K. & Greer, A. *Nucleation in condensed matter: Applications in materials and biology* vol. 15 A Pergamon Title, 2010.

[83] Kesselring, T., Franzese, G., Buldyrev, S., Herrmann, H. & Stanley, H. 2012 Nanoscale dynamics of phase flipping in water near its hypothesized liquid-liquid critical point *Scientific Reports* **2**.

[84] Kim, T., Lee, G., Sieve, B., Gangopadhyay, A., Hyers, R., Rathz, T., Rogers, J., Robinson, D., Kelton, K. & Goldman, A. 2005 In situ high-energy x-ray diffraction study of the local structure of supercooled liquid si *Physical Review Letters* **95(8)**, 85501.

[85] Kimura, H., Watanabe, M., Izumi, K., Hibiya, T., Holland-Moritz, D., Schenk, T., Bauchspiess, K. R., Schneider, S., Egry, I., Funakoshi, K. & Hanfland, M. 2001 X-ray diffraction study of undercooled molten silicon *Applied Physics Letters* **78**, 604.

[86] Krishnan, S., Hennet, L., Key, T., Glorieux, B., Saboungi, M. & Price, D. 2007 The structures of normal and supercooled liquid silicon metal and sige alloy *Journal of Non-Crystalline Solids* **353(32-40)**, 2975–2981.

[87] Kumar, P., Buldyrev, S., Becker, S., Poole, P., Starr, F. & Stanley, H. E. 2007 Relation between the widom line and the breakdown of the stokes–einstein relation in supercooled water *Proceedings of the National Academy of Sciences* **104(23)**, 9575.

[88] Kurita, R., Murata, K.-I. & Tanaka, H. 2008 Control of fluidity and miscibility of a binary liquid mixture by the liquid-liquid transition *Nature Materials* **7**, 647–652.

[89] Kurita, R. & Tanaka, H. 2004 Critical-like phenomena associated with liquid-liquid transition in a molecular liquid *Science* **306**, 845–848.

[90] La Nave, E., Sastry, S., Sciortino, F. & Tartaglia, P. 1999 Solution of lattice gas models in the generalized ensemble on the Bethe lattice *Physical Review E* **59**, 6348–6355.

[91] Langen, M. 1998 Measurement of the density and the thermal expansion coefficient of molten silicon using electromagnetic levitation *Journal of Crystal Growth* **186**, 550–556.

[92] Lechner, W., Dellago, C. & Bolhuis, P. 2011 Role of the prestructured surface cloud in crystal nucleation *Physical Review Letters* **106(8)**, 85701.

[93] Leyssale, J., Delhommelle, J. & Millot, C. 2005 Atomistic simulation of the homogeneous nucleation and of the growth of n crystallites *The Journal of Chemical Physics* **122**, 104510.

[94] Li, T., Donadio, D. & Galli, G. 2009 Nucleation of tetrahedral solids: A molecular dynamics study of supercooled liquid silicon *The Journal of Chemical Physics* **131**, 224519.

[95] Limmer, D. T. & Chandler, D. 2011 The putative liquid-liquid transition is a liquid-solid transition in atomistic models of water *The Journal of Chemical Physics* **135(13)**, 134503.

[96] Liu, D., Zhang, Y., Chen, C., Mou, C., Poole, P. & Chen, S. 2007 Observation of the density minimum in deeply supercooled confined water *Proceedings of the National Academy of Sciences* **104(23)**, 9570.

[97] Liu, L., Chen, S.-H., Faraone, A., Yen, C.-W. & Mou, C.-Y. 2005 Pressure dependence of fragile-to-strong transition and a possible second critical point in supercooled confined water *Physical Review Letters* **95(11)**, 117802.

[98] Lu, H. M., Wang, T. H. & Jiang, Q. 2006 Surface tension and self-diffusion coefficient of liquid Si and Ge *Journal of Crystal Growth* **293**, 294–298.

[99] Luedtke, W. D. & Landman, U. 1989 Preparation, structure, dynamics, and energetics of amorphous silicon: A molecular-dynamics study *Physical Review B* **40**, 1164–1174.

[100] Lynden-Bell, R. M. & Debenedetti, P. G. 2005 Computational Investigation of Order, Structure, and Dynamics in Modified Water Models *The Journal of Physical Chemistry B* **109(14)**, 6527–6534.

[101] Makhov, D. V. & Lewis, L. 2003 Isotherms for the liquid-gas phase transition in silicon from npt monte carlo simulations *Physical Review B* **67(15)**, 153202.

[102] Mallamace, F., Broccio, M., Corsaro, C., Faraone, A., Majolino, D., Venuti, V., Liu, L., Mou, C.-Y. & Chen, S.-H. 2007 Evidence of the existence of the low-density liquid phase in supercooled, confined water *Proceedings of the National Academy of Science* **104**, 424–428.

[103] Mancinelli, R., Bruni, F. & Ricci, M. A. 2010 Controversial evidence on the point of minimum density in deeply supercooled confined water *The Journal of Physical Chemistry Letters* **1(8)**, 1277–1282.

[104] Maria, T. & Barend, J. 2010 Thermodynamic properties and phase transitions of silicon using a new meam potential *Computational Materials Science* **48(3)**, 609 – 620.

[105] Matsumoto, M. & Nishimura, T. 1998 Mersenne twister: a 623-dimensionally equidistributed uniform pseudo-random number generator *ACM Transactions on Modeling and Computer Simulation (TOMACS)* **8(1)**, 3–30.

[106] McMillan, P. F. 2004 Amorphous materials: Relaxing times for silicon *Nature Materials* **3**, 755–756.

[107] McMillan, P. F., Wilson, M., Daisenberger, D. & Machon, D. 2005 A density-driven phase transition between semiconducting and metallic polyamorphs of silicon *Nature Materials* **4**, 680–684.

[108] Miranda, C. R. & Antonelli, A. 2004 Transitions between disordered phases in supercooled liquid silicon *The Journal of Chemical Physics* **120**, 11672–11677.

[109] Mishima, O. & Stanley, H. E. 1998 Decompression-induced melting of ice IV and the liquid-liquid transition in water *Nature* **392**, 164–168.

[110] Mishima, O. & Stanley, H. E. 1998 The relationship between liquid, supercooled and glassy water *Nature* **396**, 329–335.

[111] Molinero, V., Sastry, S. & Angell, C. A. 2006 Tuning of tetrahedrality in a silicon potential yields a series of monatomic (metal-like) glass formers of very high fragility *Physical Review Letters* **97(7)**, 075701.

[112] Monaco, G., Falconi, S., Crichton, W. A. & Mezouar, M. 2003 Nature of the first-order phase transition in fluid phosphorus at high temperature and pressure *Physical Review Letters* **90(25)**, 255701.

[113] Moore, E. B. & Molinero, V. 2011 Structural transformation in supercooled water controls the crystallization rate of ice *Nature* **479**, 506–508.

[114] Morales, M., Pierleoni, C., Schwegler, E. & Ceperley, D. 2010 Evidence for a first-order liquid-liquid transition in high-pressure hydrogen from ab initio simulations *Proceedings of the National Academy of Sciences* **107(29)**, 12799.

[115] Morishita, T. 2001 Liquid-liquid phase transitions of phosphorus via constant-pressure first-principles molecular dynamics simulations *Physical Review Letters* **87(10)**, 105701.

[116] Morishita, T. 2004 High density amorphous form and polyamorphic transformations of silicon *Physical Review Letters* **93(5)**, 055503.

[117] Morishita, T. 2006 How does tetrahedral structure grow in liquid silicon upon supercooling? *Physical Review Letters* **97(16)**, 165502.

[118] Moynihan, C. & Angell, C. A. 2000 Bond lattice or excitation model analysis of the configurational entropy of molecular liquids *Journal of Non-Crystalline Solids* **274**, 131–138.

[119] Nettleton, R. E. & Green, M. S. 1958 Expression in terms of molecular distribution functions for the entropy density in an infinite system *The Journal of Chemical Physics* **29**, 1365–1370.

[120] Okada, J. T., Sit, P. H.-L., Watanabe, Y., Wang, Y. J., Barbiellini, B., Ishikawa, T., Itou, M., Sakurai, Y., Bansil, A., Ishikawa, R., Hamaishi, M., Masaki, T., Paradis, P.-F., Kimura, K., Ishikawa, T. & Nanao, S. 2012 Persistence of covalent bonding in liquid silicon probed by inelastic x-ray scattering *Physical Review Letters* **108**, 067402.

[121] Plimpton, S. 1995 Fast parallel algorithms for short-range molecular dynamics *Journal of Computational Physics* **117(1)**, 1–19.

[122] Plimpton, S. 1995 Fast parallel algorithms for short-range molecular dynamics *Journal of Computational Physics* **117(1)**, 1 – 19.

[123] Ponyatovsky, E. G. 2003 A thermodynamic approach to T P phase diagrams of substances in liquid and amorphous states *Journal of Physics: Condensed Matter* **15**, 6123–6141.

[124] Poole, P., Saika-Voivod, I. & Sciortino, F. 2005 Density minimum and liquid-liquid phase transition *Journal of Physics: Condensed Matter* **17**, L431.

[125] Poole, P. H., Sciortino, F., Essmann, U. & Stanley, H. E. 1992 Phase behaviour of metastable water *Nature* **360**, 324–328.

[126] Poole, P. H., Sciortino, F., Essmann, U. & Stanley, H. E. 1993 Spinodal of liquid water *Physical Review E* **48**, 3799–3817.

[127] Rahman, A. 1964 Correlations in the motion of atoms in liquid argon *Physical Review* **136(2A)**, 405–411.

[128] Rapoport, E. 1967 Model for melting-Curve maxima at high Pressure *The Journal of Chemical Physics* **46**, 2891–2895.

[129] Rebelo, L. P. N., Debenedetti, P. G. & Sastry, S. 1998 Singularity-free interpretation of the thermodynamics of supercooled water. II. Thermal and volumetric behavior *The Journal of Chemical Physics* **109**, 626–633.

[130] Rhim, W. 2000 Thermophysical properties measurement of molten silicon by high-temperature electrostatic levitator: density, volume expansion, specific heat capacity, emissivity, surface tension and viscosity *Journal of Crystal Growth* **208**, 313–321.

[131] Rosato, V. & Celino, M. 1999 Tight binding simulation of the thermodynamic behavior of amorphous silicon *Journal of Applied Physics* **86**, 6826–6834.

[132] Rosato, V. & Celino, M. 2000 Thermodynamic properties of amorphous silicon via tight binding simulations *Computational Materials Science* **17(24)**, 374 – 379.

[133] Rosenfeld, Y. 1999 A quasi-universal scaling law for atomic transport in simple fluids *Journal of Physics: Condensed Matter* **11**, 5415.

[134] Saika-Voivod, I., Poole, P. & Bowles, R. 2006 Test of classical nucleation theory on deeply supercooled high-pressure simulated silica *The Journal of Chemical Physics* **124**, 224709.

[135] Saika-Voivod, I., Sciortino, F. & Poole, P. 2000 Computer simulations of liquid silica: Equation of state and liquid˘liquid phase transition *Physical Review E* **63(1)**, 011202.

[136] Sanders, P. G. & Aziz, M. J. 1999 Self-diffusivity of liquid silicon measured by pulsed laser melting *Journal of Applied Physics* **86**, 4258–4261.

[137] Sanz, E., Vega, C., Abascal, J. L. F. & MacDowell, L. G. 2004 Phase diagram of water from computer simulation *Physical Review Letters* **92**, 255701.

[138] Sasai, M. 1993 The random graph model of hydrogen bond network *Bulletin of the Chemical Society of Japan* **66(11)**, 3362–3371.

[139] Sastry, S. 2001 Water structure: Order and oddities *Nature* **409**, 300–301.

[140] Sastry, S. 2002 Onset of slow dynamics in supercooled liquid silicon *Physica A: Statistical Mechanics and its Applications* **315(12)**, 267 – 273.

[141] Sastry, S. 2010 Illuminating liquid polymorphism in silicon *Proceedings of the National Academy of Science* **107**, 17063–17064.

[142] Sastry, S. & Angell, C. 2003 Liquid-liquid phase transition in supercooled silicon *Nature Materials* **2**, 739–743.

[143] Sastry, S., Debenedetti, P., Sciortino, F. & Stanley, H. E. 1996 Singularity-free interpretation of the thermodynamics of supercooled water *Physical Review E* **53(6)**, 6144–6154.

[144] Sastry, S., Sciortino, F. & Stanley, H. E. 1993 Limits of stability of the liquid phase in a lattice model with water-like properties *The Journal of Chemical Physics* **98**, 9863–9872.

[145] Sato, Y., Nishizuka, T., Hara, K., Yamamura, T. & Waseda, Y. 2000 Density measurement of molten silicon by a pycnometric method *International Journal of Thermophysics* **21**, 1463–1471.

[146] Saw, S., Ellegaard, N. L., Kob, W. & Sastry, S. 2011 Computer simulation study of the phase behavior and structural relaxation in a gel-former modeled by three-body interactions *The Journal of Chemical Physics* **134(16)**, 164506.

[147] Scandolo, S. 2003 Liquid-liquid phase transition in compressed hydrogen from first-principles simulations *Proceedings of the National Academy of Sciences* **100(6)**, 3051.

[148] Sciortino, F. 2011 Liquid-liquid transitions: Silicon in silico *Nature Physics* **7**, 523–524.

[149] Sciortino, F., Geiger, A. & Stanley, H. 1991 Effect of defects on molecular mobility in liquid water *Nature* **354(6350)**, 218–221.

[150] Sciortino, F., Geiger, A. & Stanley, H. E. 1992 Network defects and molecular mobility in liquid water *The Journal of Chemical physics* **96**, 3857–3865.

[151] Sciortino, F., Saika-Voivod, I. & Poole, P. 2011 Study of the st2 model of water close to the liquid-liquid critical point *Physical Chemistry Chemical Physics* **13(44)**, 19759–19764.

[152] Sharma, R., Chakraborty, S. N. & Chakravarty, C. 2006 Entropy, diffusivity, and structural order in liquids with waterlike anomalies *The Journal of Chemical Physics* **125(20)**, 204501.

[153] Shell, M., Debenedetti, P. & Panagiotopoulos, A. 2002 Molecular structural order and anomalies in liquid silica *Physical Review E* **66(1)**, 011202.

[154] Spaepen, F. & Turnbull, D. Kinetics of motion of crystal-melt interfaces in *American Institute of Physics Conference Series* vol. 50 of *American Institute of Physics Conference Series* 1979.

[155] Speedy, R. 1982 Stability-limit conjecture. an interpretation of the properties of water *The Journal of Physical Chemistry* **86(6)**, 982–991.

[156] Speedy, R. J. & Angell, C. A. 1976 Isothermal compressibility of supercooled water and evidence for a thermodynamic singularity at -45deg$C$ *The Journal of Chemical Physics* **65**, 851–858.

[157] Starr, F. W., Douglas, J. F. & Sastry, S. 2013 The relationship of dynamical heterogeneity to the adam-gibbs and random first-order transition theories of glass formation *The Journal of Chemical Physics* **138**, 12A541.

[158] Steinhardt, P., Nelson, D. & Ronchetti, M. 1983 Bond-orientational order in liquids and glasses *Physical Review B* **28(2)**, 784.

[159] Stillinger, F. & Weber, T. 1985 Computer simulation of local order in condensed phases of silicon *Physical Review B* **31(8)**, 5262–5271.

[160] Stokely, K., Mazza, M., Stanley, H. & Franzese, G. 2010 Effect of hydrogen bond cooperativity on the behavior of water *Proceedings of the National Academy of Sciences* **107(4)**, 1301–1306.

[161] Talanquer, V. & Oxtoby, D. 1998 Crystal nucleation in the presence of a metastable critical point *The Journal of Chemical Physics* **109**, 223.

[162] Tanaka, H., Kurita, R. & Mataki, H. 2004 Liquid-liquid transition in the molecular liquid triphenyl phosphite *Physical Review Letters* **92(2)**, 025701.

[163] Tarazona, Y. R. P. 1998 Density functional theory and the asymptotic high density expansion of the free energy of classical solids and fluids *Molecular Physics* **95**, 141–150.

[164] Tarjus, G. & Kivelson, D. 1995 Breakdown of the stokes–einstein relation in supercooled liquids *The Journal of Chemical Physics* **103**, 3071.

[165] Ten Wolde, P., Ruiz-Montero, M. & Frenkel, D. 1996 Simulation of homogeneous crystal nucleation close to coexistence *Faraday Discussions* **104(0)**, 93–110.

[166] ten Wolde, P. R. 1998 Numerical study of pathways for homogeneous nucleation *Ph.D. thesis* .

[167] Thompson, M. O., Galvin, G. J., Mayer, J. W., Peercy, P. S., Poate, J. M., Jacobson, D. C., Cullis, A. G. & Chew, N. G. 1984 Melting temperature and explosive crystallization of amorphous silicon during pulsed laser irradiation *Physical Review Letters* **52**, 2360–2363.

[168] Togaya, M. 1997 Pressure dependences of the melting temperature of graphite and the electrical resistivity of liquid carbon *Physical Review Letters* **79**, 2474–2477.

[169] Toninelli, C., Wyart, M., Berthier, L., Biroli, G. & Bouchaud, J. 2005 Dynamical susceptibility of glass formers: Contrasting the predictions of theoretical scenarios *Physical Review E* **71(4)**, 041505.

[170] Torrie, G. & Valleau, J. 1974 Monte carlo free energy estimates using non-boltzmann sampling: Application to the sub-critical lennard-jones fluid *Chemical Physics Letters* **28(4)**, 578–581.

[171] Torrie, G. & Valleau, J. 1977 Nonphysical sampling distributions in monte carlo free-energy estimation: Umbrella sampling *Journal of Computational Physics* **23(2)**, 187–199.

[172] Truskett, T. M., Torquato, S. & Debenedetti, P. G. 2000 Towards a quantification of disorder in materials: Distinguishing equilibrium and glassy sphere packings *Physical Review E* **62**, 993–1001.

[173] Štich, I., Car, R. & Parrinello, M. 1989 Bonding and disorder in liquid silicon *Physical Review Letters* **63**, 2240–2243.

[174] Štich, I., Car, R. & Parrinello, M. 1991 Amorphous silicon studied by ab initio molecular dynamics: Preparation, structure, and properties *Physical Review B* **44**, 11092–11104.

[175] van Erp, T. 2011 Dynamical rare event simulation techniques for equilibrium and non-equilibrium systems *Arxiv preprint arXiv:1101.0927* .

[176] Vasisht, V. V., Saw, S. & Sastry, S. 2011 Liquid-liquid critical point in supercooled silicon *Nature Physics* **7**, 549–553.

[177] Vekilov, P. 2004 Dense liquid precursor for the nucleation of ordered solid phases from solution *Crystal Growth & Design* **4(4)**, 671–685.

[178] Vekilov, P. 2005 Two-step mechanism for the nucleation of crystals from solution *Journal of Crystal Growth* **275(1)**, 65–76.

[179] Voronin, G., Pantea, C., Zerda, T., Wang, L. & Zhao, Y. 2003 In situ x-ray diffraction study of silicon at pressures up to 15.5 GPa and temperatures up to 1073 K *Physical Review B* **68(2)**, 020102.

[180] Wang, Y., Zhao, G., Liu, C. & Zhu, Z. 2011 Ab initio molecular dynamics simulations on structural change of supercooled liquid Si at different temperatures from 1700 to 1100 K *Physica B: Condensed Matter* **406**, 3991–3996.

[181] Waseda, Y., Shinoda, K., Sugiyama, K., Takeda, S., Terashima, K. & Toguri, J. 1995 High temperature X-ray diffraction study of melt structure of silicon *Japanese Journal of Applied Physics* **34**, 4124.

[182] Watanabe, M., Adachi, M., Morishita, T., Higuchi, K., Kobatake, H. & Fukuyama, H. 2007 Does supercooled liquid Si have a density maximum? *Faraday Discussions* **136**, 279.

[183] Wautelet, M. 1990 On the transitions between the crystalline, amorphous, and liquid phases of silicon and germanium, when their size decreases *Physica Status Solidi B Basic Research* **159**, 43.

[184] Wedekind, J., Strey, R. & Reguera, D. 2007 New method to analyze simulations of activated processes *The Journal of Chemical Physics* **126**, 134103.

[185] Weeks, M. E. 1932 The discovery of the elements. xii. other elements isolated with the aid of potassium and sodium: Beryllium, boron, silicon, and aluminum *Journal of Chemical Education* **9(8)**, 1386.

[186] Wolde, P. R. t. & Frenkel, D. 1997 Enhancement of protein crystal nucleation by critical density fluctuations *Science* **277(5334)**, 1975–1978.

[187] Wu, C., Glosli, J., Galli, G. & Ree, F. 2002 Liquid-liquid phase transition in elemental carbon: A first-principles investigation *Physical Review Letters* **89(13)**, 135701.

[188] Xu, L., Mallamace, F., Yan, Z., Starr, F., Buldyrev, S. & Stanley, H. E. 2009 Appearance of a fractional stokes–einstein relation in water and a structural interpretation of its onset *Nature Physics* **5(8)**, 565–569.

[189] Xu, L. & Molinero, V. 2011 Is there a liquidliquid transition in confined water? *The Journal of Physical Chemistry B* **115(48)**, 14210–14216.

[190] Yamada, M., Mossa, S., Stanley, H. E. & Sciortino, F. 2002 Interplay between time-temperature transformation and the liquid-liquid phase transition in water *Physical Review Letters* **88(19)**, 195701.

[191] Zanotti, J.-M., Bellissent-Funel, M.-C. & Chen, S.-H. 2005 Experimental evidence of a liquid-liquid transition in interfacial water *EPL (Europhysics Letters)* **71**, 91–97.